DI Antonius Dorda, BSc

Auxiliary master equation approach for correlated quantum impurity problems out of equilibrium

DOCTORAL THESIS

to achieve the university degree of

Doktor der Naturwissenschaften

submitted to

Graz University of Technology

Supervisor

Univ.-Prof. Dr. Enrico Arrigoni

Institute of Theoretical and Computational Physics

Graz, June 2016

Abstract

The main topic of this thesis was the development of a method for the solution of nonequilibrium quantum impurity problems, which we termed auxiliary master equation approach (AMEA). The approach enables one to obtain accurate spectral functions in equilibrium and nonequilibrium situations, especially in the steady state regime but also for time-dependent cases. As such it can be applied, on the one hand, to a direct simulation of transport through small quantum systems such as quantum dots or molecular transistors, and on the other hand, as an impurity solver for dynamical mean field theory (DMFT). In the latter case, an investigation of nonequilibrium phenomena in extended systems such as correlated heterostructures, layers or similar geometries is possible. Within DMFT, we analyzed transport across a correlated layer and the transition from a nearly insulating Mott state to a strongly correlated metal, together with the temperature dependence of its transport characteristics. In the context of quantum dots, we applied the solver to study the challenging nonequilibrium Kondo regime and in particular the splitting behavior of the Kondo resonance at low energy scales. The combination of AMEA with matrix product states techniques has hereby proven to yield highly accurate spectral functions and observables at temperatures well below the Kondo scale, which enabled us to resolve the underlying physics in detail.

The detailed elaboration of the approach and the application and development of different solution strategies was the main topic and achievement of this PhD thesis. A series of articles on AMEA was published which now constitutes the main part of this cumulative dissertation and presents the results mentioned above. As customary for this type of thesis, an overarching introduction and summary is given. It provides a unified picture and complementary information to the descriptions in the publications, together with an overview over the main findings. In the introduction, more technical details on AMEA are presented and a recap of the nowadays well-understood equilibrium properties of Kondo systems is provided. This lays the ground and outlines the motivation to study the not yet clarified nonequilibrium Kondo regime in the subsequent articles section.

Key words: Nonequilibrium impurity solver, single impurity Anderson model, Kondo physics, dynamical mean field theory (DMFT), nonequilibrium Green's functions, exact diagonalization, matrix product states, multi-dimensional optimization.

Acknowledgements

First of all I want to express my sincere gratitude to Prof. Dr. Enrico Arrigoni for supervising my thesis and for the large amount of personal time and effort he put into its realization. I am very grateful for the possibility to have worked on this interesting and promising topic. I also want to thank him for the large support and for enabling me to travel to that many conferences, workshops and schools each year. I could benefit a lot from these experiences and it is not a thing to be taken for granted. Also, many thanks for the great ski tours.

I furthermore want to thank Prof. Dr. Wolfgang von der Linden and Prof. Dr. Hans Gerd Evertz for co-supervising this thesis, and also for their dedication and the time they invested. It was of great value and help to get additional advise and support in the joint discussions, and an ideal situation for me to be able to profit from the combined expertise of my three supervisors. In addition to it, I want to thank all three for a kind and pleasant collaboration.

Also, I am very thankful to Prof. Jan von Delft for inviting me to Munich and the inspiring and fruitful discussions with him and his group members Dr. Andreas Weichselbaum and DI Frauke Schwarz.

Thank you also to all the other members in the research group at the TU Graz, not only for fruitful discussions but especially for the nice time together in and outside of university. In particular I would like to thank my colleagues Dr. Martin Nuss, DI Max Sorantin, Prof. Dr. Markus Aichhorn, Dr. Elias Assmann, Dr. Irakli Titvinidze, Dr. Mohammad Zhian Asadzadeh, Dr. Martin Ganahl, DI Gerhard Dorn, DI Delia Fugger, DI Daniel Bauernfeind, DI Florian Maislinger, DI Robert Triebl, DI Manuel Zingl, DI Jakob Neumayer, DI Gernot Kraberger, Dr. Faruk Geles, DI Werner Dobrautz, DI Peter Schlosser, DI Manuel Pfeifenberger, and DI Michael Rumetshofer for a lot of fun during conferences, sports and various other activities.

Last but not least, a big thank you to my whole family and to all my friends. Most of all I would like to thank my parents, my sister Alice and my girlfriend Lisa for being there for me and for all their support and encouragement. And thank you to my friends for an amazing time during my studies here in Graz - I'd love to do it all over again!

AFFIDAVIT

I declare that I have authored this thesis independently, that I have not used other than the declared sources/resources, and that I have explicitly indicated all material which has been quoted either literally or by content from the sources used. The text document uploaded to TUGRAZonline is identical to the present doctoral thesis.

Date

Signature

Contents

1. Introduction

Strongly correlated electron systems are an interesting, challenging, and intensively studied field in condensed matter physics. Important emergent phenomena such as magnetism, high temperature superconductivity, Mott transition, or systems such as strange metals, which exhibit non-Fermi liquid properties, transition metal oxides and similar materials can only be explained and described theoretically when taking electron-electron interactions into account. The direct treatment of such interacting quantum manybody systems is generally unfeasible, so that approximations and appropriate models have to be devised. Famous lattice models in this respect are for instance the Hubbard, Heisenberg and Ising model, to mention just a few [7]. The Hubbard model was hereby introduced as an effective model to describe the physics of electrons in partially filled d or f shells, which have a very flat dispersion so that a localized description is suitable. It treats the kinetic part of the Hamiltonian as hoppings t from site to site and the electron-electron interaction only in leading order, by taking the on-site Coulomb repulsion U into account. However, despite of its simple mathematical form the solution of the Hubbard model constitutes a major challenge. Numerous different numerical and analytical techniques have been applied to clarify its physics in certain parameter regimes, see e.g. Ref. [8] for a recent review. Large progress has been made in the past quarter century, after the invention of the so-called dynamical mean field theory (DMFT) [9–12]. The method opened the possibility to describe delocalized wave-like states and localized quasi-bound states in a unified framework and thus, to properly address the Mott transition. It relies on the approximation to treat correlations between electrons only locally in space, but in contrast to an ordinary mean field theory it includes their dynamical effects. This approximation becomes exact in the limit of infinite dimensions $D \to \infty$, the atomic limit $U/t \to \infty$ and also in the non-interacting case $U \to 0$, so that one generally assumes to be able to interpolate between these points and to describe especially the physics in higher-dimensional cases appropriately.[1] Furthermore, DMFT laid the ground for extensions and more sophisticated methods which also take non-local correlations into account, see e.g. Ref. [13–15], by which the low-temperature properties of 2D systems are more reliably described. Nowadays, it is possible to address within DMFT multi-band Hubbard models and to compute also the equilibrium properties of realistic materials in DFT+DMFT[2], due to the invention of powerful impurity solvers [16–18].

Impurity solvers are of great importance for DMFT. Within this approach the interacting dynamics on the original lattice is mapped onto a self-consistent impurity problem, in which only a single interacting site is embedded into a continuous bath of noninteracting electrons. The complexity of the overall problem is by this significantly reduced and, independent of the original lattice parameters or geometry, the same type of manybody problem must be solved in the end. However, also impurity problems pose a theoretical

[1] In practice the approximation often yields accurate results already for 3D.

[2] For ab-initio calculations of strongly correlated materials one possible and successful approach is to combine DMFT with density functional theory (DFT).

challenge on their own, and the calculation of the interacting Green's functions is in general not exactly possible. Impurity models were devised much earlier in the context of the Kondo effect, in the combined effort of experimentalists and theoreticians, to shed light on the intriguing behavior of metal hosts with dilute magnetic impurities. The detailed explanation of the effect and the solution of the corresponding impurity models posed a longstanding problem, which lead to the development of dedicated numerical schemes [19]. In the course of the development of DMFT, findings based on this investigations could be used and renewed interest in the efficient solution of impurity problems arose. Nowadays, highly accurate impurity solvers for equilibrium situations exist, which are based on Monte Carlo schemes or renormalization group ideas [16–18]. For the nonequilibrium regime, however, new challenges have to be met and established solvers are not yet available.

Nonequilibrium DMFT and this work: The motivations and demands to extend the very successful DMFT ideas to the nonequilibrium case are twofold. On the one hand, advances in experimental techniques now make it possible to excite materials and in particular their electronic system far away from its equilibrium state together with probing it at ultrafast timescales, so that its internal dynamics can be studied in great detail. On the other hand, in most electronic applications such as transistors, memories, detectors or solar cells, materials have to operate under nonequilibrium conditions. It is therefore of great importance to be able to accurately describe and study the physics of driven strongly correlated systems. For the time-dependent case different numerical methods were devised which allow one to especially address ultrafast phenomena [20–24]. Most of all, Monte Carlo schemes such as Ref. [24, 25] are here very well applicable. But, in order to treat steady state physics such time-dependent approaches are generally cumbersome and their accuracy degrades in the long time limit. It is thus very desirable to employ solvers which work directly in the steady state. Numerous approaches exist, which were listed and discussed already in publications of this thesis in Ref. [1], Sec. 3.1, and Ref. [2], Sec. 3.2. However, it is challenging to reliably account for Kondo physics and nonequilibrium phenomena on an equal footing. The first results obtained with our solver were promising and we hope to contribute further to progress in this direction. In fact, our studies outlined in Ref. [1], Sec. 3.1, and especially in Ref. [2], Sec. 3.2, have demonstrated that the developed solver can very accurately address finite temperature Kondo physics in the equilibrium limit together with its successive suppression when making the transition to the large current-carrying nonequilibrium state. Furthermore, in the works Ref. [3], Sec. 3.3, and in Ref. [4], Sec. 3.4, we applied the solver within DMFT to steady state transport through a correlated layer. This sets the motivation to further extend the capabilities of the approach in future and to study also other properties of nonequilibrium Kondo physics and more interesting correlated systems within DMFT.

Before focusing on the approach and thus the main topic of this thesis itself, let us briefly recapitulate the Kondo effect and some of its basic and nowadays well-known equilibrium properties, and furthermore, introduce the corresponding impurity models. Many standard textbooks treat the topic in detail and we refer to Ref. [26,27] and especially to Ref. [28] for an in-depth explanation. At the end of the section, a brief outlook to the nonequilibrium regime is given together with the main motivation and the leading questions for the studies performed in Ref. [2], Sec. 3.2.

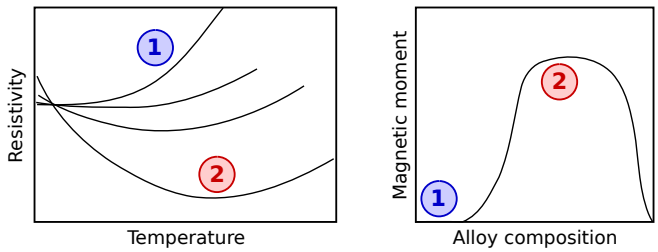

Figure 1.1.: Schematic drawing of the experimental findings by Clogston *et al.* and Sarachik *et al.* in Ref. [29,30]. Impurities in different metal alloys may develop a local magnetic moment, see (2), and exactly in this cases an unusual minimum in the resistivity is found when lowering the temperature, the Kondo effect.

1.1. Impurity problems and the Kondo effect

Kondo effect: The Kondo effect was first discovered in 1934 when de Haas *et al.* investigated gold samples with a small amount of magnetic impurities [31]. At that time the conventional wisdom was that the resistivity of normal conducting metals at low temperature is a monotonic function of T, and should thus decrease and then saturate at a finite value when approaching temperature $T \approx 0\,K$. The leading contribution to the resistivity was believed to be due to phonons, which scales as T^5, and impurity scattering was supposed to contribute only a constant background. However, what was found in the metal samples with dilute magnetic impurities was, that the resistivity exhibited a minimum when lowering the temperature and rose again when approaching $T \to 0$. This effect was later on termed Kondo effect and its proper explanation posed a longstanding problem. Important input from the experimental side was the correlation between the magnetic moment of impurities and the resistivity minimum, which was found in measurements carried out by Clogston *et al.* and Sarachik *et al.* in the 1960s [29,30], see also the sketch in Fig. 1.1. Based on the particular trends in this measurements, Kondo argued 1964 that the resistivity minimum must originate from the spin degree of freedom of the impurities, and furthermore, was evidently a single impurity effect rather than a collective behavior of all impurities together [28,32]. To show this, Kondo calculated perturbatively the scattering of conduction electrons off the local impurity spin up to third order. The high order in this perturbative analysis of the spin-flip scattering was crucial since the terms encountered up to second order were essentially the same as when calculating the ordinary potential scattering off the impurity. Due to this the relevance of spin-flip scattering was overlooked up to this time and Kondo was the first to point out that the higher orders in the perturbation series contain new and conspicuous terms [26]. In particular, the third-order analysis revealed a scattering term which depended on the occupation number of the conduction electrons and thus introduced a cut-off in the transport integrals at the Fermi energy. This lead to the appearance of logarithmic corrections and Kondo found the following temperature dependence of the resistivity [26–28][3]

$$R(T) = a + bT^5 - c\log\left(\frac{T}{D}\right), \tag{1.1}$$

[3]Throughout this work we adopt units so that $k_B = \hbar = e = 1$.

whereby the resistivity constants a and c depend on the impurity concentration, and D represents the half bandwidth of the conduction electrons. By this the minimum in the resistivity could be explained since $c > 0$ in the considered case. However, the logarithmic term in Eq. (1.1) does not predict a saturation of the resistivity for $T \to 0$ but instead a divergence. This is unphysical, of course, and demonstrates the breakdown of this perturbative analysis. Higher-order perturbative calculations carried out in the subsequent years revealed logarithmic corrections in the higher terms as well, so that it became clear that the effect must be properly addressed in a non-perturbative manner. Due to this, the result in Eq. (1.1) can be seen as an expansion valid in the high temperature regime $T \gg T_K$, with T_K the Kondo temperature as discussed below, and the solution of the $T \to 0$ limit posed an unresolved issue for years, which became known as the Kondo problem [28].

Kondo model and low temperature physics: Two important and related impurity models in the context of Kondo physics are the Anderson and the Kondo model. The Anderson model is hereby richer in structure since it allows spin as well as charge degrees of freedom for the impurity. This is more realistic, since the magnetic moment of impurities is caused by an electron in a partially filled shell. However, in appropriate parameter regimes (see below) the two models exhibit the same low-energy physics. It is convenient for our purposes here to discuss the Anderson model directly in the context of quantum dots, which is done in the next paragraph below, and to focus for the moment solely on the Kondo model. In this model one considers a single localized spin $\boldsymbol{S}$, representing the impurity degree of freedom, which interacts with the spins of the surrounding conduction electrons via an exchange coupling J, so that the Hamiltonian is given by [26, 27]

$$H = \sum_{k\sigma} \varepsilon_k c^\dagger_{k\sigma} c_{k\sigma} + J \sum_{kk'\alpha\beta} c^\dagger_{k\alpha} c_{k'\beta} \boldsymbol{\sigma}_{\alpha\beta} \boldsymbol{S} \,. \tag{1.2}$$

A value $J < 0$ favors a ferromagnetic ordering and $J > 0$ an antiferromagnetic one, whereby only in the latter case Kondo physics is found. Here, $c^\dagger_{k\sigma}/c_{k\sigma}$ represent the fermionic creation and annihilation operators of the conduction electrons with quantum number k and spin σ, ε_k is the corresponding dispersion relation, and $\boldsymbol{\sigma}_{\alpha\beta}$ denotes the vector of Pauli matrices. We assume for $\boldsymbol{S}$ a single spin-1/2 particle and it is important to note that the isolated impurity states with up or down spin are energetically degenerate. The exchange term may be rewritten in the z-basis as [26]

$$\sum_{\alpha\beta} c^\dagger_{k\alpha} c_{k'\beta} \boldsymbol{\sigma}_{\alpha\beta} \boldsymbol{S} = \left(c^\dagger_{k\uparrow} c_{k'\uparrow} - c^\dagger_{k\downarrow} c_{k'\downarrow} \right) S^z + c^\dagger_{k\uparrow} c_{k'\downarrow} S^- + c^\dagger_{k\downarrow} c_{k'\uparrow} S^+ \,, \tag{1.3}$$

by which the spin flip terms become apparent. At low T the occupation number $c^\dagger_{k\sigma} c_{k\sigma}$ exhibits a sharp jump at the Fermi energy E_F, so that only conduction electrons with energy $\omega \approx E_F$ can undergo a spin flip process. When lowering the temperature, one finds that this resonant spin flip scattering completely entangles the impurity spin with the conduction electrons and ultimately forms a collective singlet state for $T \to 0$. As a result, the magnetic moment of the impurity is fully compensated by the surrounding electrons [26–28], which form the so-called Kondo screening cloud.

The change in the ground state energy due to the spin flip processes is associated with a low-energy scale, the Kondo temperature T_K, which depends exponentially on the parameters of the model [27]

$$T_K = D\sqrt{2J\rho_0}\exp\left(-\frac{1}{2J\rho_0}\right), \tag{1.4}$$

with D the half bandwidth and $\rho(\omega) \approx \rho_0$ the density of conduction electron states. The remarkable feature of the Kondo model is its universal low-energy physics which depends solely on the dynamic scale T_K. Various measurable quantities such as the magnetic susceptibility, specific heat or scattering rates are universal functions of T/T_K [27, 28]. In the crossover regime $T \approx T_K$ one finds a logarithmic dependence, see also Eq. (1.1) above, and in the very low temperature regime $T \ll T_K$ a power law behavior. The scaling properties together with the exponentially small energy scale could only be fully accounted for with renormalization group (RG) methods. Anderson's "poor man's scaling" gave important insights [27,28], and with the invention of Wilson's numerical RG in 1975 (NRG) [19] the Kondo model could eventually be solved. The corresponding RG scheme is based on successively integrating out high-energy excitations to obtain a renormalized low-energy model, and as soon as the model parameters become invariant under the RG transformation a fixed point is reached. The so-called weak coupling fixed point $J = 0$ is relevant for the ferromagnetic model for $T \to 0$, and in the antiferromagnetic case the $T \to 0$ physics is determined by the strong coupling fixed point $J = \infty$, which builds up the above mentioned Kondo singlet as ground state [27, 28].[4]

The singular coupling of the impurity spin to conduction electrons at $\omega \approx E_F$ has drastic consequences for the local density of states on the impurity. A sharp resonance with a width $\propto T_K$ is formed at $\omega = E_F$, the so-called Kondo peak or Abrikosov-Suhl resonance [26–28]. This is addressed below in the context of the Anderson impurity model in more detail. It is important to note further that exact results for these impurity models could later be obtained by Bethe's ansatz, which gave complementary information to the RG approaches and resolved thermodynamic properties. Furthermore, important insights were provided by the connection of the strong coupling fixed point to a local Fermi liquid [27,28]. From this it is known that the inverse lifetime of the low-energy excitations at $\omega \approx E_F$ scales as $\Im\{\Sigma^R(\omega)\} \propto (\omega - E_F)^2$, resulting in long-lived quasi particles, and the particular power law behavior can be computed when introducing a small temperature $T \ll T_K$ or other source of decoherence such as a bias voltage, see below [27, 28, 33].

Anderson model: In the single impurity Anderson model (SIAM) the impurity is given by a single spin-dependent site with on-site energy $\varepsilon_{f\sigma}$ and an on-site Coulomb repulsion determined by the Hubbard U, which hybridizes via hoppings V_k with the conduction electrons $c^\dagger_{k\sigma}/c_{k\sigma}$ [27, 28, 34]:[5]

$$H = \sum_\sigma \varepsilon_{f\sigma} n_{f\sigma} + U n_{f\uparrow} n_{f\downarrow} + \sum_{k\sigma} \varepsilon_k c^\dagger_{k\sigma} c_{k\sigma} + \sum_{k\sigma} \left(V_k c^\dagger_{k\sigma} c_{f\sigma} + \text{h.c.} \right). \tag{1.5}$$

The index f indicates the impurity site, $c^\dagger_{f\sigma}/c_{f\sigma}$ are the fermionic creation and annihilation operators and the particle density is given by $n_{f\sigma} = c^\dagger_{f\sigma} c_{f\sigma}$. The continuous density of states $\rho(\omega) = \sum_k \delta(\varepsilon_k - \omega) \approx \rho_0$ of conduction electrons is assumed to exhibit a sufficiently

[4] Note that $J = 0$ represents a decoupling into an isolated spin, and in Wilson's representation of the bath in Eq. (1.2) as a tight-binding chain, $J = \infty$ corresponds to the formation of a singlet between the impurity and the first site of the Wilson chain together with a decoupling of the remaining sites [28].

[5] Here and in the following equations h.c. denotes Hermitian conjugate.

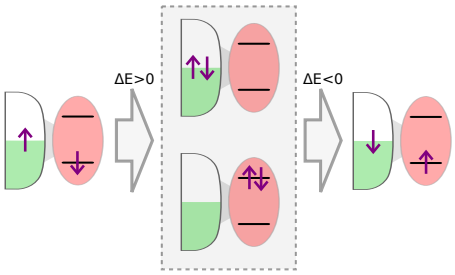

Figure 1.2.: Effective spin-flip via a second-order hopping process and an intermediate virtual state. The impurity is drawn in red, together with its possible single and double occupied states, and the filling of the bath for the conduction electrons is indicated in green. Only electrons at the Fermi edge can undergo a spin-flip.

large half bandwidth D, larger than all bare impurity energies. The Fermi energy E_F of these bath electrons is taken to be zero. The only relevant quantity of the bath for the low-energy physics is then given by the so-called hybridization strength Γ,

$$\Gamma = -\Im\left\{\Delta^R(\omega=0)\right\} = \pi \sum_k |V_k|^2 \delta(\varepsilon_k - \omega) = \pi V^2 \rho_0 \,, \tag{1.6}$$

related to the retarded hybridization function $\Delta^R(\omega)$ as defined below in Sec. 1.2.

For fully developed Kondo physics one needs degeneracy in spin and one thus typically considers $\varepsilon_{f\sigma} = \varepsilon_f$. In the atomic limit the decoupled impurity has four possible states: The empty state has energy $E_{|0\rangle} = 0$, the single occupied states have $E_{|\sigma\rangle} = \varepsilon_f$, and the double occupied state $E_{|\uparrow\downarrow\rangle} = 2\varepsilon_f + U$. In the particle-hole symmetric case $\varepsilon_f = -U/2$ the states $|\sigma\rangle$ are lowest in energy for $U > 0$. When taking the hybridization with the conduction electrons into account one finds in a mean field treatment that a local moment on the impurity can develop for $U > \pi\Gamma$ [27]. The mean field approximation is a drastic one, of course, but it indicates the regime in which a local moment on the impurity site can form at high temperatures. An effective spin flip is possible via a second order hopping process into the bath, as sketched in Fig. 1.2. In the large interaction limit $U \gg \Gamma$ one thus obtains the analogous behavior as in the Kondo model above, namely that the impurity is essentially in single occupied states and interacts with the bath through spin flip processes. With a projection technique or a canonical transformation, as done by Schrieffer and Wolff [35], the Anderson model can be mapped onto the Kondo model. By the restriction to the single occupied sector and by integrating out the charge fluctuations a renormalization to the low-energy physics is performed. The obtained exchanged coupling J is given in terms of the SIAM parameters by $J = 4|V|^2/U$, so that one finds for the Kondo temperature the expression [27, 28]

$$T_K = \sqrt{\frac{2U\Gamma}{\pi}} \exp\left(-\frac{\pi U}{8\Gamma}\right) , \tag{1.7}$$

when replacing in Eq. (1.4) the high-energy cutoff D by $U/2$ [27].[6] Due to this the Anderson model is governed on a low-energy scale by the same Kondo physics as described above.

[6] One should note that various slightly different definitions for T_K exist, also based on measurable quantities, see e.g. Ref. [2], Sec. 3.2. Common to all is the exponential dependence on the ratio U/Γ.

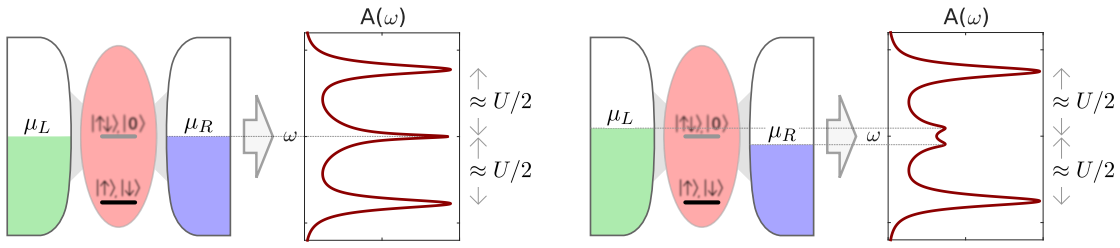

Figure 1.3.: Anderson impurity coupled to two leads at chemical potentials μ_L and μ_R, on the left in the equilibrium case $\mu_L = \mu_R$, and on the right in nonequilibrium driven by a nonzero bias voltage $\phi = \mu_L - \mu_R > 0$. The corresponding spectral functions $A(\omega)$ are shown, with a split Kondo peak on the right.

When analyzing the symmetric SIAM with NRG, one finds that the strong coupling fixed point is the only stable point in the low-energy limit [28]. Furthermore, the Fermi liquid properties of the ground state tell one that the low-energy excitations at $\omega \approx E_F$ are adiabatically connected to the noninteracting case $U = 0$. As a result, by the so-called Friedel sum rule it is ensured that the spectral function $A(\omega)$, which represents the local density of states on the impurity, see Sec. 1.2 below, takes on its unitary limit at the Fermi energy [27, 28, 36]

$$A(\omega = E_F) = \frac{1}{\pi\Gamma}\,, \tag{1.8}$$

for $T = 0$ and any value of U. The relevant energy scale for this low-energy physics is T_K, so that $A(\omega)$ develops a sharp Kondo peak at $\omega \approx E_F$ with a width determined by T_K. The peak width thus becomes exponentially small with increasing U due to Eq. (1.7). A typical situation for the overall spectral function for the equilibrium SIAM is displayed on the left-hand side in Fig. 1.3.[7] The characteristic three-peak structure is visible. The peak in the middle corresponds to the Kondo resonance and the Hubbard bands at $\omega \approx \pm U/2$ to incoherent charge excitations, with a width determined by the local value of the frequency-dependent hybridization strength $-\Im\left\{\Delta^R(\omega)\right\}$.

Kondo effect in quantum dots: Besides its relevance for bulk metals with dilute magnetic impurities, the Kondo effect has regained attention in recent years also due to its realization and significance in quantum dot experiments, see e.g. Ref. [37,38]. The confined electronic states in a quantum dot are often very well approximated by a SIAM, similar as discussed above but now attached to two baths of electrons instead of one, which we refer to as leads, see also Fig. 1.3. The chemical potentials of the leads are labeled by μ_L and μ_R.[8] In the single occupied state $\varepsilon_f = -U/2$, with nonzero U and weak dot-lead coupling $\Gamma \ll 1$, one finds at high enough temperatures $T \gg T_K$ a Coulomb blockade, so that transport from one lead to the other is suppressed. However, when approaching the limit $T \to 0$ for $\mu_L = \mu_R = 0$ so that a Kondo effect can develop, the singular coupling between the dot and the leads at $\omega \approx 0$ causes a perfect conductance at zero bias. This comes about since the current for an infinitesimal bias voltage $\phi = \mu_L - \mu_R \approx 0$ is determined by $A(\omega = 0)$, which takes on the maximally possible value by virtue of Eq. (1.8). The

[7] Note that the conduction electrons are represented in this figure by two leads, see next paragraph below.
[8] In this context we adopt the more common notation of a chemical potential instead of Fermi energy.

Coulomb blockade is thus completely compensated for and the effect is referred to as zero bias anomaly. On the whole, the Kondo effect manifests itself in quantum dots in sort of an opposite manner when compared to bulk metals. Above it was stated that a minimum in the resistivity curve $R(T)$ is found, but in quantum dots one finds instead a minimum in the conductivity $G(T)$ as a function of temperature.

A very interesting and yet not completely resolved question is the fate of the Kondo resonance when a nonzero bias voltage is applied, which was one of the main topics addressed in this thesis. The field of nonequilibrium Kondo physics has been a very active area of research in recent years and numerous different approaches were applied to clarify the physics in certain parameter regimes. An overview of previous literature is listed in Ref. [2], attached in Sec. 3.2 below. Here, we solely want to outline in a qualitative manner the main focus. In the very low-energy limit $\phi \approx 0$ linear response is applicable, and for $T \approx 0$ the transport coefficients are known from Fermi liquid theory. A very large bias voltage, on the other hand, represents a major source of decoherence similar to a large temperature and one effectively obtains a weak coupling problem. In the latter case perturbative techniques can be applied, which revealed weak excitations in $A(\omega)$ at the positions of μ_L and μ_R [39, 40]. In the intermediate region, beyond linear response and thus in a true nonequilibrium regime but still at voltages comparable with T_K, exact results are not yet available. It is precisely this regime that we aimed at in the studies presented in Ref. [2], Sec. 3.2. What we found were two distinct excitations close to μ_L and μ_R for voltages just above T_K, as sketched in Fig. 1.3 on the right, and a linear splitting behavior when increasing ϕ (compare also Ref. [1], Sec. 3.1). The transition from the single to the split Kondo peak occurred hereby in a simple and smooth way. At first, the bias voltage suppressed, then broadened and finally split the Kondo resonance in two peaks. For the onset of splitting we could estimate a value of $\phi \approx 1 - 2\,T_K$. All the calculations presented in Ref. [2] were performed at a finite temperature T, but well below T_K. Especially the excellent agreement with a NRG reference calculation in the equilibrium limit $\phi = 0$ demonstrated the high achievable accuracy of the approach, and thus motivates us to further pursue these studies in future.

1.2. Nonequilibrium Green's functions

Since the approach presented in this thesis is formulated in terms of nonequilibrium Green's functions, we briefly recap the basics here. Green's functions are a powerful and well-developed framework to address strongly correlated manybody systems in the equilibrium and also in the nonequilibrium regime. Their appealing feature is that a systematic perturbation series is available with an intuitive diagrammatic representation. Furthermore, they are closely related to response functions of interacting manybody systems and thus enable one to compute measurable quantities relevant for experiments, without the need to fully diagonalize the interacting system [7, 41]. The formalism was generalized to the nonequilibrium case by Kadanoff, Baym and separately by Keldysh [42–44], and allows one to make use of the same basic concepts and an analogous perturbative expansion. Since a profound introduction to nonequilibrium Green's functions is beyond the scope of this thesis we refer to excellent textbooks and reviews on the topic, for instance Ref. [41,45,46], and also to the articles Ref. [47–49].

At the heart of the nonequilibrium Green's functions lies the introduction of a special

contour ordering on the time axis. Since the two time limits $t \to \pm\infty$ are not equivalent anymore, as in the equilibrium case, the only available reference point is the infinite past. When neglecting any initial correlations and therefore the so-called Matsubara branch, cf. Ref. [45–48], which is correct in the steady state for instance, one ends up with a 2×2 structure in Keldysh space and has to consider Green's functions of the form

$$\underline{G}(\omega) = \begin{pmatrix} G^R(\omega) & G^K(\omega) \\ 0 & G^A(\omega) \end{pmatrix} . \tag{1.9}$$

Since we are interested in the steady state regime where time translational invariance applies, one can write all functions in the frequency domain ω. In contrast to the equilibrium case, a single Green's function does not suffice anymore to describe all the relevant physics on a single particle level. Due to the relation of the advanced to the retarded Green's function $G^A(\omega) = G^R(\omega)^\dagger$, a common choice is to consider $G^R(\omega)$ and the Keldysh component $G^K(\omega)$ as independent functions. For actual computations it is furthermore convenient to introduce the so-called lesser $G^<(\omega)$ and greater $G^>(\omega)$ functions. In the steady state limit they are defined by the following correlation functions in the time domain

$$\begin{aligned} G^<(t) &= i \left\langle c^\dagger c(t) \right\rangle_\infty , \\ G^>(t) &= -i \left\langle c(t) c^\dagger \right\rangle_\infty , \\ G^R(t) &= -i\Theta(t) \left\langle \left\{ c(t), c^\dagger \right\} \right\rangle_\infty , \\ G^K(t) &= -i \left\langle \left[c(t), c^\dagger \right] \right\rangle_\infty . \end{aligned} \tag{1.10}$$

Here $c^\dagger/c$ denote fermionic creation / annihilation operators, whereby a spin or site index was neglected for clarity,[9] $\langle \ldots \rangle_\infty$ indicates expectation values in the steady state limit, $\{A, B\}$ represents the anti- and $[A, B]$ the commutator of A and B, and $\Theta(t)$ is the Heaviside step function. The Green's functions in frequency domain are obtained by a Fourier transformation $G(\omega) = \int G(t) \exp(i\omega t) dt$. Another central object is the so-called spectral function $A(\omega)$, which is related to the functions above by

$$A(\omega) = \frac{i}{2\pi} \left(G^R(\omega) - G^A(\omega) \right) = \frac{i}{2\pi} \left(G^>(\omega) - G^<(\omega) \right) . \tag{1.11}$$

The meaning of the spectral function is the same as in equilibrium, namely it corresponds to the local density of states at the considered site. From the definitions in Eq. (1.10) it follows further that $G^K(\omega) = G^>(\omega) + G^<(\omega)$. In the equilibrium limit the Green's functions obey the so-called fluctuation dissipation theorem and are related to each other via the Fermi-Dirac distribution function $f(\omega, \mu, T)$ by

$$\begin{aligned} G^<(\omega) &= 2\pi i f(\omega, \mu, T) A(\omega) , \\ G^>(\omega) &= 2\pi i \left(f(\omega, \mu, T) - 1 \right) A(\omega) , \\ G^K(\omega) &= 2\pi i \left(2f(\omega, \mu, T) - 1 \right) A(\omega) , \end{aligned} \tag{1.12}$$

so that the knowledge of the spectral function together with μ and T suffices to fully specify the physical situation. In the nonequilibrium regime this is not the case since a

[9] Objects of the form $\langle c^\dagger_{i\sigma} c(t)_{j\sigma'} \rangle$ would result in analogous matrix expressions.

distribution function is not known a priori. As one can see from Eq. (1.12), the lesser Green's function is related to the occupation of electrons, the greater to the occupation of holes and the Keldysh may be interpreted as the occupation of electrons minus the one of holes. Therefore, the three functions $G^<(\omega)$, $G^>(\omega)$ and $G^K(\omega)$ are directly related to observables, and the particle density for instance is given by

$$\begin{aligned} n &= -\frac{i}{2\pi}\int G^<(\omega)d\omega \\ &= \frac{1}{2} - \frac{i}{4\pi}\int G^K(\omega)d\omega\,. \end{aligned} \tag{1.13}$$

An expression for the current in terms of the Green's functions $G^<(\omega)$ and $G^R(\omega)$ is provided by the Meir-Wingreen expression, see Ref. [41, 49, 50].

Dyson's equation for the SIAM: When making use of the Keldysh Green's functions formalism Eq. (1.9), essentially the same expressions known from equilibrium hold true, only that each quantity has to be replaced by a 2×2 object in Keldysh space, which we denote by $\underline{\ldots}$ in the following. Let us now consider the particular case of a single spin-dependent impurity coupled to a continuous bath of electrons, i.e. the SIAM as discussed above, see Eq. (1.5). The SIAM hereby represents the physical situation itself or a self-consistent impurity problem as obtained in the DMFT cycle. For simplicity let us consider the first case, so an impurity coupled to leads λ. An important object is the so-called hybridization function

$$\underline{\Delta}(\omega) = \sum_\lambda {t'_\lambda}^2 \underline{g}_\lambda(\omega)\,, \tag{1.14}$$

which depends on the surface Green's functions $\underline{g}_\lambda(\omega)$ of lead λ, and on the hoppings t'_λ from the impurity to each lead. Note that $\underline{g}_\lambda(\omega)$ is calculated for the case of decoupled leads, and typically one assumes ideal reservoirs which were in equilibrium at $t \to -\infty$ before coupling to the impurity. Therefore, $g^R_\lambda(\omega)$ is related to the density of states in the leads and the filling $g^K_\lambda(\omega)$ is determined by their chemical potential and temperature through Eq. (1.12). A semi-circular density of states in the leads, for instance, is represented by a chain of sites with constant hopping, see also Fig. 2.1. However, one must emphasize that the particular geometry of the leads does not matter and the physics on the impurity site is invariant under unitary transformations among sites in the leads only, see e.g. Ref. [51] and also Sec. A.2 below. The hybridization function is therefore a convenient quantity which fully specifies the correlation functions on the impurity site. As can be easily checked by equations of motion techniques, see for instance [41], Dyson's equation for the noninteracting case is given by

$$\underline{G}_0^{-1}(\omega) = \underline{g}_0^{-1}(\omega) - \underline{\Delta}(\omega)\,. \tag{1.15}$$

Here, $\underline{g}_0(\omega)$ is the Green's function of the decoupled central system without interaction, and $\underline{G}_0(\omega)$ is the noninteracting Green's function of the central system coupled to the leads, i.e. in the steady state. For the isolated impurity we have $g_0^{R\,-1}(\omega) = \omega - \varepsilon_f + i0^+$ and $g_0^K(\omega) \propto \delta(\omega - \varepsilon_f)$, with the prefactor depending on the initial filling. The latter, however, is irrelevant in the steady state.

To evaluate equations in Keldysh formalism the Langreth rules are useful, which state how products of contour-ordered objects are transformed [41]. For our purposes we need especially the inverse of a Keldysh "object", i.e.

$$\begin{aligned}\left(\underline{G}^{-1}\right)^R &= \left(G^R\right)^{-1}\,,\\ \left(\underline{G}^{-1}\right)^K &= -\left(G^R\right)^{-1} G^K \left(G^A\right)^{-1}\,.\end{aligned} \tag{1.16}$$

Evidently, the retarded component transforms in a simple way and only the Keldysh component is more involved. By this, Dyson's equation (1.15) can be rewritten as [41]

$$\begin{aligned}G_0^{R^{-1}}(\omega) &= g_0^{R^{-1}}(\omega) - \Delta^R(\omega)\,,\\ G_0^K(\omega) &= \left[1 + G_0^R(\omega)\Delta^R(\omega)\right] g_0^K(\omega) \left[1 + \Delta^A(\omega)G_0^A(\omega)\right] + G_0^R(\omega)\Delta^K(\omega)G_0^A(\omega)\\ &= G_0^R(\omega)\Delta^K(\omega)G_0^A(\omega)\,,\end{aligned} \tag{1.17}$$

where the last line is valid for a sufficiently large support of the lead density of states $\propto \Im\{\Delta^R(\omega)\}$, since the term with $g_0^K(\omega)$ is then infinitesimal.[10] The physical meaning of this is, that a connected system without bound states takes on a unique steady state in which the initial filling of the finite central region, i.e. $g_0^K(\omega)$, does not play a role. This is the situation we are considering in the following.

For the interacting case one introduces a self-energy $\underline{\Sigma}(\omega)$, as usual, which accounts for all manybody effects on the level of the single-particle Green's functions. Dyson's equation for the interacting Green's function $\underline{G}(\omega)$ of the coupled impurity in the steady state is

$$\begin{aligned}\underline{G}^{-1}(\omega) &= \underline{g}_0^{-1}(\omega) - \underline{\Delta}(\omega) - \underline{\Sigma}(\omega)\\ &= \underline{G}_0^{-1}(\omega) - \underline{\Sigma}(\omega)\,,\end{aligned} \tag{1.18}$$

and with Eqs. (1.16) and (1.17)[11] one finds

$$\begin{aligned}G^{R^{-1}}(\omega) &= G_0^{R^{-1}}(\omega) - \Sigma^R(\omega)\\ &= g_0^{R^{-1}}(\omega) - \Delta^R(\omega) - \Sigma^R(\omega)\,,\\ G^K(\omega) &= \left[1 + G^R(\omega)\Sigma^R(\omega)\right] G_0^K(\omega) \left[1 + \Sigma^A(\omega)G^A(\omega)\right] + G^R(\omega)\Sigma^K(\omega)G^A(\omega)\\ &= G^R(\omega)\left[\Delta^K(\omega) + \Sigma^K(\omega)\right] G^A(\omega)\,.\end{aligned} \tag{1.19}$$

In an equilibrium calculation, $\Delta^K(\omega)$ as well as $\Sigma^K(\omega)$ fulfill the fluctuation dissipation theorem Eq. (1.12), and as a consequence, also $G^K(\omega)$ does. In nonequilibrium this is not the case anymore, of course, and $\Sigma^K(\omega)$ accounts for the changes in the occupation when interactions are taken into account, whereas $\Sigma^R(\omega)$ determines how the local density of states $A(\omega)$ is modified. In equilibrium and even more in nonequilibrium, the computation of the Keldysh self-energy $\underline{\Sigma}(\omega)$ for such an interacting quantum system of infinite size is a difficult task. Exact results are available only in rare cases and one has to resort to approximations in general. A numerical scheme, whose development was the main task of this thesis, and which allows for an accurate calculation of $\underline{\Sigma}(\omega)$ for general nonequilibrium impurity problems is presented in the following chapter.

[10] The term is equal to $G_0^R g_0^{R^{-1}} g_0^K g_0^{A^{-1}} G_0^A \propto i0^+ / \left[(\omega - \varepsilon_f - \Re\{\Delta^R\})^2 + (0^+ - \Im\{\Delta^R\})^2\right]$ and thus infinitesimal when $\Im\{\Delta^R(\omega)\} \neq 0$ at all roots of $(\omega - \varepsilon_f - \Re\{\Delta^R(\omega)\})$. This is not the case, for instance, when the coupling t_λ in Eq. (1.14) is so large that (bound) states lie outside the support of $\Im\{\Delta^R(\omega)\}$.

[11] The last line for $G_0^K(\omega)$ is used.

2. Auxiliary master equation approach

As discussed in Sec. 1, the accurate solution of quantum impurity problems is of great interest due to its relevance for nanoscale transport and for DMFT, and currently a very active area of research. The auxiliary master equation approach (AMEA), which is the main topic of this thesis, is a versatile impurity solver for general nonequilibrium or equilibrium situations and is especially suited to treat the steady state. It can be applied, on the one hand, directly to transport across quantum dots or small molecules and on the other hand, as an impurity solver within (nonequilibrium) DMFT in order to consider transport in extended systems. Its major advantages compared to other approaches are: (i) it can be directly formulated in the steady state limit, (ii) it does not rely on perturbative techniques and instead exhibits a control parameter N_B by which the results can be systematically improved, and (iii) the calculated self-energy is obtained from a true nonequilibrium system, see below.

This chapter is structured as follows: At first an overview over the approach is given in Sec. 2.1 and implementation details are provided later in Sec. 2.2. In Sec. 2.1, after the basic principle is sketched, we briefly show how measurable quantities and correlation functions are computed. These topics are largely contained in standard textbooks on open quantum systems and the points listed here are meant to serve as a guidance. The more technical section 2.2 can be safely skipped by readers not concerned with details on numerics. However, it may be of help for those interested in a practical implementation. In general, this chapter serves the purpose to outline the approach in a complementary way to the publications listed in Sec. 3.

2.1. Overview

2.1.1. Basic principle and major steps

The basic principle of the approach consists in mapping the original physical impurity problem ($\mathrm{IM_{ph}}$), which cannot be solved since it is interacting and of infinite size, onto an auxiliary one ($\mathrm{IM_{aux}}$), which is effectively of finite size and can thus be solved exactly or at least accurately by numerical techniques. For $\mathrm{IM_{aux}}$ we choose a small number of bath sites N_B which are in addition coupled to two Markovian environments, see also Fig. 2.1. By this we arrive at a finite but open quantum system which exhibits dissipative dynamics and relaxes to a true nonequilibrium steady state in the long-time limit. The approach is similar to what is known as exact diagonalization DMFT (ED-DMFT) in equilibrium, cf. Ref. [52], but with the important modification to consider an open instead of a closed quantum system. Introducing an open quantum system for $\mathrm{IM_{aux}}$ automatically results in a continuous spectrum and there is no need for artificial broadening in order to compute Green's functions for real ω and most important, the additional couplings to Markovian environments greatly improve the accuracy of the mapping. Due to this we obtain very accurate spectral functions and observables already for rather small system

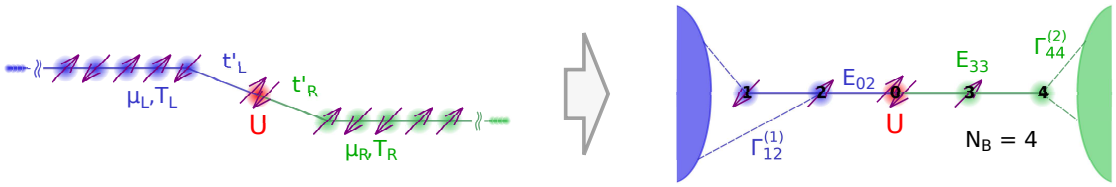

Figure 2.1.: Sketch of the mapping from the physical impurity system ($\mathrm{IM_{ph}}$) on the left to the auxiliary one ($\mathrm{IM_{aux}}$) on the right, by requiring that the hybridization functions are almost the same, Eq. (2.3). For $\mathrm{IM_{ph}}$ an Anderson impurity, Eq. (1.5), connected via $t'_{L/R}$ to two leads at different chemical potentials $\mu_{L/R}$ and/or temperatures $T_{L/R}$ is chosen, which are depicted here as two semi-infinite chains. $\mathrm{IM_{aux}}$ is represented by an open quantum system, consisting of a finite number of bath sites N_B, with the noninteracting Hamiltonian defined by E_{ij}, and additional couplings $\Gamma^{(1/2)}_{ij}$ to two Markovian environments which are either filled or empty.

sizes of $N_B = \mathcal{O}(10)$. It is also important to stress that despite of the fact that we choose the auxiliary system to be embedded in Markovian environments, the overall dynamics seen at the impurity site is clearly *non-Markovian*. This is due to the intermediate bath sites and to the non-diagonal couplings to the Markovian environments, see below.

As outlined in Sec. 1.2, for a general impurity problem $\mathrm{IM_{ph}}$ one can always write Dyson's equation in the following form

$$\underline{G}^{-1}_{\mathrm{ph}}(\omega) = \underline{g}^{-1}_{0}(\omega) - \underline{\Delta}_{\mathrm{ph}}(\omega) - \underline{\Sigma}_{\mathrm{ph}}(\omega)\,, \tag{2.1}$$

where the hybridization function $\underline{\Delta}_{\mathrm{ph}}(\omega)$ fully specifies all relevant information of the physical bath for Green's functions at the impurity site, and the self-energy $\underline{\Sigma}_{\mathrm{ph}}(\omega)$ takes the onsite interaction U into account, cf. Eq. (1.5). In the same way one specifies Dyson's equation for $\mathrm{IM_{aux}}$ by

$$\underline{G}^{-1}_{\mathrm{aux}}(\omega) = \underline{g}^{-1}_{0}(\omega) - \underline{\Delta}_{\mathrm{aux}}(\omega) - \underline{\Sigma}_{\mathrm{aux}}(\omega)\,, \tag{2.2}$$

with the same noninteracting Green's function of the decoupled impurity $\underline{g}_0(\omega)$ and the same U as above in Eq. (2.1). The crucial point is that the interacting Green's function, and thus the self-energy, depend solely on the impurity quantities $\{U, \underline{g}_0(\omega)\}$ and the hybridization function, independent of the specific realization of the bath. Therefore, in the limit $\underline{\Delta}_{\mathrm{aux}}(\omega) = \underline{\Delta}_{\mathrm{ph}}(\omega)$, $\mathrm{IM_{aux}}$ describes exactly the same impurity physics as $\mathrm{IM_{ph}}$. In practice, $\underline{\Delta}_{\mathrm{aux}}(\omega) = \underline{\Delta}_{\mathrm{ph}}(\omega)$ is only possible in some special cases or when $N_B \to \infty$. Nevertheless, one can seek for a mapping which achieves that the hybridization functions are almost the same

$$\underline{\Delta}_{\mathrm{aux}}(\omega) \approx \underline{\Delta}_{\mathrm{ph}}(\omega)\,. \tag{2.3}$$

For this condition we find in practice that it can be fulfilled with high accuracy already for rather small values of N_B, and we obtain an exponential convergence of Eq. (2.3) when increasing N_B. For the latter it is important that one makes optimal use of all bath parameters in $\mathrm{IM_{aux}}$, as described below in Sec. 2.2.1.

Once the bath parameters of $\mathrm{IM_{aux}}$ which best fulfill Eq. (2.3) are found, we solve the manybody Lindblad problem. In this way we obtain the auxiliary interacting Green's function $\underline{G}_{\mathrm{aux}}(\omega)$ from which we calculate $\underline{\Sigma}_{\mathrm{aux}}(\omega)$. The interacting solution of $\mathrm{IM_{aux}}$ then

serves as an approximate solution for $\mathrm{IM}_{\mathrm{ph}}$, whose accuracy is controlled and determined by Eq. (2.3). We generally make use of the self-energy $\underline{\Sigma}_{\mathrm{ph}}(\omega) = \underline{\Sigma}_{\mathrm{aux}}(\omega) =: \underline{\Sigma}(\omega)$ instead of $\underline{G}_{\mathrm{aux}}(\omega)$, by which the noninteracting limit $U = 0$ is exactly fulfilled and errors in the single-particle terms are reduced.

On the whole, the two major steps of AMEA are:

(I) Mapping procedure from $\mathrm{IM}_{\mathrm{ph}}$ to $\mathrm{IM}_{\mathrm{aux}}$ by optimizing the auxiliary bath parameters in order to fulfill the condition $\underline{\Delta}_{\mathrm{aux}}(\omega) \approx \underline{\Delta}_{\mathrm{ph}}(\omega)$.

(II) Manybody solution of $\mathrm{IM}_{\mathrm{aux}}$ by which an approximation to the self-energy of $\mathrm{IM}_{\mathrm{ph}}$ is obtained by $\underline{\Sigma}_{\mathrm{ph}}(\omega) = \underline{\Sigma}_{\mathrm{aux}}(\omega)$.

Details on (I) are presented below in Sec. 2.2.1 and for (II) in Sec. 2.2.2. As usual, the solution of interacting nonequilibrium manybody systems is challenging. Also in our case step (II) sets the main limitations to the method with respect to the accessible values of N_B. Below, two different strategies for the manybody solution are presented, which both solve the interacting $\mathrm{IM}_{\mathrm{aux}}$ with high accuracy so that errors stemming from step (II) are of minor importance and step (I) determines the overall accuracy of the approach.

2.1.2. Lindblad equation for the auxiliary impurity problem

For $\mathrm{IM}_{\mathrm{aux}}$ we choose the most general form of a Markovian open quantum system which preserves trace, Hermiticity and positive semi-definiteness of the density operator ρ, namely one described by a Lindblad equation [53, 54]:

$$\frac{d}{dt}\rho = \mathcal{L}\rho\,. \tag{2.4}$$

Here, ρ represents the system density operator and $\mathcal{L}$ the Lindblad superoperator which is the generator of the quantum dynamical semigroup $V(t) = \exp(\mathcal{L}t)$. The semigroup property [53]

$$V(t) = V(t-t')V(t')\,, \qquad t \geq t' \geq 0\,, \tag{2.5}$$

tells us that one can work with essentially the same techniques as known from unitary time evolutions $U(t) = \exp(-iHt)$ for Hermitian systems $H = H^\dagger$, only that a direction of time is prescribed due to the irreversible nature of dissipative systems. The locality of the time evolution operator $V(t)$, without any memory kernel for the previous history of the state is exactly the Markov property. In standard textbooks such as Ref. [53–55] it is shown how to arrive at the Lindblad equation when starting from a system embedded in a bath and integrating out the bath degrees of freedom within the Born, Markov and secular approximation.[1] In the end, this yields analytical expressions for the coefficients of the Lindblad equation which depend on system parameters and details of the bath correlation functions. This approach is usually adopted when applying the Lindblad equation to certain situations, see e.g. Ref. [5, 53–56]. Here, however, we take a different route and simply write down a generic Lindblad equation whose coefficients (bath parameters) are determined through an optimization procedure (cf. Sec. 2.2.1) instead. In particular, for

[1] For this one usually considers explicitly the reduced density matrices for the system and the bath. Here, we skip this point in the derivation and work with system dynamics only, so that ρ already refers to the reduced density operator of the system alone.

a chosen system size we optimize the bath parameters in order to fulfill the condition Eq. (2.3) to best approximation.

The Lindblad operator in Eq. (2.4) is commonly decomposed in two components $\mathcal{L} = \mathcal{L}_H + \mathcal{L}_D$, namely a unitary part

$$\mathcal{L}_H \rho = -i[H_{\mathrm{aux}}, \rho]\,, \tag{2.6}$$

as known from the usual von-Neumann equation, and the dissipator $\mathcal{L}_D$ which accounts for the couplings to the Markovian environments. As noted above, in addition to the impurity site f we consider N_B bath sites, arranged either in a "linear", "star" or any other geometry, so that the auxiliary system Hamiltonian can be written as

$$H_{\mathrm{aux}} = \sum_{ij\sigma} E_{ij} c^\dagger_{i\sigma} c_{j\sigma} + U n_{f\uparrow} n_{f\downarrow}\,. \tag{2.7}$$

The operators $c^\dagger_{i\sigma}/c_{i\sigma}$ are hereby the fermionic creation/annihilation operators for site i and spin σ, and $n_{f\sigma} = c^\dagger_{f\sigma} c_{f\sigma}$. The $(N_B+1)\times(N_B+1)$ matrix $\boldsymbol{E}$ accounts for all single-particle hoppings and on-site energies and thus specifies the geometry of $\mathrm{IM}_{\mathrm{aux}}$, and U is the Hubbard on-site interaction. Furthermore, the impurity site f is contained in the summation over $\{ij\}$. For the dissipator $\mathcal{L}_D$ we choose the following form

$$\begin{aligned}\mathcal{L}_D \rho = {} & 2 \sum_{ij\sigma} \Gamma^{(1)}_{ij} \left(c_{j\sigma} \rho c^\dagger_{i\sigma} - \frac{1}{2} \left\{ \rho, c^\dagger_{i\sigma} c_{j\sigma} \right\} \right) \\ & + 2 \sum_{ij\sigma} \Gamma^{(2)}_{ij} \left(c^\dagger_{i\sigma} \rho c_{j\sigma} - \frac{1}{2} \left\{ \rho, c_{j\sigma} c^\dagger_{i\sigma} \right\} \right)\,,\end{aligned} \tag{2.8}$$

with two types of Lindblad operators proportional to the annihilation and creation operators with coupling constants $\boldsymbol{\Gamma^{(1)}}$ and $\boldsymbol{\Gamma^{(2)}}$, respectively. Also here the impurity index f is contained in $\{ij\}$ and the summation runs over all $N_B + 1$ sites. The structure of Eqs. (2.6) and (2.8) together with the requirement that the matrix $\boldsymbol{E}$ is Hermitian, and $\boldsymbol{\Gamma^{(1)}}$ and $\boldsymbol{\Gamma^{(2)}}$ positive semi-definite, ensures that any initial physical density operator ρ remains physical and therefore preserves trace, Hermiticity and positive semi-definiteness. For more details on the choice Eq. (2.8) for the dissipator see also App. A.1.

For the form stated above, the auxiliary bath of a particular $\mathrm{IM}_{\mathrm{aux}}$ is fully specified by the three matrices $\boldsymbol{E}$, $\boldsymbol{\Gamma^{(1)}}$ and $\boldsymbol{\Gamma^{(2)}}$, which we denote as bath parameters.[2] One should note that some redundancy exists and one can always perform unitary transformations among bath sites, see also App. A.2 below. From the same freedom in the Hermitian case (ED-DMFT), one could expect to be able to reduce all terms to a diagonal from, i.e. a "star" representation. However, the noninteracting terms in the unitary part Eq. (2.7) and in the dissipator Eq. (2.8) do not share the same eigenbasis (cf. Eq. (A.1)) and are "rotated" against each other. Due to this, a large number of effective bath parameters for the mapping procedure is available, which enables one to fulfill the requirement $\underline{\Delta}_{\mathrm{aux}}(\omega) \approx \underline{\Delta}_{\mathrm{ph}}(\omega)$ very accurately even for small system sizes $N_B + 1$. This is the main reason why AMEA is also for equilibrium situations superior to an usual Hermitian bath as used in ED-DMFT.

[2] To be specific, E_{ff} is the on-site energy of the impurity and is thus not a bath parameter and all terms $\Gamma^{(\alpha)}_{ij}$ with either $i = f$ or/and $j = f$ are set to zero since this ensures that the hybridization function goes asymptotically to zero for $\omega = \pm\infty$.

Steady state density matrix and correlation functions: In order to calculate static observables and dynamic correlation functions in the stationary limit we need to find the steady state density operator ρ_∞ first. This corresponds to the eigenstate of the Lindblad superoperator $\mathcal{L}$ with eigenvalue zero

$$\mathcal{L}\rho_\infty = 0\,, \tag{2.9}$$

or is equally well obtained in the long-time limit by

$$\rho_\infty = \lim_{t\to\infty} \rho(t) = \lim_{t\to\infty} e^{\mathcal{L}t}\rho(0)\,. \tag{2.10}$$

Since we generally assume that ρ_∞ is unique, the particular initial state $\rho(0)$ does not matter. The uniqueness is always fulfilled when considering for $\mathrm{IM}_{\mathrm{aux}}$ connected systems without bound states and nonzero dissipation. Therefore, the eigenspectrum of $\mathcal{L}$ consists in general of oscillating but exponentially damped modes and exactly one eigenvalue zero. This leads to a contracting property for $V(t) = \exp(\mathcal{L}t)$ [53].

Static observables for system operators A are computed in the usual way by

$$\langle A(t)\rangle = \mathrm{tr}\{A\rho(t)\}\,, \tag{2.11}$$

when $\rho(t)$ is a valid density operator which has trace one, is Hermitian and positive semi-definite:

$$\mathrm{tr}\{\rho(t)\} = 1\,, \qquad \rho(t)^\dagger = \rho(t)\,, \qquad \langle v|\,\rho(t)\,|v\rangle \geq 0 \quad \forall\,|v\rangle \in \mathcal{H}\,. \tag{2.12}$$

The computation of two- or multi-time correlation functions can be done with the aid of the so-called quantum regression theorem [53–55]. The bare Lindblad equation Eq. (2.4) is originally only formulated to propagate reduced density matrices of the system forward in time. For correlation functions we need to time evolve non-proper density matrices such as $A\rho$. However, in the quantum regression theorem it is shown that within the same approximations for the Markovian environments also the time evolution of $A\rho$ is determined by system operators alone and in fact by the same Lindblad equation Eq. (2.4). For fermionic operators, however, one has to pay attention to the anti-commutation rules so that one encounters an additional sign when A contains an odd number of fermionic operators. This is addressed in detail in the appendix of Ref. [6]. In the end one is able to compute correlation functions by

$$iG_{BA}(t_2,t_1) = \langle B(t_2)A(t_1)\rangle = \mathrm{tr}\{BA_{t_1,t_2-t_1}\}\,, \tag{2.13}$$

with

$$\frac{d}{dt}A_{t_1,t} = \mathcal{L}'A_{t_1,t}\,, \tag{2.14}$$

and

$$A_{t_1,0} = A\rho(t_1)\,, \tag{2.15}$$

which yields the formal solution [53, 54]

$$iG_{BA}(t_2,t_1) = \mathrm{tr}\{Be^{\mathcal{L}'(t_2-t_1)}\,[A\rho(t_1)]\}\,, \quad t_2 \geq t_1\,. \tag{2.16}$$

Here, the superoperator $\mathcal{L}'$ is assumed to act on every operator on the right, i.e. everything in square brackets. The expression allows for a simple interpretation, namely that one has

to propagate the density operator of the system ρ at first up to time t_1, apply the operator A on it, and then propagate the resulting operator up to time t_2, at which B is applied and the trace evaluated. The Lindblad operator $\mathcal{L}' = \mathcal{L}_H + \mathcal{L}'_D$ is nearly the same as above only that the jump operator terms $c_{j\sigma}\rho c^\dagger_{i\sigma}$ and $c^\dagger_{i\sigma}\rho c_{j\sigma}$ in Eq. (2.8) introduce a minus sign when A anti-commutes with $c_{i\sigma}/c^\dagger_{i\sigma}$. The semigroup property does not allow one to directly consider $t_2 < t_1$, however, by using the identity

$$iG_{BA}(t_2, t_1) = -iG_{A^\dagger B^\dagger}(t_1, t_2)^* \,, \tag{2.17}$$

one attains the desired result. Since a complete derivation on this was published we refer to Ref. [1], Sec. 3.1, and Ref. [2], Sec. 3.2, for more details in the context of AMEA, and furthermore to Ref. [53–55] for detailed information on the quantum regression theorem and the Lindblad equation in general.

2.2. Implementation details

In the following we provide more technical details on the two major steps of the approach, the mapping procedure and the manybody solution of the auxiliary Lindblad problem. Hereby, in each part at first a qualitative overview is presented before we focus on the actual algorithms that we used and by which the results in Sec. 3 were obtained.

2.2.1. Mapping procedure

As outlined in the previous section, our starting point is a general Lindblad equation of the form Eq. (2.4) with Eqs. (2.6) and (2.8), which contains a set of bath parameters $\boldsymbol{E}$, $\boldsymbol{\Gamma^{(1)}}$ and $\boldsymbol{\Gamma^{(2)}}$ that need to be determined. As criterion for this we demand that Eq. (2.3) is fulfilled to best approximation, given the chosen size $N_B + 1$ of the auxiliary system. For this purpose we need to compute the hybridization function $\underline{\Delta}_{\mathrm{aux}}(\omega)$ of $\mathrm{IM}_{\mathrm{aux}}$. Since this quantity contains solely the effect of the noninteracting bath sites plus Markovian environments on the impurity site, and is per definition independent of the on-site interaction on the impurity, we only need to compute the noninteracting Green's functions $\underline{G}_0(\omega)$ of $\mathrm{IM}_{\mathrm{aux}}$.[3] In Ref. [1], Sec. 3.1, or also Ref. [6], expressions for $\underline{G}_0(\omega)$ were derived and we recap here only the result, namely

$$\begin{aligned} \boldsymbol{G}_0^R(\omega) &= \left(\omega - \boldsymbol{E} + i\left(\boldsymbol{\Gamma^{(1)}} + \boldsymbol{\Gamma^{(2)}}\right)\right)^{-1} \,, \\ \boldsymbol{G}_0^K(\omega) &= 2i\boldsymbol{G}_0^R(\omega)\left(\boldsymbol{\Gamma^{(2)}} - \boldsymbol{\Gamma^{(1)}}\right)\boldsymbol{G}_0^A(\omega) \,. \end{aligned} \tag{2.18}$$

As one can see, since we deal here with a noninteracting problem the expressions are only of size $(N_B + 1) \times (N_B + 1)$ and depend on the single-particle coefficients $\boldsymbol{E}$, $\boldsymbol{\Gamma^{(1)}}$ and $\boldsymbol{\Gamma^{(2)}}$.[4] As a result, a single computation of Eq. (2.18) is numerically very cheap. The hybridization function is hereby obtained by

$$\begin{aligned} \Delta^R_{\mathrm{aux}}(\omega) &= 1/g_0^R(\omega) - 1/G^R_{0ff}(\omega) \,, \\ \Delta^K_{\mathrm{aux}}(\omega) &= G^K_{0ff}(\omega) \,/\, |G^R_{0ff}(\omega)|^2 \,, \end{aligned} \tag{2.19}$$

[3] The subscript aux. is dropped in $\underline{G}_0(\omega)$ in favor of the readability of equations.

[4] Besides these equations, in Ref. [1] also a non-optimal set of expressions with twice the matrix size was stated in the derivation. Since $N_B + 1$ is the size of the single-particle Hilbert space it is very unlikely to find a more compact expression in the general case.

where ff denotes the matrix element of $\boldsymbol{G}_0^{R/K}(\omega)$ on the impurity site with index f. As is generally the case for connected systems without bound states and a unique stationary state, the initial occupation of the decoupled impurity $g_0^K(\omega)$ drops out of the equations, see Eq. (1.17).

Once the exact equations for $\underline{\Delta}_{\mathrm{aux}}(\omega)$ are stated, we can specify the mapping condition $\underline{\Delta}_{\mathrm{aux}}(\omega) \approx \underline{\Delta}_{\mathrm{ph}}(\omega)$, Eq. (2.3), in more detail. We choose a certain parametrization which yields a unique set of matrices $\boldsymbol{E}$, $\boldsymbol{\Gamma^{(1)}}$ and $\boldsymbol{\Gamma^{(2)}}$ with the proper symmetries for every parameter vector $\boldsymbol{x}$. Additionally, we quantify the mean squared error between $\underline{\Delta}_{\mathrm{aux}}(\omega)$ and $\underline{\Delta}_{\mathrm{ph}}(\omega)$ in terms of a cost function

$$\mathcal{C}(\boldsymbol{x})^2 = \sum_{\alpha\in\{R,K\}} \int_{-\omega_c}^{\omega_c} \Im\left\{\Delta^\alpha_{\mathrm{ph}}(\omega) - \Delta^\alpha_{\mathrm{aux}}(\omega;\boldsymbol{x})\right\}^2 W(\omega) d\omega\,, \tag{2.20}$$

which depends on the parameter vector of size $\dim(\boldsymbol{x})$. The form is well-suited to apply multi-dimensional minimization techniques, see below. The absolute minimum of $\mathcal{C}(\boldsymbol{x})$ with respect to $\boldsymbol{x}$ then specifies the optimal set of bath parameters $\boldsymbol{E}$, $\boldsymbol{\Gamma^{(1)}}$ and $\boldsymbol{\Gamma^{(2)}}$. In Eq. (2.20), $W(\omega)$ denotes an optional weighting function and ω_c the cut-off frequency. In the form stated here we only compute the mean squared difference for the imaginary part of the hybridization functions on a finite ω-domain. This is sufficient provided $\underline{\Delta}_{\mathrm{ph}}(\omega)$ and $\underline{\Delta}_{\mathrm{aux}}(\omega)$ obey the same asymptotic limit, which we ensure. In this case the real part is always fixed by the Kramers-Kronig relations. In Eq. (2.20), $\underline{\Delta}_{\mathrm{ph}}(\omega)$ is seen as a fixed input reference that we want to approximate as precisely as possible by $\underline{\Delta}_{\mathrm{aux}}(\omega)$. Important is the fact that both, the retarded and the Keldysh component must be specified and fitted.[5] The temperature enters through the Keldysh component of $\underline{\Delta}_{\mathrm{ph}}(\omega)$. In principle, one can formally consider $T = 0$, however, the continuous set of functions defined by Eqs. (2.18) and (2.19) allows one to resolve only a certain energy scale T_{eff} for a finite number N_B. Therefore, it is useful to choose a nonzero T in $\underline{\Delta}_{\mathrm{ph}}(\omega)$ for the purpose of dealing with a well-defined temperature and to avoid Gibbs oscillations in high-accuracy calculations, cf. Ref. [2], Sec. 3.2.

Besides the requirement $\underline{\Delta}_{\mathrm{aux}}(\omega) \approx \underline{\Delta}_{\mathrm{ph}}(\omega)$ large freedom exists in choosing the particular geometry for $\mathrm{IM}_{\mathrm{aux}}$. For the ED-solver we consider the most general case with a sparse matrix $\boldsymbol{E}$ and dense matrices $\boldsymbol{\Gamma^{(1)}}$ and $\boldsymbol{\Gamma^{(2)}}$ and thus $\mathcal{O}(N_B^2)$ fit parameters, see also App. A.2. For the MPS-solver introduced in Sec. 2.2.2.2 below, it is however convenient to restrict all three matrices to a sparse form, so that we arrive at $\dim(\boldsymbol{x}) \propto \mathcal{O}(N_B)$.

Multi-dimensional minimization: As stated above, a single evaluation of Eqs. (2.18) and (2.19) is rather cheap since it involves only one matrix inversion and matrix multiplications with size $N_B + 1$. Thus, the increase in computation time with N_B is rather moderate. However, the multi-dimensional optimization problem itself is demanding and strongly depends on the particular behavior of $\mathcal{C}(\boldsymbol{x})$ when varying $\boldsymbol{x}$. In the worst case scenario, when $\mathcal{C}(\boldsymbol{x})$ is a rough potential landscape with many local minima and short-scaled variations, one could imagine that it becomes necessary to nearly explore the whole parameter space. However, $\boldsymbol{x}$ is a continuous vector and even when assuming a fixed number of discrete values for each component in $\boldsymbol{x}$, one faces a number of points in parameter space

[5] In contrast to the Hermitian case the filling in $\mathrm{IM}_{\mathrm{aux}}$ is not specified by some chemical potential and temperature, but by the appropriate combination of $\boldsymbol{\Gamma^{(1)}}$ and $\boldsymbol{\Gamma^{(2)}}$.

that grows exponentially with $\dim(\boldsymbol{x})$. In the other extreme, for the case that $\mathcal{C}(\boldsymbol{x})$ is quadratic in $\boldsymbol{x}$ it is well-known that a conjugate gradient scheme leads to the exact minimum in $\dim(\boldsymbol{x})$ iterations. What we found in practice, when performing the minimization within AMEA, is, that we have an intermediate situation which exhibits local minima, but gradient-based methods still work fine especially for smaller values of N_B. In the first work on the ED-solver, Ref. [1] or Sec. 3.1, we employed a quasi-Newton line search with many random starting points. This was particularly useful for $N_B < 6$ but the necessary number of starting points increased rapidly with N_B. Therefore, in the course of the work on the MPS-solver, Ref. [2] or Sec. 3.2, more efficient solution strategies were sought for. In the end we implemented a parallel tempering (PT) approach with feedback optimization, which is a Monte Carlo scheme that is able to overcome local minima. It is described in the following in more detail. By this, the minimization problem for the ED-solver with $N_B = 6$ and for the MPS-solver with up to $N_B = 16$ can be solved in reasonable time.[6] In future, in order to perform the mapping for even larger systems efficiently it may be of interest to improve further on that, for example by combining the parallel tempering approach with gradient based methods.

Markov chain Monte Carlo (MCMC) techniques were originally developed to calculate thermodynamic properties of classical systems which exhibit a very large phase space where simple sampling strategies fail. For our purposes here, we are interested in minimizing the cost function $\mathcal{C}(\boldsymbol{x})$ as defined in Eq. (2.20) with respect to the parameter vector $\boldsymbol{x}$. For such high-dimensional minimization problems one can adapt MCMC schemes by viewing $\mathcal{C}(\boldsymbol{x})$ as an artificial energy and by introducing an artificial inverse temperature β. In the so-called simulated annealing one samples from the Boltzmann distribution $p(\boldsymbol{x}) = 1/Z \exp(-\mathcal{C}(\boldsymbol{x})\beta)$ at a certain β, and then successively cools down the artificial temperature. Motivated by the behavior of true physical systems one expects to end up in the low-energy state when letting the system equilibrate and when cooling sufficiently slowly. Analogous to thermodynamics one can calculate the specific heat $C_H = \beta^2 \langle \Delta\mathcal{C}(\boldsymbol{x})^2 \rangle$ and by this locate regions with large changes, i.e. phase transitions, where a slow cooling is critical. However, in practice it may be time consuming to realize the equilibration and sufficiently slow cooling, and for tests within AMEA we often ended up in local minima. In order to obtain a robust algorithm, which can also start from previous solutions as needed for instance within DMFT, we sought for a method which is able to efficiently overcome local minima and still systematically targets the low-energy states. For this a multicanonical and a PT algorithm were tested, whereby we favored the latter in the end. In the following we briefly outline the PT scheme used within AMEA, and refer to Ref. [57–61] for a thorough introduction to MCMC, simulated annealing, multicanonical sampling and PT.

As just stated, in a MCMC scheme one typically samples from the Boltzmann distribution $p(\boldsymbol{x}) = 1/Z \exp(-\mathcal{C}(\boldsymbol{x})\beta)$ at some chosen inverse temperature β. This is done through an iteratively created chain of states $\{\boldsymbol{x}_l\}$ and one circumvents the explicit calculation of the partition function Z. An effective and well-known scheme for this is the Metropolis-Hastings algorithm [57, 58]. One starts out with some state $\boldsymbol{x}_l$ and proposes a new configuration $\boldsymbol{x}_k$, whereby it has to be ensured that every state of the system can be reached in order to achieve ergodicity. The proposed state $\boldsymbol{x}_k$ is accepted with

[6] In both geometries this amounts to $\dim(\boldsymbol{x}) \approx 30 - 60$, depending on whether particle-hole symmetry is applicable or not. And of course, a large number of parameters enables a good fit in principle, but any restriction in $\dim(\boldsymbol{x})$ which leaves the results completely or essentially invariant is highly desirable.

probability[7] [57, 58]

$$p_{\text{pacc.}}^{l,k} = \min\left\{1, \frac{p(\boldsymbol{x}_k)}{p(\boldsymbol{x}_l)}\right\} = \min\left\{1, e^{-(\mathcal{C}(\boldsymbol{x}_k)-\mathcal{C}(\boldsymbol{x}_l))\beta}\right\} . \tag{2.21}$$

If the proposed configuration is accepted, then the next element $\boldsymbol{x}_{l+1}$ in the chain is $\boldsymbol{x}_k$, otherwise $\boldsymbol{x}_l$ again. From Eq. (2.21) it is obvious that $p_{\text{pacc.}}^{l,k} = 1$ when $p(\boldsymbol{x}_k) > p(\boldsymbol{x}_l)$, so that an importance sampling towards regions where $p(\boldsymbol{x})$ is large is achieved. One can show that the algorithm fulfills detailed balance and draws a set of samples $\{\boldsymbol{x}_l\}$ from the desired distribution $p(\boldsymbol{x})$. However, stemming from the iterative construction, correlations in the chain are present which require a careful analysis for the purpose of statistical physics [57, 58]. For optimization problems, on the other hand, the situation is much simpler and one is just interested in the element in $\{\boldsymbol{x}_l\}$ which minimizes $\mathcal{C}(\boldsymbol{x})$. Since a proposed step with $\mathcal{C}(\boldsymbol{x}_k) < \mathcal{C}(\boldsymbol{x}_l)$ is always accepted the algorithm targets minima, however, also uphill moves in configuration space are allowed with a probability depending exponentially on the barrier height $\Delta\mathcal{C}_{k,l} = \mathcal{C}(\boldsymbol{x}_k) - \mathcal{C}(\boldsymbol{x}_l)$ and β. Effectively, uphill moves take only place when $\Delta\mathcal{C}_{k,l}\beta \lesssim \mathcal{O}(1)$. For low values of β large moves in configuration space with large $\Delta\mathcal{C}_{k,l}$ are likely to be accepted, whereas for high β the distribution $p(\boldsymbol{x})$ is peaked at minima in $\mathcal{C}(\boldsymbol{x})$, so that especially those regions are sampled. For the latter case configurations in the chain $\{\boldsymbol{x}_l\}$ are generally more correlated and once a $\boldsymbol{x}_l$ corresponds to a local minimum the algorithm may reside there for very long times.

One has great freedom in defining a proposal distribution from which the new state $\boldsymbol{x}_k$ is drawn given the current configuration $\boldsymbol{x}_l$.[8] Common choices are for instance a Gaussian or a Lorentzian distribution with the vector difference $\boldsymbol{x}_k - \boldsymbol{x}_l$ as argument. We favored the former and updated each component i with a probability according to [57]

$$q_{l,k}^i = \frac{1}{\sqrt{2\pi}\sigma_i} e^{-\frac{(\boldsymbol{x}_k-\boldsymbol{x}_l)_i^2}{2\sigma_i^2}} . \tag{2.22}$$

Hereby, a different step size σ_i for each component is expedient since the potential landscape $\mathcal{C}(\boldsymbol{x})$ around $\boldsymbol{x}_l$ is typically highly anisotropic. Ideally, one should make use of the covariance matrix Σ_l of $\mathcal{C}(\boldsymbol{x}_l)$ and consider as argument for the Gaussian instead $(\boldsymbol{x}_k - \boldsymbol{x}_l)^T\Sigma_l^{-1}(\boldsymbol{x}_k - \boldsymbol{x}_l)$ [57]. However, we encountered the problem that the estimation of the covariance matrix at run time was strongly affected by noise and thus not feasible. The adjustment of the step sizes σ_i, on the contrary, can be done after a short number of updates by demanding that a value of $p_{\text{pacc.}}^{l,k} \approx 0.5$ is reached on average when modifying the component i. For this we implemented a check at every single proposal, that increases $\sigma_i \to 1.1\,\sigma_i$ when $p_{\text{pacc.}}^{l,k} > 0.6$ and decreases $\sigma_i \to 0.9\,\sigma_i$ when $p_{\text{pacc.}}^{l,k} < 0.4$. Analogous to the treatment of spin systems, we define one sweep as updating each of the $\dim(\boldsymbol{x})$ components i once.[9]

In a PT algorithm one considers instead of sampling at one certain temperature a set of different temperatures β_m^{-1} and corresponding replicas $\boldsymbol{x}_l^m$, each of which is evolved through a Markov chain. The highest β_m thereby target local minima whereas low β_m

[7] In principle one has to take the proposal probabilities $q_{k,l}$ and $q_{l,k}$ into account. However, since we only consider the case $q_{k,l} = q_{l,k}$ here, the terms drop out of the equations and are neglected everywhere.

[8] Note that for minimization purposes only one has in general the flexibility in designing the algorithm and also the Boltzmann distribution or detailed balance are not compulsory.

[9] Again, different choices are possible. For instance in cases where $\dim(\boldsymbol{x})$ is very large random updates of the most relevant components could be more appropriate.

values allow for large moves in configuration space. The key idea of the PT approach is to let the individual replicas evolve dynamically in the set of β_m. By this one achieves that a replica at high β_m values systematically targets local minima but can overcome potential barriers again when its inverse temperature is changed to lower values. As a result, the time scales are drastically reduced and an efficient sampling of the low-energy states is achieved. For the purpose of calculating thermodynamic properties one usually chooses a Metropolis-Hastings probability to swap two replicas with adjacent temperatures [60, 61]

$$p_{\mathrm{swap},l}^{m,m+1} = \min\left\{1, \frac{p^m(\boldsymbol{x}_l^{m+1})p^{m+1}(\boldsymbol{x}_l^m)}{p^{m+1}(\boldsymbol{x}_l^{m+1})p^m(\boldsymbol{x}_l^m)}\right\} = \min\left\{1, e^{(\beta_{m+1}-\beta_m)(\mathcal{C}(\boldsymbol{x}_l^{m+1})-\mathcal{C}(\boldsymbol{x}_l^m))}\right\}, \quad (2.23)$$

with the Boltzmann distribution for each β_m given by $p^m(\boldsymbol{x}) = 1/Z_m \exp\left(-\mathcal{C}(\boldsymbol{x})\beta_m\right)$. Such swap moves are conveniently proposed after a certain number of sweeps, which satisfies the sufficient condition of balance for thermodynamics [61]. In practice we chose 10 sweeps before swapping replicas. For the exchange to effectively take place the underlying requirement is that the adjacent β_m and β_{m+1} values are close enough to each other, so that the two energy distributions $\Omega[\mathcal{C}(\boldsymbol{x})]p^m(\boldsymbol{x})$ and $\Omega[\mathcal{C}(\boldsymbol{x})]p^{m+1}(\boldsymbol{x})$ overlap, with $\Omega[\mathcal{C}]$ the density of states. This means that a replica at one temperature must represent a likely configuration for the neighboring temperature [61, 62]. In order to achieve this, a crucial point in the PT algorithm is to adjust the distribution of the inverse temperatures properly to the considered situation. Various criteria for this have been devised, see e.g. Ref. [61]. A common choice is to demand that the swapping probability Eq. (2.23) becomes constant as a function of temperature [63, 64], and in Ref. [65] a feedback strategy was presented which optimizes the round trip times of replicas. We tested the latter within AMEA but favored the simpler former criterion in the end, since it allows for a rapid feedback and quick adjustment to large changes in $\mathcal{C}(\boldsymbol{x}_l^m)$. In the simple situation of a constant specific heat C_H with respect to energy $\mathcal{C}$ for instance, an optimal strategy is known since a geometric progression $\beta_m/\beta_{m+1} = \text{const.}$ of temperatures yields a constant swapping probability [61, 62]. For interesting cases in practice this is rarely fulfilled, but within AMEA it served as a good starting point. The set of inverse temperatures is then optimized by averaging $p_{\mathrm{swap},l}^{m,m+1}$ over a couple of swappings to obtain the mean probability $\bar{p}_{\mathrm{swap}}^{m,m+1}$ and adjusting the β_m thereafter. For this we chose a fixed lowest and highest β_m value and changed the spacings in between according to

$$\Delta\beta_m' = c\frac{\Delta\beta_m}{\log\left(\bar{p}_{\mathrm{swap}}^{m,m+1}\right)}, \quad (2.24)$$

with $\Delta\beta_m = \beta_{m+1} - \beta_m$ and c adjusted properly so that $\max(\beta_m') - \min(\beta_m') = \max(\beta_m) - \min(\beta_m)$. In the works by Ref. [63, 64] it was shown that a constant swapping probability of $20\% - 23\%$ seems to be optimal. We determined the highest and lowest β_m values by the changes in $\mathcal{C}(\boldsymbol{x})$ we want to resolve or allow for, and the number of inverse temperatures β_m was then set accordingly in order to roughly obtain $\bar{p}_{\mathrm{swap}}^{m,m+1} \approx 0.25$. Fixing the lowest and highest β_m is again only one possible but for our purposes convenient choice.

However, despite of the feedback optimization of temperatures as just described above, we often encountered in practice the unwanted behavior that the set of parallel replicas effectively decoupled into several clusters. To understand this let us imagine the situation that the replica with $T_0 = \min(\beta_m^{-1})$ just dropped into a local minimum $\mathcal{C}_0$ well below the

other replicas. For convenience we denote the temperature of the next higher inverse β_m by T_1, and by $\mathcal{C}_1$ its mean value at the moment. Since $\mathcal{C}_0$ just changed drastically it does not overlap with the momentary distribution of $\mathcal{C}(\boldsymbol{x})$ at T_1, so that $\mathcal{C}_1 - \mathcal{C}_0$ in Eq. (2.23) is too large and swapping therefore effectively disabled. The temperature optimization Eq. (2.24) attempts to cure this by shifting the two adjacent temperatures together, in this case $T_1 \to T_0$ since $T_0 = \text{const}$. For $\Delta\beta_m \approx 0$ swapping sets in again even though $\mathcal{C}_1 - \mathcal{C}_0$ is large.[10] Such a swapping, however, is inefficient since T_1 and T_0 are essentially the same and once the replica at $\mathcal{C}_0$ is swapped to T_1 it cannot propagate further to the next higher temperature since the difference in $\mathcal{C}(\boldsymbol{x})$ is large again. Therefore, an undesired oscillating behavior occurs. In order to suppress such an effective decoupling we found it advantageous to introduce the following simple modification to Eq. (2.23)

$$p_{\text{swap},l}^{m,m+1} = \max\left\{p_{\text{swap},l}^{m,m+1}, p_{\text{swap}}^{\text{th.}}\right\} , \tag{2.25}$$

with a certain threshold probability $p_{\text{swap}}^{\text{th.}}$. By this one avoids that temperatures are shifted unnecessarily close to each other and regains the desired effect in parallel tempering that the best minima at high β_m can be swapped to lower β_m and by this overcome local potential barriers. One should note that the modification violates balance conditions and therefore the applicability in statistical physics. But, it is perfectly valid for the purpose of minimization problems and we could obtain a speed up of the computations in practice. We found it suitable to choose the threshold probability below half of the mean acceptance probability $\bar{p}_{\text{swap}}$, e.g. $p_{\text{swap}}^{\text{th.}} = 0.1$ or 0.05.

2.2.2. Manybody solution of the auxiliary Lindblad problem

Once the bath parameters $\boldsymbol{E}$, $\boldsymbol{\Gamma^{(1)}}$ and $\boldsymbol{\Gamma^{(2)}}$ for the Lindblad equation are set the main objective is to solve the manybody problem. Different strategies exist for interacting Lindblad equations. These can be divided into two major categories: On the one hand, quantum jump or stochastic wave function approaches have been devised [66–69], which sample $\rho(t)$ by stochastically time evolving a set of pure states, and on the other hand, the Lindblad equation for the density operator can be solved directly. The former was not tested in the course of this thesis and one still needs to clarify how accurately correlation functions can be calculated. Instead, we follow here the second path and aim for calculating the full manybody density operator $\rho(t)$ directly. This has the appealing feature to be formally very similar to what is known for Hamiltonian systems, only that appropriate methods for non-Hermitian problems must be applied.

In particular, we employ a so-called super-fermionic representation which maps the density operator $\rho(t)$ onto a state vector $|\rho(t)\rangle$, and the superoperator $\mathcal{L}$ onto an ordinary non-Hermitian operator L which acts on states instead of operators [70]. By this Eq. (2.4) is mapped onto

$$\frac{d}{dt}\,|\rho(t)\rangle = L\,|\rho(t)\rangle\ . \tag{2.26}$$

In detail this can be done by introducing an augmented fermion Fock space with twice as many sites. The additional sites are labeled by a "tilde" and following the derivation in

[10] Note that in most cases $T_1 \to T_0$ does not yield $\mathcal{C}_1 \to \mathcal{C}_0$. $\mathcal{C}_1$ approaches only the next local minimum.

Ref. [70] we introduce the so-called left vacuum[11]

$$|I\rangle = \sum_{\{n_{i\sigma}\}} (-i)^{N(\{n_{i\sigma}\})} |\{n_{i\sigma}\}\rangle \otimes |\widetilde{\{\bar{n}_{i\sigma}\}}\rangle \; . \tag{2.27}$$

Here, $|\{n_{i\sigma}\}\rangle$ denotes a configuration state of the original system and $|\widetilde{\{\bar{n}_{i\sigma}\}}\rangle$ specifies the corresponding one in the tilde system with inverted occupation numbers $\bar{n}_{i\sigma} = 1 - n_{i\sigma}$. The summation runs over all possible manybody basis states in the original system. A proper phase factor depending on the total particle number $N(\{n_{i\sigma}\}) = \sum_{i\sigma} n_{i\sigma}$ of state $|\{n_{i\sigma}\}\rangle$ is introduced, so that the following "tilde conjugation rules" hold true [2, 70]

$$\begin{aligned} c_{j\sigma} |I\rangle &= -i\tilde{c}_{j\sigma} |I\rangle \; , \\ c^\dagger_{j\sigma} |I\rangle &= -i\tilde{c}^\dagger_{j\sigma} |I\rangle \; , \end{aligned} \tag{2.28}$$

with $c^\dagger_{j\sigma}/c_{j\sigma}$ and $\tilde{c}^\dagger_{j\sigma}/\tilde{c}_{j\sigma}$ fermionic operators for original and tilde sites.[12] With the left vacuum one defines the following state vector for the density operator [70]

$$|\rho(t)\rangle = \rho(t) |I\rangle \; , \tag{2.29}$$

so that normalization and expectation values for system operators translate into

$$\langle I|\rho(t)\rangle = 1 \, , \qquad \langle A(t)\rangle = \langle I| A |\rho(t)\rangle \; . \tag{2.30}$$

To transform the Lindblad equation (2.4), with Eqs. (2.6) and (2.8), one needs to evaluate $(\mathcal{L}\rho)|I\rangle \to L|\rho(t)\rangle$ with the "tilde conjugation rules" Eq. (2.28) and the commuting property $[\tilde{c}_{j\sigma}, \rho(t)] = 0$ and $[\tilde{c}^\dagger_{j\sigma}, \rho(t)] = 0$. For the purpose of writing the result in compact form we introduce the vector notation

$$\boldsymbol{c}^\dagger_\sigma = \left(c^\dagger_{0\sigma}, \ldots, c^\dagger_{N_B\sigma}, \tilde{c}^\dagger_{0\sigma}, \ldots, \tilde{c}^\dagger_{N_B\sigma} \right) . \tag{2.31}$$

With this we arrive at the following Lindblad operator [2]

$$\begin{aligned} iL = &\sum_\sigma \boldsymbol{c}^\dagger_\sigma \begin{pmatrix} \boldsymbol{E} + i\boldsymbol{\Omega} & 2\boldsymbol{\Gamma}^{(2)} \\ -2\boldsymbol{\Gamma}^{(1)} & \boldsymbol{E} - i\boldsymbol{\Omega} \end{pmatrix} \boldsymbol{c}_\sigma - 2\,\mathrm{Tr}\,(\boldsymbol{E} + i\boldsymbol{\Lambda}) \\ &+ U \left(n_{f\uparrow} n_{f\downarrow} - \tilde{n}_{f\uparrow}\tilde{n}_{f\downarrow} + \sum_\sigma \tilde{n}_{f\sigma} + 1 \right) , \end{aligned} \tag{2.32}$$

where $\boldsymbol{\Omega} = \boldsymbol{\Gamma^{(2)}} - \boldsymbol{\Gamma^{(1)}}$ and $\boldsymbol{\Lambda} = \boldsymbol{\Gamma^{(1)}} + \boldsymbol{\Gamma^{(2)}}$. In this form it is apparent that L obeys a SU(2) spin symmetry. However, in the implemented programs we accounted only for the simpler U(1) particle conservation per spin:

$$\left[L, N_\sigma + \tilde{N}_\sigma \right] = 0 \, , \quad \text{with } \; N_\sigma = \sum_{j=0}^{N_B} n_{j\sigma} \, , \;\; \tilde{N}_\sigma = \sum_{j=0}^{N_B} \tilde{n}_{j\sigma} \, . \tag{2.33}$$

[11] The particular definition differs from Ref. [70] since we introduced a particle-hole transformation in the augmented space, which avoids anomalous terms in the transformed Lindblad operator, Eq. (2.32).

[12] One should note that the particular phase factor in Eq. (2.27), which is needed for Eq. (2.28) to hold true, is dependent on the chosen ordering of fermionic operators in the basis states. The factor $(-i)^{N(\{n_{i\sigma}\})}$, for instance, is consistent with an ordering of the form $\ldots c^\dagger_j \tilde{c}^\dagger_j c^\dagger_{j+1} \tilde{c}^\dagger_{j+1} \ldots$ per spin component.

With the "tilde conjugation rules" Eq. (2.28) we find that

$$\langle I| \left(N_\sigma + \tilde{N}_\sigma\right) |I\rangle = N_B + 1\,, \tag{2.34}$$

and the designation left vacuum is motivated by Eq. (2.28) and the relation [70]

$$\langle I| L = 0\,. \tag{2.35}$$

Thus, $\langle I|$ is a left-sided eigenstate of the Lindblad operator. Its right-sided counterpart is just the steady state $|\rho_\infty\rangle$ that we are interested in

$$L\,|\rho_\infty\rangle = 0\,, \quad \text{or} \quad |\rho_\infty\rangle = \lim_{t\to\infty} e^{Lt}\,|\rho(0)\rangle\ . \tag{2.36}$$

From Eqs. (2.30) and (2.34) we know that the eigenstates $|I\rangle$ and $|\rho_\infty\rangle$ must be located in the half-filled, spin-symmetric sector. For the time-dependent case $|\rho(t)\rangle$ one should note that if the initial state $|\rho(0)\rangle$ has well-defined particle numbers $N_\sigma + \tilde{N}_\sigma$ they are conserved during the time evolution. If this is not the case for $|\rho(0)\rangle$, then the components with $N_\sigma + \tilde{N}_\sigma \neq N_B + 1$ are exponentially damped due to the contracting property of $\exp(Lt)$.[13] Finally, Eq. (2.16) for correlation functions is translated into [14]

$$iG_{BA}(t_2, t_1) = \langle I|\, B e^{L(t_2-t_1)} A\,|\rho(t_1)\rangle\ , \quad t_2 \geq t_1\,. \tag{2.37}$$

With this and Eq. (1.10) we find the following expressions for the lesser and greater Green's functions in the steady state $|\rho_\infty\rangle$ on the impurity site

$$\begin{aligned} G^<_\sigma(-t) &= i\,\langle I|\, c^\dagger_{f\sigma} e^{Lt} c_{f\sigma}\,|\rho_\infty\rangle\ , \quad t \geq 0\,, \\ G^>_\sigma(t) &= -i\,\langle I|\, c_{f\sigma} e^{Lt} c^\dagger_{f\sigma}\,|\rho_\infty\rangle\ , \quad t \geq 0\,. \end{aligned} \tag{2.38}$$

The expressions above can be computed directly through a time evolution in $\mathrm{IM}_{\mathrm{aux}}$ and the missing information in the other time direction is obtained by Eq. (2.17), i.e. by $G^<_\sigma(t) = -G^<_\sigma(-t)^\dagger$ and $G^>_\sigma(-t) = -G^>_\sigma(t)^\dagger$. The retarded and Keldysh Green's functions are given by, see Eq. (1.10),

$$\begin{aligned} G^R_\sigma(t) &= \Theta(t)\left(G^>_\sigma(t) + G^<_\sigma(-t)^\dagger\right)\,, \\ G^K_\sigma(t) &= G^>_\sigma(t) + G^<_\sigma(t)\,. \end{aligned} \tag{2.39}$$

The corresponding expressions in frequency space are

$$\begin{aligned} G^<_\sigma(\omega) &= \langle I|\, c^\dagger_{f\sigma} \frac{1}{\omega + iL}\, c_{f\sigma}\,|\rho_\infty\rangle - \ \text{h.c.}\,, \\ G^>_\sigma(\omega) &= \langle I|\, c_{f\sigma} \frac{1}{\omega - iL}\, c^\dagger_{f\sigma}\,|\rho_\infty\rangle - \ \text{h.c.}\,, \end{aligned} \tag{2.40}$$

and for the retarded and Keldysh functions we find

$$\begin{aligned} G^R_\sigma(\omega) &= \langle I|\, c_{f\sigma} \frac{1}{\omega - iL}\, c^\dagger_{f\sigma}\,|\rho_\infty\rangle + \ \left(\langle I|\, c^\dagger_{f\sigma} \frac{1}{\omega + iL}\, c_{f\sigma}\,|\rho_\infty\rangle\right)^*\,, \\ G^K_\sigma(\omega) &= \langle I|\, c_{f\sigma} \frac{1}{\omega - iL}\, c^\dagger_{f\sigma}\,|\rho_\infty\rangle + \ \langle I|\, c^\dagger_{f\sigma} \frac{1}{\omega + iL}\, c_{f\sigma}\,|\rho_\infty\rangle - \ \text{h.c.}\,. \end{aligned} \tag{2.41}$$

[13] To reach $|\rho_\infty\rangle$ through a time evolution a convenient starting point is for instance $|I\rangle$.

[14] One should stress that in the super-fermionic representation the Lindblad operator L for the time evolution of $|\rho(t_1)\rangle$ as well as for $A\,|\rho(t_1)\rangle$ is the same. The additional sign factors in front of the jump operator terms mentioned above cancel again.

2.2.2.1. Exact diagonalization (ED)

The exact diagonalization (ED) approach enables one to solve the equations numerically exactly and for arbitrary parameters, i.e. for any bath couplings and values for the interaction strength U. But, its disadvantage is that the memory and computation demands increase exponentially with system size, since one has to set up the full manybody basis with Hilbert space size $N_{\mathcal{H}} \sim \exp(N_B)$. For rather small systems, in our case $N_B \lesssim 3$ and $N_{\mathcal{H}} = \mathcal{O}(10^3)$, one can employ a so-called full diagonalization and calculate all eigenvalues and excited states. Since this full information is generally not needed it is much more efficient to employ Krylov space methods for sparse systems which extend the range in our case up to $N_B = 6$ or $N_{\mathcal{H}} \approx 10^7$. Due to the fact that we need to solve for the density operator instead of a pure state, the complexity of the manybody solution for a $N_B + 1$ sites $\mathrm{IM}_{\mathrm{aux}}$ corresponds to the one of a $2(N_B + 1)$ sites Hubbard problem. Therefore, the accessible system sizes within ED are $N_B = \{2, 4, 6\}$ bath sites and $N_B = 8$ is already prohibitive with standard computing resources.[15] Of course it is important to make use of symmetries of the underlying operator, such as Eq. (2.33). Since ED is one of the standard methods for interacting quantum manybody systems, we refer to Ref. [71–73] for details on how to treat large-scale eigenvalue problems, and here we only list the most important steps and the particular modifications that are needed to solve the non-Hermitian Lindblad problem Eqs. (2.26) and (2.32). Before considering how to calculate the steady state or Green's functions let us briefly outline two important Krylov space methods for sparse, non-Hermitian matrices.

Arnoldi scheme: The Arnoldi scheme is a general method to build up a right-sided Krylov space basis for an arbitrary non-Hermitian matrix $\boldsymbol{L}$, of size $N_{\mathcal{H}} \times N_{\mathcal{H}}$ and for a given initial vector $\boldsymbol{r}_0$ of size $N_{\mathcal{H}} \times 1$ [71–73]. The Krylov subspace $\mathcal{K}_{N_K} = \mathrm{span}\left\{\boldsymbol{r}_0, \boldsymbol{L}\boldsymbol{r}_0, \ldots, \boldsymbol{L}^{N_K-1}\boldsymbol{r}_0\right\}$ is an orthonormal set of N_K vectors, based on the powers of $\boldsymbol{L}$ applied to $\boldsymbol{r}_0$. In general, a Krylov space method is superior to an ordinary power method $\boldsymbol{L}^n\boldsymbol{r}_0$ as it makes optimal use of the computed matrix-vector products. The Arnoldi scheme may be used to estimate eigenvalues of $\boldsymbol{L}$ or to evaluate expressions of the form $f(\boldsymbol{L})\boldsymbol{r}_0$ with $f(x)$ an analytic function. $\mathcal{K}_{N_K}$ is calculated in an iterative fashion by computing each time a matrix-vector product followed by a Gram-Schmidt or QR orthogonalization process:

$$\begin{aligned} \boldsymbol{r}'_n &= \boldsymbol{L}\boldsymbol{r}_{n-1} - \sum_{j=0}^{n-1} \boldsymbol{r}_j \left(\boldsymbol{r}_j^\dagger \boldsymbol{L}\boldsymbol{r}_{n-1}\right) , \\ \boldsymbol{r}_n &= \frac{\boldsymbol{r}'_n}{\|\boldsymbol{r}'_n\|} . \end{aligned} \tag{2.42}$$

In the case $\|\boldsymbol{r}'_{\mu+1}\| = 0$ an invariant subspace was found so that $\mathcal{K}_n = \mathcal{K}_\mu \; \forall\, n \geq \mu$, and the degree of the minimal polynomial of $\boldsymbol{L}$ with respect to $\boldsymbol{r}_0$ is μ [71, 72]. With the Krylov matrix $\boldsymbol{Q}_{N_K} = [\boldsymbol{r}_0, \boldsymbol{r}_1, \ldots, \boldsymbol{r}_{N_K-1}]$ of size $N_{\mathcal{H}} \times N_K$ we can compute the Krylov subspace representation of L

$$\boldsymbol{H}_{N_K} = \boldsymbol{Q}_{N_K}^\dagger \boldsymbol{L}\, \boldsymbol{Q}_{N_K} , \tag{2.43}$$

[15] In principle on could also consider odd values for N_B, however, practical tests have shown that the extra bath site does not give significant advantages, see also Ref. [1].

which is of size $N_K \times N_K$ and of upper Hessenberg form. The latter property follows from the recurrence relation Eq. (2.42), and note that the matrix elements of $\boldsymbol{H}_{N_K}$ are directly obtained during the iteration from $[H_{N_K}]_{j,n-1} = \boldsymbol{r}_j^\dagger \boldsymbol{L} \boldsymbol{r}_{n-1}$ and $[H_{N_K}]_{n,n-1} = \|\boldsymbol{r}_n'\|$.[16] For the case that an invariant subspace is found the eigenvalues of $\boldsymbol{H}_{N_K}$ represent those of $\boldsymbol{L}$ exactly and the corresponding eigenvectors are found from Eq. (2.42) or $\boldsymbol{L}\boldsymbol{Q}_{N_K} = \boldsymbol{Q}_{N_K}\boldsymbol{H}_{N_K}$.

In practice, $\|\boldsymbol{r}_n'\| = 0$ is only obtained in rare cases[17] and thus the eigenvalues of $\boldsymbol{H}_{N_K}$ serve as an approximation to those of $\boldsymbol{L}$. However, by virtue of its relation to the power method, one finds for the Krylov space methods that especially extremal eigenvalues converge very quickly and in general it suffices to consider $N_K \ll N_\mathcal{H}$. If large values of N_K are needed it may be advisable to consider a restarted version of the algorithm, see e.g. Ref. [71–73], since the computational effort for the orthogonalization in Eq. (2.42) increases with N_K. From the definitions above it follows that the Krylov matrix generally fulfills the properties

$$\boldsymbol{Q}_{N_K}^\dagger \boldsymbol{Q}_{N_K} = \mathbb{1}_{N_K}\,, \quad \boldsymbol{Q}_{N_K}\boldsymbol{Q}_{N_K}^\dagger \neq \mathbb{1}_{N_\mathcal{H}}\,. \tag{2.44}$$

In order to evaluate analytic functions of $\boldsymbol{L}$ such as $f(\boldsymbol{L})\boldsymbol{r}_0$ one can set to good approximation

$$\begin{aligned} f(\boldsymbol{L})\boldsymbol{r}_0 &\approx f(\boldsymbol{Q}_{N_K}\boldsymbol{H}_{N_K}\boldsymbol{Q}_{N_K}^\dagger)\boldsymbol{r}_0 \\ &= \boldsymbol{Q}_{N_K} f(\boldsymbol{H}_{N_K})\boldsymbol{Q}_{N_K}^\dagger \boldsymbol{r}_0\,, \end{aligned} \tag{2.45}$$

when the Arnoldi iteration is initialized by $\boldsymbol{r}_0$. We then have $(\boldsymbol{Q}_{N_K}^\dagger \boldsymbol{r}_0)_j = \delta_{0,j}$ and the leading error term is given by $\mathcal{O}(\|\boldsymbol{L}^{N_K}\boldsymbol{r}_0\|)$. As a result, the error decreases exponentially when increasing N_K and is thus well-controlled.

Two-sided Lanczos scheme: The algorithm is also called Bi-Lanczos scheme and is the non-Hermitian analogue to the well-known Lanczos iteration [71, 73, 74]. It works in a very similar manner, only that one explicitly constructs left- and right-sided Krylov space vectors and orthogonalizes them against each other. Thus, we consider here a general non-Hermitian matrix $\boldsymbol{L}$ of size $N_\mathcal{H} \times N_\mathcal{H}$ and two initial vectors $\boldsymbol{l}_0$ and $\boldsymbol{r}_0$ of size $N_\mathcal{H} \times 1$. From these we build up the two bi-orthogonal Krylov subspaces $\mathcal{K}_{N_K}^l = \text{span}\left\{\boldsymbol{l}_0^\dagger, \boldsymbol{l}_0^\dagger\boldsymbol{L}, \ldots, \boldsymbol{l}_0^\dagger\boldsymbol{L}^{N_K-1}\right\}$ and $\mathcal{K}_{N_K}^r = \text{span}\left\{\boldsymbol{r}_0, \boldsymbol{L}\boldsymbol{r}_0, \ldots, \boldsymbol{L}^{N_K-1}\boldsymbol{r}_0\right\}$. The iteration

[16] In the special case that $\boldsymbol{L}$ is Hermitian, the same must be true for $\boldsymbol{H}_{N_K}$ so that the upper Hessenberg form reduces to a tridiagonal one, and the Arnoldi scheme to the well-known Hermitian Lanczos algorithm with its three-term recurrence.

[17] For instance, such a situation may occur when considering a noninteracting situation in the full many-body basis, and hereby especially with the (two-sided) Lanczos algorithm.

works as follows

$$\begin{aligned}
\boldsymbol{l'}^{\dagger}_{n+1} &= \boldsymbol{l}^{\dagger}_{n}\boldsymbol{L} - e_n\boldsymbol{l}^{\dagger}_{n} - k_n\boldsymbol{l}^{\dagger}_{n-1}\,,\\
\boldsymbol{r}'_{n+1} &= \boldsymbol{L}\boldsymbol{r}_n - e_n\boldsymbol{r}_n - k_n\boldsymbol{r}_{n-1}\,,\\
e_n &= \boldsymbol{l}^{\dagger}_{n}\boldsymbol{L}\boldsymbol{r}_n\,,\\
k_{n+1} &= \boldsymbol{l}^{\dagger}_{n}\boldsymbol{L}\boldsymbol{r}_{n+1} = \boldsymbol{l}^{\dagger}_{n+1}\boldsymbol{L}\boldsymbol{r}_n\\
&= (\boldsymbol{l'}^{\dagger}_{n+1}\boldsymbol{r}'_{n+1})^{1/2}\,,\\
\boldsymbol{l}^{\dagger}_{n+1} &= \boldsymbol{l'}^{\dagger}_{n+1}/k_{n+1}\,,\\
\boldsymbol{r}_{n+1} &= \boldsymbol{r}'_{n+1}/k_{n+1}\,.
\end{aligned} \tag{2.46}$$

Since only products between left- and right-sided vectors are involved some ambiguity exists in how to define the prefactors, and the expressions stated above are thus only one of the possible choices. It is evident that two matrix vector multiplications $\boldsymbol{l}^{\dagger}_{n}\boldsymbol{L}$ and $\boldsymbol{L}\boldsymbol{r}_n$ are needed in each iteration and as in the Hermitian case, a three-term recurrence suffices to build up the bi-orthogonal basis set $\boldsymbol{l}^{\dagger}_{n}\boldsymbol{r}_m = \delta_{n,m}$. As a result, the explicit Gram-Schmidt orthogonalization against all previous vectors, as in the Arnoldi scheme, is not needed here and the computational effort does not increase with the iteration number. Similar to the condition above, the iteration must be stopped when the norm of the newest Krylov space vector is (essentially) zero. However, since only products between left- and right-sided vectors are considered several situations may occur. One speaks of a normal termination when $k_{n+1} = 0$ together with $\|\boldsymbol{l}'_{n+1}\| = 0$ and/or $\|\boldsymbol{r}'_{n+1}\| = 0$, which means that an invariant left $\mathcal{K}^{l}_{N_K}$ and/or right Krylov subspace $\mathcal{K}^{r}_{N_K}$ was found. A breakdown occurs when $k_{n+1} = 0$ together with $\|\boldsymbol{l}'_{n+1}\| \neq 0$ and $\|\boldsymbol{r}'_{n+1}\| \neq 0$. So-called look-ahead strategies exist in order to cure such cases and to continue the iteration [74–76]. However, in actual calculations within AMEA we never encountered it so that we did not implement look-ahead strategies.

With the left- and right sided Krylov matrices $\boldsymbol{V}^{-1}_{N_K} = [\boldsymbol{l}^{\dagger}_{0}, \boldsymbol{l}^{\dagger}_{1}, \ldots, \boldsymbol{l}^{\dagger}_{N_K-1}]$ and $\boldsymbol{V}_{N_K} = [\boldsymbol{r}_0, \boldsymbol{r}_1, \ldots, \boldsymbol{r}_{N_K-1}]$, of size $N_K \times N_{\mathcal{H}}$ and $N_{\mathcal{H}} \times N_K$, one obtains for the Krylov subspace projection of $\boldsymbol{L}$ a tridiagonal form

$$\boldsymbol{T}_{N_K} = \boldsymbol{V}^{-1}_{N_K}\boldsymbol{L}\boldsymbol{V}_{N_K}\,. \tag{2.47}$$

The diagonal components are given by $e_n \in \mathbb{C}$ and both off-diagonals by $k_n \in \mathbb{C}$, as defined in Eq. (2.46). Similar to the Arnoldi scheme above the following relations hold true

$$\boldsymbol{V}^{-1}_{N_K}\boldsymbol{V}_{N_K} = \mathbb{1}_{N_K}\,, \quad \boldsymbol{V}_{N_K}\boldsymbol{V}^{-1}_{N_K} \neq \mathbb{1}_{N_{\mathcal{H}}}\,, \tag{2.48}$$

and expressions of the form $\boldsymbol{l}^{\dagger}_{0}f(\boldsymbol{L})\boldsymbol{r}_0$ for analytic functions $f(x)$ can be efficiently calculated in the Krylov subspace by [77]

$$\begin{aligned}
\boldsymbol{l}^{\dagger}_{0}f(\boldsymbol{L})\boldsymbol{r}_0 &\approx \boldsymbol{l}^{\dagger}_{0}f(\boldsymbol{V}_{N_K}\boldsymbol{T}_{N_K}\boldsymbol{V}^{-1}_{N_K})\boldsymbol{r}_0\\
&= \boldsymbol{l}^{\dagger}_{0}\boldsymbol{V}_{N_K}f(\boldsymbol{T}_{N_K})\boldsymbol{V}^{-1}_{N_K}\boldsymbol{r}_0\\
&= [f(\boldsymbol{T}_{N_K})]_{0,0}\,.
\end{aligned} \tag{2.49}$$

In the last line we made again use of the fact that the Bi-Lanczos iteration is initialized with $\boldsymbol{l}^{\dagger}_{0}$ and $\boldsymbol{r}_0$. As before, an exponential convergence is obtained and one even finds that the leading order error is proportional to $\mathcal{O}(\boldsymbol{l}^{\dagger}_{0}\boldsymbol{L}^{2N_K-1}\boldsymbol{r}_0)$, see also Ref. [77–80].

Steady state and correlation functions: The Arnoldi and Bi-Lanczos scheme described above enable us to efficiently solve for the steady state as well as for Green's functions. Let us begin with the former. Various strategies exist to calculate the steady state, for instance by searching for the eigenstate with eigenvalue zero $L\,|\rho_\infty\rangle = 0$. As noted above, Krylov space iterations generally converge particularly well for extremal eigenvalues. However, since the eigenvalues λ_ν of L fulfill $\Re\{\lambda_\nu\} \leq 0$ and $\Im\{\lambda_\nu\} \in \mathbb{R}$, it is thus not well-controlled to get the steady state in a direct fashion. One approach for instance is to formulate a variational principle which minimizes $\|L\,|\rho_\infty\rangle\|$. In the 2−norm this corresponds to searching for the smallest eigenvalue of the Hermitian operator $L^\dagger L$. It was tested in practice, however, we found that such a strategy is very inefficient since one ends up with the squared singular value spectrum of L and thus with a very unfavorable condition number. As a result, a huge number of (Hermitian) Lanczos iterations is needed. A systematic approach to target eigenvectors to certain eigenvalues is given by the shift-and-invert procedure [73]. For the steady state one hereby introduces a small shift $s > 0$ and searches for the largest eigenvalue of

$$(L - s\mathbb{1})^{-1}\,|\rho_\infty\rangle = \lambda'_{\max}\,|\rho_\infty\rangle\ , \tag{2.50}$$

with an Arnoldi scheme. The inverse of the matrix is not needed since one can replace operations of the form $\tilde{\boldsymbol{r}}_{n+1} = (\boldsymbol{L} - s\mathbb{1})^{-1}\,\boldsymbol{r}_n$ by $(\boldsymbol{L} - s\mathbb{1})\,\tilde{\boldsymbol{r}}_{n+1} = \boldsymbol{r}_n$. An efficient solver for non-Hermitian sparse systems of equations is for instance the stabilized biconjugate gradient method, ideally with an incomplete LU decomposition as preconditioner. Since such a scheme is based on Krylov space methods as well, one ends up with an inner and an outer iteration. The convergence properties of the two iterations are affected and controlled by the shift s. Small values of s target the eigenvalue of the steady state better so that the outer iteration converges faster, but, a too small s results in an ill-conditioned problem for the solution of the linear system, so that the inner iteration becomes problematic. One thus has to search for the optimal point. Since we found that the solution of the linear system is numerically demanding, even with a memory consuming iLU decomposition, this strategy was not favored in the end.

Eventually, we concluded that a plain time evolution is the most robust and even most efficient way to obtain the steady state within AMEA. This is especially true when employing time evolution algorithms based on Krylov space methods. Furthermore, the same scheme can also be applied to calculate Green's functions in the time domain. We are thus interested in a general time evolution of the form

$$\begin{aligned} |\rho(t)\rangle &= e^{Lt}\,|\rho(0)\rangle\ , \\ \boldsymbol{r}(t) &= e^{\boldsymbol{L}t}\boldsymbol{r}_0\,, \end{aligned} \tag{2.51}$$

where the second line corresponds to the resulting matrix expression in the manybody basis. In principle, both the Bi-Lanczos and the Arnoldi scheme are applicable but due to the fact that only right-sided vectors are needed it is more natural and clearer to use the latter. The expression is already in the form as needed in Eq. (2.45) so that we obtain

$$\boldsymbol{r}(t) = \boldsymbol{Q}_{N_K} e^{\boldsymbol{H}_{N_K} t} \boldsymbol{Q}^\dagger_{N_K} \boldsymbol{r}_0\,, \tag{2.52}$$

where H_{N_K} denotes again the Krylov space projection of $\boldsymbol{L}$ and the iteration is initialized with $\boldsymbol{r}_0$, i.e. $\boldsymbol{Q}_{N_K} = [\boldsymbol{r}_0, \boldsymbol{r}_1, \ldots, \boldsymbol{r}_{N_K-1}]$. From this we arrive with $\boldsymbol{c}(0) = \boldsymbol{Q}^\dagger_{N_K}\boldsymbol{r}_0$ at the

following equation [81]

$$\begin{aligned} \boldsymbol{r}(t) &= \sum_{k=0}^{N_K-1} c_k(t)\boldsymbol{r}_k\,, \\ \boldsymbol{c}(t) &= e^{\boldsymbol{H}_{N_K}t}\boldsymbol{c}(0)\,, \end{aligned} \tag{2.53}$$

and as before $c_k(0) = \delta_{0,k}$. We thus see that the time evolution can be represented as a sum of Krylov space vectors with complex weights. Generally, the absolute value of $c_k(t)$ decays rapidly as a function of k and an intuitive criterion for convergence is thus to demand that the last coefficient is negligible [81, 82]

$$\frac{c_{N_K-1}(t)}{\|\boldsymbol{c}(t)\|} < \varepsilon\,, \tag{2.54}$$

where ε determines the overall accuracy. Note that the denominator in Eq. (2.54) is important in the case of non-Hermitian time evolutions. Usually, one is interested in time evolving a state over a sequence of discrete time intervals. For this one simply calculates in Eq. (2.53) a sufficient number of Krylov space vectors N_K to obtain $\boldsymbol{r}(t)$ in the desired accuracy, and then restarts the Krylov space iteration for the next time step with $\boldsymbol{r}(t)$. The value for N_K strongly depends on the size of the time step and also whether one deals with strongly excited states. In either limits, when $t = 0$ or when $\boldsymbol{r}_0$ is an eigenstate of $\boldsymbol{L}$ it is obvious that $N_K = 1$ suffices. The latter is particularly useful when searching for the stationary state $|\rho_\infty\rangle$. We found it efficient to fix a value of $N_K \approx 20$ and to take for each time step the longest possible t which still fulfills Eq. (2.54). By this, the time steps are initially rather short but become longer when getting closer to the steady state, which in turn accelerates convergence.

In order to calculate correlation functions directly in the frequency domain, as defined in Eqs. (2.40) and (2.41), we employ the two-sided Lanczos scheme. When written in the manybody basis we need to solve for expressions of the form

$$G(\omega) = \boldsymbol{l}_0^\dagger \frac{1}{\omega - i\boldsymbol{L}}\boldsymbol{r}_0\,, \tag{2.55}$$

where we assume that the states have been normalized before $\boldsymbol{l}_0^\dagger\boldsymbol{r}_0 = 1$. This is of the form as stated in Eq. (2.49), so that we build up with $\boldsymbol{l}_0^\dagger$ and $\boldsymbol{r}_0$ the bi-orthogonal Krylov subspace, calculate the projection $\boldsymbol{T}_{N_K}$ of $\boldsymbol{L}$ into this subspace, and estimate the Green's function by

$$G(\omega) = \left[(\omega - i\boldsymbol{T}_{N_K})^{-1}\right]_{0,0}\,. \tag{2.56}$$

The matrix inversion in Krylov space is very cheap since $N_K \approx 100-1000$ typically suffices for accurate results. As stated above, the scheme converges exponentially when increasing N_K. We found that this is even then the case when round-off errors are present, which cause the Krylov space vectors to become linearly dependent at larger values of N_K. The only effect is that finite precision arithmetic slows down the rate of convergence. On the contrary, in the usual Hermitian ground state Lanczos problems with round-off errors may appear at high iteration numbers.

2.2.2.2. Matrix product states (MPS)

Matrix product states (MPS) are an efficient representation of manybody states of one-dimensional systems. In particular, ground states of 1D short-ranged Hamiltonians with an excitation gap, where an area law applies, are very suitable for MPS [83–85]. But the range has been greatly extended in recent years to the treatment of excited states, finite temperature situations, correlation functions, time-dependent situations and higher or quasi-higher (stripes, tubes, ...) dimensional systems [84–91]. Also within the density matrix renormalization group (DMRG) [84] and NRG [16], matrix product states have gained great significance and these algorithms are nowadays conveniently formulated in the language of MPS. Moreover, the applicability to and the treatment of open quantum systems with MPS techniques was investigated by various groups, see e.g. Ref. [92–99]. Since the important field of matrix product states and the related tensor network approaches [85, 91] is a very active and vast area of research, a thorough introduction cannot be given here and is beyond the scope of this thesis. Due to this we refer in this respect mainly to literature and outline solely the algorithms which are of importance for AMEA. For instance, the review article Ref. [84] gives a very good introduction to the field of MPS and provides an overview over different techniques. In particular, for AMEA we make use of the so-called time evolving block decimation (TEBD) [100, 101], which is an efficient and directly parallelizable time evolution technique for short-ranged Hamiltonians.

Geometry of $\mathrm{IM}_{\mathrm{aux}}$: For MPS in general and especially for TEBD it is of advantage to have a one-dimensional system with short-ranged couplings only. As mentioned above in Sec. 2.2.1, besides the mapping criterion $\underline{\Delta}_{\mathrm{aux}}(\omega) \approx \underline{\Delta}_{\mathrm{ph}}(\omega)$, Eq. (2.3), we have great freedom in choosing the particular geometry of $\mathrm{IM}_{\mathrm{aux}}$. With the applicability of MPS-methods in view we restrict $\mathrm{IM}_{\mathrm{aux}}$ in the following to a setup where all three matrices $\boldsymbol{E}$, $\boldsymbol{\Gamma^{(1)}}$ and $\boldsymbol{\Gamma^{(2)}}$ are sparse and of tridiagonal form. This results in a suboptimal mapping for a given number of bath sites N_B when compared with the ED-solver. But, since MPS methods allow one to deal with much larger system sizes in the manybody solution, the overall accuracy is considerably better in the end.

A sketch for the chosen $\mathrm{IM}_{\mathrm{aux}}$ geometry in the super-fermionic formulation is depicted in Fig. 2.2. The couplings between sites correspond hereby to a graphical representation of Eq. (2.32). We display sites for the augmented fermion Fock space below sites of the original system. If one restricts to nearest neighbor terms in $\boldsymbol{E}$, $\boldsymbol{\Gamma^{(1)}}$ and $\boldsymbol{\Gamma^{(2)}}$ only, a simple picture of a ladder of fermionic sites is obtained, and we choose the impurity to be situated in the center. Sites on the upper chain are coupled by the terms $\boldsymbol{E} + i(\boldsymbol{\Gamma^{(2)}} - \boldsymbol{\Gamma^{(1)}})$, augmented sites on the lower chain by $\boldsymbol{E} - i(\boldsymbol{\Gamma^{(2)}} - \boldsymbol{\Gamma^{(1)}})$, and a directional hopping from the lower to the upper chain is given by $\boldsymbol{\Gamma}^{(2)}$ and in the opposite direction by $\boldsymbol{\Gamma}^{(1)}$. In order to minimize entanglement and thus for an optimal applicability of MPS, we found it convenient to further restrict the geometry of $\mathrm{IM}_{\mathrm{aux}}$ to one, in which $\boldsymbol{\Gamma}^{(2)}$ is nonzero only for one side of the ladder (left side here) and $\boldsymbol{\Gamma}^{(1)}$ on the other side.[18] When labeling the impurity site with f this means that $\Gamma^{(2)}_{ij} = 0$ for $i \geq f$ or $j \geq f$, and that $\Gamma^{(1)}_{ij} = 0$ for $i \leq f$ or $j \leq f$. By this one arrives at a setup in which the sites of the original system on the left are filled and sites on the right are empty when decoupled from the impurity.[19] We thus refer to this geometry for $\mathrm{IM}_{\mathrm{aux}}$ as filled/empty. Note that the

[18] For a discussion on this see below at the end of this section and also Ref. [2], Sec. 3.2.

[19] Note that the hybridization function is just defined through such a cavity construction.

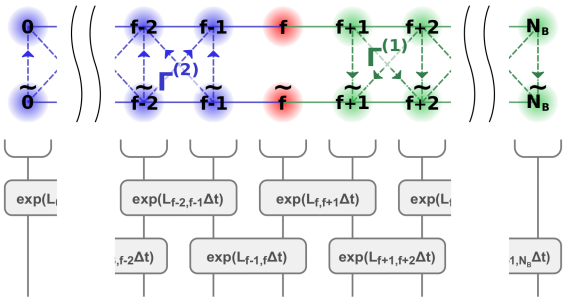

Figure 2.2.: Graphic illustration of the auxiliary impurity system as used within MPS. The impurity is at site f and coupled to a filled/empty chain on the left/right. In the super-fermionic representation and with nearest neighbor couplings only, Eq. (2.32) corresponds to a ladder geometry. At the bottom a sketch of the time evolution within the TEBD scheme is shown, whereby the two-site gates act on original and on "tilde" sites. Figure from Ref. [2], Sec. 3.2.

situation with respect to left/right is reversed when looking at sites in the augmented system. For the coupled system, due to the directional hoppings produced by $\mathbf{\Gamma^{(1)}}$ and $\mathbf{\Gamma^{(2)}}$, this means that a circular current is driven through $\mathrm{IM}_{\mathrm{aux}}$. Interestingly, we find in practice that the mapping procedure is affected by this second restriction only in a minor and nearly negligible way, so that it seems that the filled/empty-geometry is even a natural representation for a single impurity $\mathrm{IM}_{\mathrm{aux}}$ with a number of bath parameters that scales linearly in N_B. For more details on this see also App. A.2.

MPS representation and entanglement: For the ladder geometry depicted in Fig. 2.2 it is natural to combine two sites into a single vertical MPS-"site". In this way we end up with a linear "chain" with nearest neighbor terms only, even if we use tridiagonal Γ-matrices as already assumed above. The negative aspect is that by this grouping of sites one obtains for a single MPS-site a local Hilbert space size of $d = 16$. When denoting each local basis state by $|s_i\rangle$, with $s_i = \{1, 2, \ldots, 16\}$, we can write the manybody state of $\mathrm{IM}_{\mathrm{aux}}$ as follows

$$|\rho\rangle \;=\; \sum_{\{s_i\}} c_{\{s_i\}} \,|\{s_i\}\rangle \;=\; \sum_{\{s_i\}} c_{\{s_i\}} \bigotimes_{i=0}^{N_B} |s_i\rangle \;. \tag{2.57}$$

The summation over $\{s_i\}$ denotes hereby all d^{N_B+1} possibilities for the manybody basis states of the system, and $c_{\{s_i\}}$ labels the corresponding coefficients of $|\rho\rangle$ in this basis. Such a generic manybody state can always be rewritten in terms of a matrix product state of the form

$$|\rho\rangle \;=\; \sum_{\{s_i\}} \boldsymbol{A}_0^{s_0} \boldsymbol{A}_1^{s_1} \boldsymbol{A}_2^{s_2} \ldots \boldsymbol{A}_{N_B}^{s_{N_B}} \,|\{s_i\}\rangle = \bigotimes_{i=0}^{N_B} \left(\sum_{s_i=1}^{d} \boldsymbol{A}_i^{s_i} \,|s_i\rangle \right) , \tag{2.58}$$

whereby $\boldsymbol{A}_0^{s_0}$ corresponds to a row and $\boldsymbol{A}_{N_B}^{s_{N_B}}$ to a column vector, and the matrices in between are rectangular. This is exactly true for any state, no matter how strongly entangled it is, only that the needed matrix dimension $\chi_{\max} = \dim(\boldsymbol{A}_f^{s_f}) = d^{N_B/2}$ grows exponentially with system size. In the limit that all of the matrices are scalars with matrix dimension 1 one ends up with an ordinary tensor product state.

A full derivation and many details on MPS are given for instance in Ref. [84, 85]. Here, we outline only briefly the steps on how to obtain Eq. (2.58), in order to sketch the basic idea of the MPS truncation. Imagine that one writes the coefficients in Eq. (2.57) as a vector of size $1 \times d^{N_B+1}$ and reshapes it into a matrix $C_{s_0,(s_1,s_2,\ldots,s_{N_B})}$ of size $d \times d^{N_B}$ when taking s_0 as first index. For this object one now performs a singular value decomposition (SVD) [84][20]

$$C_{s_0,(s_1,s_2,\ldots,s_{N_B})} = \sum_{a_0=1}^{d} U_{s_0,a_0} S_{a_0,a_0} \left(V^\dagger\right)_{a_0,(s_1,s_2,\ldots,s_{N_B})} = \sum_{a_0=1}^{d} U_{s_0,a_0} C'_{a_0,(s_1,s_2,\ldots,s_{N_B})} \,, \tag{2.59}$$

which introduces an auxiliary index a_0. When regrouping elements again and rewriting the obtained coefficient matrix on the right as $C'_{(a_0,s_1),(s_2,\ldots,s_{N_B})}$, thus of size $d^2 \times d^{N_B-1}$, a subsequent SVD yields

$$C'_{(a_0,s_1),(s_2,\ldots,s_{N_B})} = \sum_{a_1=1}^{d^2} U_{(a_0,s_1),a_1} C''_{a_1,(s_2,\ldots,s_{N_B})} \,. \tag{2.60}$$

By repeating this scheme in a recursive manner one can decompose the coefficients into local matrices $U_{(a_{i-1},s_i),a_i}$, each of which is reshaped into a set of matrices $A^{s_i}_{a_{i-1},a_i}$ by taking its columns. In the end this tensor train just represents the original coefficients by

$$c_{\{s_i\}} = \sum_{a_0=1}^{d} \sum_{a_1=1}^{d^2} \cdots \sum_{a_{f-1}=1}^{d^{N_B/2}} \sum_{a_f=1}^{d^{N_B/2}} \cdots \sum_{a_{N_B-1}=1}^{d} A^{s_0}_{1,a_0} A^{s_1}_{a_0,a_1} \ldots A^{s_{N_B}}_{a_{N_B-1},1} \,, \tag{2.61}$$

when the impurity index is placed in the center at $f = N_B/2$ with N_B even. This relation is exact and shows how to transform any set of coefficients $c_{\{s_i\}}$ into a product of matrices where each physical index s_i enters only locally. On each bond $(i, i+1)$, an auxiliary index a_i corresponding to the matrix index must be introduced. As follows from the successive SVDs, the bond dimensions χ_i increase hereby exponentially as d^{i+1} and the maximum is reached in the center of the chain.

In fact, in the equations stated so far the dimensionality of the underlying system did not enter explicitly and we simply introduced an ordering of the physical indices s_i. Now, the essential point is that many states of one-dimensional systems, in particular ground states, can be very accurately represented by a MPS with very small bond dimensions $\chi_i \ll d^{N_B/2}$. It is thus possible to identify components of minor importance and to truncate the state. The singular values, i.e. the entries of the diagonal matrices $\lambda_{a_i} = S_{a_i,a_i}$ in the SVDs play for this purpose a central role in the MPS formalism. In general they fulfill $\lambda_{a_i} \geq 0$ and for a normalized state $\langle\rho|\rho\rangle = 1$ one has

$$\sum_{a_i=1}^{\chi_i} \lambda_{a_i}^2 = 1 \,. \tag{2.62}$$

For convenience one assumes an ordering so that $\lambda_1 > \lambda_2 > \cdots > \lambda_{\chi_i}$. For 1D-systems it is typically true that the spectrum of singular values λ_{a_i} decays rapidly. Therefore, when

[20] A SVD decomposes any rectangular matrix M of size $a \times b$ into $M = USV^\dagger$, with U of size $a \times \min(a,b)$ and $U^\dagger U = \mathbb{1}$, $V^\dagger$ of size $\min(a,b) \times b$ and $V^\dagger V = \mathbb{1}$, and the diagonal matrix S of size $\min(a,b) \times \min(a,b)$ and $S_{i,i} \geq 0$.

introducing a smaller bond dimension $\chi < \chi_i$ and discarding all λ_{a_i} with $a_i > \chi$ one can expect to introduce only a small error. This is quantified by the so-called truncated weight

$$w_i^{\text{tr.}} = \sum_{a_i=\chi+1}^{\chi_i} \lambda_{a_i}^2 \,, \tag{2.63}$$

and one finds that the error between the truncated state $|\rho\rangle_{\text{tr.}}$ and the original one $|\rho\rangle$ is just determined by Eq. (2.63). Even more one can show that this prescription is optimal in the 2-norm error when constructing out of $|\rho\rangle$ a state with reduced bond dimension. When performing each of the SVDs outlined above with an upper bound χ for the bond dimensions χ_i, and keeping track of the truncated weight according to Eq. (2.63), one finds that the overall error is bound by [84]

$$\| |\rho\rangle_{\text{tr.}} - |\rho\rangle \|_2^2 \leq 2 \sum_{i=0}^{N_B-1} w_i^{\text{tr.}} \,. \tag{2.64}$$

Another important quantity in this context is the bipartite entanglement entropy $S_i^{A|B}$, which is given by [84]

$$S_i^{A|B} = -\sum_{a_i=1}^{\chi_i} \lambda_{a_i}^2 \log_2\left(\lambda_{a_i}^2\right) \,, \tag{2.65}$$

and related to the Schmidt decomposition of quantum states. It is a measure for the entanglement between the left and the right side of the system when performing a bipartition at bond i. For a product state one has $S_i^{A|B} = 0$ since $\chi_i = 1$, and in the extreme case that all states are equally important $\lambda_{a_i}^2 = 1/\chi_i$ one finds $S_i^{A|B} = \log_2(\chi_i)$, i.e. [84, 85]

$$\chi_i \propto e^{S_i^{A|B}} \,. \tag{2.66}$$

This simple expression is for usual quantum states not exactly true but allows one to estimate the functional behavior of the necessary bond dimension χ with respect to the entanglement entropy $S^{A|B}$. Since ground states of gapped, short-ranged Hamiltonians obey so-called area laws [83], which state that their entanglement entropy scales with the area of a subsystem instead of its volume, i.e. $S^{A|B} \sim L^{D-1}$, one obtains the estimate $\chi \sim$ const. for 1D and $\chi \sim \exp(L)$ for 2D. For 1D this means that a MPS representation is valid for arbitrarily large systems in principle, but the exponential scaling in higher-dimensional cases greatly limits the applicability of MPS to such systems [84]. In general, the dependence of $S^{A|B}$ on the system size crucially determines whether MPS methods are well-applicable or not. Within AMEA we obtained an intermediate situation since the chosen IM_{aux} is one-dimensional but an area law does not apply to the steady state $|\rho_\infty\rangle$. We found that the bipartite entanglement in IM_{aux} typically increased with N_B, however, in a sublinear way similar to a critical quantum system. This has the consequence that larger values of χ are generally required for larger N_B, and the bond dimension crucially affects the computational effort which approximately scales as $\mathcal{O}(N_B\chi^3)$. However, the increase of $S^{A|B}$ with N_B is rather moderate so that sufficiently large systems with $N_B \approx 16$ or more are accessible. As a result, a very good overall accuracy within AMEA is possible and we found a significant improvement compared to the ED-solver.

Measurements and TEBD: For expectation values in the super-fermionic formalism one needs to normalize $|\rho\rangle$ against $|I\rangle$. A MPS representation of $|I\rangle$ is directly obtained when rewriting Eq. (2.27) as a tensor product of local terms $|I\rangle_j$

$$|I\rangle = \bigotimes_{j=0}^{N_B} |I\rangle_j \ , \tag{2.67}$$

which are given by[21]

$$\begin{aligned} |I\rangle_j &= \left(\tilde{c}^\dagger_{j\uparrow} - i\, c^\dagger_{j\uparrow}\right)\left(\tilde{c}^\dagger_{j\downarrow} - i\, c^\dagger_{j\downarrow}\right)|0\rangle \\ &= \left(\tilde{c}^\dagger_{j\uparrow}\tilde{c}^\dagger_{j\downarrow} + i\,\tilde{c}^\dagger_{j\downarrow}c^\dagger_{j\uparrow} - 1\, c^\dagger_{j\uparrow}c^\dagger_{j\downarrow} - i\,\tilde{c}^\dagger_{j\uparrow}c^\dagger_{j\downarrow}\right)|0\rangle \ . \end{aligned} \tag{2.68}$$

The phase factors $\{1, i, -1, -i\}$ are chosen to fulfill the "tilde conjugation" rules Eq. (2.28) with a basis ordering at site j defined by $\tilde{c}^\dagger_{j\uparrow}\tilde{c}^\dagger_{j\downarrow}c^\dagger_{j\uparrow}c^\dagger_{j\downarrow}$. Note that these factors just correspond to the nonzero entries of the 1×1 MPS-matrices of state $|I\rangle$, which is thus a simple product state. When denoting the MPS-matrices by $v_j^{s_j}$ we find for the overlap $\langle I|\rho\rangle$ the following expression

$$\langle I|\rho\rangle = \sum_{\{s_i\}} {v_{N_B}^{s_{N_B}}}^\dagger \ldots v_1^{s_1\dagger} v_0^{s_0\dagger} \boldsymbol{A}_0^{s_0}\boldsymbol{A}_1^{s_1}\ldots\boldsymbol{A}_{N_B}^{s_{N_B}} \ . \tag{2.69}$$

It is hereby important to first perform the summation over physical indices before multiplying the auxiliary matrix indices in order to avoid exponentially many terms [84]. The action of local operations on a state is particularly simple in the MPS representation. For instance, consider a local operator at site j of the form

$$O_j = \sum_{s'_j, s_j} O_j^{s'_j, s_j} \, |s'_j\rangle\langle s_j| \ . \tag{2.70}$$

When applied to the state of Eq. (2.58), $|\rho'\rangle = O_j\,|\rho\rangle$, only the matrices at site j are modified by[22]

$$\boldsymbol{A}_j^{s'_j} = \sum_{s_j} O_j^{s'_j, s_j}\, \boldsymbol{A}_j^{s_j} \ . \tag{2.71}$$

In analogous manner one applies a tensor product of local operators $O_1 \otimes O_2 \otimes \cdots \otimes O_{N_B}$ to a MPS. However, in more complicated operators such as Hamiltonians or the Lindblad operator in AMEA, a large sum of different tensor products of local operators appears. The MPS ideas can be directly extended to this case and one defines matrix product operators (MPO) by

$$O = \sum_{\{s'_i\},\{s_i\}} \boldsymbol{O}_0^{s'_0, s_0}\boldsymbol{O}_1^{s'_1, s_1}\ldots\boldsymbol{O}_{N_B}^{s'_{N_B}, s_{N_B}} \, |\{s'_i\}\rangle\langle\{s_i\}| \ . \tag{2.72}$$

For a tensor product operator $O_1 \otimes O_2 \otimes \cdots \otimes O_{N_B}$ the individual matrices $\boldsymbol{O}_i^{s'_i, s_i}$ would be scalars and their values given by the on-site matrix elements $\langle s'_i|\, O_i\, |s_i\rangle$. We refer to

[21] A prefactor $1/2$ may be included in $|I\rangle_j$ for normalization.

[22] Fermionic signs from neighboring sites are neglected here.

Ref. [84] for more details on how to construct the MPO for a given Hamiltonian. In the end, one finds that Eq. (2.72) is an effective representation for operators with short-ranged couplings. The Lindblad operator Eqs. (2.26) and (2.32), for instance, can be written as a MPO with bond dimension $D = 10$, whereby D refers to the size of the matrices $\boldsymbol{O}_i^{s_i',s_i}$.[23] For the case that we start with a state $|\rho\rangle$ with bond dimension χ and apply L to it, the resulting state $|\rho\rangle' = L\,|\rho\rangle$ has an increased bond dimension of $\chi' = D\chi$. A repeated application would thus result in an exponential growth of the bond dimension. To circumvent this, one needs to truncate the state $|\rho\rangle'$ again and reduce $\chi' \to \chi$. Similar to the steps outlined above, the MPS compression can be done for instance by SVDs, or more optimally in a variational manner [84]. With this truncation scheme one can apply in principle the same Krylov space methods as described above in Sec. 2.2.2.1 to time evolve the state $|\rho(t)\rangle = \exp(Lt)\,|\rho(0)\rangle$. However, one has to bear in mind that the reduced state space of MPS with bond dimension $\chi \ll d^{N_B/2}$ does not represent a complete vector space. Therefore, if the Krylov space vectors $L^n\,|\rho\rangle$ are not well-represented in this state space the scheme cannot work. We tested a Krylov space time stepping with MPS for AMEA, but, its performance was very limited and problems with too large truncation errors occurred. For the same reason we discarded also the other Krylov space techniques, and instead of calculating the Green's functions in the frequency domain as in ED, we chose to perform time evolutions only. An efficient and accurate scheme for time evolutions is TEBD, which we found to perform well in AMEA. It is briefly presented in the following and for technical details we refer again to Ref. [84, 100, 101].

Eq. (2.58) stated above is not the only possible form and various MPS representations exist. When $\sum_{s_i} \boldsymbol{A}_i^{s_i\dagger}\boldsymbol{A}_i^{s_i} = \mathbb{1}$, as in Eq. (2.58), a MPS state is called left-canonical. A so-called right-canonical state with $\sum_{s_i} \boldsymbol{B}_i^{s_i}\boldsymbol{B}_i^{s_i\dagger} = \mathbb{1}$ is constructed by performing the SVDs outlined above from right to left instead of left to right [84]. In this way a MPS in one given form can be transformed into another. A third important representation was introduced in Ref. [100, 101] and is called canonical

$$|\rho\rangle \;=\; \sum_{\{s_i\}} \boldsymbol{\Gamma}_0^{s_0}\boldsymbol{\Lambda}_0\boldsymbol{\Gamma}_1^{s_1}\boldsymbol{\Lambda}_1\boldsymbol{\Gamma}_2^{s_2}\boldsymbol{\Lambda}_2\ldots\boldsymbol{\Lambda}_{N_B-1}\boldsymbol{\Gamma}_{N_B}^{s_{N_B}}\,|\{s_i\}\rangle\;. \tag{2.73}$$

Hereby, the matrices $\boldsymbol{\Lambda}_i$ are diagonal and contain the singular values for each bond. By this, one can immediately perform a Schmidt decomposition of the system at any bond μ with a correctly left-orthogonal side $i \le \mu$ and $\boldsymbol{A}_i^{s_i} = \boldsymbol{\Lambda}_{i-1}\boldsymbol{\Gamma}_i^{s_i}$, a right-orthogonal side $j > \mu$ and $\boldsymbol{B}_j^{s_j} = \boldsymbol{\Gamma}_j^{s_j}\boldsymbol{\Lambda}_j$, and the corresponding Schmidt values at bond μ given by $\boldsymbol{\Lambda}_\mu$. As a result, the entanglement at each bond is directly accessible by $\boldsymbol{\Lambda}_i$ and Eq. (2.65), and much more importantly, the representation allows for effective local modifications of the MPS states when applying few-site operators together with successive SVD truncations.

In particular, the time evolution operator $\exp(Lt)$ can be decomposed into individual parts by the well-known Trotter-Suzuki decomposition [84, 102]. For this one divides the time evolution into small intervals Δt and splits L into two parts L_e and L_o, acting on even and odd bonds only. Since $[L_e, L_o] \neq 0$, a Trotter error is encountered when decomposing the time evolution into

$$\exp(L\Delta t) = \exp(L_e\Delta t)\exp(L_o\Delta t) + \mathcal{O}(\Delta t^2)\,. \tag{2.74}$$

[23] This is true for the chosen geometry with nearest neighbor terms at most in $\boldsymbol{E}$, $\boldsymbol{\Gamma}^{(1)}$ and $\boldsymbol{\Gamma}^{(2)}$.

A time propagation with the simple splitting scheme above is only first order accurate in the step size Δt. Especially for the purpose of calculating the steady state it is advantageous to implement a higher-order splitting. An often applied second order scheme is the so-called Strang splitting [103]. However, we obtained better results with the second order scheme by McLachlan [102, 104]

$$\exp(L\Delta t) = \exp(L_o\Delta t_1)\exp(L_e\Delta t_2)\exp(L_o\Delta t_2)\exp(L_e\Delta t_1) + \mathcal{O}(\Delta t^3)\,, \tag{2.75}$$

with $\Delta t_1 = (1 - 1/\sqrt{2})\Delta t$ and $\Delta t_2 = 1/\sqrt{2}\Delta t$. By this the Trotter error in $|\rho_\infty\rangle$ could be further reduced. Independent of the particular splitting schemes, L_e and L_o by themselves are given by a sum of commuting parts $L_{i,i+1}$. As a result, the individual terms in $\exp(L_e\Delta t)$ can be applied to $|\rho(t)\rangle$ independently of each other and in parallel, see also Fig. 2.2. We thus have to consider solely the action of two-site gates $V^{(s_i',s_{i+1}'),(s_i,s_{i+1})} = \exp(L_{i,i+1}\Delta t)$ on $|\rho(t)\rangle$. When applied to the state in Eq. (2.73) additional entanglement between site i and site $i+1$ is created which causes the bond dimension to increase. In this algorithm, the increase is determined by the local Hilbert space size via $\chi' = d\chi$. The advantage of the representation Eq. (2.73) is that the state $|\rho(t)\rangle' = \exp(L_{i,i+1}\Delta t)\,|\rho(t)\rangle$ can be brought back into its canonical form with one SVD and local operations on the sites i and $i+1$ only, and a systematic truncation via the singular values $\mathbf{\Lambda}_i'$ is readily accessible.[24] Therefore, the TEBD algorithm allows for an efficient and directly parallelizable time evolution of $|\rho(t)\rangle$ when L has short-ranged couplings only.

Steady state and correlation functions: As discussed above, for the $\mathrm{IM}_{\mathrm{aux}}$ encountered in AMEA the application of Krylov space methods within MPS was rather inefficient and problematic. Much better results were obtained by using a TEBD scheme for the time evolution. On the one hand, the achievable accuracy was superior and on the other hand, the algorithm was better parallelizable and in general much faster. However, one should note that Krylov space methods and also variational formulations have been applied in recent works to Lindblad problems within MPS, see e.g. Ref. [97–99]. Most probably, the applicability of such schemes strongly depends on the size of the local Hilbert space d and the entanglement properties.

To calculate the steady state through a time evolution we used a series of time intervals with successively smaller time steps Δt. By this, the Trotter error could be systematically suppressed and controlled. However, for a fixed length of the time intervals the number of steps, and thus the computational effort, increases as $1/\Delta t$. In practice it was sufficient to use Δt values not smaller than $0.01\,\Gamma^{-1}$. The convergence can be monitored by applying the full Lindblad MPO to the state and evaluating $\|L\,|\rho(t)\rangle\|$, and also by computing local observables $\langle I|\,O\,|\rho(t)\rangle$. Once the steady state $|\rho_\infty\rangle$ is obtained the Green's function are calculated in the time domain according to Eqs. (2.38) and (2.39). It is hereby of advantage, even though not of crucial importance, to employ a linear prediction of the time-dependent Green's functions $G(t)$. This is well-applicable since the behavior of $G(t)$ after a sufficiently long relaxation time is very predictive and consists out of a sum of oscillating and exponentially decaying terms. Details on linear prediction can be found for instance in Ref. [87]. Finally, a discrete Fourier transform is employed to obtain Green's functions in the frequency domain. To avoid Gibbs oscillations it is advantageous to

[24] Note that one has to perform a re-canonization of the state when dealing with a non-Hermitian generator in the time evolution. In practice we did this after one application of L_e or L_o.

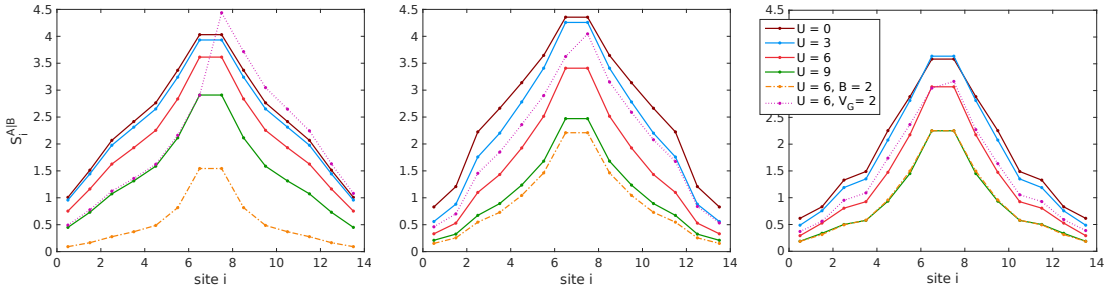

Figure 2.3.: Trend of the bipartite entanglement entropy $S_i^{A|B}$ in $\mathrm{IM}_{\mathrm{aux}}$, Eq. (2.65), for various impurity parameters. On the left for a bias voltage $\phi = 0$, middle for $\phi = 2\,\Gamma$, and on the right for $\phi = 4\,\Gamma$. Leads have been chosen as in Ref. [2], Sec. 3.2, with a temperature of $T = 0.05\,\Gamma$. Different values for the interaction strength U, magnetic field B and gate voltage V_G are shown, with $\varepsilon_{f\uparrow/\downarrow} = -U/2 + V_G \pm B/2$ in Eq. (1.5).

transform $G^R - G^A$ and to complement the real part thereafter with the Kramers-Kronig relation.

Concerning the entanglement properties of the steady state $|\rho_\infty\rangle$ and excited states $c_{f,\sigma}^{(\dagger)}|\rho_\infty\rangle$, as needed for Green's functions, one can say that the situation is sort of reversed when compared to the Hermitian case of unitary time evolutions. Normally, a ground state $|\psi_0\rangle$ can be represented very well by a MPS with small bond dimensions, and only in the time evolution of excited states $c_{f,\sigma}^{(\dagger)}|\psi_0\rangle$ a rapid growth of entanglement is observed. In many cases the entanglement increases even linearly in time $S \sim t$ which has the drastic consequence that the bond dimensions in $c_{f,\sigma}^{(\dagger)}|\psi_0\rangle$ should be increased exponentially [84]. Due to this, a hard limit is set to the possible simulation times.[25] Within AMEA we generally find the situation that the steady state $|\rho_\infty\rangle$ possesses already a rather high amount of entanglement, so that large bond dimensions are needed ($\chi \approx 1000$ with $U(1)$ symmetry, cf. Eq. (2.33)). But, when time evolving excited states $c_{f,\sigma}^{(\dagger)}|\rho_\infty\rangle$ we obtain only a short transient behavior with rapid entanglement growth, which then saturates quickly. Therefore, very long simulation times are accessible and from a comparison to ED we even found that the relative error is quite constant as a function of time. Most probably this originates in the contracting property of $V(t) = \exp(Lt)$ and the resulting exponential damping of excited states. A plot illustrating this entanglement behavior is given in Ref. [2], Sec. 3.2. In Fig. 2.3 various plots for the entanglement in $|\rho_\infty\rangle$ as a function of the bond index are shown. Two things are apparent: On the one hand, the largest entanglement entropy builds up in the center of the system at the impurity site, and on the other hand, a drastic decrease with increasing interaction strength is observed. Both are a consequence of the special geometry chosen for $\mathrm{IM}_{\mathrm{aux}}$, consisting of a filled and an empty bath chain. Due to this, possible hopping processes inside the chains are strongly suppressed which results in a low entanglement entropy there. Hoppings from the filled to the empty side are only possible across the impurity site, which in turn are limited when increasing the on-site Coulomb repulsion U. A similar effect is seen when including a Zeemann splitting of the on-site energy on the impurity by a magnetic field. A nonzero gate voltage, however, causes a more complicated behavior and evidently an

[25] However, different sophisticated strategies exist on how to extend this range [84, 87, 105].

asymmetry in $S_i^{A|B}$.[26] On the whole, the chosen geometry for $\mathrm{IM}_{\mathrm{aux}}$ is thus particularly applicable to situations with intermediate to strong interactions. Close to the $U = 0$ limit other geometries such as an unfolding of spin up and spin down electrons into two separate chains [84] could be of advantage. However, for the mapping procedure to work well, a geometry with two chains per spin is needed, so that an unfolding is more complicated in this case. Up to now it was not tested since especially the regime of strong interactions is challenging for numerical methods and of particular interest. With the developed MPS-solver we could obtain very accurate and promising results for this, see also Ref. [2] or Sec. 3.2 below.

[26] Note that a small gate voltage does not displace the Kondo peak and also does not affect its weight in a significant way.

3. Publications

Overview: The four articles included below constitute the main part of this thesis and are listed in chronological order. All of them deal with the auxiliary master equation approach (AMEA), which was introduced in Ref. [106]. There, the basic concept of mapping the original impurity problem onto an auxiliary open quantum system was suggested. The main topic and achievements of this thesis were to work out details in AMEA thoroughly and to adapt more efficient solution strategies for the mapping procedure and the manybody solution. In this way, a significant improvement of the capabilities of the approach could be attained. In the papers listed below, we developed two different technical improvements for the manybody solution and applied them to study, on the one hand, the nonequilibrium steady state physics of the single impurity Anderson model (SIAM), and on the other hand, transport across correlated layers within dynamical mean field theory (DMFT). We chose to only include the four articles below, since they fit together very well and build up a comprehensive picture of AMEA. Further papers published in the course of this thesis are briefly discussed at the end of this chapter and indicated in the bibliography as well.

In the first paper Ref. [1], Sec. 3.1, we presented a detailed derivation of the expressions for the noninteracting and interacting Green's functions that are needed within AMEA for the auxiliary Lindblad problem. Furthermore, we employed Krylov space methods for the exact diagonalization (ED) of the manybody problem. This enabled us to treat a larger number of bath sites of up to $N_B = 6$ instead of the $N_B = 2$ in Ref. [106]. This is an important improvement, since, on the one hand, the size of the Hilbert space basis increases exponentially and on the other hand, the overall accuracy of AMEA crucially depends on the number of bath sites and we typically find an exponential convergence when increasing N_B. The Krylov space implementation of the ED-solver enabled us to study the nonequilibrium SIAM and the behavior of the Kondo peak over a wide range of bias voltages and parameters.

In the second paper Ref. [2], Sec. 3.2, a different solution strategy for the manybody problem based on matrix product states (MPS) was presented, with the purpose of investigating the Kondo physics of the nonequilibrium SIAM in great detail. By exploiting the freedom to choose different geometries for the auxiliary Lindblad problem we could employ efficient time evolution techniques for MPS with nearest neighbor couplings only and furthermore, could drastically reduce the build-up of bipartite entanglement entropy. On the whole, this enabled us to consider up to $N_B = 16$ bath sites with the MPS solver and thus to achieve highly accurate results. A benchmark against a numerical renormalization group (NRG) calculation in the equilibrium limit revealed a remarkably close agreement for a situation with strong interaction and temperatures well below the Kondo temperature T_K. A convergence check in the nonequilibrium case showed the robustness of the results, so that a detailed investigation of the nonequilibrium spectral function and the splitting of the Kondo peak with increasing bias could be presented. Furthermore, measurable quantities relevant for experiments were calculated and discussed.

In the third paper Ref. [3], Sec. 3.3, as well as in the fourth paper Ref. [4], Sec. 3.4, an application of the ED-AMEA impurity solver within DMFT was presented. In particular, we studied charge transport across a correlated interface, which consisted of an infinitely extended 2D Hubbard layer sandwiched between two semi-infinite metallic leads. As for the SIAM discussed above, a current was driven across the system by applying a bias voltage between the two leads. One should note, that the same system was already considered in Ref. [106], however, with an ED-solver with 2 bath sites only. Due to the Krylov space ED-solver developed in this thesis, we could efficiently solve larger systems and presented DMFT calculations with up to $N_B = 6$. This enabled us to study the crossover from a nearly insulating Mott state to a strongly correlated metal up to a noninteracting metallic state, and its different manifestations in the current-voltage characteristics and in the spectral functions. In Ref. [4] we additionally introduced different lead temperatures, which enabled us to also study a temperature-induced suppression of the quasiparticle peak besides the bias-introduced decoherence. Not only the spectral function but also the current voltage characteristics revealed a very similar behavior to the Kondo physics in the nonequilibrium SIAM studied before.

Preliminary remark: In the following, a short preamble is included for each paper in order to clearly specify the contributions from each author, as required for a cumulative thesis. Furthermore, these preambles also serve the purpose to highlight important technical or numerical details of each work, which is meant to enable the reader to better assess the novelties and also the differences between each work.

3.1. Publication 1: ED impurity solver

3.1.1. Preamble

The article titled *Auxiliary master equation approach to nonequilibrium correlated impurities* was published in Physical Review B, **89** 165105, April 2014 [1].

This work was done by Antonius Dorda (AD) as first author and Martin Nuss (MN) as co-author, supervised by Wolfgang von der Linden (WL), and Enrico Arrigoni (EA). EA predefined and guided this research to large extent. AD, MN and EA worked together on the analytical derivation of expressions for the nonequilibrium Green's functions for the auxiliary impurity problem. AD then wrote the corresponding Matlab- and C-code for the solution of the noninteracting and interacting Lindblad problem. Hereby, different variants for the solution of the interacting problem were tested and compared. In the end, especially sparse methods for non-Hermitian matrices were employed: A shift-and-invert Arnoldi (rather small systems, $N_B < 6$) or a simple time evolution with a 2nd order Runge-Kutta stepping for the steady state, and thereafter, a two-sided Lanczos iteration for the ω-dependent Green's functions from a Lehmann representation. For the second important part, the mapping procedure, AD implemented and tested different minimization routines, and finally employed a quasi-Newton line search method with many random starting points. Especially EA and also the other authors contributed to assessing the efficiency of the different numerical approaches and thus to the design of the program. With this program, AD carried out the investigations and produced the data presented in the article below. All authors together analyzed and discussed the data, and decided for the topics to be investigated. MN and EA conducted most of the literature research and AD, MN and EA wrote a first version of the manuscript. All authors contributed in writing, revising and discussing the manuscript.

3.1.2. Original article

(see next page)

PHYSICAL REVIEW B **89**, 165105 (2014)

Auxiliary master equation approach to nonequilibrium correlated impurities

Antonius Dorda,* Martin Nuss, Wolfgang von der Linden, and Enrico Arrigoni
Institute of Theoretical and Computational Physics, Graz University of Technology, 8010 Graz, Austria
(Received 23 December 2013; published 7 April 2014)

We present a numerical method for the study of correlated quantum impurity problems out of equilibrium, which is particularly suited to address steady-state properties within dynamical mean field theory. The approach, recently introduced by Arrigoni *et al*. [Phys. Rev. Lett. **110**, 086403 (2013)], is based upon a mapping of the original impurity problem onto an auxiliary open quantum system, consisting of the interacting impurity coupled to bath sites as well as to a Markovian environment. The dynamics of the auxiliary system is governed by a Lindblad master equation whose parameters are used to optimize the mapping. The accuracy of the results can be readily estimated and systematically improved by increasing the number of auxiliary bath sites, or by introducing a linear correction. Here, we focus on a detailed discussion of the proposed approach including technical remarks. To solve for the Green's functions of the auxiliary impurity problem, a non-Hermitian Lanczos diagonalization is applied. As a benchmark, results for the steady-state current-voltage characteristics of the single-impurity Anderson model are presented. Furthermore, the bias dependence of the single-particle spectral function and the splitting of the Kondo resonance are discussed. In its present form, the method is fast, efficient, and features a controlled accuracy.

DOI: 10.1103/PhysRevB.89.165105 PACS number(s): 71.15.−m, 71.27.+a, 73.63.Kv, 73.23.−b

I. INTRODUCTION

Correlated systems out of equilibrium have recently attracted increasing interest due to the significant progress in a number of related experimental fields. Advances in microscopic control and manipulation of quantum mechanical many-body systems within quantum optics [1] and ultracold quantum gases, for example in optical lattices [2–6], have long reached high accuracy and versatility. Ultrafast laser spectroscopy [7,8] offers the possibility to explore and understand electronic dynamics in unprecedented detail. Experiments in condensed matter nanotechnology [9], spintronics [10], molecular junctions [11–16], and quantum wires or quantum dots [17,18] are able to reveal effects of the interference of few microscopic quantum states. The nonequilibrium nature of such experiments does not only offer a new route to explore fundamental aspects of quantum physics, such as nonequilibrium quantum phase transitions [19], the interplay between quantum entanglement, dissipation, and decoherence [20], or the pathway to thermalization [21,22], but also suggests the possibility of exciting future applications [11,23].

Addressing the dynamics of correlated quantum systems poses a major challenge to theoretical endeavors. In this respect, quantum impurity models help improving our understanding of fermionic many-body systems. In particular, the single-impurity Anderson model (SIAM) [24], which was originally devised to study magnetic impurities in metallic hosts [25,26], has become an important tool in many areas of condensed matter physics [27,28]. Most prominently, it features nonperturbative many-body physics which manifest in the Kondo effect [29]. It provides the backbone for all calculations within dynamical mean field theory (DMFT) [28,30], a technique which allows us to understand the properties of a broad range of correlated systems and becomes exact in the limit of infinite dimensions [31]. The basic physical properties of the SIAM in equilibrium are quite well understood [29] thanks to the pioneering work from Kondo [32], renormalization group [33], as well as perturbation theory (PT) [34–37] and the mapping to its low-energy realization, the Kondo model [38].

The SIAM out of equilibrium provides a description for several physical processes such as, for example, nonlinear transport through quantum dots [17,39], correlated molecules [13,14,40–42], or the influence of adsorbed atoms on surfaces or bulk transport [43]. As in the equilibrium case, the solution of the SIAM constitutes the bottleneck of nonequilibrium DMFT [44–51] calculations. Therefore, accurate and efficient methods to obtain dynamical correlation functions of impurity models out of equilibrium are required in order to describe time-resolved experiments on strongly correlated compounds [7,8] and to understand their steady-state transport characteristics [23].

However, nonequilibrium correlated impurity models still pose an exciting challenge to theory. Our work addresses this issue with special emphasis on the steady state. But, before introducing this work in Sec. I, we briefly review previous approaches. In recent times, a number of computational techniques have been devised to handle the SIAM out of equilibrium. Among them are scattering-state Bethe ansatz (BA) [52], scattering-state NRG (SNRG) [53–55], noncrossing approximation studies [56,57], fourth-order Keldysh PT [58], other perturbative methods [59,60] in combination with the renormalization group (RG) [61–65], iterative summation of real-time path integrals [66], time-dependent NRG [67], flow equation techniques [68,69], the time-dependent density matrix RG (DMRG) [70–75] applied to the SIAM [76,77], nonequilibrium cluster PT (CPT) [78], the nonequilibrium variational cluster approach (VCA) [79,80], dual fermions

*dorda@tugraz.at

[81], the functional RG (fRG) [82,83], diagrammatic quantum Monte Carlo (QMC) [84,85], continuous time QMC (CT-QMC) calculations on an auxiliary system with an imaginary bias [86–90], superoperator techniques [91,92], many-body PT and time-dependent density functional theory [93], generalized slave-boson methods [94], real-time RG (rtRG) [95], time-dependent Gutzwiller mean field calculations [96], and generalized master equation approaches [97]. Comparisons of the results of some of these methods are available in literature [77,98,99] and time scales have been discussed in Ref. [100].

Despite this large number of approaches, only a limited number of them is applicable to nonequilibrium DMFT, and very few are still accurate for large times in steady state. Beyond the quadratic action for the Falicof-Kimball model [46,101,102], iterated PT (IPT) [45], numerical renormalization group (NRG) [48], real-time QMC [48,103], the noncrossing approximation (NCA) [104,105], and recently Hamiltonian-based impurity solvers [106] have been applied in the time-dependent case. Some of the above approaches, such as QMC [49] and DMRG [73], are very accurate in addressing the short- and medium-time dynamics, but in some cases the accuracy decreases at long times and a steady state can not be reliably identified. Some other methods are perturbative and/or valid only in certain parameter regions or for restricted models. RG approaches (e.g., [61]) are certainly more appropriate to identify the low-energy behavior.

This work

In this paper, we discuss a method, first proposed in [51], which addresses the correlated impurity problem out of equilibrium, and is particularly efficient for the steady state. The accuracy of the results is *controlled* as it can be directly estimated by analyzing the bath hybridization function (details following). Here, we extend, test, and provide details of this approach and its implementation. The basic idea is to map the impurity problem onto an auxiliary open system, consisting of a small number of bath sites coupled to the interacting impurity and, additionally, to a so-called Markovian environment [107]. The parameters of this auxiliary open quantum system are obtained by optimization in order to represent the original impurity problem as accurately as possible. The auxiliary system dynamics are governed by a Lindblad master equation which is solved exactly with the non-Hermitian Lanczos method. The crucial point is that the overall accuracy of the method is thus solely determined by how well the auxiliary system reproduces the original one. This can be, in principle, improved by increasing the number of auxiliary bath sites.

In this study, we provide convincing benchmarks for the steady-state properties of the SIAM coupled to two metallic leads under bias voltage. We include a discussion of convergence as a function of the number of bath sites and present a scheme to estimate the error and partially correct for it. In its presented form, the method is fast, efficient, and is directly applicable to steady-state dynamical mean field theory [51] for which previously suggested methods are less reliable. Extending the method to treat time-dependent properties and multiorbital systems is possible, in principle, however with a much heavier computational effort.

The paper is organized as follows: In Sec. II A, the SIAM under bias voltage is introduced. In Sec. II B, we introduce nonequilibrium Green's functions and in Secs. II C and II D, we outline the auxiliary master equation approach where we also focus on details of our particular implementation. Results for the steady state, including the equilibrium situation, are presented in Sec. III. This includes the steady-state current-voltage characteristics which we compare with exact results from matrix product state (MPS) time evolution [77] as well as data for the spectral function under bias which we compare with nonequilibrium NRG [54]. We conclude and give an outlook in Sec. IV.

II. AUXILIARY MASTER EQUATION APPROACH

As discussed above, the method is particularly suited to deal with nonequilibrium steady-state properties caused by different temperatures and/or chemical potential in the leads of a correlated quantum impurity system. As such, it can be readily used as impurity solver for nonequilibrium DMFT [46,51]. Here, we illustrate its application to the fermionic SIAM with two leads having different chemical potentials, and, in principle, different temperatures.

A. Nonequilibrium single-impurity Anderson model

We consider a single Anderson impurity coupled to electronic leads under bias voltage [see Fig. 1(a)]

$$\hat{\mathcal{H}} = \hat{\mathcal{H}}_{\text{imp}} + \hat{\mathcal{H}}_{\text{res}} + \hat{\mathcal{H}}_{\text{coup}}. \tag{1}$$

The impurity orbital features charge as well as spin degrees of freedom and is subject to a local Coulomb repulsion U:

$$\hat{\mathcal{H}}_{\text{imp}} = \epsilon_f \sum_\sigma f_\sigma^\dagger f_\sigma + U\, \hat{n}_\uparrow^f \hat{n}_\downarrow^f.$$

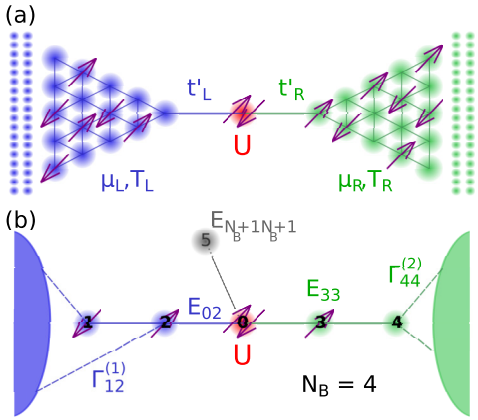

FIG. 1. (Color online) (a) Sketch of the quantum impurity model (1) consisting of an impurity with interaction U coupled via hybridizations t'_λ to noninteracting leads at chemical potential μ_λ and temperature T_λ, $\lambda \in \{L, R\}$. (b) Illustration of the auxiliary open quantum system [Eq. (10a)] with single-particle parameters $E_{\mu\nu}$ and Lindblad dissipators $\Gamma^\kappa_{\mu\nu}$ consisting of the impurity at site $f = 0$, N_B bath sites ($N_B = 4$ in the plot), as well as a Markovian environment (shaded areas). When evaluating linear corrections (see Appendix C), an additional site $N_B + 1$ is used.

Here, $f_\sigma^\dagger/f_\sigma$ denote fermionic creation/annihilation operators for the impurity orbital with spin $\sigma \in \{\uparrow,\downarrow\}$, respectively. The particle-number operator is defined in the usual way $\hat{n}_\sigma^f = f_\sigma^\dagger f_\sigma$ and the impurity onsite potential is $\epsilon_f = (V_G - \frac{U}{2})$, with gate voltage $V_G = 0$ at particle-hole symmetry. The impurity is coupled to two noninteracting electronic leads $\lambda \in \{L,R\}$ with dispersion $\epsilon_{\lambda k}$:

$$\hat{\mathcal{H}}_{\rm res} = \sum_{\lambda k\sigma} (\epsilon_\lambda + \epsilon_{\lambda k})\, c_{k\lambda\sigma}^\dagger\, c_{k\lambda\sigma}.$$

The effect of a bias voltage ϕ is to shift the chemical potential and the onsite energies of the two leads by $\epsilon_\lambda = \pm\frac{\phi}{2}$, respectively. For the energies $\epsilon_{\lambda k}$ of the leads we will consider two cases.

(i) Two tight-binding semi-infinite chains with nearest-neighbor hopping t, corresponding to a semicircular electronic density of states (DOS): In this case, the boundary retarded single-particle Green's function of the two uncoupled leads is given by [108–110]

$$g_\lambda^R(\omega) = g_{{\rm SC},\lambda}^R(\omega) = \frac{\omega-\epsilon_\lambda}{2t^2} - i\frac{\sqrt{4t^2-(\omega-\epsilon_\lambda)^2}}{2t^2}, \qquad (2)$$

with a bandwidth of $D_{\rm SC} = 4\,t$.

(ii) A constant DOS with a bandwidth $D_{\rm WB} = \pi\, t$ results in boundary Green's functions [109]

$$g_\lambda^R(\omega) = g_{{\rm WB},\lambda}^R(\omega) = -\frac{1}{D_{\rm WB}} \ln\left(\frac{\omega-\epsilon_\lambda-\frac{D_{\rm WB}}{2}}{\omega-\epsilon_\lambda+\frac{D_{\rm WB}}{2}}\right). \qquad (3)$$

The choice $D_{\rm WB} = \pi\, t$ makes sure that the DOS at $\omega = 0$ of both lead types coincide. The leads are coupled to the impurity orbital by

$$\hat{\mathcal{H}}_{\rm coup} = \sum_{\lambda\sigma} t'_\lambda \frac{1}{\sqrt{N_k}} \sum_k (c_{k\lambda\sigma}^\dagger\, f_\sigma + f_\sigma^\dagger\, c_{k\lambda\sigma}),$$

where we take the same hybridization $t'_\lambda = -0.3162\,t$ for both leads, and $N_k \to \infty$ is the number of k points. Expressions presented below are valid for arbitrary temperatures, although we will show results for zero temperature only, which is numerically the most unfavorable case [111]. The setup chosen here represents by no means a limitation of the method and extensions to more complicated situations, such as nonsymmetric couplings, off particle-hole symmetry, etc., are straightforward.

B. Steady-state nonequilibrium Green's functions

We are interested in the steady-state behavior under bias voltage of the model described by Eq. (1). We assume that such a steady state exists and is unique [112]. We denote the single-particle Green's function of the impurity in the nonequilibrium Green's function (Keldysh) formalism by [113–117]

$$\underline{G}(\omega) = \begin{pmatrix} G^R(\omega) & G^K(\omega) \\ 0 & G^A(\omega) \end{pmatrix}. \qquad (4)$$

Fourier transformation to energy ω is possible since in the steady state the system becomes time translationally invariant. In that case, the memory of the initial condition has been fully washed away, so there is no contribution from the Matsubara branch [118]. We will use an underline $\underline{\ldots}$ to denote two-point functions with the Keldysh matrix structure as in Eq. (4).

The Green's function of the correlated impurity can be expressed via Dyson's equation

$$\underline{G}^{-1}(\omega) = \underline{G}_0^{-1}(\omega) - \underline{\Sigma}(\omega), \qquad (5)$$

where $\underline{\Sigma}(\omega)$ is the impurity self-energy. The noninteracting impurity Green's function $\underline{G}_0(\omega)$ can be written in the form

$$\underline{G}_0^{-1}(\omega) = \underline{g}_0^{-1}(\omega) - \underline{\Delta}(\omega), \qquad (6)$$

$\underline{g}_0(\omega)$ being the noninteracting Green's function of the disconnected impurity [108], and

$$\underline{\Delta}(\omega) = \sum_\lambda {t'_\lambda}^2\, \underline{g}_\lambda(\omega) \qquad (7)$$

is the hybridization function of the leads (a 2×2 Keldysh object, in contrast to the equilibrium case, where it is convenient to work in Matsubara space). We define an equilibrium Anderson width [29] for each lead $\Delta_0 \equiv -\frac{1}{2}\,{\rm Im}[\underline{\Delta}^R(\omega = 0)] = \frac{t'^2_\lambda}{t} \approx 0.1\,t$. In the following, we will use Δ_0 as a unit of energy and in addition we choose $\hbar = e = 1$.

The boundary Green's functions $\underline{g}_\lambda$ of each disconnected lead is determined by (a) its retarded component g_λ^R [either Eqs. (2) or (3)], (b) its advanced component $g_\lambda^A = g_\lambda^{R*}$, and (c) its Keldysh component, which satisfies the fluctuation dissipation theorem

$$g_\lambda^K(\omega) = 2i\,[1 - 2p_{\rm F}(\omega-\mu_\lambda)]\,{\rm Im}\big[g_\lambda^R(\omega)\big] \qquad (8)$$

since the disconnected leads are in equilibrium. Here, $p_{\rm F}(\omega-\mu_\lambda)$ is the Fermi distribution with chemical potential μ_λ. For the noninteracting isolated impurity, one can take $(g_0^{-1})^R = \omega - \epsilon_f$ and $(g_0^{-1})^K = 0$ since infinitesimals 0^+ can be neglected after coupling to the leads (unless there are bound states). As usual, the presence of the interaction U makes the solution of the problem impurity plus leads a major challenge both in equilibrium as well as out of equilibrium, which we plan to address in this paper.

Similarly to the equilibrium case, the action of the leads on the impurity is completely determined by the hybridization function $\underline{\Delta}(\omega)$, *independently of how the leads are represented in detail*. In other words, if one constructs a different configuration of leads (e.g., with more leads with different temperatures, DOS, etc.), which has the same $\underline{\Delta}(\omega)$, i.e. the same $\Delta^R(\omega)$ and $\Delta^K(\omega)$ as Eq. (7), then the resulting local properties of the interacting impurity, e.g., the Green's function $\underline{G}(\omega)$ are the same. This holds provided the leads contain *noninteracting* fermions only.

The approach we suggested in Ref. [51] precisely exploits this property. The idea is to replace the impurity plus leads system [Eq. (1)] by an auxiliary one which reproduces $\underline{\Delta}(\omega)$ as accurately as possible, and at the same time can be solved exactly by numerical methods, such as Lanczos exact diagonalization. Details on the construction of the auxiliary impurity system are given in the following.

The self-energy $\underline{\Sigma}_{\rm aux}(\omega)$ of the auxiliary system, obtained by exact diagonalization, is used in analogy to DMFT [28,119]

as an approximation to the physical self-energy of the original impurity system. Inserting $\underline{\Sigma}(\omega) \approx \underline{\Sigma}_{\rm aux}(\omega)$ into Eqs. (5) and (6), together with the exact hybridization function $\underline{\Delta}(\omega)$ yields an approximation for the physical Green's function. From this, observables such as the current or the spectral function are then calculated. We emphasize that the accuracy of this approximation can be controlled by the difference between the $\underline{\Delta}_{\rm aux}(\omega)$ of the auxiliary system and the physical one $\underline{\Delta}(\omega)$, and that this can be, in principle, systematically improved, as discussed below.

C. Auxiliary open quantum system

The idea presented here is strongly related to the exact diagonalization (ED) approach for the DMFT impurity problem in *equilibrium* [28,119]. Here, the infinite leads are replaced by a small number of bath sites, whose parameters are optimized by fitting the hybridization function in Matsubara space. The reduced system of bath sites plus impurity is then solved by Lanczos ED [120]. This approach can not be straightforwardly extended to the nonequilibrium steady-state case for several reasons: (i) since the small bath is finite, its time dependence is (quasi)periodic, i.e., no steady state is reached, (ii) there is no Matsubara representation out of equilibrium [121], thus, one is forced to use real energies but (iii) in this case $\mathrm{Im}[\Delta^R_{\rm aux}(\omega)]$ of the small bath consists of δ peaks and can hardly be fitted to a smooth $\Delta^R(\omega)$. The solution we suggested in Ref. [51] consists in additionally coupling the small bath to a Markovian environment, which makes it effectively "infinitely large," and solves problems (i) and (iii) above. Specifically, we replace the impurity plus leads model [Eq. (1)] by an auxiliary *open* quantum system consisting of the impurity plus a small number of bath sites, which in turn are coupled to a Markovian environment.

The dynamics of the system (consisting of bath sites and impurity), including the effect of the Markovian environment is expressed in terms of the Lindblad quantum master equation which controls the time dependence of its reduced density operator $\hat{\rho}$ [107,122]:

$$\dot{\hat{\rho}} = \hat{\hat{\mathcal{L}}}\hat{\rho}. \tag{9}$$

The Lindblad superoperator [123]

$$\hat{\hat{\mathcal{L}}} = \hat{\hat{\mathcal{L}}}_H + \hat{\hat{\mathcal{L}}}_D \tag{10a}$$

consists of a unitary contribution

$$\hat{\hat{\mathcal{L}}}_H\hat{\rho} = -i[\hat{\mathcal{H}}_{\rm aux},\hat{\rho}],$$

as well as a nonunitary, dissipative term originating from the coupling to the Markovian environment

$$\hat{\hat{\mathcal{L}}}_D\hat{\rho} \equiv 2\sum_{\mu\nu=0}^{N_B}\sum_{\sigma}\left[\Gamma^{(1)}_{\nu\mu}\left(d_{\mu\sigma}\hat{\rho}\,d^\dagger_{\nu\sigma} - \frac{1}{2}\{\hat{\rho},d^\dagger_{\nu\sigma}d_{\mu\sigma}\}\right) + \Gamma^{(2)}_{\nu\mu}\left(d^\dagger_{\nu\sigma}\hat{\rho}\,d_{\mu\sigma} - \frac{1}{2}\{\hat{\rho},d_{\mu\sigma}d^\dagger_{\nu\sigma}\}\right)\right], \tag{10b}$$

where $[\hat{A},\hat{B}]$ and $\{\hat{A},\hat{B}\}$ denote the commutator and anticommutator, respectively. The unitary time evolution is generated by the Hamiltonian

$$\hat{\mathcal{H}}_{\rm aux} = \sum_{\mu\nu=0}^{N_B}\sum_{\sigma}E_{\mu\nu}d^\dagger_{\mu\sigma}d_{\nu\sigma} + Ud^\dagger_{f\uparrow}d_{f\uparrow}d^\dagger_{f\downarrow}d_{f\downarrow}, \tag{11}$$

describing a fermionic "chain" ($E_{\mu\nu}$ is nonzero only for onsite and nearest-neighbor terms). It is convenient to choose the interacting impurity at site $f = 0$ and N_B auxiliary bath sites at $\mu,\nu = 1,\ldots,N_B$ (see Fig. 1(b)). As usual, $d^\dagger_{\mu\sigma}/d_{\mu\sigma}$ create/annihilate the corresponding auxiliary particles. The quadratic form of the dissipator [Eq. (10b)] corresponds to a noninteracting Markovian environment. The dissipation matrices $\Gamma^{(\kappa)}_{\mu\nu}$, $\kappa \in \{1,2\}$, are Hermitian and positive semidefinite [122]. The advantage of replacing the impurity problem by the auxiliary one described by Eqs. (9)–(11), is that for a small number of bath sites the dynamics of the interacting auxiliary system can be solved exactly by diagonalization of the superoperator $\hat{\hat{\mathcal{L}}}$ in the space of many-body density operators (see Sec. II D 2).

Intuitively, one can consider the effective system as a truncation of the original chain described by Eq. (1), whereby the Markovian environment compensates for the missing "pieces." However, this would still be a crude approximation and, in addition, it would not be clear how to introduce the chemical potential in the Markovian environment (except for weak coupling). Our strategy, similarly to the equilibrium case, consists in simply using the parameters of the auxiliary system in order to provide an optimal fit to the bath spectral function $\underline{\Delta}(\omega)$. The parameters for the fit are, in principle, $E_{\mu\nu}$ and $\Gamma^{(\kappa)}_{\mu\nu}$. However, one should consider that there is a certain redundancy. In other words, several combinations of parameters lead to the same $\underline{\Delta}(\omega)$. For example, it is well known in equilibrium that in the case of the $E_{\mu\nu}$ one can restrict to diagonal and nearest-neighbor terms only [124].

The accuracy of the results will be directly related to the accuracy of the fit to $\underline{\Delta}(\omega)$, and this is expected to increase rapidly with the number of fit parameters, which obviously increases with N_B. On the other hand, also the computational complexity necessary to exactly diagonalize the interacting auxiliary system increases exponentially with N_B. The fit does not present a major numerical difficulty, as the determination of the hybridization functions of both the original model [Eq. (7)], as well as the one of the auxiliary system $\underline{\Delta}_{\rm aux}(\omega)$ described by the Lindblad equation (10) require the evaluation of $\underline{G}_0$ [cf. (6)], i.e., the solution of a *noninteracting* problem.

The fit is obtained by minimizing the cost function

$$\chi\left(E_{\mu\nu},\Gamma^{(\kappa)}_{\mu\nu}\right) = \sum_{\alpha\in\{R,K\}}\int_{-\infty}^{\infty}d\omega\,W^\alpha(\omega) \times \left|\Delta^\alpha(\omega) - \Delta^\alpha_{\rm aux}\left(\omega;E_{\mu\nu},\Gamma^{(\kappa)}_{\mu\nu}\right)\right|^n \tag{12}$$

with respect to the parameters of the auxiliary system. The advanced component does not need to be considered as $\Delta^A = \Delta^{R*}$. Of course, as in ED-based DMFT, there exists an ambiguity which is related to the choice of the weight function $W^\alpha(\omega)$, which also sets the integral boundaries. This uncertainty is clearly reduced upon increasing N_B.

Depending on the expected physics, it might be useful to adopt an energy-dependent weight function. This could be

used, for example, to describe the physics around the chemical potentials more accurately.

Once the auxiliary system is defined in terms of $E_{\mu\nu}$ and $\Gamma^{(\kappa)}_{\mu\nu}$, the corresponding interacting nonequilibrium problem (10) can be solved by an exact diagonalization of the non-Hermitian superoperator $\hat{\hat{\mathcal{L}}}$ within the space of many-body density operators. The dimension of this space is equal to the square of the dimension of the many-body Hilbert space, and thus it grows exponentially as a function of N_B. Therefore, for $N_B \geqslant 4$, a non-Hermitian Lanczos treatment must be used. The solution of the noninteracting Lindblad problem is nonstandard (see, e.g., Ref. [125]), and a method particularly suited for the present approach is discussed in Sec. II D 1.

D. Green's functions of the auxiliary Lindblad problem

In this section, we present expressions for the Green's functions of the auxiliary system. Specifically, we will derive an analytic expression for the noninteracting Green's functions in Sec. II D 1, and illustrate the numerical procedure to determine the interacting ones in Sec. II D 2. The derivations make largely use of the formalism of [126] (see also [127]). For an alternative appealing approach to the noninteracting case, see also Ref. [125]. All Green's functions discussed in Sec. II D are the ones of the auxiliary system, which are different from the physical ones for $N_B < \infty$.

The dynamics of the auxiliary open quantum system described by the superoperator $\hat{\hat{\mathcal{L}}}$ [Eq. (10)] can be recast in an elegant way as a standard operator problem in an augmented fermion Fock space with twice as many sites [125–128]. Specifically, one introduces "tilde" operators $\tilde{d}_\mu/\tilde{d}^\dagger_\mu$ together with the original ones $d_\mu/d^\dagger_\mu$ [129]. Introducing the so-called left vacuum

$$|I\rangle = \sum_S (-i)^{N_S} |S\rangle \otimes |\tilde{S}\rangle , \tag{13}$$

where $|S\rangle$ are many-body states of the original Fock space, $|\tilde{S}\rangle$ the corresponding ones of the tilde space [126], and N_S the number of particles in S. The nonequilibrium density operator can be written as a state vector in this augmented space

$$|\rho(t)\rangle\rangle \equiv \hat{\rho}(t)\,|I\rangle . \tag{14}$$

The Lindblad equation is rewritten in a Schrödinger-type fashion [123,126]

$$\frac{d}{dt}\,|\rho(t)\rangle\rangle = \hat{\mathcal{L}}\,|\rho(t)\rangle\rangle , \tag{15}$$

where now $\hat{\mathcal{L}}$ is an ordinary *operator* in the augmented space. $\hat{\mathcal{L}} = \hat{\mathcal{L}}_0 + \hat{\mathcal{L}}_I$ is conveniently represented in terms of the operators of the augmented space in a vector notation [129]:

$$\boldsymbol{d}^\dagger = \left(d^\dagger_0, \ldots, d^\dagger_{N_B}, \tilde{d}_0, \ldots \tilde{d}_{N_B}\right).$$

Its noninteracting part $\mathcal{L}_0$ reads in the augmented space [123,126] as

$$i\hat{\mathcal{L}}_0 = \sum_\sigma (\boldsymbol{d}^\dagger \boldsymbol{h} \boldsymbol{d} - \mathrm{Tr}(\boldsymbol{E} + i\boldsymbol{\Lambda})), \tag{16}$$

where Tr denotes the matrix trace and the matrix $\boldsymbol{h}$ is given by

$$\boldsymbol{h} = \begin{pmatrix} \boldsymbol{E} + i\boldsymbol{\Omega} & 2\boldsymbol{\Gamma}^{(2)} \\ -2\boldsymbol{\Gamma}^{(1)} & \boldsymbol{E} - i\boldsymbol{\Omega} \end{pmatrix}, \tag{17}$$

with

$$\boldsymbol{\Lambda} = (\boldsymbol{\Gamma}^{(2)} + \boldsymbol{\Gamma}^{(1)}), \quad \boldsymbol{\Omega} = (\boldsymbol{\Gamma}^{(2)} - \boldsymbol{\Gamma}^{(1)}).$$

Its interacting part has the form [126]

$$i\mathcal{L}_I = U d^\dagger_{f\uparrow} d_{f\uparrow} d^\dagger_{f\downarrow} d_{f\downarrow} - U \tilde{d}^\dagger_{f\uparrow} \tilde{d}_{f\uparrow} \tilde{d}^\dagger_{f\downarrow} \tilde{d}_{f\downarrow}.$$

In this auxiliary open system, dynamic two-time correlation functions for two operators $\hat{A}$ and $\hat{B}$ of the system can be expressed as

$$\begin{aligned} iG_{BA}(t_2,t_1) &\equiv \langle \hat{B}_{\mathcal{U}}(t_2)\hat{A}_{\mathcal{U}}(t_1)\rangle \\ &= \mathrm{tr}_{\mathcal{U}}(\hat{B}_{\mathcal{U}}(t_2)\hat{A}_{\mathcal{U}}(t_1)\hat{\rho}_{\mathcal{U}}) = \mathrm{tr}\left(\hat{B}\,\hat{A}_{t_1,t_2-t_1}\right), \end{aligned} \tag{18}$$

where $\hat{\rho}_{\mathcal{U}}$ is the density operator of the "universe" $\mathcal{U}$ composed of the system and Markovian environment, tr is the trace over the system degrees of freedom, tr_E the one over the environment, $\mathrm{tr}_{\mathcal{U}} = \mathrm{tr} \otimes \mathrm{tr}_E$ the one over the universe, $\hat{O}_{\mathcal{U}}(\ldots)$ denotes the unitary time evolution of an operator $\hat{O}$ according to the Hamiltonian of the universe $\hat{\mathcal{H}}_{\mathcal{U}}$. Here [107],

$$\hat{A}_{t_1,t} \equiv \mathrm{tr}_E(e^{-i\hat{\mathcal{H}}_{\mathcal{U}}t}\,\hat{A}\hat{\rho}_{\mathcal{U}}(t_1)e^{+i\hat{\mathcal{H}}_{\mathcal{U}}t}). \tag{19}$$

Notice that the time evolution of $\hat{\rho}_{\mathcal{U}}(t)$, as well as the one in Eq. (19), are *opposite with respect to the Heisenberg time evolution of operators*. This is the convention for density operators. For $t = t_2 - t_1 > 0$ one can use the quantum regression theorem [107] which holds under the same assumptions as for Eq. (9). It states that

$$\frac{d}{dt}\hat{A}_{t_1,t} = \hat{\hat{\mathcal{L}}}\hat{A}_{t_1,t}. \tag{20}$$

In the augmented space, in the same way as for (14) and (15), one can associate the operator (19) with the state vector $|A_{t_1,t}\rangle\rangle = \hat{A}_{t_1,t}\,|I\rangle$. For this vector, (20) translates into

$$\frac{d}{dt}\left|A_{t_1,t}\right\rangle\rangle = \hat{\mathcal{L}}\left|A_{t_1,t}\right\rangle\rangle . \tag{21}$$

Considering its initial value (time $t = 0$)

$$\left|A_{t_1,0}\right\rangle\rangle = \hat{A}\,|\rho(t_1)\rangle\rangle ,$$

the solution of (21) reads as

$$\left|A_{t_1,t}\right\rangle\rangle = e^{\hat{\mathcal{L}}t}\hat{A}\,|\rho(t_1)\rangle\rangle . \tag{22}$$

Therefore, we have for the correlation function (18) for $t_2 > t_1$, which we denote as $G^+_{BA}(t_2,t_1)$:

$$iG^+_{BA}(t_2,t_1) = \langle I|\hat{B}e^{\hat{\mathcal{L}}(t_2-t_1)}\hat{A}|\rho(t_1)\rangle\rangle = \langle I|\hat{B}(t_2-t_1)\hat{A}|\rho(t_1)\rangle\rangle,$$

where

$$\hat{B}(t) := e^{-\hat{\mathcal{L}}t}\hat{B}e^{\hat{\mathcal{L}}t} \tag{23}$$

is the non-Hermitian time evolution of the operator $\hat{B}$, and we have exploited the relation [126] $\langle I|\,\hat{\mathcal{L}} = 0$. For the steady-state correlation function, which depends on $t = t_2 - t_1$, we have

$$iG^+_{BA}(t) = \langle I|\,\hat{B}(t)\hat{A}\,|\rho_\infty\rangle\rangle , \tag{24}$$

where $\hat{\rho}_\infty$ is the steady-state density operator. Since the quantum regression theorem only propagates forward in time, for $t < 0$ one has to take the complex conjugate of Eq. (18), which gives for the $t < 0$ steady-state correlation function denoted as G^-_{BA}

$$iG^-_{BA}(t) = -iG^+_{A^\dagger B^\dagger}(-t)^* = \langle I|\,\hat{A}^\dagger(-t)\hat{B}^\dagger\,|\rho_\infty\rangle^* . \quad (25)$$

Using (24), the steady-state greater Green's function for times $t > 0$ reads as [130]

$$\begin{aligned} G^{>+}_{\mu\nu}(t) &\equiv -i\theta(t)\,\langle d_\mu(t+t_1)d^\dagger_\nu(t_1)\rangle_{t1\to\infty} \\ &= -i\theta(t)\;\langle I|\,d_\mu(t)d^\dagger_\nu\,|\rho_\infty\rangle\,. \end{aligned} \quad (26)$$

We can use (24) also for the lesser Green's function, however, for [130] $t < 0$,

$$\begin{aligned} G^{<+}_{\mu\nu}(t) &\equiv i\theta(-t)\,\langle d^\dagger_\nu(t_1)d_\mu(t+t_1)\rangle_{t1\to\infty} \\ &= i\theta(-t)\;\langle I|\,d^\dagger_\nu(-t)d_\mu\,|\rho_\infty\rangle\,. \end{aligned}$$

For the opposite sign of t, we can use (25), so that for both Green's functions one has [123,130]

$$\boldsymbol{G}^{\gtrless -}(t) = -\boldsymbol{G}^{\gtrless +}(-t)^\dagger. \quad (27)$$

For the Fourier-transformed Green's function, defined, with abuse of notation as

$$\boldsymbol{G}^{\gtrless\pm}(\omega) = \int dt\, e^{i\omega t}\boldsymbol{G}^{\gtrless\pm}(t)\,, \quad (28)$$

relation (27) translates into

$$\boldsymbol{G}^{\gtrless -}(\omega) = -\boldsymbol{G}^{\gtrless +}(\omega)^\dagger. \quad (29)$$

We need the retarded and the Keldysh Green's functions

$$\begin{aligned} \boldsymbol{G}^R &= \boldsymbol{G}^{>+} - \boldsymbol{G}^{<-} = \boldsymbol{G}^{>+} + \boldsymbol{G}^{<+\dagger}, \\ \boldsymbol{G}^K &= \boldsymbol{G}^{>+} + \boldsymbol{G}^{<-} + \boldsymbol{G}^{>-} + \boldsymbol{G}^{<+} = \boldsymbol{G}^{>+} + \boldsymbol{G}^{<+} - \text{H.c.}, \end{aligned} \quad (30)$$

whereby both relations hold for the time-dependent as well as for the Fourier-transformed ones.

1. Noninteracting case

To solve the noninteracting Lindblad problem described by (16), one first diagonalizes the non-Hermitian matrix [126] $\boldsymbol{h}$ in Eq. (17):

$$\boldsymbol{\varepsilon} = \boldsymbol{V}^{-1}\boldsymbol{h}\boldsymbol{V}, \quad (31)$$

where $\boldsymbol{\varepsilon}$ is a diagonal matrix of eigenvalues ε_μ. The noninteracting Lindbladian (16) can then be written as

$$i\hat{\mathcal{L}}_0 = \bar{\boldsymbol{\xi}}\,\boldsymbol{\varepsilon}\,\boldsymbol{\xi} + \eta$$

in terms of the normal modes

$$\boldsymbol{\xi} = \boldsymbol{V}^{-1}\boldsymbol{d}, \quad \bar{\boldsymbol{\xi}} = \boldsymbol{d}^\dagger\boldsymbol{V}, \quad (32)$$

and a constant η. The normal modes still obey canonical anticommutation rules

$$\{\xi_\mu, \bar{\xi}_\nu\} = \delta_{\mu\nu}, \quad (33)$$

but are not mutually Hermitian conjugate.

The steady state $|\rho_\infty\rangle$ obeys the equation

$$\hat{\mathcal{L}}\,|\rho_\infty\rangle = 0.$$

Let us now consider the time evolution (22) of a state initially consisting of the normal mode operators applied to the steady-state density matrix

$$e^{\hat{\mathcal{L}}_0 t}\xi_\mu\,|\rho_\infty\rangle = e^{\hat{\mathcal{L}}_0 t}\xi_\mu e^{-\hat{\mathcal{L}}_0 t}\,|\rho_\infty\rangle = e^{i\varepsilon_\mu t}\xi_\mu\,|\rho_\infty\rangle\,.$$

If $\mathrm{Im}(\varepsilon_\mu) < 0$, this term diverges exponentially in the long-time limit, which would be in contradiction to the fact that $|\rho_\infty\rangle$ is a steady state, unless the state created by ξ_μ is zero. Therefore, we must have

$$\xi_\mu\,|\rho_\infty\rangle = 0 \quad \text{for } \mathrm{Im}(\varepsilon_\mu) < 0. \quad (34a)$$

Similarly, we must have

$$\bar{\xi}_\mu\,|\rho_\infty\rangle = 0 \quad \text{for } \mathrm{Im}(\varepsilon_\mu) > 0. \quad (34b)$$

These equations, thus, define the steady state as a kind of "Fermi sea." In addition, by requiring that expectation values of the form

$$\langle I|\,\xi_\mu(t)\bar{\xi}_\nu\,|\rho\rangle$$

do not diverge for large t, we obtain that

$$\langle I|\,\xi_\mu = 0 \quad \text{for } \mathrm{Im}(\varepsilon_\mu) > 0, \quad (34c)$$

$$\langle I|\,\bar{\xi}_\mu = 0 \quad \text{for } \mathrm{Im}(\varepsilon_\mu) < 0. \quad (34d)$$

From (34d) it follows that an expectation value of the form $\langle I|\,\bar{\xi}_\mu\xi_\nu\,|\rho_\infty\rangle$ vanishes for the case $\mathrm{Im}(\varepsilon_\mu) < 0$. For $\mathrm{Im}(\varepsilon_\mu) > 0$ we make use of the anticommutation rules (33) together with (34b) and the fact that [126] $\langle I|\rho_\infty\rangle = \mathrm{tr}\,\rho_\infty = 1$ and arrive at

$$\langle I|\,\bar{\xi}_\mu\xi_\nu\,|\rho_\infty\rangle = D_{\mu\nu},$$

where the matrix

$$D_{\mu\nu} = \delta_{\mu\nu}\,\theta[\mathrm{Im}(\varepsilon_\mu)].$$

Similarly,

$$\langle I|\,\xi_\mu\bar{\xi}_\nu\,|\rho_\infty\rangle = \bar{D}_{\mu\nu} \equiv \delta_{\mu\nu} - D_{\mu\nu}.$$

The expression for the steady-state correlation functions of the eigenmodes $\boldsymbol{\xi}$ of $\hat{\mathcal{L}}_0$ can be now evaluated by considering that, due to the anticommutation rules, the Heisenberg time evolution (23) gives

$$\xi_\mu(t) = e^{-i\varepsilon_\mu t}\,\xi_\mu, \quad \bar{\xi}_\mu(t) = e^{i\varepsilon_\mu t}\,\bar{\xi}_\mu.$$

Thus,

$$\langle I|\,\xi_\mu(t)\bar{\xi}_\nu\,|\rho_\infty\rangle = e^{-i\varepsilon_\mu t}\,\langle I|\,\xi_\mu\bar{\xi}_\nu\,|\rho_\infty\rangle = e^{-i\varepsilon_\mu t}D_{\mu\nu}.$$

In this way, the greater Green's function for $t > 0$ becomes

$$\begin{aligned} iG^{>+}_{0\mu\nu}(t) &= \langle I|\,d_\mu(t)d^\dagger_\nu\,|\rho_\infty\rangle \\ &= \sum_\varsigma V_{\mu\varsigma}e^{-i\varepsilon_\varsigma t}\bar{D}_{\varsigma\varsigma}(V^{-1})_{\varsigma\nu} \\ &= (\boldsymbol{V}e^{-i\boldsymbol{\varepsilon}t}\bar{\boldsymbol{D}}\boldsymbol{V}^{-1})_{\mu\nu}, \end{aligned} \quad (35)$$

where we have used (32). The Green's functions are defined with operators $d_\mu/d^\dagger_\mu$ in the original Fock space, so that it is sufficient to know the first $N_B + 1$ rows (columns) of $\boldsymbol{V}$ ($\boldsymbol{V}^{-1}$). For this purpose we introduce

$$\boldsymbol{U} = \boldsymbol{T}\boldsymbol{V}, \quad \boldsymbol{U}^{(-1)} = \boldsymbol{V}^{-1}\boldsymbol{T}^\dagger,$$

whereby $\boldsymbol{T}$ is a $(N_B+1)\times(2N_B+2)$ matrix, which in block form reads as $\boldsymbol{T}=(\mathbb{1}\quad \boldsymbol{0})$. Notice that $\boldsymbol{U}^{-1}\neq\boldsymbol{U}^{(-1)}$. With this, the Fourier transform (28) of (35) is given by [131]

$$\boldsymbol{G}_0^{>+}(\omega)=\left(\boldsymbol{U}\frac{\bar{\boldsymbol{D}}}{\omega-\boldsymbol{\varepsilon}}\boldsymbol{U}^{(-1)}\right), \tag{36}$$

and $G^{>-}_{0\mu\nu}(\omega)$ is obtained with the help of (29). Similarly, the lesser Green's function for $t<0$

$$\begin{aligned} iG^{<+}_{0\mu\nu}(t) &= -\langle I|d_\nu^\dagger d_\mu(t)\,|\rho_\infty\rangle \\ &= -\sum_\varsigma V_{\mu\varsigma}e^{-i\varepsilon_\varsigma t}D_{\varsigma\varsigma}(V^{-1})_{\varsigma\nu} \\ &= -(\boldsymbol{U}e^{-i\boldsymbol{\varepsilon}t}\boldsymbol{D}\boldsymbol{U}^{(-1)})_{\mu\nu}, \end{aligned}$$

with the Fourier transform

$$\boldsymbol{G}_0^{<+}(\omega)=\left(\boldsymbol{U}\frac{\boldsymbol{D}}{\omega-\boldsymbol{\varepsilon}}\boldsymbol{U}^{(-1)}\right), \tag{37}$$

and $\boldsymbol{G}_0^{<-}(\omega)$ is obtained from (29). Using (30) together with (36) and (37), we get

$$\boldsymbol{G}_0^R(\omega)=\boldsymbol{U}\frac{\bar{\boldsymbol{D}}}{\omega-\boldsymbol{\varepsilon}}\boldsymbol{U}^{(-1)}+\left(\boldsymbol{U}\frac{\boldsymbol{D}}{\omega-\boldsymbol{\varepsilon}}\boldsymbol{U}^{(-1)}\right)^\dagger, \tag{38}$$

and for the Keldysh Green's function using also (29)

$$\begin{aligned} \boldsymbol{G}_0^K(\omega) &= \boldsymbol{U}\left(\frac{\bar{\boldsymbol{D}}}{\omega-\boldsymbol{\varepsilon}}+\frac{\boldsymbol{D}}{\omega-\boldsymbol{\varepsilon}}\right)\boldsymbol{U}^{(-1)}-\text{H.c.} \\ &= \boldsymbol{U}\left(\frac{1}{\omega-\boldsymbol{\varepsilon}}\right)\boldsymbol{U}^{(-1)}-\text{H.c.} \end{aligned} \tag{39}$$

In principle, one could just carry out the diagonalization (31) and then evaluate (38) and (39) numerically, which is a rather lightweight task. However, it is possible to obtain a (partially) analytical expression for the Green's functions. Indeed, a lengthy but straightforward calculation yields for the retarded one

$$\boldsymbol{G}_0^R(\omega)=(\omega-\boldsymbol{E}+i\boldsymbol{\Lambda})^{-1}. \tag{40}$$

Similarly, for the Keldysh component of the inverse Green's function, we obtain

$$\left(\underline{\boldsymbol{G}_{\boldsymbol{0}}^{-1}}\right)^K\equiv-\boldsymbol{G}_0^{R-1}\boldsymbol{G}_0^K\boldsymbol{G}_0^{A-1}=-2i\boldsymbol{\Omega}. \tag{41}$$

To sum up, (40) and (41) are the main results of this section. To evaluate $\underline{\Delta}_{\text{aux}}(\omega)$, one then uses (6), whereby one should consider that the matrix $\underline{G}_0$ in Keldysh space is just the *local one*, i.e., in terms of the components local at the impurity G^R_{0ff} and G^K_{0ff}:

$$\underline{G}_0\equiv\begin{pmatrix} G^R_{0ff} & G^K_{0ff}\\ 0 & G^A_{0ff}\end{pmatrix}.$$

In turn, G^K_{0ff}, the ff component of $\boldsymbol{G}_0^K$, has to be obtained from (41) by the well-known expression [116] $\boldsymbol{G}_0^K=-\boldsymbol{G}_0^R(\underline{\boldsymbol{G}_{\boldsymbol{0}}^{-1}})^K\boldsymbol{G}_0^A$.

2. *Interacting case*

The next step consists in solving the interacting auxiliary Lindblad problem described by (10a) in order to determine the Green's function and the self-energy at the impurity site. This is done by Lanczos exact diagonalization within the many-body augmented Fock space.

First, the steady state $|\rho_\infty\rangle$ has to be determined as the right-sided eigenstate of the Lindblad operator $\hat{\mathcal{L}}$ with eigenvalue $l_0=0$. For convenience, we introduce

$$\hat{L}=i\hat{\mathcal{L}}, \tag{42}$$

which is a kind of non-Hermitian Hamiltonian with complex eigenvalues ℓ. The dimension of the Hilbert space can be reduced by exploiting symmetries similar to the equilibrium case. The conservation of the particle number per spin $\hat{N}_\sigma$ is replaced here by the conservation of $\hat{N}_\sigma-\hat{\tilde{N}}_\sigma$ [51]. The steady state lies in the sector $N_\sigma-\tilde{N}_\sigma=0$.

Starting from Eq. (26), the steady-state greater Green's function of the impurity reads as in a non-Hermitian Lehmann representation, for $t>0$,

$$G^{>+}_{\mu\nu}(t)=-i\sum_n e^{-i\ell_n^{(+1)}t}\,\langle I|\,d_\mu\,\big|R_n^{(+1)}\big\rangle\big\langle L_n^{(+1)}\big|\,d_\nu^\dagger\,|\rho_\infty\rangle\,,$$

where the identity $\sum_n|R_n^{(+1)}\rangle\langle L_n^{(+1)}|$ in the sector $N_\sigma-\tilde{N}_\sigma=+1$ has been inserted, in terms of right ($|R_n^{(+1)}\rangle$) and left ($\langle L_n^{(+1)}|$) eigenstates of $\hat{L}$ with eigenvalues $\ell_n^{(+1)}$, and $|I\rangle$ is the left vacuum (13). Its Fourier transform reads as

$$\begin{aligned} G^{>}_{\mu\nu}(\omega) &= \sum_n\frac{1}{\omega-\ell_n^{(+1)}}\,\langle I|\,d_\mu\,\big|R_n^{(+1)}\big\rangle\big\langle L_n^{(+1)}\big|\,d_\nu^\dagger\,|\rho_\infty\rangle \\ &\quad-\sum_n\frac{1}{\omega-\ell_n^{(+1)*}}\big(\,\langle I|\,d_\nu\,\big|R_n^{(+1)}\big\rangle\big\langle L_n^{(+1)}\big|\,d_\mu^\dagger\,|\rho_\infty\rangle\,\big)^*. \end{aligned} \tag{43}$$

The analogous expression for the lesser Green's function $G^{<}_{\mu\nu}(\omega)$ is obtained by inserting a complete set of eigenstates in the $N_\sigma-\tilde{N}_\sigma=-1$ sector and exchanging the elementary operators accordingly. $G^K_{\mu\nu}(\omega)$ and $G^R_{\mu\nu}(\omega)$ are obtained using Eq. (30) [see also (29)].

For a small number of bath sites $N_B\leqslant 3$, the dimension of the augmented Fock space is still moderate, and eigenvalues and eigenvectors can be determined by full diagonalization. For $N_B\geqslant 4$, a non-Hermitian Lanczos procedure has to be carried out. Especially extracting the steady state is not an easy task since it lies in the center of the spectrum. Details of our numerical procedure are given in Appendix A.

Once the interacting and noninteracting Green's functions of the auxiliary system at the impurity site $\underline{G}(\omega)$ and $\underline{G}_0(\omega)$, respectively, are determined, the corresponding self-energy is obtained via Dyson's equation in Keldysh space [Eq. (5)]. The individual components are explicitly [51]

$$\begin{aligned} \Sigma^R(\omega) &= 1/G_0^R(\omega)-1/G^R(\omega), \\ \Sigma^K(\omega) &= -G_0^K(\omega)\big/\big|G_0^R(\omega)\big|^2+G^K(\omega)/|G^R(\omega)|^2. \end{aligned}$$

As discussed in Sec. II B, this is used in the Dyson equation (5) for the physical Green's function.

III. RESULTS

In this section, results for the steady-state properties of a symmetric, correlated Anderson impurity coupled to two

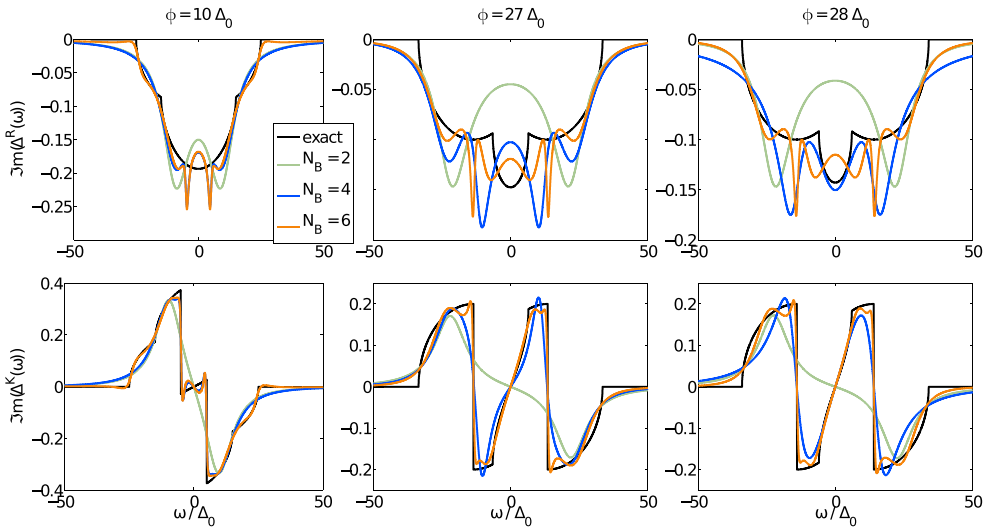

FIG. 2. (Color online) Comparison of $\mathrm{Im}[\Delta^{\alpha}(\omega)]$ from (7) (black) with $\mathrm{Im}[\underline{\Delta}^{\alpha}_{\mathrm{aux}}(\omega)]$ at the absolute minimum of the cost function (12) for auxiliary system sizes $N_B = 2,4$, and 6 bath sites (green, blue, and orange, respectively), and $\alpha = R$ (top) and K (bottom). Results are shown for tight-binding leads (2) and (8) with $t = 10\,\Delta_0$, and three different bias voltages $\phi \in \{10,27,28\}\,\Delta_0$ from left to right.

metallic leads under bias voltage are provided. We assess the validity of the proposed method by discussing the fit of the hybridization function and outline how uncertainties are estimated. Results for the current voltage characteristics and the nonequilibrium spectral function are presented and compared with data from time-evolving block decimation (TEBD) [77] and SNRG [54] calculations, respectively. The effect of a linear correction of the calculated Green's functions is illustrated.

A. Hybridization functions

The optimal representation of the exact bath $\underline{\Delta}(\omega)$ by the auxiliary one $\underline{\Delta}_{\mathrm{aux}}(\omega)$ is obtained by minimizing the cost function (12). In practice, this is done by employing a quasi-Newton line search [132,133]. In particular, we chose an equal weighting of the retarded and the Keldysh component $W^R(\omega) = W^K(\omega) = \Theta(\omega_c - |\omega|)$. After finding our results to be robust upon different values for the cutoff ω_c, as well as upon using different norms ($n = 1,2$) in Eq. (12), we finally choose $\omega_c = 50\,\Delta_0$ and consider imaginary parts $\{\mathrm{Im}[\Delta^{\alpha}(\omega) - \Delta^{\alpha}_{\mathrm{aux}}(\omega)]\}^2$ in the cost function only. This is justified since $\Delta^K_{\mathrm{aux}}(\omega)$ is purely imaginary and the real part of $\Delta^R_{\mathrm{aux}}(\omega)$ is connected to its imaginary part via the Kramers-Kronig relations [134]. The asymptotic behavior of $\Delta^R_{\mathrm{aux}}(\omega)$ is determined by Λ_{ff} whereas the one of $\Delta^K_{\mathrm{aux}}(\omega)$ by Ω_{ff}. Therefore, the correct asymptotic limit $\lim_{\omega\to\pm\infty}\underline{\Delta}_{\mathrm{aux}}(\omega) = \underline{0}$ is guaranteed by taking $\Gamma^{(1)}_{ff} = \Gamma^{(2)}_{ff} = 0$, which results in $\Gamma^{(\kappa)}_{\mu f} = \Gamma^{(\kappa)}_{f\mu} = 0$ due to the requirement of semipositive definiteness of $\Gamma^{(\kappa)}_{\mu\nu}$. Particle-hole symmetry allows for a further reduction of the auxiliary system parameters [135].

In this work, we use an even number of auxiliary bath sites $N_B = 2,4$, and 6 in a linear setup [see Fig. 1(b)] with an equal number to the left and to the right of the impurity (only Fig. 6 displays one calculation for an odd number of bath sites). In Fig. 2, the obtained auxiliary hybridization functions are compared with the exact ones for various bias voltages. We find a quick convergence as a function of N_B, which degrades for large bias voltage ϕ. The Fermi steps at the chemical potentials in $\Delta^K_{\mathrm{aux}}(\omega)$ can not be properly resolved in the case of $N_B = 2$. Especially in the case of $\phi = 10\,\Delta_0$ the auxiliary hybridization functions for $N_B = 6$ as well as for $N_B = 4$ agree fairly well with the exact one and capture all essential features, in particular the Fermi steps. The auxiliary bath develops spurious oscillations in $\Delta^R_{\mathrm{aux}}(\omega)$ at the energies of the Fermi levels of the contacts. Here, the discrepancy with $\Delta^R(\omega)$ is considerable in magnitude, but extends over small ω intervals, thus inducing only small errors in the self-energies.

When following the absolute minimum of the cost function (12) as a function of some external parameter, such as, e.g., the bias voltage ϕ, spurious discontinuities appear due to the fact that local minima cross each other. This occurs for large bias voltages and large U, and/or small N_B, for which the approach is more challenging. An example for such a situation is shown in Fig. 2 for the case $N_B = 4$, when comparing the hybridization functions just before and after such a crossing, i.e., for $\phi = 27\,\Delta_0$ and $28\,\Delta_0$. Even though the changes in the exact hybridization function are only minor, $\underline{\Delta}_{\mathrm{aux}}(\omega)$ displays a considerable difference. The influence of this spurious effect on observable quantities is shown in Fig. 3 (right panel, orange circles) for a different parameter set of $N_B = 6$ at around $\phi_c = 33\,\Delta_0$. The artificial discontinuity in the current is caused by the shift of spectral weight in $\underline{\Delta}_{\mathrm{aux}}(\omega)$.

To deal with these discontinuities, we adopt a scheme which is suitable for obtaining a continuous dependence of observables on external parameters and, in addition, allows us to estimate their uncertainties (see Fig. 3). We first identify a set of local minima of the cost function (12), obtained by a series of minimum searches starting with random initial values. These local minima are then used to calculate an average and variance of physical quantities, such as the current. We consider the distribution of local minima with a Boltzmann weight associated with an artificial "temperature," whereby the value of the cost function (12) is the associated

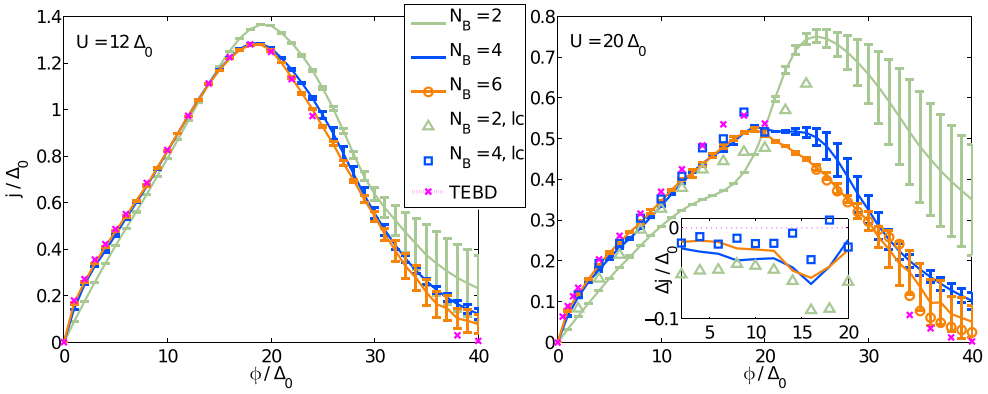

FIG. 3. (Color online) Current j vs voltage ϕ for the model (1) with tight-binding leads and onsite interaction $U = 12\,\Delta_0$ (left) and $U = 20\,\Delta_0$ (right). Results for three different auxiliary systems with $N_B \in \{2,4,6\}$ are displayed and compared with reference data from TEBD (magenta dotted and $\times$) [77]. We plot the averaged mean values connected by lines together with error bars determined according to Sec. III A and Appendix B. The additional data marks for $U = 20\,\Delta_0$ are as follows: The circles for $N_B = 6$ display $j(\phi)$ when considering the absolute minimum in the fit (12). $N_B = 2$,lc and $N_B = 4$,lc present the results of a linear correction of the current values of the absolute minima as described in Appendix C. The inset displays the difference Δj of the calculated currents to the TEBD results.

"energy." This artificial temperature for the Boltzmann weight is chosen in such a way that the averaged spectral weight of the hybridization function as a function of ϕ is as smooth as possible. Details are outlined in Appendix B. A possible pitfall, however, is that physical discontinuities, i.e., real phase transitions could be overlooked. It is thus compulsory to additionally investigate the results for the absolute minima and for different bath setups carefully. This approach has a certain degree of arbitrariness. However, we point out that it only affects regions with large error bars in Fig. 3, i.e., large ϕ and large U for which also other techniques are less accurate.

B. Current-voltage characteristics

After evaluating the interacting impurity Green's function of the physical system according to (5) with the self-energy evaluated in Sec. II D, we are able to determine the steady-state current. This is done with the help of the Meir-Wingreen expression [116,136,137] in its symmetrized form, where we have already summed over spin

$$j = i\int_{-\infty}^{\infty}\frac{d\omega}{2\pi}([\gamma_L(\omega)-\gamma_R(\omega)]G^{<}(\omega) + [p_{\mathrm{F},L}(\omega)\gamma_L(\omega)-p_{\mathrm{F},R}(\omega)\gamma_R(\omega)][G^R(\omega)-G^A(\omega)]), \tag{45}$$

$\gamma_\lambda(\omega) = -2|t'_\lambda|^2\mathrm{Im}[g^R_\lambda(\omega)]$ are the "lead self-energies" and $p_{\mathrm{F},\lambda}(\omega) = p_{\mathrm{F}}(\omega-\mu_\lambda)$ denotes the Fermi distribution of lead λ with chemical potential μ_λ.

To quantify the accuracy of the method, we compare the results for the current-voltage characteristics with quasiexact reference data from TEBD [77]. We find very good agreement for interaction strength $U < 12\,\Delta_0$. Since in this paper we want to benchmark the approach in "difficult" parameter regimes, in the following, we will discuss $U \gtrsim 12\Delta_0$ only. In Fig. 3 we display data for $U = 12\,\Delta_0$ and $20\,\Delta_0$. The data points and error bars shown are obtained by using the averaging scheme as described in Appendix B. For the universal physics at small and medium bias voltages $\phi \lesssim 20\,\Delta_0$, the current as a function of the auxiliary system size ($N_B \in \{2,4,6\}$) converges rapidly to the expected result. The convergence is even monotonic in a broad region of the parameter space. The zero-bias response is linear for all N_B and approaches the results expected from the Friedel sum rule [29] $j(\phi = 0^+) = 2\frac{e^2}{h}\phi$ quickly for increasing N_B. For $U = 12\,\Delta_0$ already the $N_B \gtrsim 4$ results yield a good reproduction of the current in this bias regime. For $U = 20\,\Delta_0$ and $\phi \gtrsim 20\,\Delta_0$, a larger difference between the $N_B = 4$ and 6 results is observed. Notice that also other available methods do not yield a satisfactory result in this parameter regime. In the lead-dependent high-bias regime, the fit becomes more challenging and large variances appear in the calculated quantities. This indicates the presence of many competing local minima with similar values for the cost function whose value tends to increase with increasing ϕ. For $\phi \geqslant 40\,\Delta_0$, the densities of states of the left and the right contacts do not overlap anymore and the current has to vanish. This limit can not be exactly reproduced by the proposed approach due to spurious long-range Lorentzian tails present in the auxiliary Markovian environment. Nevertheless, $j(\phi = 40\,\Delta_0)$ approaches zero as one increases the number of bath sites. This holds true for quantities obtained at the absolute minimum of the cost function as well as for averaged ones.

To extrapolate our results to larger N_B, a scheme for linear corrections is discussed in Appendix C. Data for $N_B = 2$,lc and 4,lc, whereby "lc" denotes "linear correction," is shown in Fig. 3. For large $U = 20\,\Delta_0$ and small- to medium-bias voltages $\phi \lesssim 20\,\Delta_0$, a solid improvement towards the TEBD reference values is observed (see inset Fig. 3). Correction ratios r (see Appendix C) close to one indicate a good applicability of the linear correction scheme. We find on average $r \approx 0.75$ for $\phi \lesssim 20\,\Delta_0$ ($N_B = 2$,lc and 4,lc). In the high-bias regime, however, the linear correction can not be applied with large magnitude and r drops below 0.5 for $N_B = 2$,lc. Nevertheless, the calculation of the effective, auxiliary hybridization function $\underline{\Delta}_{\mathrm{aux},r}(\omega)$ as described in Appendix C successfully avoids an "overcorrection" of the current values and automatically allows one to estimate the reliability of the results.

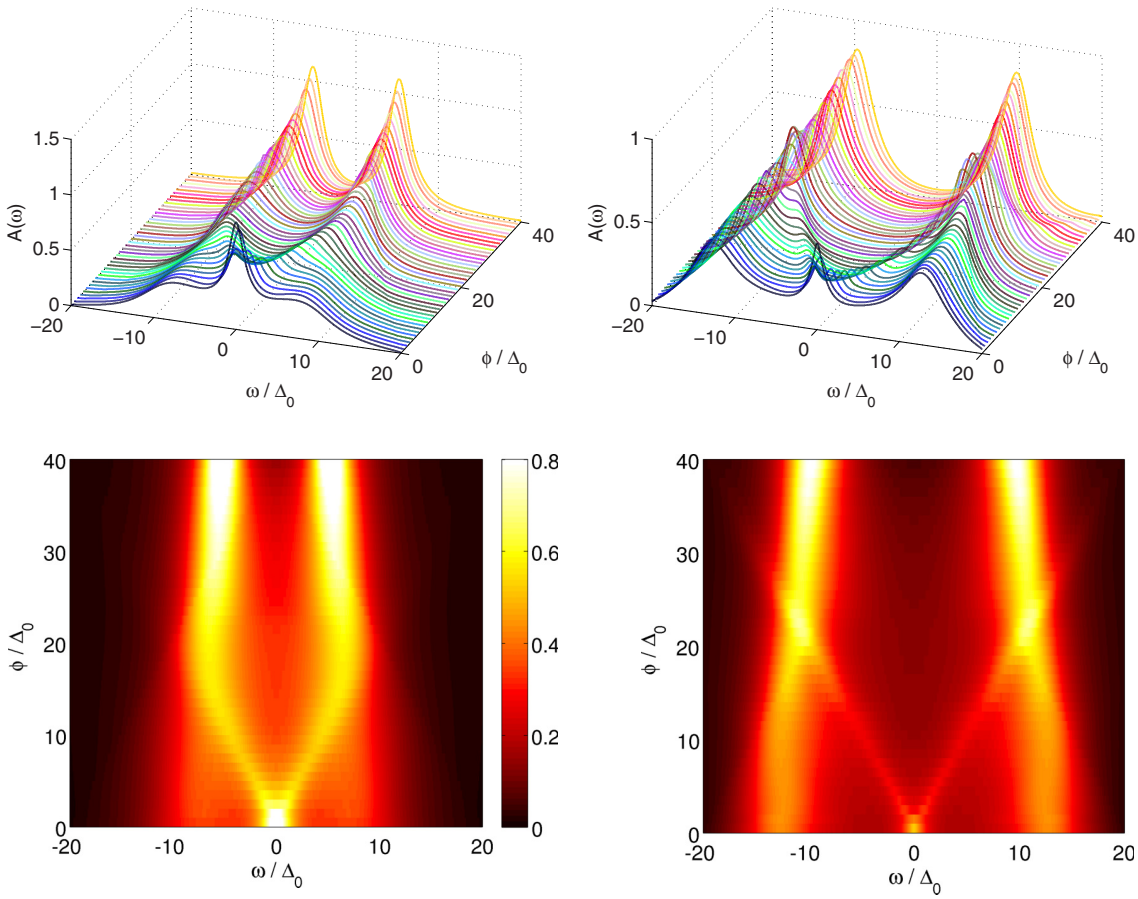

FIG. 4. (Color online) Single-particle spectral function at the impurity evaluated for $N_B = 6$, different bias voltages ϕ, and $U = 12\,\Delta_0$ (left) and $U = 20\,\Delta_0$ (right). Data are obtained according to Sec. III A and Appendix B. Other parameters are as in Fig. 3.

Judging from the larger uncertainty from the averaging procedure and the strong effects of the linear corrections, we conclude that the high-bias regime is more sensitive to the details of the fitted, auxiliary hybridization function. The universal low- and medium-bias regimes are, however, very well reproduced even with a small number of auxiliary bath sites.

C. Nonequilibrium spectral function

The bias-dependent single-particle spectral function is evaluated from the physical steady-state Green's function of the impurity $A(\omega) = -\frac{1}{\pi}\mathrm{Im}[G^R(\omega)]$. Results obtained using $N_B = 6$ for $U = 12\,\Delta_0$ and $20\,\Delta_0$ are presented for the whole bias range of interest in Fig. 4. Data for $N_B = 4$ are similar, but here the Kondo physics can not be reproduced as accurately as in the case of $N_B = 6$. Our approach does preserve the local charge density $\langle n_f \rangle = \sum_\sigma \frac{1}{2} + \frac{1}{2}\int_{-\infty}^{\infty} \frac{d\omega}{2\pi}\mathrm{Im}[G^K(\omega)] = 1$ and magnetization $\langle m_f \rangle = 0$ as well as the spectral sum rule [138].

The presented method reproduces qualitatively correctly also the equilibrium physics at $\phi = 0$ since $A(\omega)$ displays a Kondo resonance at $\omega = 0$ and two Hubbard satellites at the approximate positions $\omega \approx \pm U/2$. This renders the application to equilibrium DMFT problems an interesting perspective. The width and magnitude of the Kondo resonance are discussed in comparison with (S)NRG data in Sec. III C 1.

Upon increasing the bias voltage, the Kondo resonance splits up and two excitations are observed at the energies of the Fermi levels of the leads [78,139,140]. For $U = 12\,\Delta_0$, the splitted resonances merge into the Hubbard bands at approximately $\phi \approx 15\,\Delta_0$ and can not be clearly identified thereafter. In contrast, in the case of $U = 20\,\Delta_0$, the resonances overlap with the Hubbard satellites and can still be observed in the spectrum $A(\omega)$ at higher voltages. Calculations with increasing U in the high-bias regime $\phi \approx 40\,\Delta_0$ have shown the consistency of this effect and that a minimum value of $U \approx 15\,\Delta_0$ is needed in order for the resonances at the Fermi energies to be perceptible after having crossed the Hubbard bands.

1. Comparison with scattering states numerical renormalization group

We compare the computed spectral functions with results obtained by means of SNRG [53]. For this purpose, we use a flat DOS [Eq. (3)] for the leads, as in Ref. [53]. Focusing on the low-bias regime and $N_B = 6$, the obtained spectral functions are depicted in Fig. 5. Compared with SNRG, our results do not achieve the same accuracy in the low-energy domain, i.e., in the vicinity of $\omega \approx 0$. However, our data provide a better resolution at higher energies. When inspecting the Kondo peak in the equilibrium case $\phi = 0$, our results do not fully fulfill the Friedel sum rule [29,141,142]. Depending on parameters,

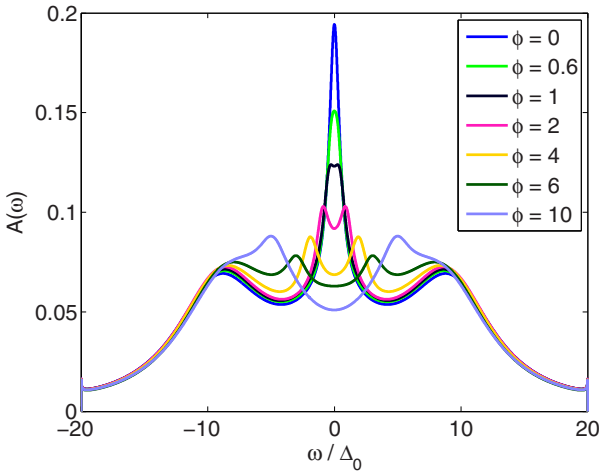

FIG. 5. (Color online) Single-particle spectral function for a constant DOS of the leads (3), with $D_{\mathrm{WB}} = 20\,\Delta_0$ and $U = 16\,\Delta_0$ and different bias voltages ϕ (in units of Δ_0). Results are obtained for $N_B = 6$ and at the absolute minimum of Eq. (12). For a comparison with SNRG [53] [Fig. 2(a) therein], note that their $\Gamma = 2\,\Delta_0$.

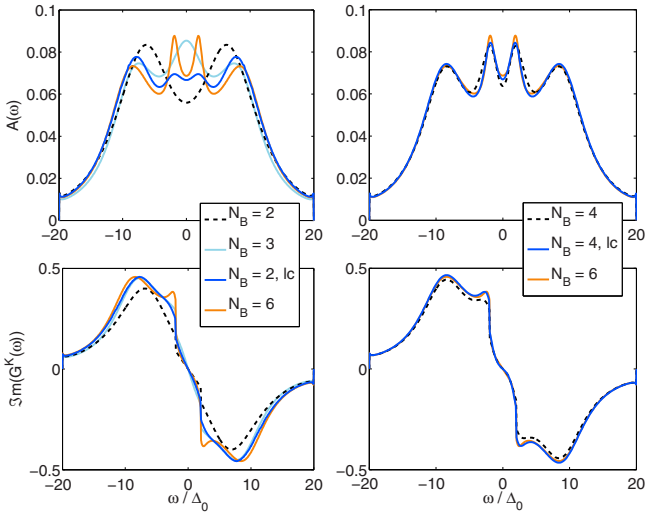

FIG. 6. (Color online) Effects of the linear corrections of the Green's functions according to Apendix C (solid blue lines). The dashed lines indicate the uncorrected $\underline{G}(\omega)$ with the same N_B, while solid orange and light blue lines display results for larger N_B for comparison. Results are shown for a constant lead DOS [Eq. (3)] with $D_{\mathrm{WB}} = 20\,\Delta_0$, $U = 16\,\Delta_0$, and $\phi = 4\,\Delta_0$.

the height of the Kondo resonance is underestimated. This is due to the fact that the imaginary part of the self-energy at $\omega = 0$ has a small finite value which is due to the Lorentzian tails of the Markovian environment.

The resolution does not suffice to tell whether a two- or a three-peak structure is present for very low-bias voltages $\phi \lesssim 2\,\Delta_0$. Nevertheless, one can say that the higher-bias regime $\phi > 4\,\Delta_0$ is resolved more accurately and one is able to clearly distinguish the excitations at the Fermi energies of the contacts from the Hubbard satellites. The observed linear splitting is consistent with experiments on nanodevices [139,140]. Within second-order Keldysh PT [58] and QMC results [143], the resonance does not split but is suppressed only. In fourth order and in NCA it splits into two, which are located near the chemical potentials of the two leads [58]. Other methods yield a splitting with features slightly different in details: real-time diagrammatics [144], VCA [78], imaginary potential QMC [90], or scaling methods [145]. Overall, a good qualitative agreement with the SNRG results is achieved which underlines the reliability of the calculated spectral functions.

2. *Linear correction of Green's functions*

Here, we consider the effect of a linear correction of the Green's functions, as outlined in Appendix C. In the left panels (right panels) of Fig. 6, we show data for $N_B = 2$ ($N_B = 4$) including linear corrections ($r = 1$) for a high interaction strength in the low-bias regime. We benchmark to data obtained using $N_B = 6$ without corrections.

For $N_B = 2$ without linear corrections, the spectral function of the auxiliary system does not feature excitations at the Fermi energies of the contacts ($\omega = \pm 2\,\Delta_0$), which are present in the $N_B = 6$ data. Also, the spectra appear washed out. The linearly corrected result, however, features not only the two resonances at the appropriate energies, but also the shoulders present in the reference data. Again, in the Keldysh Green's function a large correction towards the more accurate $N_B = 6$ results is observed. To highlight the fact that the improvement of the linear correction is not only due to the inclusion of one additional bath site, also a calculation for an auxiliary system with $N_B = 3$ is shown. Evidently, the $N_B = 3$ spectral function exhibits a large weight at low frequencies, but the resolution is rather low and only a single, smeared out peak at $\omega = 0\,\Delta_0$ is observed. It clearly does not account for the splitting of the Kondo resonance.

For $N_B = 4$, a similar enhancement is found. Clearly, the size of the corrections is much smaller. Especially in the Keldysh component, the Green's function for $N_B = 6$ and for the corrected $N_B = 4$ system nearly coincide. In general, the difference between the $N_B = 6$ and the $N_B = 4$ calculations (raw and corrected) is quite small, so that the presented spectral functions in Fig. 5 for larger values of $\phi \lesssim 12\,\Delta_0$ can be assumed to be quite accurate.

Overall, the linear correction enables a vast improvement in the universal low- and medium-bias regimes for all U, which becomes especially important for large U. For large-bias voltages, when lead band effects become prominent, the linear correction is more challenging (see also Sec. III B).

IV. CONCLUSIONS

We have presented a numerical approach to study correlated quantum impurity problems out of equilibrium [51]. The auxiliary master equation approach presented here is based on a mapping of the original Hamiltonian to an auxiliary open quantum system consisting of the interacting impurity coupled to bath sites as well as to a Markovian environment. The dynamics of the auxiliary open system is controlled by a Lindblad master equation. Its parameters are determined by a fit to the impurity-environment hybridization function.

This has many similarities to the procedure used for the exact-diagonalization dynamical mean field theory impurity solver, but has the advantage that one can work directly with real frequencies, which is mandatory for nonequilibrium systems.

We have illustrated how the accuracy of the results can be estimated, and systematically improved by increasing the number of auxiliary bath sites. A scheme to introduce linear corrections has been devised. We presented in detail how the nonequilibrium Green's functions of the correlated open quantum system are obtained by making use of non-Hermitian Lanczos diagonalization in a superoperator space. These techniques make the whole method fast and efficient as well as particularly suited as an impurity solver for steady-state dynamical mean field theory [51].

In this work, we have applied the approach to the single-impurity Anderson model, which is one of the paradigmatic quantum impurity models. We have analyzed in detail the systematic improvement of the current-voltage characteristics as a function of the number of auxiliary bath sites. Already for four auxiliary bath sites, results show a rather good agreement with quasiexact data from time-evolving block decimation [77] in the low- and medium-bias regimes. In the high-bias regime, the current deviates from the expected result with increasing interaction strength. However, we have shown how to estimate the reliability of the data from the deviation of the hybridization functions and how results can be corrected to linear order in this deviation. The impurity spectral function obtained in our calculation features a linear splitting of the Kondo resonance as a function of bias voltage. Good agreement with data from scattering-state numerical renormalization group [53] was found.

Applications of the presented method to multiorbital correlated impurities or correlated clusters is in principle straightforward, although numerically more demanding. Such systems are themselves of interest as models for transport through molecular or nanoscopic objects and as solvers for nonequilibrium cluster dynamical mean field theory. In this case, a larger number of auxiliary sites might be necessary to obtain a good representation of the various hybridization functions. For this situation, one should use numerically more efficient methods to solve for larger correlated open quantum systems, such as matrix product states and density matrix renormalization group, possibly combined with stochastic wave-function approaches [146–148], sparse polynomial space [149,150], or configuration interaction approaches [151]. A more accurate determination of low energy, and possibly critical properties, might be achieved by a combination with renormalization group iteration schemes, similar to the numerical renormalization group. Work along these lines is in progress.

Although we have presented results for the steady state, where the method is most efficient, also extensions to time-dependent phenomena provide an interesting and feasible perspective. While other approaches, such as time-dependent density matrix renormalization group [73] or quantum Monte Carlo [49] are certainly more accurate at short times, the present approach could be used to estimate directly slowly decaying modes by inspecting the behavior of the low-lying spectrum of the Lindblad operator.

ACKNOWLEDGMENTS

We acknowledge discussions with A. Rosch, W. Hofstetter, S. Diehl, M. Knap, D. Rost, and F. Schwarz. A.D. and M.N. thank the Forschungszentrum Jülich, in particular the autumn school on correlated electrons, for hospitality and support. This work was supported by the Austrian Science Fund (FWF), Grants No. P24081-N16 and No. P26508-N20, as well as SfB-ViCoM Project No. F04103.

APPENDIX A: NUMERICAL CALCULATION OF THE AUXILIARY INTERACTING GREEN'S FUNCTION

In this section, we present details of the numerical evaluation of the auxiliary Green's function, as described in Sec. II D 2. We focus on large Hilbert spaces for which a sparse-matrix approach is mandatory. To determine the steady state, which is the right-sided eigenstate of $\hat{L}$ with eigenvalue zero, one can make use of a shift-and-invert Arnoldi procedure [152–155]. The spectrum of $\hat{L}$ [Eq. (42)] has the property that $\mathrm{Im}(\ell_n) < 0$ for all eigenvalues ℓ_n (except the steady state $\ell_0 = 0$). Therefore, given a small shift $s > 0$, the eigenvector of $(\hat{L} - is\hat{\mathbb{1}})^{-1}$ with the largest eigenvalue is the steady state. Since $\hat{L}$ is non-Hermitian, the three-term recurrence of the ordinary Lanczos scheme [120] does not apply, and one has to resort to an Arnoldi scheme instead. To construct the corresponding Krylov space, a system of equations $(\hat{L} - is\hat{\mathbb{1}})\,|\tilde{\phi}_{n+1}\rangle = |\phi_n\rangle$ has to be solved in each step. For the problem at hand, we found that this can be done most efficiently by combining a stabilized biconjugate gradient method with an incomplete LU decomposition as preconditioner [156,157]. Despite using sparse-matrix methods, the memory requirements of this approach are rather high compared to the schemes presented below.

A second possible route to determine the steady state $|\rho_\infty\rangle$ is to perform an explicit time evolution. For unitary time evolutions, a well-established method relies on the Lanczos scheme to construct an approximate time evolution operator [158]. Such an approach can be adapted to the nonunitary case by using a two-sided Lanczos scheme (see below), or also by employing an Arnoldi procedure [155]. Since $\hat{L}$ is non-Hermitian, one can equally well use a simpler backward or forward Euler scheme [133] to discretize the nonunitary time evolution operator. These approaches may not yield a highly accurate time evolution of $|\rho(t)\rangle$, but can nevertheless determine the steady state within a moderate number of steps. As for the shift-and-invert approach above, to solve the implicit update of $|\rho(t_{n+1})\rangle$ at time step t_n in the case of the backward Euler, a biconjugate gradient routine has proven to be effective. For the forward time integration, a Runge-Kutta method of second order is sufficient, with the great advantage that only matrix-vector multiplications are needed, which reduces memory requirements. In practice, for the considered cases it was found that for not too large systems ($N_B < 6$), the shift-and-invert Arnoldi procedure is best suited, whereas a forward time integration is advantageous for the case $N_B = 6$.

Once the steady state is determined, Green's functions can be effectively calculated by employing a two-sided Lanczos scheme [152,159–163]. We therefore express the right- and

left-sided eigenvectors of $\hat{L}$ in Eq. (43) in a Krylov space basis

$$|R_n\rangle = \sum_k U_{kn} \left|\phi_R^k\right\rangle, \quad \langle L_n| = \sum_k (U^{-1})_{nk} \left\langle\phi_L^k\right|.$$

Here, we have omitted the $N_\sigma - \tilde{N}_\sigma$ symmetry sector index for the sake of clarity. The biorthogonal Lanczos vectors

$$\left\langle\phi_L^k\middle|\phi_R^{k'}\right\rangle = \delta_{kk'}$$

are determined by the three-term recurrence

$$\left|\phi_R^{n+1}\right\rangle = \frac{1}{c_{n+1}}\left(\hat{L}\left|\phi_R^n\right\rangle - e_n\left|\phi_R^n\right\rangle - k_n\left|\phi_R^{n-1}\right\rangle\right),$$

$$\left\langle\phi_L^{n+1}\right| = \frac{1}{c_{n+1}^*}\left(\left\langle\phi_L^n\right|\hat{L} - e_n\left\langle\phi_L^n\right| - k_n^*\left\langle\phi_L^{n-1}\right|\right),$$

with

$$e_n = \left\langle\phi_L^n\right|\hat{L}\left|\phi_R^n\right\rangle,$$

$$k_n = \left\langle\phi_L^{n-1}\right|\hat{L}\left|\phi_R^n\right\rangle = \left(\left\langle\phi_L^n\right|\hat{L}\left|\phi_R^{n-1}\right\rangle\right)^*,$$

and a normalization constant c_n such that $\langle\phi_L^n|\phi_R^n\rangle = 1$. One has a certain degree of freedom in the choice of c_n and k_n due to the relation $k_n^* = c_n$, which is fulfilled, for example, by $k_n = k_n^* = c_n$.

In the Krylov basis, $\hat{L}$ takes on a tridiagonal form $T_{nm} = \langle\phi_L^n|\hat{L}|\phi_R^m\rangle$ with the matrix elements $T_{nn} = e_n$, $T_{n-1n} = k_n$, and $T_{nn-1} = k_n^*$. When $n+1$ becomes as large as the degree of the minimal polynomial of $\hat{L}$, the eigenvalues and eigenvectors of T represent those of $\hat{L}$ [152,160]. If one truncates the Krylov basis, this statement holds still approximately true, especially for the largest eigenvalues in magnitude. Analogous to the Hermitian case [164], an exponential convergence of the eigenspectrum of T towards the one of $\hat{L}$ is observed, which is of particular importance for the calculation of Green's functions. A peculiarity of the two-sided Lanczos scheme is that not every Krylov subspace guarantees that $\mathrm{Im}(\ell_n) < 0$ for all eigenvalues ℓ_n of T. In order to obtain the appropriate pole structure for the estimated Green's functions, one has to check $\mathrm{Im}(\ell_n) < 0$ together with convergence criteria. In cases in which $\mathrm{Im}(\ell_n) < 0$ can not be fulfilled exactly, it has to be ensured at least that the corresponding weights of these eigenvalues are negligible.

For the calculation of the Green's functions needed here it is convenient to choose appropriate initial vectors, which are in the case of the greater Green's function (43)

$$\left|\phi_R^0\right\rangle = \frac{1}{c_0}(d_f^\dagger|\rho_\infty\rangle), \quad \left\langle\phi_L^0\right| = \frac{1}{c_0^*}(\langle I|\, d_f).$$

When denoting by ℓ_n and $U_{k,n}$ the eigenvalues and right-sided eigenvectors of T, respectively, Eq. (43) can be cast into the form

$$\begin{aligned} G^>(\omega) &= \sum_{n,k,k'} \frac{U_{kn}U_{nk'}^{-1}}{\omega - \ell_n}\langle I|\, d_f\left|\phi_R^k\right\rangle\left\langle\phi_L^{k'}\right| d_f^\dagger|\rho_\infty\rangle \\ &\quad - \sum_{n,k,k'} \frac{\left(U_{kn}U_{nk'}^{-1}\right)^*}{\omega - \ell_n^*}\left(\langle I|d_f\left|\phi_R^k\right\rangle\left\langle\phi_L^{k'}\right| d_f^\dagger|\rho_\infty\rangle\right)^* \\ &= |c_0|^2\sum_n \frac{U_{0n}U_{n0}^{-1}}{\omega - \ell_n} - |c_0|^2\sum_n \frac{\left(U_{0n}U_{n0}^{-1}\right)^*}{\omega - \ell_n^*}. \end{aligned}$$

APPENDIX B: AVERAGING SCHEME FOR MULTIPLE LOCAL MINIMA

This section contains details on the approach we used to determine the artificial "temperature" for the Boltzmann weights as described in Sec. III A. We consider the situation that a set of local minima for which Eq. (12) becomes stationary is known. Let us specify by $\mathbf{a}_y(\phi)$ the vector of parameters $\{E_{\mu\nu}, \Gamma_{\mu\nu}^{(\kappa)}\}_y$ corresponding to one certain local minimum for a set of model parameters, labeled by y. In order to quantify the spectral weight distribution of the corresponding hybridization function $\underline{\Delta}_{\mathrm{aux}}[\omega; \mathbf{a}_y(\phi)]$, we define

$$m_2^R[\mathbf{a}_y(\phi)] = \int_{-\omega_c}^{\omega_c} \mathrm{Im}\left\{\Delta_{\mathrm{aux}}^R[\omega; \mathbf{a}_y(\phi)]\right\}\omega^2 d\omega,$$

$$m_3^K[\mathbf{a}_y(\phi)] = \int_{-\omega_c}^{\omega_c} \mathrm{Im}\left\{\Delta_{\mathrm{aux}}^K[\omega; \mathbf{a}_y(\phi)]\right\}\omega^3 d\omega,$$

which are similar to the second and third moments of Δ_{aux}^R and Δ_{aux}^K, respectively. For the Keldysh component, a definition analogous to the first moment would yield the desired information as well but the choice above has been found to be more sensitive to details of Δ_{aux}^K. The value of the corresponding cost function $\chi[\mathbf{a}_y(\phi)]$ of the yth minimum is used as an artificial "energy" and enables one to define weights when making use of Boltzmann's statistic

$$P_y(\phi, \beta) = \frac{1}{Z}e^{-\beta\chi[\mathbf{a}_y(\phi)]},$$

where we introduced an artificial "temperature" β^{-1}. For each bias voltage separately, we are then able to calculate averaged quantities

$$\overline{m_2^R}(\phi, \beta) = \sum_y P_y(\phi, \beta) m_2^R[\mathbf{a}_y(\phi)],$$

as well as $\overline{m_3^K}(\phi, \beta)$ and $\overline{\chi}(\phi, \beta)$ in an analogous manner. The quantities $\overline{m_2^R}(\phi, \beta)$ and $\overline{m_3^K}(\phi, \beta)$ provide an estimate of the center of the spectral weight for the averaged set of hybridization functions for each bias voltage ϕ.

Our goal is that these quantities vary in a smooth way when changing the bias voltage. To achieve this, we employ a minimum curvature scheme [133], meaning that we optimize the function

$$\begin{aligned} v_c(\beta) = \int_0^{\phi_{\max}} \Bigg\{ & w^R\left|\frac{\partial^2}{\partial\phi^2}\overline{m_2^R}(\phi, \beta)\right|^2 + w^K\left|\frac{\partial^2}{\partial\phi^2}\overline{m_3^K}(\phi, \beta)\right|^2 \\ & + w^\chi\left|\frac{\partial^2}{\partial\phi^2}\overline{\chi}(\phi, \beta)\right|^2\Bigg\} d\phi, \end{aligned}$$

with respect to β. This determines the optimal artificial temperature, which ensures that the averaged cost function as well as the averaged spectral weight are as smooth functions of ϕ as possible, given the set of calculated minima $\{\mathbf{a}_y(\phi)\}$. As in many optimization problems, an arbitrariness exists in the definition of the quantities $\overline{m_2^R}(\phi, \beta)$ and $\overline{m_3^K}(\phi, \beta)$, as well as in choosing the values of the weights w^R, w^K, and w^χ. In our case, all of the weights were chosen to be equal to one in units of t.

An improvement of the results, to a certain degree at least, could be expected when making use of extensions like a

bias dependent $\beta(\phi)$. This has not been considered in this work since already a single variable β provided quite smooth observables. As mentioned in the main text, in any case, it is obligatory to examine besides the averaged results also the ones for the absolute minima and/or for different averaging schemes, in order to avoid that physical discontinuities are averaged out. We stress that this approach has to be taken with due care since it is in some aspects arbitrary. However, it is useful to give an estimate of the error of the calculation, and can certainly identify regions in parameter space where the error is negligibly small.

APPENDIX C: LINEAR CORRECTIONS

In this section, we present a scheme to correct physical quantities up to linear order in the difference [165]

$$\underline{D}(\omega) = \underline{\Delta}_{ex}(\omega) - \underline{\Delta}_{\text{aux}}(\omega)$$

between the auxiliary and the exact hybridization functions. Although $\underline{D}(\omega)$ decreases rapidly with increasing number of auxiliary bath sites N_B, the size of the Hilbert space also increases exponentially with N_B. This poses a clear limit to the maximum value of N_B.

The idea is based on the fact that each physical quantity $O[\underline{\Delta}]$ is a functional of $\underline{\Delta}(\omega)$. Its exact value is, thus, obtained as $O[\underline{\Delta}_{ex}]$. For a finite N_B there will always be a nonzero value of $\underline{D}(\omega)$ at some energies, so we will always obtain an approximate value $O[\underline{\Delta}_{\text{aux}}]$. A linear correction can be obtained by evaluating numerically the functional derivative of $O[\underline{\Delta}]$. Strictly speaking, considering that only $\text{Im}[\Delta^R(\omega)]$ and $\text{Im}[\Delta^K(\omega)]$ are independent functions, O is a functional $O[\text{Im}(\Delta^R),\text{Im}(\Delta^K)]$. Suppose one knows the functional derivatives

$$\frac{\delta O[\underline{\Delta}]}{\delta\,\text{Im}[\Delta^\alpha(\omega)]}, \quad \alpha \in \{R,K\}$$

then to linear order in $\underline{D}(\omega)$

$$\begin{aligned} O[\underline{\Delta}_{ex}] \approx\, & O[\underline{\Delta}_{\text{aux}}] \\ & + r \sum_{\alpha\in\{R,K\}} \int \frac{\delta O[\underline{\Delta}]}{\delta\,\text{Im}[\Delta^\alpha(\omega_0)]}\bigg|_{\underline{\Delta}=\underline{\Delta}_{\text{aux}}} \text{Im}[D^\alpha(\omega_0)]\, d\omega_0 \\ & + \mathcal{O}(\underline{D}^2), \end{aligned} \tag{C1}$$

with $r = 1$.

We evaluate the functional derivative numerically in the following way. One first evaluates $O[\underline{\Delta}_{\text{aux}}]$ at the optimum $\underline{\Delta}_{\text{aux}}(\omega)$. Then, O is evaluated at a "shifted" $\text{Im}[\Delta^\alpha(\omega)]$, obtained by adding a delta function peaked around a certain energy ω_0:

$$\delta_{\omega_0}(\omega) \equiv \delta(\omega - \omega_0),$$

multiplied by a small coefficient ϵ. The functional derivatives are then approximated linearly, by making use of the equations

$$\begin{aligned} & \frac{\delta O[\underline{\Delta}]}{\delta\,\text{Im}[\Delta^R(\omega_0)]} \pm 2\frac{\delta O[\underline{\Delta}]}{\delta\,\text{Im}[\Delta^K(\omega_0)]} \\ & \approx \frac{1}{\epsilon}\big(O[\text{Im}(\Delta^R),\text{Im}(\Delta^K)] \\ & \quad - O[\text{Im}(\Delta^R) - \epsilon\delta_{\omega_0},\text{Im}(\Delta^K) \mp 2\epsilon\delta_{\omega_0}]\big), \end{aligned} \tag{C2}$$

which become exact in the $\epsilon \to 0$ limit.

A (quasi)delta-peak correction $\epsilon\delta_{\omega_0}$ to $\Delta^\alpha(\omega)$ can be obtained by attaching an additional bath site $(N_B + 1)$ with onsite energy $E_{N_B+1,N_B+1} = \omega_0$ directly to the impurity site with a hopping $E_{N_B+1,f} = \sqrt{\epsilon/\pi}$. The sum of $\Gamma^{(1)}_{N_B+1,N_B+1}$ and $\Gamma^{(2)}_{N_B+1,N_B+1}$ is proportional to the width of δ_{ω_0} and, thus, should be taken as small as possible. In practice, one uses a discretization of the integration over ω_0 in Eq. (C1) and the width of the delta peaks has to be adjusted accordingly. Setting one of the components $\Gamma^\kappa_{N_B+1,N_B+1}$ to zero yields a peak in the Keldysh component with a coefficient $\pm 2\epsilon$, respectively, as used in Eq. (C2).

Notice that the functional derivative (C2) amounts to carrying out two many-body calculations for each point ω_0 on a system with $N_B + 1$ bath sites. However, it is not necessary to repeat the calculation for each physical quantity of interest. In the linearly corrected current values presented in Sec. III B, a ω_0 mesh of 200 points was used, whereby this number is likely to be reduced when optimizing the method.

Strictly speaking, the coefficient r in Eq. (C1) should be 1. However, for cases in which the linear correction is not small, this could produce an "overcorrection." In order to avoid this, we introduce a smaller ratio r which is determined as follows: We evaluate the corrected self-energy at each ω via Eq. (C1) and $O = \underline{\Sigma}(\omega)$ with some value of $r < 1$ and denote it $\underline{\Sigma}_r(\omega)$. We do the same for the Green's function of the auxiliary system and denote it $\underline{G}_r(\omega)$. Using Eqs. (5) and (6), we now have an estimate of an effective r-dependent auxiliary hybridization function of the linearly corrected system via

$$\underline{\Delta}_{\text{aux},r}(\omega) \equiv \underline{g}_0^{-1}(\omega) - \underline{G}_r^{-1}(\omega) - \underline{\Sigma}_r(\omega).$$

In principle, for $r = 1$ this gives $\underline{\Delta}_{ex}(\omega)$ up to $\mathcal{O}(\underline{D}^2)$. In practice, for finite $\underline{D}(\omega)$, one can introduce a cost function $\chi(r)$ analogous to Eq. (12) to minimize the difference $|\underline{\Delta}_{\text{aux},r}(\omega) - \underline{\Delta}_{ex}(\omega)|$ as a function of r. We checked that for the case in which the linear correction is a good approximation, the minimum occurs at $r = 1$. If the minimum of $\chi(r)$ is situated at some value $r_{\min} < 1$, then one corrects also other physical quantities according to Eq. (C1) with the same $r = r_{\min}$.

Alternatively to the correction (C1) discussed above, one can use the numerical functional derivative evaluated via Eq. (C2) in order to estimate the sensitivity of the value of O with respect to variations of $\text{Im}[\Delta^\alpha_{\text{aux}}(\omega)]$ as a function of ω and α. This is of use, in a second step, to adjust the weight function $W^\alpha(\omega)$ in Eq. (12), so that more sensitive ω regions acquire a larger weight.

[1] M. Hartmann, F. Brandão, and M. Plenio, Laser Photonics Rev. **2**, 527 (2008).

[2] M. Raizen, C. Salomon, and Q. Niu, Phys. Today **50**(7), 30 (1997).

[3] D. Jaksch, C. Bruder, J. I. Cirac, C. W. Gardiner, and P. Zoller, Phys. Rev. Lett. **81**, 3108 (1998).
[4] M. Greiner, O. Mandel, T. Esslinger, T. W. Hänsch, and I. Bloch, Nature (London) **415**, 39 (2002).
[5] S. Trotzky, P. Cheinet, S. Fölling, M. Feld, U. Schnorrberger, A. M. Rey, A. Polkovnikov, E. A. Demler, M. D. Lukin, and I. Bloch, Science **319**, 295 (2008).
[6] U. Schneider, L. Hackermuller, J. P. Ronzheimer, S. Will, S. Braun, T. Best, I. Bloch, E. Demler, S. Mandt, D. Rasch *et al.*, Nat. Phys. **8**, 213 (2012).
[7] S. Iwai, M. Ono, A. Maeda, H. Matsuzaki, H. Kishida, H. Okamoto, and Y. Tokura, Phys. Rev. Lett. **91**, 057401 (2003).
[8] A. Cavalleri, T. Dekorsy, H. H. W. Chong, J. C. Kieffer, and R. W. Schoenlein, Phys. Rev. B **70**, 161102 (2004).
[9] L. L. Bonilla and H. T. Grahn, Rep. Prog. Phys. **68**, 577 (2005).
[10] I. Zutic, J. Fabian, and S. D. Sarma, Rev. Mod. Phys. **76**, 323 (2004).
[11] G. Cuniberti, G. Fagas, and K. Richter, *Introducing Molecular Electronics* (Springer, Berlin, 2005).
[12] R. H. M. Smit, Y. Noat, C. Untiedt, N. D. Lang, M. C. van Hemert, and J. M. van Ruitenbeek, Nature (London) **419**, 906 (2002).
[13] J. Park, A. N. Pasupathy, J. I. Goldsmith, C. Chang, Y. Yaish, J. R. Petta, M. Rinkoski, J. P. Sethna, H. D. Abruna, P. L. McEuen *et al.*, Nature (London) **417**, 722 (2002).
[14] W. Liang, M. P. Shores, M. Bockrath, J. R. Long, and H. Park, Nature (London) **417**, 725 (2002).
[15] N. Agrait, A. L. Yeyati, and J. M. van Ruitenbeek, Phys. Rep. **377**, 81 (2003).
[16] L. Venkataraman, J. E. Klare, C. Nuckolls, M. S. Hybertsen, and M. L. Steigerwald, Nature (London) **442**, 904 (2006).
[17] D. Goldhaber-Gordon, J. Göres, M. A. Kastner, H. Shtrikman, D. Mahalu, and U. Meirav, Phys. Rev. Lett. **81**, 5225 (1998).
[18] A. V. Kretinin, H. Shtrikman, and D. Mahalu, Phys. Rev. B **85**, 201301 (2012).
[19] A. Mitra, S. Takei, Y. B. Kim, and A. J. Millis, Phys. Rev. Lett. **97**, 236808 (2006).
[20] A. J. Leggett, S. Chakravarty, A. T. Dorsey, M. P. A. Fisher, A. Garg, and W. Zwerger, Rev. Mod. Phys. **59**, 1 (1987).
[21] M. A. Cazalilla, Phys. Rev. Lett. **97**, 156403 (2006).
[22] M. Rigol, V. Dunjko, and M. Olshanii, Nature (London) **452**, 854 (2008).
[23] A. Nitzan and M. A. Ratner, Science **300**, 1384 (2003).
[24] P. W. Anderson, Phys. Rev. **124**, 41 (1961).
[25] J. Friedel, Can. J. Phys. **34**, 1190 (1956).
[26] A. M. Clogston, B. T. Matthias, M. Peter, H. J. Williams, E. Corenzwit, and R. C. Sherwood, Phys. Rev. **125**, 541 (1962).
[27] W. Brenig and K. Schönhammer, Z. Phys. **267**, 201 (1974).
[28] A. Georges, G. Kotliar, W. Krauth, and M. J. Rozenberg, Rev. Mod. Phys. **68**, 13 (1996).
[29] A. Cyril, *The Kondo Problem to Heavy Fermions* (Cambridge University Press, Cambridge, UK, 1997).
[30] D. Vollhardt, in *Lecture Notes on the Physics of Strongly Correlated Systems*, Vol. 1297 of *AIP Conference Proceedings*, edited by A. Avella and F. Mancini (AIP, New York, 2010), p. 339.
[31] W. Metzner and D. Vollhardt, Phys. Rev. Lett. **62**, 324 (1989).
[32] J. Kondo, Prog. Theor. Phys. **32**, 37 (1964).
[33] P. W. Anderson, J. Phys. C: Solid State Phys. **3**, 2436 (1970).
[34] K. Yosida and K. Yamada, Prog. Theor. Phys. Suppl. **46**, 244 (1970).
[35] K. Yamada, Prog. Theor. Phys. **53**, 970 (1975).
[36] K. Yosida and K. Yamada, Prog. Theor. Phys. **53**, 1286 (1975).
[37] K. Yamada, Prog. Theor. Phys. **54**, 316 (1975).
[38] J. R. Schrieffer and P. A. Wolff, Phys. Rev. **149**, 491 (1966).
[39] S. Y. Müller, M. Pletyukhov, D. Schuricht, and S. Andergassen, Phys. Rev. B **87**, 245115 (2013).
[40] D. Bohr and P. Schmitteckert, Ann. Phys. (NY) **524**, 199 (2012).
[41] L. H. Yu, Z. K. Keane, J. W. Ciszek, L. Cheng, J. M. Tour, T. Baruah, M. R. Pederson, and D. Natelson, Phys. Rev. Lett. **95**, 256803 (2005).
[42] L. Tosi, P. Roura-Bas, and A. A. Aligia, J. Phys.: Condens. Matter **24**, 365301 (2012).
[43] H. Prüser, M. Wenderoth, P. E. Dargel, A. Weismann, R. Peters, T. Pruschke, and R. G. Ulbrich, Nat. Phys. **7**, 203 (2011).
[44] H. Aoki, N. Tsuji, M. Eckstein, M. Kollar, T. Oka, and W. Philipp, arXiv:1310.5329.
[45] P. Schmidt and H. Monien, arXiv:cond-mat/0202046.
[46] J. K. Freericks, V. M. Turkowski, and V. Zlatić, Phys. Rev. Lett. **97**, 266408 (2006).
[47] J. K. Freericks, Phys. Rev. B **77**, 075109 (2008).
[48] A. V. Joura, J. K. Freericks, and T. Pruschke, Phys. Rev. Lett. **101**, 196401 (2008).
[49] M. Eckstein, M. Kollar, and P. Werner, Phys. Rev. Lett. **103**, 056403 (2009).
[50] S. Okamoto, Phys. Rev. B **76**, 035105 (2007).
[51] E. Arrigoni, M. Knap, and W. von der Linden, Phys. Rev. Lett. **110**, 086403 (2013).
[52] P. Mehta and N. Andrei, Phys. Rev. Lett. **96**, 216802 (2006).
[53] F. B. Anders, Phys. Rev. Lett. **101**, 066804 (2008).
[54] F. B. Anders and S. Schmitt, J. Phys.: Conf. Ser. **220**, 012021 (2010).
[55] A. Rosch, Eur. Phys. J. B **85**, 6 (2012).
[56] Y. Meir, N. S. Wingreen, and P. A. Lee, Phys. Rev. Lett. **70**, 2601 (1993).
[57] N. S. Wingreen and Y. Meir, Phys. Rev. B **49**, 11040 (1994).
[58] T. Fujii and K. Ueda, Phys. Rev. B **68**, 155310 (2003).
[59] H. Schoeller and G. Schön, Phys. Rev. B **50**, 18436 (1994).
[60] S. Hershfield, J. H. Davies, and J. W. Wilkins, Phys. Rev. Lett. **67**, 3720 (1991).
[61] H. Schoeller, Eur. Phys. J.: Spec. Top. **168**, 179 (2009).
[62] A. Rosch, J. Paaske, J. Kroha, and P. Wölfle, J. Phys. Soc. Jpn. **74**, 118 (2005).
[63] F. B. Anders and A. Schiller, Phys. Rev. B **74**, 245113 (2006).
[64] D. Roosen, M. R. Wegewijs, and W. Hofstetter, Phys. Rev. Lett. **100**, 087201 (2008).
[65] B. Doyon and N. Andrei, Phys. Rev. B **73**, 245326 (2006).
[66] S. Weiss, J. Eckel, M. Thorwart, and R. Egger, Phys. Rev. B **77**, 195316 (2008).
[67] F. B. Anders and A. Schiller, Phys. Rev. Lett. **95**, 196801 (2005).
[68] M. Moeckel and S. Kehrein, Phys. Rev. Lett. **100**, 175702 (2008).
[69] S. Kehrein, Phys. Rev. Lett. **95**, 056602 (2005).
[70] G. Vidal, Phys. Rev. Lett. **93**, 040502 (2004).
[71] S. R. White, Phys. Rev. B **48**, 10345 (1993).

[72] A. J. Daley, C. Kollath, U. Schollwöck, and G. Vidal, J. Stat. Mech. (2004) P04005.

[73] S. R. White and A. E. Feiguin, Phys. Rev. Lett. **93**, 076401 (2004).

[74] U. Schollwoeck, Ann. Phys. (NY) **326**, 96 (2011).

[75] P. Schmitteckert, Phys. Rev. B **70**, 121302 (2004).

[76] F. Heidrich-Meisner, A. E. Feiguin, and E. Dagotto, Phys. Rev. B **79**, 235336 (2009).

[77] M. Nuss, M. Ganahl, H. G. Evertz, E. Arrigoni, and W. von der Linden, Phys. Rev. B **88**, 045132 (2013).

[78] M. Nuss, C. Heil, M. Ganahl, M. Knap, H. G. Evertz, E. Arrigoni, and W. von der Linden, Phys. Rev. B **86**, 245119 (2012).

[79] M. Knap, W. von der Linden, and E. Arrigoni, Phys. Rev. B **84**, 115145 (2011).

[80] F. Hofmann, M. Eckstein, E. Arrigoni, and M. Potthoff, Phys. Rev. B **88**, 165124 (2013).

[81] C. Jung, A. Lieder, S. Brener, H. Hafermann, B. Baxevanis, A. Chudnovskiy, A. Rubtsov, M. Katsnelson, and A. Lichtenstein, Ann. Phys. (NY) **524**, 49 (2012).

[82] R. Gezzi, T. Pruschke, and V. Meden, Phys. Rev. B **75**, 045324 (2007).

[83] S. G. Jakobs, V. Meden, and H. Schoeller, Phys. Rev. Lett. **99**, 150603 (2007).

[84] P. Werner, T. Oka, M. Eckstein, and A. J. Millis, Phys. Rev. B **81**, 035108 (2010).

[85] G. Cohen, E. Gull, D. R. Reichman, and A. J. Millis, arXiv:1310.4151.

[86] J. E. Han, Phys. Rev. B **73**, 125319 (2006).

[87] J. E. Han and R. J. Heary, Phys. Rev. Lett. **99**, 236808 (2007).

[88] A. Dirks, P. Werner, M. Jarrell, and T. Pruschke, Phys. Rev. E **82**, 026701 (2010).

[89] J. E. Han, A. Dirks, and T. Pruschke, Phys. Rev. B **86**, 155130 (2012).

[90] A. Dirks, J. E. Han, M. Jarrell, and T. Pruschke, Phys. Rev. B **87**, 235140 (2013).

[91] P. Dutt, J. Koch, J. Han, and K. Le Hur, Ann. Phys. (NY) **326**, 2963 (2011).

[92] E. Muñoz, C. J. Bolech, and S. Kirchner, Phys. Rev. Lett. **110**, 016601 (2013).

[93] A. M. Uimonen, E. Khosravi, A. Stan, G. Stefanucci, S. Kurth, R. van Leeuwen, and E. K. U. Gross, Phys. Rev. B **84**, 115103 (2011).

[94] S. Smirnov and M. Grifoni, Phys. Rev. B **84**, 125303 (2011).

[95] H. Schoeller and J. König, Phys. Rev. Lett. **84**, 3686 (2000).

[96] M. Schiro and M. Fabrizio, Phys. Rev. Lett. **105**, 076401 (2010).

[97] C. Timm, Phys. Rev. B **77**, 195416 (2008).

[98] J. Eckel, F. Heidrich-Meisner, S. G. Jakobs, M. Thorwart, M. Pletyukhov, and R. Egger, New J. Phys. **12**, 043042 (2010).

[99] S. Andergassen, V. Meden, H. Schoeller, J. Splettstoesser, and M. R. Wegewijs, Nanotechnology **21**, 272001 (2010).

[100] L. D. Contreras-Pulido, J. Splettstoesser, M. Governale, J. König, and M. Büttiker, Phys. Rev. B **85**, 075301 (2012).

[101] L. M. Falicov and J. C. Kimball, Phys. Rev. Lett. **22**, 997 (1969).

[102] M. Eckstein and M. Kollar, Phys. Rev. Lett. **100**, 120404 (2008).

[103] M. Eckstein, M. Kollar, and P. Werner, Phys. Rev. B **81**, 115131 (2010).

[104] S. Okamoto, Phys. Rev. Lett. **101**, 116807 (2008).

[105] C. Aron, G. Kotliar, and C. Weber, Phys. Rev. Lett. **108**, 086401 (2012).

[106] C. Gramsch, K. Balzer, M. Eckstein, and M. Kollar, Phys. Rev. B **88**, 235106 (2013).

[107] H. J. Carmichael, *Statistical Methods in Quantum Optics: Master Equations and Fokker-Planck Equations*, Vol. 1 of Texts and Monographs in Physics (Springer, Singapore, 2002).

[108] In our convention, lowercase g denotes Green's functions of the system where the impurity is disconnected from the reservoirs, while capital G denotes Green's functions of the connected system.

[109] Conventions for branch cuts are such that g^R is causal.

[110] E. N. Economou, *Green's Functions in Quantum Physics* (Springer, Heidelberg, 2006).

[111] Note that in the present formalism, temperature would enter through the hybridization function $\Delta^K(\omega)$ only.

[112] This is in general true unless the system has bound states.

[113] L. P. Kadanoff and G. Baym, *Quantum Statistical Mechanics: Green's Function Methods in Equilibrium and Nonequilibrium Problems* (Addison-Wesley, Redwood City, CA, 1962).

[114] J. Schwinger, J. Math. Phys. **2**, 407 (1961).

[115] L. V. Keldysh, Zh. Eksp. Teor. Fiz. **47**, 1515 (1965) [JETP **20**, 1018 (1965)].

[116] H. Haug and A.-P. Jauho, *Quantum Kinetics in Transport and Optics of Semiconductors* (Springer, Heidelberg, 1998).

[117] J. Rammer and H. Smith, Rev. Mod. Phys. **58**, 323 (1986).

[118] A. Kamenev, *Field Theory of Non-Equilibrium Systems* (Cambridge University Press, Cambridge, 2011).

[119] M. Caffarel and W. Krauth, Phys. Rev. Lett. **72**, 1545 (1994).

[120] C. Lanczos, J. Res. Natl. Bur. Stand. **45**, 255 (1951).

[121] See Ref. [87].

[122] H.-P. Breuer and F. Petruccione, *The Theory of Open Quantum Systems* (Oxford University Press, Oxford, England, 2009).

[123] Operators are denoted by a hat $\hat{o}$, while superoperators acting on operators are denoted by a double hat $\hat{\hat{o}}$. For elementary fermionic creation/annihilation operators, we omit the hat. Finally, we use boldface for matrices and vectors in orbital indices.

[124] Alternatively, one could use the "star" representation, in which only diagonal and $E_{f,v}$ terms are nonzero.

[125] T. Prosen, New J. Phys. **10**, 043026 (2008).

[126] A. A. Dzhioev and D. S. Kosov, J. Chem. Phys. **134**, 044121 (2011).

[127] M. Schmutz, Z. Phys. B **30**, 97 (1978).

[128] U. Harbola and S. Mukamel, Phys. Rep. **465**, 191 (2008).

[129] From now on, we will omit the spin index, unless necessary.

[130] In our convention, $G^{>+}_{\mu\nu}(t)$ and $G^{<-}_{\mu\nu}(t)$ are zero for $t < 0$, and vice versa.

[131] Notice that $\boldsymbol{D}$ commutes with $\boldsymbol{\lambda}$, so $\frac{\boldsymbol{D}}{\omega - i\boldsymbol{\lambda}}$ is well defined.

[132] D. F. Shanno, Math. Comp. **24**, 647 (1970).

[133] W. H. Press, S. A. Teukolsky, W. T. Vetterling, and B. P. Flannery, *Numerical Recipes 3rd Edition: The Art of Scientific Computing* (Cambridge University Press, Cambridge, UK, 2007).

[134] J. D. Jackson, *Classical Electrodynamics*, 2nd ed. (Wiley, New York, 1975).

[135] For the particle-hole-symmetric model, the auxiliary system onsite energies are restricted to $E_{ff} = -\frac{U}{2}$ and $E_{\mu\mu} = -E_{N_B+1-\mu,N_B+1-\mu}$ for $\mu \neq f$ as well as nearest-neighbor

$\langle \ldots \rangle$ hopping to $E_{\langle \mu\nu \rangle} = (-1)^{\mu+\nu+1} E_{\langle N_B+1-\mu, N_B+1-\nu \rangle}$ while the dissipation matrices have to fulfill $\Gamma^{(1)}_{\mu\nu} = (-1)^{\mu+\nu} \Gamma^{(2)}_{N_B+1-\mu, N_B+1-\nu}$.

[136] Y. Meir and N. S. Wingreen, Phys. Rev. Lett. **68**, 2512 (1992).

[137] A.-P. Jauho, https://nanohub.org/resources/1877.

[138] J. W. Negele and H. Orland, *Quantum Many-Particle Systems*, Vol. 68 of Frontiers in Physics (Addison-Wesley, Redwood City, Calif., 1988).

[139] S. De Franceschi, R. Hanson, W. G. van der Wiel, J. M. Elzerman, J. J. Wijpkema, T. Fujisawa, S. Tarucha, and L. P. Kouwenhoven, Phys. Rev. Lett. **89**, 156801 (2002).

[140] R. Leturcq, L. Schmid, K. Ensslin, Y. Meir, D. C. Driscoll, and A. C. Gossard, Phys. Rev. Lett. **95**, 126603 (2005).

[141] J. S. Langer and V. Ambegaokar, Phys. Rev. **121**, 1090 (1961).

[142] D. C. Langreth, Phys. Rev. **150**, 516 (1966).

[143] L. Mühlbacher, D. F. Urban, and A. Komnik, Phys. Rev. B **83**, 075107 (2011).

[144] J. König, J. Schmid, H. Schoeller, and G. Schön, Phys. Rev. B **54**, 16820 (1996).

[145] A. Rosch, J. Paaske, J. Kroha, and P. Wölfle, Phys. Rev. Lett. **90**, 076804 (2003).

[146] J. Dalibard, Y. Castin, and K. Mølmer, Phys. Rev. Lett. **68**, 580 (1992).

[147] A. J. Daley, J. M. Taylor, S. Diehl, M. Baranov, and P. Zoller, Phys. Rev. Lett. **102**, 040402 (2009).

[148] T. Prosen and M. Znidaric, J. Stat. Mech. (2009) P02035.

[149] A. Alvermann and H. Fehske, Phys. Rev. Lett. **102**, 150601 (2009).

[150] A. Weisse, G. Wellein, A. Alvermann, and H. Fehske, Rev. Mod. Phys. **78**, 275 (2006).

[151] C. D. Sherrill and H. F. Schaefer III, Adv. Quantum Chem. **34**, 143 (1999).

[152] Y. Saad, *Numerical Methods for Large Eigenvalue Problems, Revised Edition* (Society for Industrial and Applied Mathematics, Philadelphia, 2011).

[153] P. Arbenz, *Lecture Notes on Solving Large Scale Eigenvalue Problems*, http://people.inf.ethz.ch/arbenz/ewp/lnotes.html.

[154] Z. Bai, J. Demmel, J. Dongarra, A. Ruhe, and H. van der Vorst, *Templates for the Solution of Algebraic Eigenvalue Problems: A Practical Guide (Software, Environments and Tools)* (Society for Industrial and Applied Mathematics, Philadelphia, 1987).

[155] M. Knap, E. Arrigoni, W. von der Linden, and J. H. Cole, Phys. Rev. A **83**, 023821 (2011).

[156] Y. Saad, *Iterative Methods for Sparse Linear Systems*, 2nd ed. (Society for Industrial and Applied Mathematics, Philadelphia, 2003).

[157] R. Barrett, M. Berry, T. F. Chan, J. Demmel, J. Donato, J. Dongarra, V. Eijkhout, R. Pozo, C. Romine, and H. V. der Vorst, *Templates for the Solution of Linear Systems: Building Blocks for Iterative Methods*, 2nd ed. (SIAM, Philadelphia, PA, 1994).

[158] T. J. Park and J. C. Light, J. Chem. Phys. **85**, 5870 (1986).

[159] Y. B. Bazaliy, E. Demler, and S.-C. Zhang, Phys. Rev. Lett. **79**, 1921 (1997).

[160] M. H. Gutknecht, The unsymmetric Lanczos algorithms and their relations to Pade approximation, continued fractions, and the qd algorithm, http://www.math.ethz.ch/~mhg/.

[161] M. H. Gutknecht, Lanczos-type solvers for non-Hermitian linear systems, http://www.math.ethz.ch/~mhg/.

[162] R. Freund, M. Gutknecht, and N. Nachtigal, SIAM J. Sci. Comput. **14**, 137 (1993).

[163] B. N. Parlett, D. R. Taylor, and Z. A. Liu, Math. Comp. **44**, 105 (1985).

[164] H.-G. Weikert, H.-D. Meyer, L. S. Cederbaum, and F. Tarantelli, J. Chem. Phys. **104**, 7122 (1996).

[165] For the sake of clarity, we specifically introduce the subscript $_{ex}$ to denote the exact hybridization function $\underline{\Delta}_{ex}$. This will be used only in this section.

3.2. Publication 2: MPS impurity solver

3.2.1. Preamble

The article titled *Auxiliary master equation approach within matrix product states: Spectral properties of the nonequilibrium Anderson impurity model* was published in Physical Review B, **92**, 125145, September 2015 with an editor's suggestion [2].

This work was carried out by Antonius Dorda (AD) as first author and Martin Ganahl (MG) as co-author, under the supervision of Hans Gerd Evertz (HE), Wolfgang von der Linden (WL), and Enrico Arrigoni (EA). EA initiated the collaboration, put forward the idea of making use of matrix product states (MPS) to solve the auxiliary impurity problem more efficiently, and guided actively the course of this work. The original C++ code package for MPS was previously developed by MG, which was then extended by AD in order to apply it within AMEA. In particular, the code had to be extended to the treatment of non-Hermitian generators in the time evolution, the particular Lindblad operator, measurement objects and initial states were implemented, and different operator-splitting techniques were included and tested in order to reduce the Trotter error. MG assisted in debugging and profiling, and under the guidance of HE a careful analysis of the errors in the MPS time evolution was conducted by AD. AD, EA and WL investigated different strategies in the mapping procedure, which lead to the consideration of filled and empty bath chains and could significantly reduce the build-up of bipartite entanglement entropy. Secondly, AD, HE, WL, and EA worked on minimization methods for the fit in order to improve the mapping procedure. Some gradient-based and especially Monte Carlo methods were implemented and tested. In the end, a parallel tempering approach with feedback optimization has proven to be most efficient. For this AD implemented a general C++ code that was later on also incorporated in the ED-solver for DMFT, see Sec. 3.3 and 3.4. All of the calculations presented in the article were performed by AD. After a literature research, AD wrote a first version of the manuscript which was then revised by EA, HE, WL, and MG. All authors contributed to discussing results and the manuscript itself.

3.2.2. Original article

(see next page)

PHYSICAL REVIEW B **92**, 125145 (2015)

Auxiliary master equation approach within matrix product states: Spectral properties of the nonequilibrium Anderson impurity model

Antonius Dorda,[1,*] Martin Ganahl,[1,2] Hans Gerd Evertz,[1] Wolfgang von der Linden,[1] and Enrico Arrigoni[1,†]

[1]*Institute of Theoretical and Computational Physics, Graz University of Technology, 8010 Graz, Austria*

[2]*Perimeter Institute for Theoretical Physics, Waterloo, Ontario, Canada*

(Received 15 July 2015; published 24 September 2015)

Within the recently introduced auxiliary master equation approach it is possible to address steady state properties of strongly correlated impurity models, small molecules, or clusters efficiently and with high accuracy. It is particularly suited for dynamical mean field theory in the nonequilibrium as well as in the equilibrium case. The method is based on the solution of an auxiliary open quantum system, which can be made quickly equivalent to the original impurity problem. In its first implementation a Krylov space method was employed. Here, we aim at extending the capabilities of the approach by adopting matrix product states for the solution of the corresponding auxiliary quantum master equation. This allows for a drastic increase in accuracy and permits us to access the Kondo regime for large values of the interaction. In particular, we investigate the nonequilibrium steady state of a single-impurity Anderson model and focus on the spectral properties for temperatures T below the Kondo temperature T_K and for small bias voltages ϕ. For the two cases considered, with $T \approx T_K/4$ and $T \approx T_K/10$, we find a clear splitting of the Kondo resonance into a two-peak structure for ϕ close above T_K. In the equilibrium case ($\phi = 0$) and for $T \approx T_K/4$, the obtained spectral function essentially coincides with the one from numerical renormalization group.

DOI: 10.1103/PhysRevB.92.125145 PACS number(s): 71.15.−m, 72.15.Qm, 73.21.La, 73.63.Kv

I. INTRODUCTION

The equilibrium properties of the single-impurity Anderson model (SIAM) and the associated Kondo model [1–3], originally devised in the process of investigating metal hosts with dilute magnetic impurities [4–6], are nowadays well understood [7,8]. Renormalization group (RG) methods provided the first perturbative analyses [9], and especially the development of Wilson's numerical RG (NRG) [10] allowed one to properly capture the universal low-energy physics, governed by an exponentially small energy scale, the Kondo temperature T_K [8]. The field of correlated impurity models has gained renewed interest due to novel experimental realizations in quantum dots [11–15], single-molecule transistors [16–20], and from a theoretical point of view, due to its importance for dynamical mean field theory (DMFT) [8,21–26]. The extension of DMFT to the nonequilibrium case can be carried out within the Keldysh formalism [27–29]. Nonequilibrium DMFT and different applicable impurity solvers have been thoroughly discussed in other work; see for instance Refs. [29–37].

In the present study we want to focus on the physics of the impurity problem out of equilibrium itself, with an implementation of the auxiliary master equation approach (AMEA) [35,36] based on matrix product states (MPS). Already in a first study, where Krylov space methods were employed [36], AMEA has proven to feature a systematically improvable accuracy and to yield a well-defined Kondo peak in equilibrium together with a splitting in the nonequilibrium case. However, the exponential scaling of Krylov space methods with system size sets a "hard limit" to the achievable accuracy, and thus to the lowest temperatures accessible. The MPS extension presented here turns out to be crucial in order to achieve highly accurate results in the Kondo regime down to low temperatures and up to large interactions. In the equilibrium case, the accuracy of our results becomes even comparable to NRG.

Specifically, we investigate the nonequilibrium steady state dynamics of a SIAM, which is driven by the coupling to two leads at different chemical potentials, caused by an external bias voltage ϕ. Impurity models in such a setup were considered already by many groups, numerically as well as analytically [38–40]. To give a brief nonexhaustive overview, different techniques employed are the noncrossing approximation [41–43], real-time diagrammatic methods [44], Keldysh perturbation theory [45], Keldysh effective field theory [46,47], dual fermions [48,49], perturbative RG [50,51], flow equations [52,53], functional RG [54,55], real-time RG [56–59], time-dependent density matrix RG [60–63], NRG [64–66], Monte Carlo methods [67–69], as well as cluster approaches [70]. The properties of the correlated impurity have been established in certain limits, for example for high temperatures $T \gg T_K$ or high biases $\phi \gg T_K$, where the Kondo effect is strongly suppressed by decoherence and the problem reduces to a weak-coupling one [43,53,57,71–73]. A splitting of the Kondo peak in the spectral function was found at sufficiently high bias voltages and low T, with a two-peak structure pinned to the chemical potentials of the leads [41–45,51,53,64,68–70]. In the other limit $\phi \ll T_K$ and $T \ll T_K$, linear response as well as Fermi liquid theory are applicable [49,58,74,75]. Nevertheless, the intermediate and low-energy nonequilibrium regime, where both T and ϕ are of the order of and especially below T_K, remains challenging and the spectral properties could not yet be completely resolved. Work in this direction has for example been done in Refs. [64,68,69]. However, the extension of NRG to the nonequilibrium case still leaves open questions [76], and the Monte Carlo approaches, even though numerically exact, are either limited to relatively high temperatures and short times, or involve a demanding double analytical

*dorda@tugraz.at

†arrigoni@tugraz.at

continuation [77,78]. With the work presented here, we want to contribute to these findings and present well-resolved spectral data for cases where both $T \lesssim T_K$ and $\phi \lesssim T_K$.

II. MODEL AND METHOD

The basic idea of AMEA is to map a general correlated impurity model in or out of equilibrium, here referred to as the physical impurity model ($\mathrm{IM_{ph}}$), onto an appropriately chosen auxiliary one ($\mathrm{IM_{aux}}$), which is small enough to be solvable precisely by numerical techniques. The self-energy of $\mathrm{IM_{aux}}$ serves then as an approximation to the one of $\mathrm{IM_{ph}}$. Specifically, $\mathrm{IM_{aux}}$ is modeled by an open quantum system described by a Lindblad equation, which consists of a finite number of bath sites and additional Markovian environments. In the mapping procedure, the bath parameters of $\mathrm{IM_{aux}}$ are optimized in order to reproduce the dynamics of $\mathrm{IM_{ph}}$ as closely as possible. By increasing the number of bath sites N_B, more optimization parameters are available and a convergence (typically exponential) towards the exact solution of $\mathrm{IM_{ph}}$ is achieved. The mapping is formulated in terms of the hybridization function of $\mathrm{IM_{aux}}$, which is obtained through a single-particle calculation, and the many-body problem is solved thereafter.

AMEA itself and a solution strategy for the correlated $\mathrm{IM_{aux}}$ based on exact diagonalization (ED) was presented in detail in Refs. [35,36]. Here, we make use of MPS in order to solve for the correlation functions, which enables us to treat auxiliary systems with a larger number of bath sites. In the following we briefly summarize the governing equations in AMEA and point out modifications in the construction of $\mathrm{IM_{aux}}$ favorable for an MPS treatment. After that, the MPS implementation is discussed.

A. Keldysh Green's functions

In general, for nonequilibrium situations Green's functions are conveniently defined on the Keldysh contour [79–84]. Since we are particularly interested in the long-time limit, where a steady state is reached, time translational invariance applies and the Keldysh Green's functions can be written in the frequency domain

$$\underline{G}(\omega) = \begin{pmatrix} G^R(\omega) & G^K(\omega) \\ 0 & G^A(\omega) \end{pmatrix}, \tag{1}$$

with $G^A = (G^R)^\dagger$, and we denote by an underscore $\underline{\cdots}$ a 2×2 object in Keldysh space. Only in an equilibrium situation the Keldysh component is related to the retarded one via the fluctuation dissipation theorem

$$G^K(\omega) = 2i[1 - 2p_{\mathrm{FD}}(\omega,\mu,T)]\mathrm{Im}\{G^R(\omega)\}, \tag{2}$$

where $p_{\mathrm{FD}}(\omega,\mu,T)$ represents the Fermi-Dirac distribution. In contrast, in a general nonequilibrium situation a distribution function is not known *a priori* and the Keldysh and the retarded component have to be considered as independent functions.

It is convenient to introduce the steady state lesser and greater Green's functions

$$G^<(t) = i\,\langle c^\dagger(t)c\rangle\,, \quad G^>(t) = -i\,\langle c(t)c^\dagger\rangle\,, \tag{3}$$

for generic fermionic creation/annihilation operators $c^\dagger/c$, which are related to G^R and G^K by

$$G^R(\omega) - G^A(\omega) = G^>(\omega) - G^<(\omega) = -2i\pi A(\omega),$$
$$G^K(\omega) = G^>(\omega) + G^<(\omega), \tag{4}$$

and $A(\omega)$ is the spectral function. Throughout this work we consider solely steady state expectation values and denote them in compact notation by $\langle\ldots\rangle$; cf. Eq. (3).

B. Physical impurity model

In this work, we consider for $\mathrm{IM_{ph}}$ a single-impurity Anderson model in a nonequilibrium setup, given by an impurity Hamiltonian H_{imp}, two noninteracting fermionic leads representing the electronic reservoir H_{res}, and an impurity-reservoir coupling H_{coup}:

$$H_{\mathrm{ph}} = H_{\mathrm{imp}} + H_{\mathrm{res}} + H_{\mathrm{coup}}. \tag{5}$$

The correlated impurity consists of a single level with energy ε_d and on-site Hubbard interaction U,

$$H_{\mathrm{imp}} = \varepsilon_d \sum_{\sigma\in\{\uparrow,\downarrow\}} d_\sigma^\dagger d_\sigma + U\left(d_\uparrow^\dagger d_\uparrow - \frac{1}{2}\right)\left(d_\downarrow^\dagger d_\downarrow - \frac{1}{2}\right), \tag{6}$$

where $d_\sigma^\dagger/d_\sigma$ are fermionic creation and annihilation operators on the impurity site. The reservoir Hamiltonian can be written in terms of the energy levels $\varepsilon_{\lambda k}$ and potentials ε_λ for the two leads λ,

$$H_{\mathrm{res}} = \sum_{\lambda\in\{L,R\}} \sum_{k\sigma} (\varepsilon_\lambda + \varepsilon_{\lambda k}) a_{\lambda k\sigma}^\dagger a_{\lambda k\sigma}, \tag{7}$$

and the impurity-reservoir coupling is given by

$$H_{\mathrm{coup}} = \frac{1}{\sqrt{N_k}} \sum_{\lambda k\sigma} t'_\lambda (a_{\lambda k\sigma}^\dagger d_\sigma + \mathrm{H.c.}), \tag{8}$$

with $a_{\lambda k\sigma}^\dagger/a_{\lambda k\sigma}$ representing creation and annihilation operators for lead electrons.

Throughout this work we consider the particle-hole symmetric case with $\varepsilon_d = 0$, $t'_L = t'_R$, $\varepsilon_{Lk} = \varepsilon_{Rk}$. An externally applied bias voltage ϕ results in an antisymmetrical shift of the chemical potentials $\mu_{L/R} = \pm\frac{\phi}{2}$. In Sec. III C we further consider for the on-site energies the case $\varepsilon_{L/R} = \pm\frac{\phi}{2}$, whereas in the rest of the work the voltage does not shift the lead energies. This is irrelevant for ϕ much smaller than the bandwidth.

The Green's function of $\mathrm{IM_{ph}}$ is given by the Dyson equation

$$\underline{G}_{\mathrm{ph}}^{-1}(\omega) = \underline{g}_0^{-1}(\omega) - \underline{\Delta}_{\mathrm{ph}}(\omega) - \underline{\Sigma}_{\mathrm{ph}}(\omega). \tag{9}$$

Here, $\underline{g}_0$ denotes the noninteracting Keldysh Green's function of the decoupled impurity, i.e., $g_0^R = (\omega - \varepsilon_d)^{-1}$, and $(\underline{g}_0^{-1})^K$ can be neglected. The hybridization function $\underline{\Delta}_{\mathrm{ph}}$ is given by the sum of contributions from the two leads

$$\underline{\Delta}_{\mathrm{ph}}(\omega) = \sum_\lambda t'^2_\lambda \underline{g}_\lambda(\omega), \tag{10}$$

where $\underline{g}_\lambda(\omega)$ denote lead Green's functions at the contact point in the decoupled case. Except in the calculations presented in Sec. III C, we consider throughout this work a flat band model

with the retarded component of $\underline{g}_\lambda(\omega)$ given by

$$-\mathrm{Im}\{g^R_\lambda(\omega)\} = \frac{\pi}{2D}\Theta(D-|\omega|), \tag{11}$$

where we choose the hybridization strength $\Gamma = t'^2_\lambda \pi/D$ as unit of energy and take $D = 10\,\Gamma$. The real part is determined via the Kramers-Kronig relation. For the fit in the mapping procedure (see Sec. II D) it is of advantage to deal with smooth functions of ω, so that we introduce in Eq. (11) a smearing of the cutoffs in the Heaviside function, determined by Fermi functions $p_{\mathrm{FD}}(\omega,\pm D,0.5\,\Gamma)$ with an artificial temperature $0.5\,\Gamma$. Since this modification is well outside the scale of the impurity energies, it does not affect the low-energy physics.

The decoupled leads are in equilibrium, so that the Keldysh component $g^K_\lambda(\omega)$ of each lead is given by Eq. (2) with the corresponding chemical potential μ_λ. The temperature T is taken to be the same in both of the leads. Notice that the Keldysh component is the only T-dependent quantity and results for different T shown below differ only in the smearing of the Fermi edge in $g^K_\lambda(\omega)$. In particular, we are interested in temperatures close to and below the Kondo temperature T_K. As for other methods, the low-temperature regime is most challenging (cf. Sec. II D and Appendix B). For a Hubbard interaction of $U = 6\,\Gamma$, as considered throughout the work, one finds for the flat band model $T_K \approx 0.2\,\Gamma$ [8,85–88].

The remaining unknown quantity in Eq. (9) is the self-energy $\underline{\Sigma}_{\mathrm{ph}}(\omega)$, which cannot be determined exactly since $\mathrm{IM}_{\mathrm{ph}}$ is interacting and of infinite size. This is evaluated by means of the mapping to $\mathrm{IM}_{\mathrm{aux}}$.

C. Auxiliary impurity model

For $\mathrm{IM}_{\mathrm{aux}}$ we take an open quantum system of finite size, embedded in Markovian environments and described by a Lindblad equation for the system density operator ρ:

$$\frac{d}{dt}\rho = \mathcal{L}\rho. \tag{12}$$

The Lindblad superoperator $\mathcal{L} = \mathcal{L}_H + \mathcal{L}_D$ consists of a unitary part $\mathcal{L}_H\rho = -i[H_{\mathrm{aux}},\rho]$ and the dissipator $\mathcal{L}_D$ as described below [89].

Additionally to the original impurity site we consider N_B bath sites arranged in a linear geometry. For convenience we choose N_B even and the impurity site at the center, specified by the index f. The Hamiltonian for $\mathrm{IM}_{\mathrm{aux}}$ is given by

$$H_{\mathrm{aux}} = \sum_{ij\sigma} E_{ij} c^\dagger_{i\sigma} c_{j\sigma} + U n_{f\uparrow} n_{f\downarrow}. \tag{13}$$

Here $n_{f\sigma} = c^\dagger_{f\sigma} c_{f\sigma}$ with $c^\dagger_{i\sigma}/c_{i\sigma}$ the fermionic creation/annihilation operators and the $(N_B+1)\times(N_B+1)$ matrix $\boldsymbol{E}$ couples only nearest neighbor (n.n.) terms; i.e., it is tridiagonal in the chosen geometry. To end up with a noninteracting bath we allow at most for Lindblad operators that are linear in $c^\dagger_{i\sigma}/c_{i\sigma}$. The dissipator is then given by [89]

$$\mathcal{L}_D\rho = 2\sum_{ij\sigma}\Gamma^{(1)}_{ij}\left(c_{j\sigma}\rho c^\dagger_{i\sigma} - \frac{1}{2}\{\rho, c^\dagger_{i\sigma}c_{j\sigma}\}\right) + 2\sum_{ij\sigma}\Gamma^{(2)}_{ij}\left(c^\dagger_{i\sigma}\rho c_{j\sigma} - \frac{1}{2}\{\rho, c_{j\sigma}c^\dagger_{i\sigma}\}\right). \tag{14}$$

Both matrices of coupling constants $\boldsymbol{\Gamma}^{(1)}$ and $\boldsymbol{\Gamma}^{(2)}$ are symmetric and positive definite [90].

A key aspect in AMEA is that the bath parameters in the Lindblad equation are not determined within conventional Born-Markov approximations [91–93] but are only used as fit parameters to optimally reproduce $\underline{\Delta}_{\mathrm{ph}}(\omega)$ by $\underline{\Delta}_{\mathrm{aux}}(\omega)$; see Sec. II D.

Once the parameters of $\mathrm{IM}_{\mathrm{aux}}$ are determined, the many-body problem is solved (cf. Sec. II E) in order to obtain the interacting Green's function

$$\underline{G}^{-1}_{\mathrm{aux}}(\omega) = \underline{g}^{-1}_0(\omega) - \underline{\Delta}_{\mathrm{aux}}(\omega) - \underline{\Sigma}_{\mathrm{aux}}(\omega). \tag{15}$$

At this point it is convenient to set $\underline{\Sigma}_{\mathrm{ph}}(\omega) = \underline{\Sigma}_{\mathrm{aux}}(\omega) = \underline{\Sigma}(\omega)$, so that we obtain from Eq. (9) a very accurate result for the Green's function of $\mathrm{IM}_{\mathrm{ph}}$. In this way, the $U = 0$ limit is recovered exactly.

D. Mapping procedure

In order to have a faithful representation of the dynamics of $\mathrm{IM}_{\mathrm{ph}}$ by $\mathrm{IM}_{\mathrm{aux}}$, we need to fulfill $\underline{\Delta}_{\mathrm{aux}}(\omega) \approx \underline{\Delta}_{\mathrm{ph}}(\omega)$ as closely as possible. For local quantities and correlation functions on the impurity, the influence of the bath is completely determined by the hybridization function only, independently of the specific bath geometry. Therefore, the mapping becomes exact in the limit $\underline{\Delta}_{\mathrm{aux}}(\omega) \equiv \underline{\Delta}_{\mathrm{ph}}(\omega)$. To achieve $\underline{\Delta}_{\mathrm{aux}}(\omega) \approx \underline{\Delta}_{\mathrm{ph}}(\omega)$, we minimize the mean-squared error between them as a function of the bath parameters in the Lindblad equation, i.e., the matrices $\boldsymbol{E}$, $\boldsymbol{\Gamma}^{(1)}$, and $\boldsymbol{\Gamma}^{(2)}$.

It is important to stress that a single-particle calculation is sufficient to determine $\underline{\Delta}_{\mathrm{aux}}(\omega)$, for which the Green's functions read [35,36]

$$\begin{aligned}\boldsymbol{G}^R_0(\omega) &= [\omega - \boldsymbol{E} + i(\boldsymbol{\Gamma}^{(1)} + \boldsymbol{\Gamma}^{(2)})]^{-1},\\ \boldsymbol{G}^K_0(\omega) &= 2i\boldsymbol{G}^R_0(\omega)(\boldsymbol{\Gamma}^{(2)} - \boldsymbol{\Gamma}^{(1)})\boldsymbol{G}^A_0(\omega).\end{aligned} \tag{16}$$

Here, the inversion and multiplications are carried out for matrices in the site indices. The hybridization function is given in terms of the elements with impurity index f:

$$\begin{aligned}\Delta^R_{\mathrm{aux}}(\omega) &= 1/g^R_0(\omega) - 1/G^R_{0ff}(\omega),\\ \Delta^K_{\mathrm{aux}}(\omega) &= G^K_{0ff}(\omega)\,/\,\left|G^R_{0ff}(\omega)\right|^2.\end{aligned} \tag{17}$$

A single evaluation of the hybridization function is at most of $\mathcal{O}(N_B^3)$ and thus not time consuming. However, for a large number of bath parameters ($\gtrsim$20) the multidimensional optimization problem may become demanding and appropriate methods are needed. In particular, a parallel tempering approach has proven to be effective, which is discussed in some more detail in Appendix A.

Beyond the requirement $\underline{\Delta}_{\mathrm{aux}}(\omega) \approx \underline{\Delta}_{\mathrm{ph}}(\omega)$, complete freedom exists in choosing a suitable auxiliary system. For the many-body solution with MPS it is convenient to allow for nearest neighbor terms in the Lindblad couplings only, i.e., to restrict not only $\boldsymbol{E}$ but also the matrices $\boldsymbol{\Gamma}^{(1)}$ and $\boldsymbol{\Gamma}^{(2)}$ to a tridiagonal form. In this way one ends up with a geometry where the impurity couples to a bath with n.n. terms only. As discussed below, the bipartite entanglement entropy of $\mathrm{IM}_{\mathrm{aux}}$ can be reduced when imposing further that $\Gamma^{(1)}_{i,j}$ has nonzero terms only for bath sites in one of the chains, e.g., for $i,j > f$, and $\Gamma^{(2)}_{i,j}$ on the other side, i.e., for $i,j < f$. For the latter

restriction we found that it affects the quality of the fit only in a minor way but significantly improves the applicability of MPS.

It is important to note that the relevant energy scale for the mapping procedure is not Γ but the bandwidth $2D$. For a certain $\mathrm{IM}_{\mathrm{aux}}$, one can adjust to different Γ values by simply rescaling all terms in $\boldsymbol{E}$ with index f, i.e., the hoppings to the impurity site, without changing other properties of $\underline{\Delta}_{\mathrm{aux}}(\omega)$ [90]. On the other hand, one can rescale the whole hybridization function by multiplying the matrices $\boldsymbol{E}$, $\boldsymbol{\Gamma}^{(1)}$, and $\boldsymbol{\Gamma}^{(2)}$ by the desired factor. Therefore, the complexity of the mapping procedure is dominated by the smallest ω scale compared to the largest one. For the flat band model, this essentially means that one has to regard T and ϕ in units of D. With increasing number of bath sites N_B we observe that sharper features can be resolved. Therefore, a maximal considered value of N_B converts to a lower bound for the ratio of temperature T to bandwidth $2D$ which can be reproduced by $\underline{\Delta}_{\mathrm{aux}}(\omega)$. More details on the mapping procedure are given in Appendix B and Ref. [94].

E. Many-body solution

1. Superfermion representation

As introduced in Refs. [95,96] and made use of in Refs. [35,36], the Lindblad equation (12) can be recast into a standard operator problem when considering an augmented fermion Fock space with twice as many sites. We use the notation of Ref. [95], to which we refer for further details, in combination with a particle-hole transformation in the "tilde" space [97]. The so-called left vacuum reads

$$|I\rangle = \sum_{\{n_{i\sigma}\}} (-i)^{N(\{n_{i\sigma}\})} |\{n_{i\sigma}\}\rangle \otimes |\widetilde{\{\bar{n}_{i\sigma}\}}\rangle \,. \tag{18}$$

The summation runs over all possible many-body basis states $|\{n_{i\sigma}\}\rangle$ of the original system and $|\widetilde{\{\bar{n}_{i\sigma}\}}\rangle$ specifies those in the tilde system with inverted occupation numbers. $N(\{n_{i\sigma}\}) = \sum_{i\sigma} n_{i\sigma}$ is the total number of particles in state $|\{n_{i\sigma}\}\rangle$.

The left vacuum maps the density operator $\rho(t)$ onto the state vector $|\rho(t)\rangle = \rho(t)\,|I\rangle$. Thermodynamic expectation values are determined in this framework by expressions of the form $\langle O(t)\rangle = \langle I|\, O\,|\rho(t)\rangle$. When evaluating $(\mathcal{L}\rho)\,|I\rangle$ for the Lindblad equation (12), one finds

$$\frac{d}{dt}\,|\rho(t)\rangle = L\,|\rho(t)\rangle \,, \tag{19}$$

where the superoperator $\mathcal{L}$ is replaced by an ordinary non-Hermitian operator L. In vector notation

$$\boldsymbol{c}_\sigma^\dagger = \left(c_{0\sigma}^\dagger, \ldots, c_{N_B\sigma}^\dagger, \tilde{c}_{0\sigma}^\dagger, \ldots, \tilde{c}_{N_B\sigma}^\dagger\right), \tag{20}$$

with $c_{i\sigma}^\dagger/c_{i\sigma}$ and $\tilde{c}_{i\sigma}^\dagger/\tilde{c}_{i\sigma}$ fermionic operators in the original and in the tilde system, respectively, the Lindblad operator L is given by

$$\begin{aligned} iL = &\sum_\sigma \boldsymbol{c}_\sigma^\dagger \begin{pmatrix} \boldsymbol{E} + i\boldsymbol{\Omega} & 2\boldsymbol{\Gamma}^{(2)} \\ -2\boldsymbol{\Gamma}^{(1)} & \boldsymbol{E} - i\boldsymbol{\Omega} \end{pmatrix} \boldsymbol{c}_\sigma - 2\,\mathrm{Tr}(\boldsymbol{E} + i\boldsymbol{\Lambda}) \\ &+ U\left(n_{f\uparrow}n_{f\downarrow} - \tilde{n}_{f\uparrow}\tilde{n}_{f\downarrow} + \sum_\sigma \tilde{n}_{f\sigma} + 1\right), \end{aligned} \tag{21}$$

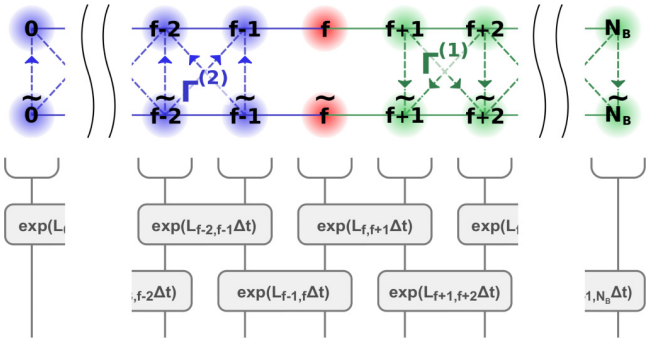

FIG. 1. (Color online) The upper part of the figure shows a schematic drawing of the auxiliary system in the superfermion representation, for N_B bath sites and with the impurity located at the central site $f = N_B/2$. The upper chain corresponds to original sites and the lower chain to the additionally introduced "tilde" sites; see Sec. II E 1. In the chosen fit restriction, see Sec. II D, the coupling terms of the Lindblad operator L, Eq. (21), represent a ladder geometry with cross links. $\Gamma^{(1)}$ causes a directional hopping from the upper to the lower chain and for $\Gamma^{(2)}$ it is vice versa. Moreover, $\Gamma^{(2)}_{i,j}$ is nonzero only for $i,j < f$ and $\Gamma^{(1)}_{i,j}$ only for $i,j > f$. In the lower part, in gray scale, we schematically depict the tensor network for TEBD (Sec. II E 2), where L is decomposed in nearest neighbor terms $L_{i,i+1}$ which are applied in an alternating manner.

where $\boldsymbol{\Omega} = \boldsymbol{\Gamma}^{(2)} - \boldsymbol{\Gamma}^{(1)}$ and $\boldsymbol{\Lambda} = \boldsymbol{\Gamma}^{(1)} + \boldsymbol{\Gamma}^{(2)}$. Clearly, L conserves the total particle number per spin $\sum_i (n_{i\sigma} + \tilde{n}_{i\sigma})$. The steady state $|\rho_\infty\rangle = \lim_{t\to\infty} |\rho(t)\rangle$ as well as $|I\rangle$ are situated in the half-filled, spin-symmetric sector. Steady state expectation values and correlation functions are calculated by [36,98]

$$\langle A(t)B\rangle = \langle I|\, A e^{Lt} B\,|\rho_\infty\rangle \,, \quad \text{for } t \geqslant 0. \tag{22}$$

For tridiagonal matrices $\boldsymbol{E}$, $\boldsymbol{\Gamma}^{(1)}$, and $\boldsymbol{\Gamma}^{(2)}$, see Sec. II D, the coupling terms in Eq. (21) represent a ladder system as depicted in Fig. 1. Sites on the original and the tilde system with the same index ($i = j$) or $i = j \pm 1$ are coupled with rates $\Gamma^{(1)}_{i,j}$ and $\Gamma^{(2)}_{i,j}$ by a directional hopping. The restriction of $\Gamma^{(2)}_{i,j}$ to the left side $i,j < f$ and for $\Gamma^{(1)}_{i,j}$ to the right side $i,j > f$ leads to the situation that a circular current flows through the system. In this geometry one finds the tendency that sites on the left are filled in the original system and empty in the tilde system, whereas for the right side it is vice versa. This limits the possible hopping processes inside the chains and is in favor of a small bipartite entanglement entropy [99].

2. Matrix product states

A large amount of literature exists on MPS in general and for Lindblad-type problems in particular [99–115]. Here we briefly state the governing equations for the well-known MPS methods made use of in this work.

We combine sites with the same index i in the original and in the tilde system to one "MPS site," with a local Hilbert space dimension $d = 16$ (see also Fig. 1). For the resulting one-dimensional chain of sites it is straight-forward to write

down a MPS representation [100]:

$$|\rho\rangle = \sum_{\{s_i\}} c_{\{s_i\}} |\{s_i\}\rangle = \prod_{i=0}^{N_B} \left(\sum_{s_i=1}^{d} \boldsymbol{A}_i^{s_i} \right) |\{s_i\}\rangle . \quad (23)$$

Here, $|\rho\rangle$ is a generic many-body state with coefficients $c_{\{s_i\}}$ and $\boldsymbol{A}_i^{s_i}$ represents MPS matrices for site i with local quantum numbers s_i [116]. The mapping Eq. (23) is exact for matrices which are exponentially large in N_B. However, even for much smaller matrix dimensions $\chi \ll d^{N_B/2}$ a very accurate representation of $|\rho\rangle$ is possible in many cases. For the auxiliary systems considered in this work, see also Sec. III A, $\chi \approx 1000$ is sufficient when making use of Abelian symmetries of the Lindblad operator Eq. (21). Concerning the positivity of ρ, one should note that the form of Eq. (23) does not ensure it per construction [114,115]. However, we did not encounter unphysical results even for very small values of χ.

In order to calculate observables, a MPS representation of $|I\rangle$ is needed. One finds that Eq. (18) can be recast into a state with $\chi = 1$, i.e., a product state, in which $|I\rangle$ is maximally entangled between original and tilde sites for the same index i. This is analogous to a purification of the identity operator [103,104,108].

When rewriting the Lindblad operator Eq. (21) with tridiagonal matrices $\boldsymbol{E}$, $\boldsymbol{\Gamma}^{(1)}$, and $\boldsymbol{\Gamma}^{(2)}$ in the form of a matrix product operator, one has couplings of n.n. sites only. This enables us to use very efficient time evolution techniques as for example the time evolving block decimation (TEBD) [101]. Here, a Trotter decomposition is used to split the full time evolution $\exp(L\Delta t)$ into small parts $\exp(L_{i,i+1}\Delta t)$ for neighboring sites, and terms with even and odd i are applied in an alternating manner; see also Fig. 1. In this work we use splitting methods accurate to second order in Δt [117–120]. We found that reducing the time step to $\Delta t = 0.01\,\Gamma^{-1}$ for the steady state and to $\Delta t = 0.05\,\Gamma^{-1}$ for the Green's functions is usually sufficient.

To obtain the desired steady state correlation functions of $\mathrm{IM}_{\mathrm{aux}}$, for example $G^<$, we proceed as follows:

(1) Calculate the steady state $|\rho_\infty\rangle$ by time evolution with TEBD. Successively smaller time steps Δt are used in order to eliminate the Trotter error. Static observables and $L\,|\rho_\infty\rangle = 0$ may serve as convergence criteria [121].

(2) Apply $c_{f\sigma}$ to $|\rho_\infty\rangle$ and time-evolve the excited state to get $G^<_\sigma(t_n) = i\,\langle I|\, c^\dagger_{f\sigma} e^{Lt_n} c_{f\sigma}\, |\rho_\infty\rangle$ at discrete points in the time domain.

(3) Employ linear prediction on the data $G^<(t_n)$ and thereafter a Fourier transformation to obtain $G^<(\omega)$ in the frequency domain [98,102,104,122].

III. RESULTS

Before focusing on the nonequilibrium physics of the single-impurity Anderson model, we briefly discuss the bipartite entanglement entropy of the auxiliary impurity model, and a benchmark for the equilibrium case. After that the spectral properties as a function of bias voltage are presented for two different temperatures, one clearly below and one above the Kondo temperature T_K. Furthermore, the bias dependence of observables such as the current and the double occupancy is discussed. In the last part of this paper a different density of states in the leads is considered, which allows to better resolve the physics at low temperatures and low bias voltages.

A. Entanglement scaling

Matrix product states are an efficient representation of many-body states with a low bipartite entanglement entropy S. The required matrix dimension χ at a certain bond $(i,i+1)$ scales exponentially with the entropy at this bond, $S_{i,i+1}$. From Hermitian systems it is known that ground states of gapped, one-dimensional systems obey an area law and are thus well suited for MPS. Also an evolution in imaginary time converges well, but the real time evolution of excited states may become problematic due to a buildup of entanglement [100]. For the auxiliary impurity model investigated here, the behavior appears to be opposite. In general, the steady state $|\rho_\infty\rangle$ of $\mathrm{IM}_{\mathrm{aux}}$ does not fulfill an area law and instead an increase of $\max_i S_{i,i+1}$ with increasing system size N_B is observed [111]. Despite this, the time evolution of excited states is unproblematic, likely because of the damping involved, and the long-time limit can easily be reached.

We observe that the optimized parameters in $\mathrm{IM}_{\mathrm{aux}}$ strongly depend on the number of bath sites and on the external, physical parameters (ϕ, T, ...). Therefore, it is difficult to infer a reliable quantitative entanglement scaling with N_B. Qualitatively we find that $\max_i S_{i,i+1}$ increases moderately with N_B and slower than linear. The magnitude of the entanglement is considerably reduced by the restricted setup for $\mathrm{IM}_{\mathrm{aux}}$ described in Sec. II D, which has the tendency towards a filled and an empty bath chain in the steady state. In this setup, $S_{i,i+1}$ takes on the largest value at the central bonds which connect to the impurity site and falls off quickly with distance from the center.

Independent of the actual scaling, the increase of bipartite entanglement with N_B has the consequence that one is limited to certain system sizes. In this work we consider up to $N_B = 16$ with $\chi = 1000$, which is feasible in a reasonable amount of time. Most likely, one would need higher values of χ in order to treat even larger systems precisely. We checked the reliability of the results presented below by increasing the matrix dimension to $\chi = 1500$ in several cases, for different

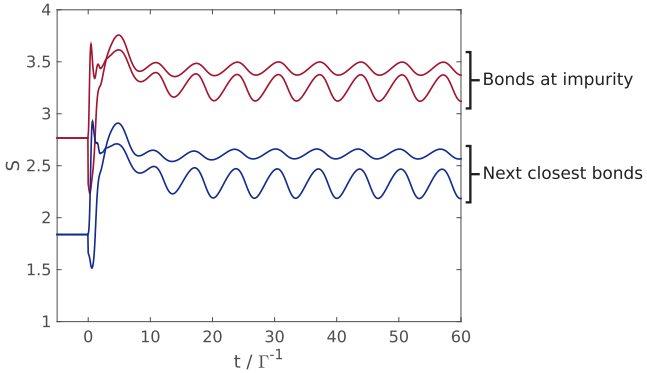

FIG. 2. (Color online) Temporal evolution of the bipartite entanglement entropy S in a typical $\mathrm{IM}_{\mathrm{aux}}$ with $N_B = 12$, representing the case $\phi = 1\,\Gamma$. The system is in the steady state for $t < 0$ and $c_{f\sigma}$ is applied to $|\rho_\infty\rangle$ at $t = 0$. We show $S(t)$ where it is largest, namely for the innermost bonds at the impurity, as well as for the next ones to the outside.

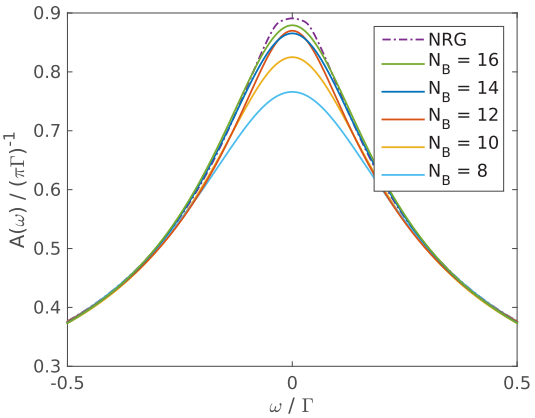

FIG. 3. (Color online) Spectral function in equilibrium: plotted for different number of bath sites N_B and compared with reference data from NRG [86]. Results are for $U = 6\,\Gamma$ and flat band leads, Eq. (11), with $D = 10\,\Gamma$ and $T = 0.05\,\Gamma$.

values of ϕ and T. Furthermore, the time evolution for the Green's functions was validated by reducing the time step to $\Delta t = 0.01\,\Gamma^{-1}$. Overall, we found in the worst cases relative differences in $A(\omega)$ up to $\mathcal{O}(10^{-3})$. These errors are small enough for our purposes, so that we focus in the following on the accuracy of the mapping procedure, i.e., versus N_B.

To analyze the temporal evolution of S, a typical time-dependent case is shown in Fig. 2. Here, $t < 0$ indicates the steady state regime and at $t = 0$ an annihilation operator is applied to $|\rho_\infty\rangle$ in order to calculate the lesser Green's function. To estimate the relevant time scale, $\mathrm{Im}\{G^<(t)\}$ (not plotted) drops from 0.5 at $t = 0$ to 10^{-2} at $t = 3\,\Gamma^{-1}$. As one can see, $S_{i,i+1}$ changes at first rapidly but saturates then and oscillates in time around a constant value. Thus, it is unproblematic to resolve $G^<(t)$ even on very large time scales. This was furthermore checked for small N_B with an exact diagonalization solution as reference [123]. When inspecting the short-time behavior of $S_{i,i+1}$, an asymmetry is evident. This results from the application of an operator to the original system alone, without changing the tilde system.

B. Spectral and transport properties

Before focusing on the nonequilibrium physics, we briefly present results for the equilibrium situation $\phi = 0$ in Fig. 3. Here, a quasiexact solution is provided by means of NRG [86]. For $T = 0.05\,\Gamma \approx T_K/4$ the system is well inside the Kondo regime and the peak height of $A(0)\pi\Gamma \approx 0.9$ almost fulfills the $T = 0$ Friedel sum rule [$A(0)\pi\Gamma = 1$ for $T \to 0$] [85,124,125]. Results obtained with AMEA are shown for different system sizes, with particular focus on the low-energy physics. Noticeable differences are apparent for $N_B = 8$, but, upon increasing the number of bath sites quick convergence is observed and excellent agreement with the NRG data is found. This shows that AMEA, especially with MPS, is a very accurate impurity solver also in the equilibrium case for $T > 0$.

Regarding the accuracy of the calculations, we can state that $N_B = 12$ is essentially sufficient to provide reliable spectral data in equilibrium for $T = 0.05\,\Gamma$. However, for the nonequilibrium situations considered in the following one has to take into account that the accuracy of the mapping procedure is to some degree dependent on ϕ. This is analyzed in detail in Appendix B and here we solely want to note that the low bias $\phi \leqslant \frac{1}{3}\,\Gamma$ as well as the higher bias regime $\phi \geqslant 2\,\Gamma$ converge more rapidly than the intermediate values, for $T = 0.05\,\Gamma$. For the larger values of T used below the calculations are even easier, as one can achieve a very good mapping $\underline{\Delta}_{\mathrm{aux}}(\omega) \approx \underline{\Delta}_{\mathrm{ph}}(\omega)$ already for less than $N_B = 12$.

After this benchmark, we now study the steady state nonequilibrium spectral properties for two different temperatures, one below and one above the Kondo temperature. In Fig. 4 results are presented for $T = 0.05\,\Gamma$ and in Fig. 5 for $T = 0.5\,\Gamma$. In the first case, it is apparent that small bias voltages $\phi < \Gamma$ cause a decrease and smearing of the Kondo peak, whereas larger voltages result in a splitting; see also Refs. [41–45,64,68–70]. It is known that with increasing current, resonant spin-flip scattering is prevented due to decoherence. Despite this, distinct excitations are clearly visible even at rather high bias voltages and located approximately at the positions of the chemical potentials $\mu_{L/R} = \pm\frac{\phi}{2}$. This can be attributed to intralead processes, which however are strongly suppressed. In Fig. 4 we present furthermore the

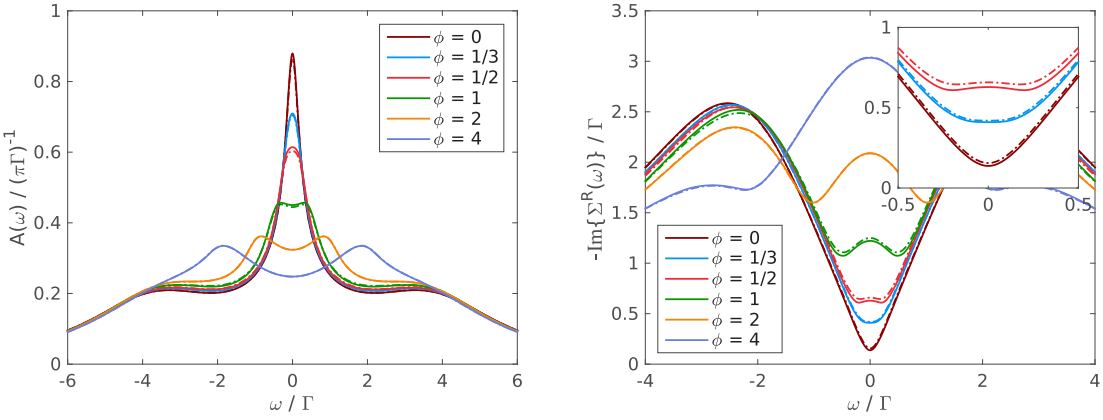

FIG. 4. (Color online) Bias-dependent spectral function (left) and retarded self-energy (right) for $T = 0.05\,\Gamma$. Solid lines correspond to calculations with $N_B = 16$ and dash-dotted lines to $N_B = 14$, but in many cases they cannot be distinguished. Bias voltage ϕ is given in units of Γ. Results are for $U = 6\,\Gamma$ and flat band leads, Eq. (11), with $D = 10\,\Gamma$.

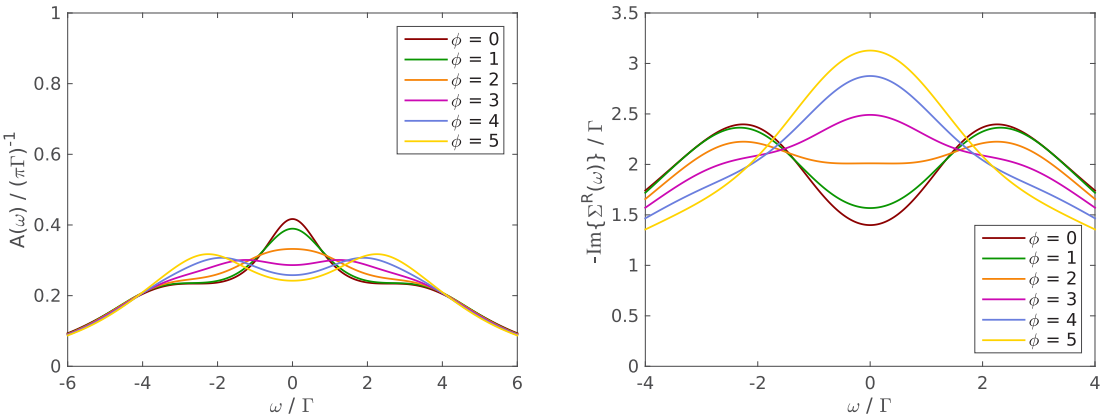

FIG. 5. (Color online) Bias-dependent spectral function (left) and retarded self-energy (right) for $T = 0.5\,\Gamma$. Calculations are performed with $N_B = 10$ and other parameters are the same as in Fig. 4.

retarded self-energy, which enables us to better locate at which ϕ value splitting sets in. An upper bound can be estimated by the value $\phi = 0.5\,\Gamma$, where $-\mathrm{Im}\{\Sigma^R(\omega)\}$ exhibits two minima. In Sec. III C we resolve the physics at low bias in some more detail.

In Fig. 5 the same system is considered for $T = 0.5\,\Gamma$. As expected, the features are much broader and the Kondo peak for $\phi = 0$ is strongly suppressed [126]. Despite this, one can still note splitting and weak excitations at $\mu_{L/R} = \pm\frac{\phi}{2}$ at rather high voltages $\phi \gtrsim 3\,\Gamma$. In $-\mathrm{Im}\{\Sigma^R(\omega)\}$, only the result for $\phi = 2\,\Gamma$ exhibits two slight minima. One can thus infer that the temperature dominates the decoherence processes on the impurity in this case and excitations at $\mu_{L/R}$ are further suppressed and strongly smeared out.

For both temperatures $T = 0.05\,\Gamma$ and $T = 0.5\,\Gamma$, we present two observables of interest, the double occupancy and the current, in Fig. 6. The latter is obtained from the standard Meir-Wingreen expression [83,127,128]. In the current it is obvious that the temperature strongly influences the low bias regime, as is expected from linear response considerations. Especially the differential conductance enables us to resolve the low bias physics and we find a typical Kondo behavior [57,58]. At higher voltages $\phi \gtrsim 2\,\Gamma$, however, one observes for $T = 0.05\,\Gamma$ a slight increase of $\partial j/\partial\phi$ due to charge fluctuations. At even higher voltages ($\phi \gtrsim 3\Gamma$) both temperatures result in a similar linear current-voltage characteristic since the two spectral functions nearly merge into each other. The double occupancy $\langle n_{f\uparrow} n_{f\downarrow}\rangle$ exhibits an interesting behavior for $T = 0.05\,\Gamma < T_K$. In this case, $\langle n_{f\uparrow} n_{f\downarrow}\rangle$ and thus the charge fluctuation as well exhibit a minimum (at $\phi \approx 2\,\Gamma$). It originates from two competing mechanisms evolving with increasing ϕ: On the one hand, the enlarged transport window, approximately given by the interval $(-\frac{\phi}{2}, \frac{\phi}{2})$, increases $\langle n_{f\uparrow} n_{f\downarrow}\rangle$, and on the other hand, the suppression of resonant spin-flip scattering has the opposite effect. Apparently, the latter dominates initially at low bias. We observe a similar behavior in the temperature dependence of the double occupancy $\langle n_{f\uparrow} n_{f\downarrow}\rangle_T$ in the equilibrium case. We find a minimum in $\langle n_{f\uparrow} n_{f\downarrow}\rangle_T$ at $T \approx 0.5\,\Gamma$. Therefore, the impurity is at this value in the local moment regime. When applying a bias voltage in the case of $T = 0.5\,\Gamma$, the double occupancy increases monotonically with ϕ, as can be seen in Fig. 6. One can therefore conclude that the Kondo effect and its suppression with increasing ϕ has a significant effect on

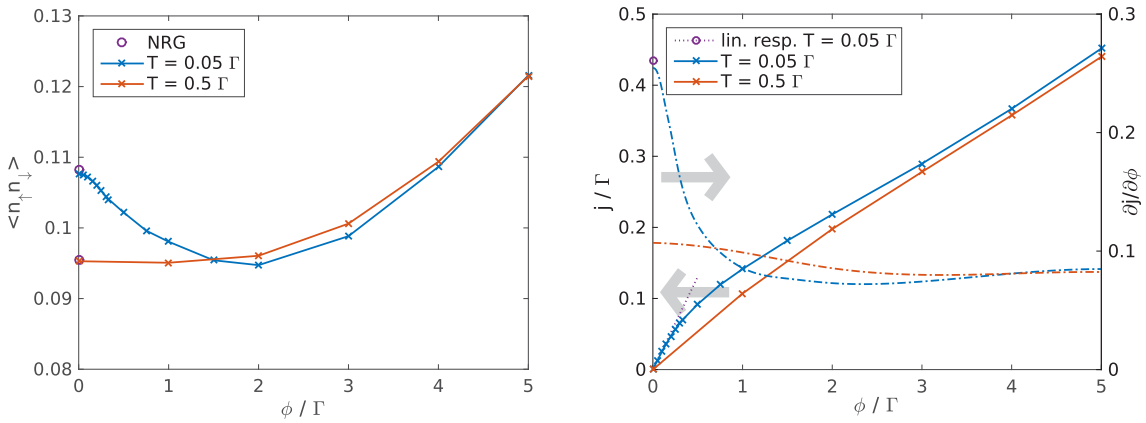

FIG. 6. (Color online) Double occupancy (left) and transport properties (right) as a function of bias voltage ϕ. Current j is depicted with solid lines and the differential conductance $\partial j/\partial\phi$ with dash-dotted lines. The latter is calculated with three-point Lagrange polynomials, based on the data for j as marked in the plot. Results are shown for $T = 0.5\,\Gamma$ with $N_B = 10$, and for $T = 0.05\,\Gamma$ with $N_B = 14$. Other parameters are as in Fig. 4. The linear response and equilibrium values for $\langle n_{f\uparrow} n_{f\downarrow}\rangle$ are from NRG [86].

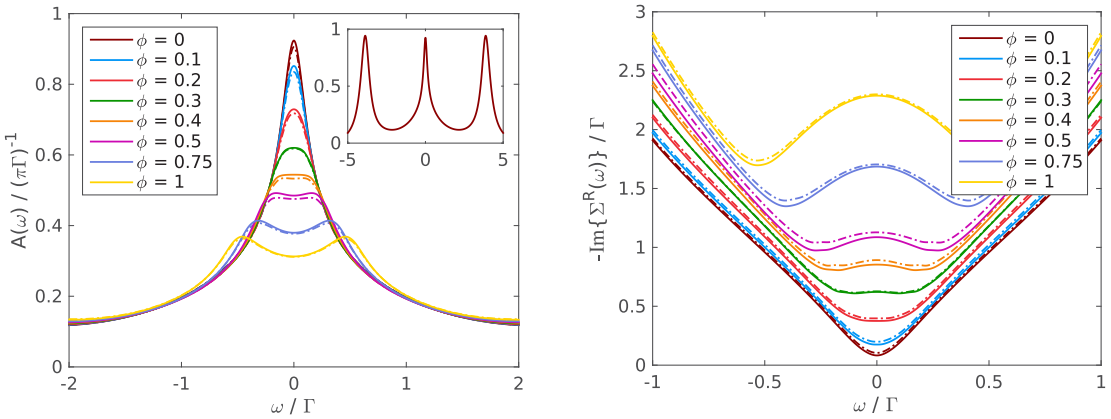

FIG. 7. (Color online) Bias-dependent spectral function (left) and retarded self-energy (right) for $U = 6\,\Gamma$, $T = 0.02\,\Gamma$, and a Lorentzian density of states in the leads; see Eq. (24). Solid lines correspond to calculations with $N_B = 16$ whereas dash-dotted lines to ones with $N_B = 14$. The bias voltage ϕ is in units of Γ. The inset on the left is for $N_B = 16$ and $\phi = 0$.

the double occupancy. However, the particular position of the minimum is not related to T_K but essentially only determined by the energy scale Γ, as discussed in Refs. [129,130]. The reliability of our results is corroborated by the close agreement for $\phi = 0$ with the equilibrium values obtained by NRG (marked by circles in Fig. 6).

C. Low bias spectrum

In order to better resolve the low-energy spectral properties of the Anderson impurity model, we now consider briefly the case of a Lorentzian density of states in the leads. In particular we replace Eq. (11) with

$$g^R_\lambda(\omega) = (\omega - \varepsilon_\lambda + i\gamma)^{-1}, \tag{24}$$

where $\varepsilon_{L/R} = \pm\frac{\phi}{2}$. This can be produced by a bath consisting of one site with on-site energy ε_λ which further connects to a wide band given by γ. We take $\Gamma = -\mathrm{Im}\{\Delta^R(0)\}$ again as unit of energy and choose $\gamma = 5/\pi\ \Gamma$ together with $2t'^2_\lambda/\gamma = \Gamma$. The Keldysh component is given by Eq. (2) with $\mu_{L/R} = \pm\frac{\phi}{2}$, as before.

A Lorentzian density of states is particularly suited for AMEA, since the retarded part $\Delta^R_{\mathrm{aux}}(\omega)$ alone can be fitted exactly with a single bath site. This simplification does not apply to the Keldysh component with its Fermi edges. Still, one can expect that the mapping procedure is more accurate than for a flat density of states and indeed we find that we are able to reproduce $\underline{\Delta}_{\mathrm{ph}}(\omega)$ by $\underline{\Delta}_{\mathrm{aux}}(\omega)$ more precisely for the same N_B. As a result, we can reach lower T with the same system sizes. For details on the achievable accuracy we refer to Appendix B.

In particular we investigate the case $T = 0.02\,\Gamma$ and $U = 6\,\Gamma$ and focus on bias voltages close to T_K. In addition to the lower temperature especially the smaller effective hybridization strength at the position of the Hubbard bands leads to an increased separation of Kondo and Hubbard features in the spectral function, and thus, to an improved resolution. This can be seen in the peaked structure of the inset in Fig. 7. The smaller temperature allows us to analyze the behavior for lower bias voltages down to $\phi = 0.1\,\Gamma$ [131]. Also for this setup we find a similar dependence of the spectrum as a function of voltage to that before, only at a decreased energy scale. The self-energy in Fig. 7 indicates that a splitting is first perceptible at a bias of $\phi \approx 0.2$–$0.3\,\Gamma$. From our data we can thus conclude that for bias voltages just above the Kondo temperature, a clear splitting of the Kondo resonance into a simple two-peak structure occurs.

IV. CONCLUSIONS

In this work we presented an improved formulation of AMEA, introduced in Refs. [35,36], obtained by employing matrix product states for the solution of the auxiliary master equation in the interacting case. This allowed us to treat larger auxiliary systems with more optimization parameters for the mapping procedure, as compared to the ED-based solver in Ref. [36]. This is crucial, since the accuracy in AMEA increases exponentially with the number of optimization parameters. As a result, we obtained well-converged spectral data and static observables, whose accuracy for the equilibrium case was comparable to NRG down to low temperatures and for large interactions. More specifically, in the calculations presented here, we were able to investigate the steady state properties of the single-impurity Anderson model as a function of bias voltage ϕ and at temperatures T well below the Kondo temperature T_K. In the spectral function we obtained a prominent Kondo peak for $\phi = 0$ and $T \approx T_K/4$, which compared very well to an equilibrium NRG calculation, and a broadening and subsequent splitting of the peak when considering $\phi > 0$. Also for the case of a Lorentzian density of states in the leads, which enabled us to lower the temperature to $T \approx T_K/10$, we found no evidence of a different behavior than a simple splitting of the Kondo peak. In order to locate the value of ϕ at which the peak starts to split, it was advantageous to inspect the retarded self-energy. From this we concluded that two excitations become visible for bias voltages just above the Kondo temperature, at $\phi \approx 1$–$2\,T_K$.

For the many-body solution with MPS it was of advantage to adjust the geometry of the auxiliary system and possible modifications were discussed. As in other studies of Lindblad problems with MPS, we found an increase of the bipartite entanglement entropy S with system size N_B [111]. However,

the increase was moderate and slower than linear, which made it possible to treat auxiliary open systems up to $N_B \approx 16$ reliably and within a rather short computation time (a couple of days). The value $N_B = 16$ is by no means a "hard limit" and much larger systems are expected to be feasible, especially when including additionally non-Abelian symmetries [106,107].

In general, the present MPS extension of AMEA constitutes a versatile and very accurate impurity solver for both equilibrium and nonequilibrium steady state situations. Compared to the ED-based solver presented in Ref. [36], the computation time is longer but the achievable accuracy is much higher. Therefore, the MPS impurity solver is especially suited for situations in which a high spectral resolution is needed and a detailed investigation of the underlying physics is desired.

ACKNOWLEDGMENTS

This work was supported by the Austrian Science Fund (FWF) within projects P24081, P26508, SFB-ViCoM F04103 and F04104, as well as by NaWi Graz. The calculations were partly performed on the D-cluster Graz and on the VSC-3 cluster Vienna. M.G. acknowledges support by the Simons Foundation (Many Electron Collaboration) and by Perimeter Institute for Theoretical Physics. We are grateful to Frauke Schwarz, Jan von Delft, and Andreas Weichselbaum, as well as Sabine Andergassen, Martin Nuss, Markus Aichhorn, Marko Znidaric, Ulrich Schollwöck, and Valentin Zauner for fruitful discussion. Furthermore, the authors want to thank Rok Žitko for providing his open source code NRG Ljubljana [86].

APPENDIX A: MULTIDIMENSIONAL OPTIMIZATION

In order to achieve $\underline{\Delta}_{\rm aux}(\omega) \approx \underline{\Delta}_{\rm ph}(\omega)$, we optimize the bath parameters $\boldsymbol{E}$, $\boldsymbol{\Gamma}^{(1)}$, and $\boldsymbol{\Gamma}^{(2)}$. For this a suitable parametrization is chosen, which yields a unique set of matrices $\boldsymbol{E}$, $\boldsymbol{\Gamma}^{(1)}$, and $\boldsymbol{\Gamma}^{(2)}$ for every parameter vector $\boldsymbol{x}$. The mean-squared error is quantified by a cost function

$$\mathcal{C}(\boldsymbol{x})^2 = \sum_{\alpha\in\{R,K\}} \int_{-\omega_c}^{\omega_c} \mathrm{Im}\left\{\Delta^{\alpha}_{\rm ph}(\omega) - \Delta^{\alpha}_{\rm aux}(\omega;\boldsymbol{x})\right\}^2 W(\omega) d\omega, \tag{A1}$$

with a certain cutoff ω_c and weighting $W(\omega)$, which we take to be constant in the present paper.

A variety of strategies exists to find the optimal parameter set $\boldsymbol{x}_{\rm opt}$ which minimizes a cost function as stated above. In previous work, Ref. [36], we employed a gradient-based method with a large number of random starting points. Such a deterministic minimization works well for rather small problems, but becomes inefficient in the higher-dimensional case $\dim(\boldsymbol{x}) \gtrsim 20$. It is then of great advantage to employ methods which are able to overcome local minima. Appropriate Monte Carlo (MC) sampling based methods are for instance simulated annealing, multicanonical simulations, or parallel tempering (PT) [132–137]. Especially a feedback-optimized version of the latter has proven to be useful for our purposes. For details we refer to Refs. [135,136] and in the following we outline only briefly the implementation as used in this work.

In PT, also called replica exchange, one regards $\mathcal{C}(\boldsymbol{x})$ as an artificial energy, defines a set of artificial inverse temperatures β_m, and samples for each temperature from the Boltzmann distribution $p^m(\boldsymbol{x}) = 1/Z_m \exp[-\mathcal{C}(\boldsymbol{x})\beta_m]$. A replica $\boldsymbol{x}_1^m$ is assigned to each β_m and updated through a Markov chain with the Metropolis-Hastings algorithm [138]. These MC sweeps generate a sequence of $\boldsymbol{x}_l^m$, $l = 1,2,\ldots$, which are distributed according to $p^m(\boldsymbol{x})$. In addition, a swapping of replicas $\boldsymbol{x}_l^m$ and $\boldsymbol{x}_l^{m+1}$ for neighboring inverse temperatures β_m and β_{m+1} is proposed after a certain number of sweeps. Again, a Metropolis probability is used for the swaps,

$$q_l^{m,m+1} = \min\left(1, \exp\left[\Delta\mathcal{C}_l^m(\beta_m - \beta_{m+1})\right]\right), \tag{A2}$$

with $\Delta\mathcal{C}_l^m = [\mathcal{C}(\boldsymbol{x}_l^m) - \mathcal{C}(\boldsymbol{x}_l^{m+1})]$. The set of β_m in PT has the purpose that the low temperatures enable an efficient sampling of regions where $\mathcal{C}(\boldsymbol{x})$ is small and the exchange with higher temperatures avoids trapping in local minima. To allow for an expedient exchange of replicas, the set of β_m needs to be adjusted. For our purposes we chose a feedback strategy which shifts the values β_m in order to achieve that the swapping probability Eq. (A2) becomes constant with respect to m. This strategy may not be the best possible choice in general, cf. Ref. [137], but enables a fast feedback and quickly adjusts to large changes in the values $\mathcal{C}(\boldsymbol{x}_l^m)$. In addition, we modified $q_l^{m,m+1} \to \max(q_l^{m,m+1}, q_{\rm th})$ with a certain threshold probability ($q_{\rm th} \approx 0.1$), to avoid that during a PT run a separation into several temperature sets occurs, which do not exchange replicas efficiently. This may violate balance conditions for thermodynamic observables but does not affect the applicability to minimization problems. For the other PT parameters we proceeded in the following way: In a single sweep each coordinate of $\boldsymbol{x}_l^m$ was updated once and 10 sweeps were performed before attempting a swap. Around 20–30 inverse temperatures β_m were used.

In general, one cannot expect to find the optimal solution in a nontrivial high-dimensional problem, but with the PT algorithm as outlined above we obtain an $\boldsymbol{x}_{\rm min}$ which minimizes the cost function locally and may furthermore fulfill $\mathcal{C}(\boldsymbol{x}_{\rm min}) \approx \mathcal{C}(\boldsymbol{x}_{\rm opt})$ to good approximation. For the largest

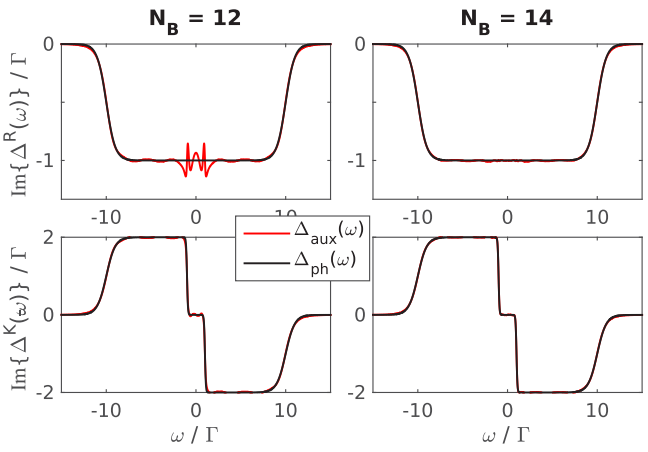

FIG. 8. (Color online) Hybridization function $\underline{\Delta}_{\rm aux}(\omega)$ as obtained from minimizing the cost function Eq. (A1) with $\omega_c = 15\,\Gamma$ and $W(\omega) = 1$, for the flat band model Eqs. (10), (11) with $\phi = 2\,\Gamma$ and $T = 0.05\,\Gamma$. Results on the left are for $N_B = 12$ and on the right for $N_B = 14$.

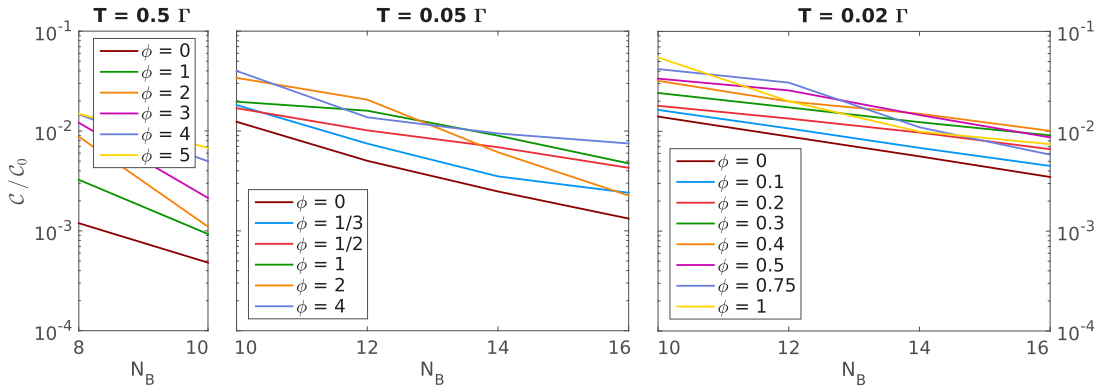

FIG. 9. (Color online) Convergence of $\underline{\Delta}_{\text{aux}}(\omega)$ with increasing N_B. Results with $T = 0.5\,\Gamma$ and $T = 0.05\,\Gamma$ are for the flat band case Eqs. (10), (11), and the ones with $T = 0.02\,\Gamma$ are for the Lorentzian density of states Eq. (24). For the cost function $\mathcal{C}$, Eq. (A1), we chose $W(\omega) = 1$ as well as $\omega_c = 15\,\Gamma$ for the flat band model and $\omega_c = 5\,\Gamma$ for the Lorentzian case. The normalization $\mathcal{C}_0$ refers to the value of $\mathcal{C}$ for $\underline{\Delta}_{\text{aux}}(\omega) \equiv 0$.

systems considered in this work, $N_B \gtrsim 14$, a good starting point was found to be important. For the case of tridiagonal $\boldsymbol{E}$, $\boldsymbol{\Gamma}^{(1)}$, and $\boldsymbol{\Gamma}^{(2)}$, a convenient choice is to make use of $\boldsymbol{x}_{\min}$ from the next smaller system with $N_B - 2$.

APPENDIX B: CONVERGENCE AS A FUNCTION OF N_B

Figure 8 depicts two typical results of the optimization described in Appendix A, for $N_B = 12$ and $N_B = 14$. It is apparent that rapid convergence is achieved when increasing N_B. For low temperatures T we find that the biggest error in $\underline{\Delta}_{\text{aux}}(\omega)$ occurs in the retarded component at the positions of the chemical potentials $\mu_{L/R} = \pm\frac{\phi}{2}$; see $N_B = 12$. This is a consequence of optimizing $\Delta^R_{\text{aux}}(\omega)$ and $\Delta^K_{\text{aux}}(\omega)$ simultaneously. For higher temperatures, for instance $T = 0.5\,\Gamma$, this effect is much less pronounced.

A brief analysis of the convergence behavior of the mapping procedure with increasing N_B is given in Fig. 9. We present values of the cost function $\mathcal{C}$, Eq. (A1), for different temperatures and bias voltages. In general one finds an exponential convergence $\mathcal{C} \propto \exp(-rN_B)$ to good approximation and the higher the temperature, the higher the rate of convergence r. By averaging over results for different ϕ we estimate a scaling of $r \propto T^{\frac{1}{4}}$. One can deduce from the order of magnitude of $\mathcal{C}$ that the calculations presented for $A(\omega)$ at $T = 0.02\,\Gamma$ (Fig. 7) are not converged to the same accuracy as the ones at $T = 0.05\,\Gamma$ (Fig. 4) or $T = 0.5\,\Gamma$ (Fig. 5), and larger systems with $N_B \gtrsim 20$ would be needed. However, the accuracy is comparable to the $N_B = 12$ results for $T = 0.05\,\Gamma$, which already yielded qualitative correct behavior and quite accurate spectral data; see also Figs. 3 and 10. The influence of ϕ is nonmonotonic and strongly dependent on the particular density of states in the leads. For the situations considered in this work we find the tendency that larger ϕ result in larger values of $\mathcal{C}$. For a more detailed analysis of the scaling with temperature and the mapping procedure in general we refer to Ref. [94].

For the flat band case with $T = 0.05\,\Gamma$ we present a more thorough investigation by comparing the spectral function in the interacting case $U = 6\,\Gamma$ for different numbers of bath sites in Fig. 10. As can be anticipated from the cost function $\mathcal{C}$ in Fig. 9, the cases $\phi = 1/3\,\Gamma$ and $\phi = 2\,\Gamma$ are well converged for $N_B = 16$, which manifests itself also in $A(\omega)$. The case $\phi = \Gamma$ exhibits larger values of $\mathcal{C}$ and one can note more significant changes in $A(\omega)$. Interestingly, rather high values of $\mathcal{C}$ are obtained for $\phi = 4\,\Gamma$, but nevertheless, the spectral function converges nicely. As discussed above for Fig. 8, the largest errors in $\underline{\Delta}_{\text{aux}}(\omega)$ correspond to short-scaled oscillations in $\Delta^R_{\text{aux}}(\omega)$. These errors are likely to be averaged out once the spectral function exhibits rather broad features. This is exactly

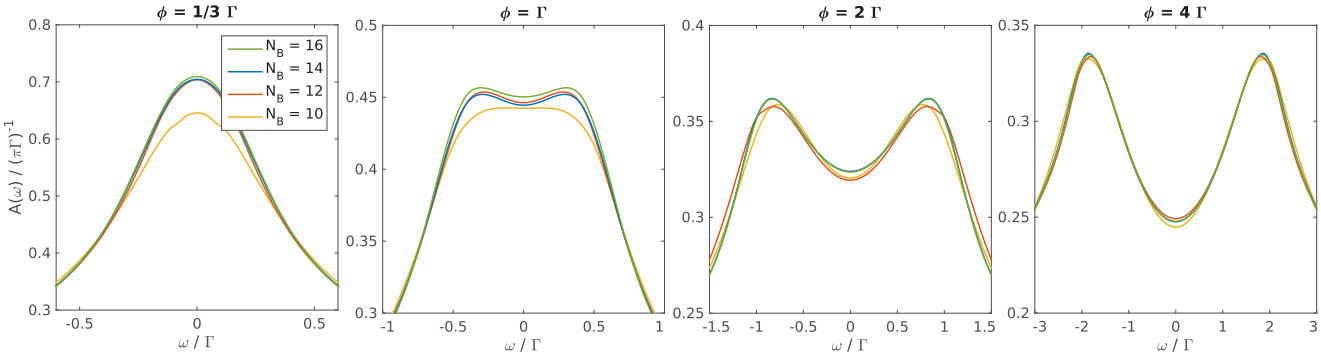

FIG. 10. (Color online) Convergence of the spectral function as depicted in Fig. 3 with increasing N_B, i.e., for the flat band model with $U = 6\,\Gamma$ and $T = 0.05\,\Gamma$.

the case for higher bias voltages where the Kondo effect is strongly suppressed. On the whole, when inspecting Fig. 10 and also Fig. 3, one can note a slightly nonsmooth convergence with N_B, especially close to the Kondo regime for low ϕ. This can be accounted for by abrupt changes of spectral weight in $\Delta^R_{\mathrm{aux}}(\omega)$ around $\omega = 0$, when changing N_B. One possibility to suppress this effect is to adjust the weighting function $W(\omega)$ in Eq. (A1) accordingly. However, this is most probably only of importance when aiming to achieve even higher accuracies in $A(\omega)$ and with the choice $W(\omega) = 1$, one can regard the calculations presented in this work as unbiased and accurate over the whole ω domain.

[1] P. W. Anderson, Phys. Rev. **124**, 41 (1961).
[2] J. Kondo, Prog. Theor. Phys. **32**, 37 (1964).
[3] J. R. Schrieffer and P. A. Wolff, Phys. Rev. **149**, 491 (1966).
[4] W. de Haas, J. de Boer, and G. van dën Berg, Physica **1**, 1115 (1934).
[5] A. H. Wilson, *The Theory of Metals* (Cambridge University Press, Cambridge, 1953).
[6] M. P. Sarachik, E. Corenzwit, and L. D. Longinotti, Phys. Rev. **135**, A1041 (1964).
[7] A. C. Hewson, *The Kondo Problem to Heavy Fermions* (Cambridge University Press, Cambridge, 1993).
[8] R. Bulla, T. A. Costi, and T. Pruschke, Rev. Mod. Phys. **80**, 395 (2008).
[9] P. W. Anderson, J. Phys. C: Solid State Phys. **3**, 2436 (1970).
[10] K. G. Wilson, Rev. Mod. Phys. **47**, 773 (1975).
[11] D. Goldhaber-Gordon, H. Shtrikman, D. Mahalu, D. Abusch-Magder, U. Meirav, and M. A. Kastner, Nature (London) **391**, 156 (1998).
[12] W. G. v. d. Wiel, S. D. Franceschi, T. Fujisawa, J. M. Elzerman, S. Tarucha, and L. P. Kouwenhoven, Science **289**, 2105 (2000).
[13] S. De Franceschi, R. Hanson, W. G. van der Wiel, J. M. Elzerman, J. J. Wijpkema, T. Fujisawa, S. Tarucha, and L. P. Kouwenhoven, Phys. Rev. Lett. **89**, 156801 (2002).
[14] R. Leturcq, L. Schmid, K. Ensslin, Y. Meir, D. C. Driscoll, and A. C. Gossard, Phys. Rev. Lett. **95**, 126603 (2005).
[15] S. De Franceschi and W. G. van der Wiel, in *Handbook of Nanophysics: Nanoparticles and Quantum Dots*, edited by K. D. Sattler (CRC, Boca Raton, FL, 2010), pp. 646–664.
[16] G. Cuniberti, G. Fagas, and K. Richter, *Introducing Molecular Electronics* (Springer, Berlin and Heidelberg, 2005).
[17] N. Agrait, A. L. Yeyati, and J. M. van Ruitenbeek, Phys. Rep. **377**, 81 (2003).
[18] R. H. M. Smit, Y. Noat, C. Untiedt, N. D. Lang, M. C. van Hemert, and J. M. van Ruitenbeek, Nature (London) **419**, 906 (2002).
[19] J. Park, A. N. Pasupathy, J. I. Goldsmith, C. Chang, Y. Yaish, J. R. Petta, M. Rinkoski, J. P. Sethna, H. D. Abruna, P. L. McEuen *et al.*, Nature (London) **417**, 722 (2002).
[20] W. Liang, M. P. Shores, M. Bockrath, J. R. Long, and H. Park, Nature (London) **417**, 725 (2002).
[21] W. Metzner and D. Vollhardt, Phys. Rev. Lett. **62**, 324 (1989).
[22] A. Georges and G. Kotliar, Phys. Rev. B **45**, 6479 (1992).
[23] A. Georges, G. Kotliar, W. Krauth, and M. J. Rozenberg, Rev. Mod. Phys. **68**, 13 (1996).
[24] G. Kotliar, S. Y. Savrasov, K. Haule, V. S. Oudovenko, O. Parcollet, and C. A. Marianetti, Rev. Mod. Phys. **78**, 865 (2006).
[25] D. Vollhardt, Ann. Phys. **524**, 1 (2012).
[26] E. Gull, A. J. Millis, A. I. Lichtenstein, A. N. Rubtsov, M. Troyer, and P. Werner, Rev. Mod. Phys. **83**, 349 (2011).
[27] J. K. Freericks, V. M. Turkowski, and V. Zlatić, Phys. Rev. Lett. **97**, 266408 (2006).
[28] P. Schmidt and H. Monien, arXiv:cond-mat/0202046.
[29] H. Aoki, N. Tsuji, M. Eckstein, M. Kollar, T. Oka, and P. Werner, Rev. Mod. Phys. **86**, 779 (2014).
[30] S. Okamoto, Phys. Rev. B **76**, 035105 (2007).
[31] S. Okamoto, Phys. Rev. Lett. **101**, 116807 (2008).
[32] A. V. Joura, J. K. Freericks, and T. Pruschke, Phys. Rev. Lett. **101**, 196401 (2008).
[33] M. Eckstein, M. Kollar, and P. Werner, Phys. Rev. Lett. **103**, 056403 (2009).
[34] C. Gramsch, K. Balzer, M. Eckstein, and M. Kollar, Phys. Rev. B **88**, 235106 (2013).
[35] E. Arrigoni, M. Knap, and W. von der Linden, Phys. Rev. Lett. **110**, 086403 (2013).
[36] A. Dorda, M. Nuss, W. von der Linden, and E. Arrigoni, Phys. Rev. B **89**, 165105 (2014).
[37] I. Titvinidze, A. Dorda, W. von der Linden, and E. Arrigoni arXiv:1508.02953.
[38] S. Andergassen, V. Meden, H. Schoeller, J. Splettstoesser, and M. R. Wegewijs, Nanotechnology **21**, 272001 (2010).
[39] S. Hershfield, Phys. Rev. Lett. **70**, 2134 (1993).
[40] P. Mehta and N. Andrei, Phys. Rev. Lett. **96**, 216802 (2006).
[41] N. S. Wingreen and Y. Meir, Phys. Rev. B **49**, 11040 (1994).
[42] E. Lebanon and A. Schiller, Phys. Rev. B **65**, 035308 (2001).
[43] A. Rosch, J. Kroha, and P. Wölfle, Phys. Rev. Lett. **87**, 156802 (2001).
[44] J. König, J. Schmid, H. Schoeller, and G. Schön, Phys. Rev. B **54**, 16820 (1996).
[45] T. Fujii and K. Ueda, Phys. Rev. B **68**, 155310 (2003).
[46] S. Smirnov and M. Grifoni, Phys. Rev. B **84**, 125303 (2011).
[47] S. Smirnov and M. Grifoni, New J. Phys. **15**, 073047 (2013).
[48] C. Jung, A. Lieder, S. Brener, H. Hafermann, B. Baxevanis, A. Chudnovskiy, A. Rubtsov, M. Katsnelson, and A. Lichtenstein, Ann. Phys. **524**, 49 (2012).
[49] E. Muñoz, C. J. Bolech, and S. Kirchner, Phys. Rev. Lett. **110**, 016601 (2013).
[50] A. Rosch, J. Paaske, J. Kroha, and P. Wölfle, Phys. Rev. Lett. **90**, 076804 (2003).
[51] N. Shah and A. Rosch, Phys. Rev. B **73**, 081309 (2006).
[52] S. Kehrein, Phys. Rev. Lett. **95**, 056602 (2005).
[53] P. Fritsch and S. Kehrein, Phys. Rev. B **81**, 035113 (2010).
[54] R. Gezzi, T. Pruschke, and V. Meden, Phys. Rev. B **75**, 045324 (2007).
[55] S. G. Jakobs, M. Pletyukhov, and H. Schoeller, Phys. Rev. B **81**, 195109 (2010).
[56] R. B. Saptsov and M. R. Wegewijs, Phys. Rev. B **86**, 235432 (2012).
[57] M. Pletyukhov and H. Schoeller, Phys. Rev. Lett. **108**, 260601 (2012).
[58] F. Reininghaus, M. Pletyukhov, and H. Schoeller, Phys. Rev. B **90**, 085121 (2014).
[59] S. Andergassen, D. Schuricht, M. Pletyukhov, and H. Schoeller, AIP Conf. Proc. **1633**, 213 (2014).

[60] F. Heidrich-Meisner, A. E. Feiguin, and E. Dagotto, Phys. Rev. B **79**, 235336 (2009).

[61] A. Holzner, I. P. McCulloch, U. Schollwöck, J. von Delft, and F. Heidrich-Meisner, Phys. Rev. B **80**, 205114 (2009).

[62] M. Nuss, M. Ganahl, H. G. Evertz, E. Arrigoni, and W. von der Linden, Phys. Rev. B **88**, 045132 (2013).

[63] M. Nuss, M. Ganahl, E. Arrigoni, W. von der Linden, and H. G. Evertz, Phys. Rev. B **91**, 085127 (2015).

[64] F. B. Anders, Phys. Rev. Lett. **101**, 066804 (2008).

[65] S. Schmitt and F. B. Anders, Phys. Rev. Lett. **107**, 056801 (2011).

[66] A. Jovchev and F. B. Anders, Phys. Rev. B **87**, 195112 (2013).

[67] P. Werner, T. Oka, M. Eckstein, and A. J. Millis, Phys. Rev. B **81**, 035108 (2010).

[68] J. E. Han and R. J. Heary, Phys. Rev. Lett. **99**, 236808 (2007).

[69] G. Cohen, E. Gull, D. R. Reichman, and A. J. Millis, Phys. Rev. Lett. **112**, 146802 (2014).

[70] M. Nuss, C. Heil, M. Ganahl, M. Knap, H. G. Evertz, E. Arrigoni, and W. von der Linden, Phys. Rev. B **86**, 245119 (2012).

[71] J. Paaske, A. Rosch, J. Kroha, and P. Wölfle, Phys. Rev. B **70**, 155301 (2004).

[72] A. Kaminski, Y. V. Nazarov, and L. I. Glazman, Phys. Rev. Lett. **83**, 384 (1999).

[73] P. Coleman, C. Hooley, and O. Parcollet, Phy. Rev. Lett. **86**, 4088 (2001).

[74] A. Oguri, J. Phys. Soc. Jpn. **74**, 110 (2005).

[75] E. Sela and J. Malecki, Phys. Rev. B **80**, 233103 (2009).

[76] A. Rosch, Eur. Phys. J. B **85**, 6 (2012).

[77] E. Gull, D. R. Reichman, and A. J. Millis, Phys. Rev. B **82**, 075109 (2010).

[78] A. Dirks, P. Werner, M. Jarrell, and T. Pruschke, Phys. Rev. E **82**, 026701 (2010).

[79] J. Schwinger, J. Math. Phys. **2**, 407 (1961).

[80] L. P. Kadanoff and G. Baym, *Quantum Statistical Mechanics: Green's Function Methods in Equilibrium and Nonequilibrium Problems* (Addison-Wesley, Redwood City, CA, 1962).

[81] L. V. Keldysh, Zh. Eksp. Teor. Fiz. **47**, 1515 (1964) [Sov. Phys. - JETP **20**, 1018 (1965)].

[82] J. Rammer and H. Smith, Rev. Mod. Phys. **58**, 323 (1986).

[83] H. Haug and A.-P. Jauho, *Quantum Kinetics in Transport and Optics of Semiconductors* (Springer, Heidelberg, 1998).

[84] M. Wagner, Phys. Rev. B **44**, 6104 (1991).

[85] We estimate T_K based on a NRG calculation. [86]. A common definition related to the linear response conductance $G(T)$ is used: $G(T_K) = G(0)/2$ [8, 87, 88].

[86] All numerical renormalization group (NRG) calculations were performed with the open source code NRG Ljubljana; see http://nrgljubljana.ijs.si.

[87] Ž. Osolin and R. Žitko, Phys. Rev. B **87**, 245135 (2013).

[88] M. Hanl and A. Weichselbaum, Phys. Rev. B **89**, 075130 (2014).

[89] $[A,B]$ denotes the commutator and $\{A,B\}$ the anticommutator of A and B.

[90] As in previous work [36], we set all couplings in $\Gamma^{(1)}$ and $\Gamma^{(2)}$ which connect the impurity site to zero. This ensures that $\underline{\Delta}_{\text{aux}}(\omega)$ approaches zero for $\omega \to \pm\infty$.

[91] H.-P. Breuer and F. Petruccione, *The Theory of Open Quantum Systems* (Oxford University Press, Oxford, 2002).

[92] G. Schaller, *Open Quantum Systems Far from Equilibrium* (Springer, New York, 2014).

[93] M. Nuss, G. Dorn, A. Dorda, W. von der Linden, and E. Arrigoni, Phys. Rev. B **92**, 125128 (2015).

[94] E. Arrigoni *et al.* (unpublished).

[95] A. A. Dzhioev and D. S. Kosov, J. Chem. Phys. **134**, 044121 (2011).

[96] M. Schmutz, Z. Phys. B. **30**, 97 (1978).

[97] The "tilde conjugation rules" [95] are here $c_j |I\rangle = -i\tilde{c}_j |I\rangle$ and $c_j^\dagger |I\rangle = -i\tilde{c}_j^\dagger |I\rangle$.

[98] Steady state correlation functions for the case $t < 0$ can be obtained via $\langle A(t)B\rangle_\infty^\dagger = \langle I| B^\dagger e^{-Lt} A^\dagger |\rho_\infty\rangle$.

[99] F. A. Wolf, I. P. McCulloch, and U. Schollwöck, Phys. Rev. B **90**, 235131 (2014).

[100] U. Schollwöck, Ann. Phys. **326**, 96 (2011).

[101] G. Vidal, Phys. Rev. Lett. **93**, 040502 (2004).

[102] S. R. White and A. E. Feiguin, Phys. Rev. Lett. **93**, 076401 (2004).

[103] M. Zwolak and G. Vidal, Phys. Rev. Lett. **93**, 207205 (2004).

[104] T. Barthel, U. Schollwöck, and S. R. White, Phys. Rev. B **79**, 245101 (2009).

[105] C. Karrasch, J. H. Bardarson, and J. E. Moore, Phys. Rev. Lett. **108**, 227206 (2012).

[106] I. P. McCulloch, J. Stat. Mech.: Theory Exp. (2007) P10014.

[107] A. Weichselbaum, Ann. Phys. **327**, 2972 (2012).

[108] T. Prosen and M. Žnidarič, Phys. Rev. B **86**, 125118 (2012).

[109] T. Prosen and M. Znidaric, J. Stat. Mech.: Theory Exp. (2009) P02035.

[110] L. Bonnes, D. Charrier, and A. M. Läuchli, Phys. Rev. A **90**, 033612 (2014).

[111] L. Bonnes and A. M. Läuchli, arXiv:1411.4831.

[112] J. Cui, J. I. Cirac, and M. C. Bañuls, Phys. Rev. Lett. **114**, 220601 (2015).

[113] E. Mascarenhas, H. Flayac, and V. Savona, Phys. Rev. A **92**, 022116 (2015).

[114] F. Verstraete, J. J. García-Ripoll, and J. I. Cirac, Phys. Rev. Lett. **93**, 207204 (2004).

[115] A. H. Werner, D. Jaschke, P. Silvi, T. Calarco, J. Eisert, and S. Montangero, arXiv:1412.5746.

[116] The MPS matrices for the first and the last site are row and column vectors to be precise.

[117] For the second-order splitting we used in particular the method of Strang (also known as Trotter-Suzuki) and of McLachlan [118–120], where the latter was advantageous.

[118] G. Strang, SIAM J. Numer. Anal. **5**, 506 (1968).

[119] R. I. McLachlan and P. Atela, Nonlinearity **5**, 541 (1992).

[120] X. Wang and H.-G. Matuttis, J. Phys. Soc. Jpn. **81**, 104002 (2012).

[121] The particular initial state is not of importance, only the appropriate half filling of the system in order to arrive at $|\rho_\infty\rangle$. A convenient choice is to use $|I\rangle$, for instance.

[122] Note that in the particle-hole symmetric case it is sufficient to calculate a single Green's function $G^<$ or $G^>$.

[123] It was even found that the relative error saturates over time. This is likely due to the exponential damping of excited states $c_{i\sigma}^{(\dagger)} |\rho_\infty\rangle$ and the resulting contraction.

[124] D. C. Langreth, Phys. Rev. **150**, 516 (1966).

[125] J. S. Langer and V. Ambegaokar, Phys. Rev. **121**, 1090 (1961).

[126] T. A. Costi, Phys. Rev. Lett. **85**, 1504 (2000).
[127] Y. Meir and N. S. Wingreen, Phys. Rev. Lett. **68**, 2512 (1992).
[128] A.-P. Jauho (2006), https://nanohub.org/resources/1877.
[129] A. Dirks, S. Schmitt, J. E. Han, F. Anders, P. Werner, and T. Pruschke, Europhys. Lett. **102**, 37011 (2013).
[130] J. E. Han, A. Dirks, and T. Pruschke, Phys. Rev. B **86**, 155130 (2012).
[131] $T = 0.02\,\Gamma$ is small enough to observe two distinct "Fermi edges" in $\Delta^K_{\rm aux}(\omega)$ already for $\phi = 0.1\,\Gamma$ ($\lessapprox T_K$).
[132] S. Kirkpatrick, C. D. Gelatt, and M. P. Vecchi, Science **220**, 671 (1983).
[133] B. A. Berg, in *Monte Carlo Methods*, edited by N. N. Madras, *Fields Institute Communications*, Vol. 26 (American Mathematical Society, Providence, 2000), p. 1.
[134] J. Lee and M. Y. Choi, Phys. Rev. E **50**, R651 (1994).
[135] K. Hukushima and K. Nemoto, J. Phys. Soc. Jpn. **65**, 1604 (1996).
[136] D. J. Earl and M. W. Deem, Phys. Chem. Chem. Phys. **7**, 3910 (2005).
[137] H. G. Katzgraber, S. Trebst, D. A. Huse, and M. Troyer, J. Stat. Mech.: Theory Exp. (2006) P03018.
[138] B. A. Berg, *Introduction to Markov Chain Monte Carlo Simulations and their Statistical Analysis* (World Scientific Publishing Company, Singapore, 2005), Chap. 1, pp. 1–52.

3.3. Publication 3: DMFT

3.3.1. Preamble

The article titled *Transport through a correlated interface: Auxiliary master equation approach* was published in Physical Review B, **92**, 245125, December 2015 [3].

This work was carried out by Irakli Titvinidze (IT) as first author and Antonius Dorda (AD) as co-author, supervised by Wolfgang von der Linden (WL), and Enrico Arrigoni (EA). EA guided the work to great extent and participated actively in its realization. IT wrote a DMFT-code for a general setup of multiple correlated layers attached to two leads, whereby translational invariance in the transverse direction was assumed. AD assisted in its C++ implementation and rewrote the ED-solver in order to include it in DMFT. Specifically, AD made use of the core routines for the manybody solution from the first work Ref. [1], Sec. 3.1, but the steady state solution was implemented in a faster and more stable way by making use of Krylov space methods for the time evolution as well. For the mapping procedure the parallel tempering approach from Ref. [2], Sec. 3.2, was included and the needed ED-setups for the auxiliary system were implemented. On the whole, an automated C++ code for the ED-solver was written by AD, appropriate for an inclusion within DMFT. AD and IT together did a testing, debugging and optimization of the different routines. IT then performed the major part of the calculations and investigations. Furthermore, IT wrote a first paper draft which AD, EA and WL revised and expanded. All authors contributed to deciding on the route of investigation and to the discussion of results.

3.3.2. Original article

(see next page)

PHYSICAL REVIEW B **92**, 245125 (2015)

Transport through a correlated interface: Auxiliary master equation approach

Irakli Titvinidze,* Antonius Dorda, Wolfgang von der Linden, and Enrico Arrigoni
Institute of Theoretical and Computational Physics, Graz University of Technology, 8010 Graz, Austria
(Received 25 August 2015; published 21 December 2015)

We present improvements of a recently introduced numerical method [E. Arrigoni *et al.*, Phys. Rev. Lett. **110**, 086403 (2013)] to compute steady-state properties of strongly correlated electronic systems out of equilibrium. The method can be considered as a nonequilibrium generalization of exact diagonalization based dynamical mean-field theory (DMFT). The key modification for the nonequilibrium situation consists in addressing the DMFT impurity problem within an auxiliary system consisting of the correlated impurity, N_b uncorrelated bath sites, and two Markovian environments (sink and reservoir). Algorithmic improvements in the impurity solver allow to treat efficiently larger values of N_b than previously in DMFT. This increases the accuracy of the results and is crucial for a correct description of the physical behavior of the system in the relevant parameter range including a semiquantitative description of the Kondo regime. To illustrate the approach, we consider a monoatomic layer of correlated orbitals, described by the single-band Hubbard model, attached to two metallic leads. The nonequilibrium situation is driven by a bias voltage applied to the leads. For this system, we investigate the spectral function and the steady-state current-voltage characteristics in the weakly as well as in the strongly interacting limit. In particular, we investigate the nonequilibrium behavior of quasiparticle excitations within the Mott gap of the correlated layer. We find for low-bias voltage Kondo-type behavior in the vicinity of the insulating phase. In particular, we observe a splitting of the Kondo resonance as a function of the bias voltage.

DOI: 10.1103/PhysRevB.92.245125 PACS number(s): 71.27.+a, 47.70.Nd, 73.40.−c, 05.60.Gg

I. INTRODUCTION

The recent impressive experimental progress in tailoring different microscopically controlled quantum objects has prompted increasing interest in correlated systems out of equilibrium. Of particular importance are correlated heterostructures [1–6], quantum wires [7] and quantum dots [8,9] with atomic resolution, experiments in ultracold-atomic gases in optical lattices [10–14], as well as ultrafast laser spectroscopy [15–18].

The theoretical description and understanding of these experiments in particular and of complex strongly correlated systems in general presents major challenges to theoretical solid-state physics. For this purpose, different theoretical approaches have been developed. *For the equilibrium situation*, one of the most powerful methods is dynamical mean-field theory (DMFT) [19–21], which is a comprehensive, thermodynamically consistent, and nonperturbative scheme. The only approximation in DMFT is the locality of the self-energy, which becomes exact in infinite dimensions, but usually it is a good approximation for two and three spatial dimensions. The key point of DMFT is to map the original problem onto a single-impurity Anderson model (SIAM) [22] whose parameters are determined self-consistently. For this purpose, several classes of so-called impurity solvers were developed. Among them, the most powerful methods are the numerical renormalization group (NRG) approach [23–25], quantum Monte Carlo (QMC) [26–29], and exact diagonalization (ED) [30,31].

Prompted by the success of DMFT for equilibrium systems, the approach was extended [32–38] to deal with time-dependent problems within the nonequilibrium Green's function approach originating from the works of Kubo [39], Schwinger [40], Kadanoff and Baym [41,42], and Keldysh [43]. Similar to the equilibrium case, also nonequilibrium DMFT is based on the solution of an appropriate (nonequilibrium) SIAM. Despite the fact that many approaches have been suggested to solve such impurity problems (see, e.g., Refs. [32,35,36,38,44–59]), not all of them are suited for nonequilibrium DMFT. In addition, many of these are only reliable for short times and cannot treat long time behavior and accurately describe the steady state. Therefore, developing a nonperturbative impurity solver, which can treat reliably the steady-state behavior of the SIAM is quite a challenge.

The nonequilibrium approach, that will be presented in this paper, has its roots in the exact diagonalization (ED)-based DMFT (ED-DMFT). In equilibrium ED-DMFT, one replaces the infinite bath by an auxiliary finite noninteracting electronic chain whose parameters are determined by a fit to the DMFT hybridization function Δ. This cannot be trivially extended to the steady-state situation. First of all, due to the fact that the auxiliary system is finite, there is no dissipation and a proper steady state is never reached. An additional technical aspect is that the spectrum of the auxiliary system is discrete and, therefore, the fit in real frequencies is problematic. But, only in the equilibrium case one can circumvent this problem by introducing a fit in Matsubara space [60]. A possible solution to these problems was suggested by us in Refs. [61,62] with an approach which enables direct access to the steady-state properties of the correlated impurity problem. The basic idea is that in addition to a finite number of bath sites coupled to the impurity, as in equilibrium ED, two Markovian environments are introduced, which act as particle sink and reservoir. This auxiliary model represents an open quantum system with dissipative dynamics, which allows to properly describe steady-state situations. The behavior of this auxiliary nonequilibrium impurity problem is described by a Lindblad master equation, which can be solved exactly by numerical

*irakli.titvinidze@tugraz.at

approaches such as full diagonalization [61], non-Hermitian Krylov space [62], or matrix product state (MPS) methods [63]. Its solution allows to determine both the retarded and the Keldysh self-energies, which are required by the DMFT loop, with high accuracy. Here, in particular, we apply the Krylov space approach of Ref. [62] to solve the DMFT impurity problem. This yields a much better accuracy than in Ref. [61], which allows us to resolve the splitting of the quasiparticle resonance as a function of the bias voltage.

The paper is organized as follows: In Sec. II A we shortly introduce the Hamiltonian of the system, while in Secs. II B and II C we give an overview over steady-state DMFT within the nonequilibrium Green's function formalism. In Sec. II D we discuss the auxiliary master equation approach, with focus on details of our implementation. Afterwards, in Sec. III we present our results for a simple correlated interface. In particular, in Sec. III A we benchmark the accuracy, while in Secs. III B and III C the steady-state current and spectral functions are investigated, respectively. Finally, in Sec. IV we give concluding remarks and an outlook.

II. MODEL AND METHOD

A. Model

To illustrate the approach, we consider a minimalistic model for transport across a correlated interface (see Fig. 1), which consists of a correlated infinite and transitionally invariant layer (c), with local Hubbard interaction U, onsite energy $\varepsilon_c = -U/2$, and nearest-neighbor hopping amplitude t_c, sandwiched between two semi-infinite metallic leads ($\alpha = l,r$), with onsite energies ε_α and nearest-neighbor hopping amplitudes t_α. The leads are semi-infinite and translationally invariant in the xy plane (parallel to the correlated layer). The hybridization between lead α and the correlated layer is v_α (see Fig. 1). A bias voltage Φ is applied between the leads. The Hamiltonian reads as

$$\mathcal{H} = \mathcal{H}_c + \sum_{\alpha=l,r} \mathcal{H}_\alpha + \mathcal{H}_{\text{coup}}. \tag{1}$$

Here,

$$\mathcal{H}_c = -t_c \sum_{\langle ij\rangle,\sigma} c^\dagger_{i\sigma} c_{j\sigma} + U \sum_i n_{i\uparrow} n_{i\downarrow} + \varepsilon_c \sum_{i,\sigma} n_{i\sigma} \tag{2}$$

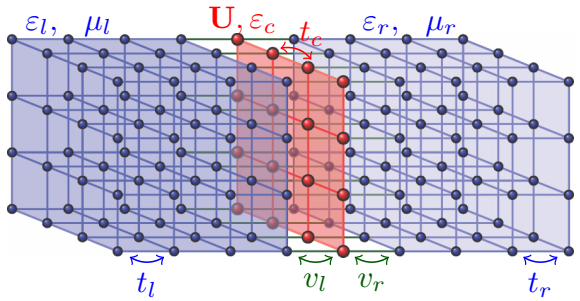

FIG. 1. (Color online) Schematic representation of the system, consisting of the correlated layer (red) with local Hubbard interaction U and onsite energy ε_c, sandwiched between two semi-infinite metallic leads (blue), with onsite energies ε_l and ε_r, respectively. The hopping between neighboring sites of the correlated layer is t_c, while the one for the left (right) lead is t_l (t_r). Hybridization between the left (right) lead and the correlated layer is v_l (v_r). A bias voltage $\Phi = \mu_l - \mu_r$ is applied between the leads.

describes the correlated layer. $\langle i,j\rangle$ stands for neighboring i and j sites, $c^\dagger_{i,\sigma}$ creates an electron at the ith site of the correlated layer with spin $\sigma = \uparrow,\downarrow$ and $n_{i\sigma} = c^\dagger_{i\sigma} c_{i\sigma}$ denote the corresponding occupation-number operators. The leads are described by the Hamiltonian

$$\mathcal{H}_\alpha = -t_\alpha \sum_{\langle ij\rangle,\sigma} c^\dagger_{\alpha i\sigma} c_{\alpha j\sigma} + \varepsilon_\alpha \sum_{i\sigma} c^\dagger_{\alpha i\sigma} c_{\alpha i\sigma}. \tag{3}$$

Here, $c^\dagger_{\alpha i\sigma}$ creates an electron at ith site of the lead α. An applied bias voltage Φ shifts the energies ε_α and chemical potentials μ_α of the leads in opposite directions by the amount $\Phi/2$. Finally,

$$\mathcal{H}_{\text{coup}} = -\sum_{\langle ij\rangle,\alpha,\sigma} v_\alpha (c^\dagger_{i\sigma} c_{\alpha j\sigma} + \text{H.c.}) \tag{4}$$

describes the hybridization between the correlated layer and leads. The hopping v_α takes place between neighboring sites of the lead and the correlated layer.

Previously similar models with many correlated layers were also investigated in Refs. [37,38,64,65]. In Refs. [37,38] steady-state behavior, while in Refs. [64,65] full time evolution were investigated. For this purpose, the authors used DMFT (Refs. [37,38,64]) and time-dependent Gutzwiller approximation (Ref. [65]). In Refs. [37,38] the impurity problem is treated by an equation-of-motion approach with a suitable decoupling scheme for the higher-order Green's functions, while in Ref. [64] the noncrossing approximation is invoked. On the other hand, our treatment of the impurity solver is controlled and can achieve extremely accurate results [63] with a moderate number of bath sites.

B. Steady-state nonequilibrium Green's functions

We consider an initial situation in which at times $\tau < 0$ the leads are disconnected from the correlated layer and all three parts of the system (l, c, r) are in equilibrium with different values for the chemical potential $\mu_l = \varepsilon_l$, $\mu_c = \varepsilon_c$, and $\mu_r = \varepsilon_r$, respectively.

Due to the fact that the system is transitionally invariant in the xy plane, it is more convenient to perform a Fourier transformation and express the Green's functions in terms of the momentum $\mathbf{k}_\parallel = (k_x,k_y)$. The retarded equilibrium Green's function for the disconnected noninteracting central layer reads as

$$g^R_0(\omega,\mathbf{k}_\parallel) = \frac{1}{\omega + i0^+ - \varepsilon_c - E_c(\mathbf{k}_\parallel)}, \tag{5}$$

with $E_c(\mathbf{k}_\parallel) = -2t_c(\cos k_x + \cos k_y)$. On the other hand, the Green's functions for the edge layers of the left ($\alpha = l$) and the right ($\alpha = r$) lead, when they are disconnected from the central layer can be expressed as [66–68]

$$g^R_\alpha(\omega,\mathbf{k}_\parallel) = \frac{\omega - \varepsilon_\alpha - E_\alpha(\mathbf{k}_\parallel)}{2t_\alpha^2} - i\frac{\sqrt{4t_\alpha^2 - [\omega - \varepsilon_\alpha - E_\alpha(\mathbf{k}_\parallel)]^2}}{2t_\alpha^2}, \tag{6}$$

with $E_\alpha(\mathbf{k}_\parallel) = -2t_\alpha(\cos k_x + \cos k_y)$. The sign of the square root for negative argument must be chosen such that the

Green's function has the correct $1/\omega$ behavior for $|\omega| \to \infty$. To investigate the system out of the equilibrium, we need to work within the Keldysh Green's function formalism [40,42,43,69,70]. Therefore, as a starting point, we need the corresponding noninteracting, disconnected Keldysh components. Since the disconnected systems are separately in equilibrium, we can obtain these from the retarded ones via the fluctuation dissipation theorem [69]

$$g^K_\alpha(\omega,\mathbf{k}_\parallel) = 2i[1-2f_\alpha(\omega)]\ \mathrm{Im}\, g^R_\alpha(\omega,\mathbf{k}_\parallel)\,. \tag{7}$$

Here, $f_\alpha(\omega)$ is the Fermi distribution for chemical potential μ_α and temperature T_α. For the noninteracting isolated central layer, the inverse Keldysh Green's function $[\underline{g}_0^{-1}(\omega,\mathbf{k}_{||})]^K$ is infinitesimal and can be neglected in a steady state in which the layer is connected to the leads. In our notation, we use an underline to denote block matrices within the nonequilibrium Green's function (Keldysh) formalism:

$$\underline{X} = \begin{pmatrix} X^R & X^K \\ 0 & X^A \end{pmatrix} \tag{8}$$

with $X^A = (X^R)^\dagger$. At time $\tau = 0$, the leads get connected to the correlated layer. After a sufficiently long time, a steady state is reached. The latter is expected to exist and to be unique unless the system has bound states. Our goal is to investigate its properties under the bias voltage Φ.

Since the steady state is time-translation invariant, we can Fourier transform in time and express all Green's functions in terms of a real frequency ω. The Green's function for the correlated layer, when connected with the leads, can be expressed via Dyson's equation

$$\underline{G}^{-1}(\omega,\mathbf{k}_\parallel) = \underline{G}_0^{-1}(\omega,\mathbf{k}_\parallel) - \underline{\Sigma}(\omega,\mathbf{k}_\parallel)\,, \tag{9}$$

where $\underline{\Sigma}(\omega,\mathbf{k}_\parallel)$ is the self-energy of the correlated layer. The Green's function of the noninteracting nonequilibrium system $\underline{G}_0(\omega,\mathbf{k}_\parallel)$ in turn can be expressed as

$$\underline{G}_0^{-1}(\omega,\mathbf{k}_\parallel) = \underline{g}_0^{-1}(\omega,\mathbf{k}_\parallel) - \sum_{\alpha=l,r} v_\alpha^2 \underline{g}_\alpha(\omega,\mathbf{k}_\parallel), \tag{10}$$

where $\underline{g}_0(\omega,\mathbf{k}_\parallel)$ is the Green's function of the noninteracting decoupled layer, i.e., $U = 0, v_\alpha = 0$ and the components of the Green's function of the isolated leads $\underline{g}_\alpha(\omega,\mathbf{k}_\parallel)$ are given in Eqs. (6) and (7). Note that all quantities are underscored, i.e., they are Keldysh block matrices.

C. Dynamical mean-field theory

As usual, to obtain the self-energy $\underline{\Sigma}(\omega,\mathbf{k}_\parallel)$ is the difficult step in the calculation of $\underline{G}(\omega,\mathbf{k}_\parallel)$ and of various steady-state properties of the system. As there is no closed expression for it, one has to resort to some approximation. Here, we employ DMFT [19–21,32,33,37,61] in its nonequilibrium, time-independent version. In this approach, the self-energy is approximated by a local quantity $\underline{\Sigma}(\omega,\mathbf{k}_\parallel) = \underline{\Sigma}(\omega)$ which can be determined by solving a (nonequilibrium) quantum impurity model with the same Hubbard interaction U and onsite energy ε_c coupled to a self-consistently determined bath. The latter is specified by its hybridization function obtained as

$$\underline{\Delta}(\omega) = \underline{g}_0^{-1}(\omega) - \underline{G}_{\mathrm{loc}}^{-1}(\omega) - \underline{\Sigma}(\omega), \tag{11}$$

where $\underline{g}_0^{-1}(\omega)$ is the noninteracting Green's function of the disconnected impurity (i.e., of a single correlated site) and

$$\underline{G}_{\mathrm{loc}}(\omega) = \int_{\mathrm{BZ}} \frac{d\mathbf{k}_\parallel}{(2\pi)^2} \underline{G}(\omega,\mathbf{k}_\parallel). \tag{12}$$

The self-consistent DMFT loop works similarly to the equilibrium case, except that in the present case the Green's functions are 2×2 block matrices [33,37,38]: One starts with an initial guess for the self-energy $\underline{\Sigma}(\omega)$, then based on Eqs. (5)–(12) calculates the bath hybridization function $\underline{\Delta}(\omega)$. We then evaluate the corresponding auxiliary Green's functions $\underline{G}_{\mathrm{aux},0}(\omega)$ and $\underline{G}_{\mathrm{aux}}(\omega)$, in the noninteracting and in the interacting case, respectively. The solution of the impurity problem is, as usual, the bottleneck of DMFT. Our scheme consists, as outlined in detail in Sec. II D, in replacing the impurity problem with an auxiliary one, which is as close as possible to the one described by (11) but is exactly solvable by numerical methods. The self-consistent loop is then closed by determining the new value of the self-energy

$$\underline{\Sigma}(\omega) = \underline{G}^{-1}_{\mathrm{aux},0}(\omega) - \underline{G}^{-1}_{\mathrm{aux}}(\omega). \tag{13}$$

We repeat this procedure until convergence is reached, i.e., until $\underline{G}_{\mathrm{aux}}(\omega) \approx \underline{G}_{\mathrm{loc}}(\omega)$ [71].

D. Impurity solver: Auxiliary master equation approach

As already mentioned, the main obstacle of DMFT is the solution of the impurity problem. One widespread approach to approximate its solution for the equilibrium case is ED-DMFT, whereby one replaces the infinite bath with an auxiliary finite one. However, this approach cannot be used straightforwardly in a nonequilibrium steady-state case, as this cannot be described correctly with a finite number of sites [62]. One way to overcome this problem, as some of us already suggested in Refs. [61,62], is to introduce, in addition to the finite number N_b of bath sites which are coupled to the impurity in the form of two chain segments, two Markovian environments, which can be seen as a particle sink and reservoir, respectively (see Fig. 2). This makes the impurity model effectively infinitely large, which is necessary in order to be able to reach a steady state. Our strategy, similar to the equilibrium ED-DMFT case, is to choose the parameters of the auxiliary model so as to provide an optimal fit to the bath hybridization function (11).

The dynamics of this auxiliary impurity model is described by the Lindblad quantum master equation, which controls the time (τ) dependence of the reduced density matrix ρ of the

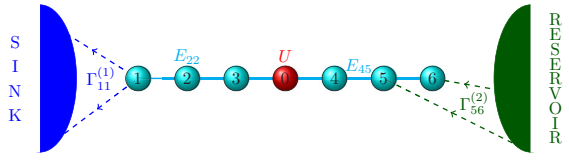

FIG. 2. (Color online) Sketch of the auxiliary open quantum impurity problem consisting of the impurity site at position $i = 0$ (red circle), $N_b = 6$ bath sites (cyan circles), and two Markovian environments sink (blue) and reservoir (green). Parameters E_{ij} and Γ_{ij} are explained in the main text.

model [72,73]

$$\frac{d}{d\tau}\rho = \mathcal{L}\rho, \tag{14}$$

where

$$\mathcal{L} = \mathcal{L}_H + \mathcal{L}_D \tag{15}$$

is a Lindblad superoperator, which consists of two terms: a unitary contribution $\mathcal{L}_H$ and a dissipative one $\mathcal{L}_D$.

The unitary contribution

$$\mathcal{L}_H\rho = -i[\mathcal{H}_{\rm aux},\rho] \tag{16}$$

is generated by the auxiliary Hamiltonian

$$\mathcal{H}_{\rm aux} = \sum_{i,j=0,\sigma}^{N_b} E_{ij} d^\dagger_{i\sigma} d_{j\sigma} + U\, n^d_{0\uparrow} n^d_{0\downarrow}, \tag{17}$$

where $d^\dagger_{i\sigma}$ creates a particle with spin σ at the impurity ($i = 0$) or at a bath site ($i = 1,\ldots,N_b$). $n^d_{0\sigma} = d^\dagger_{0\sigma} d_{0\sigma}$ is the occupation number operator for particles at the impurity site with spin σ. $E_{00} = \varepsilon_c$, while all other E_{ij} are parameters used to fit $\underline{\Delta}(\omega)$, whereby one can restrict to onsite and nearest-neighbor (NN) terms only (see Fig. 2). The nonunitary (dissipative) term

$$\mathcal{L}_D\rho = 2\sum_{i,j=0}^{N_b}\sum_{\sigma}\left[\Gamma^{(1)}_{ij}\left(d_{i\sigma}\rho\, d^\dagger_{j\sigma} - \frac{1}{2}\{\rho, d^\dagger_{j\sigma} d_{i\sigma}\}\right) + \Gamma^{(2)}_{ij}\left(d^\dagger_{j\sigma}\rho\, d_{i\sigma} - \frac{1}{2}\{\rho, d_{i\sigma} d^\dagger_{j\sigma}\}\right)\right] \tag{18}$$

describes the coupling to a Markovian environment. The dissipation matrices $\mathbf{\Gamma}^{(\kappa)}, \kappa = 1,2$ (with matrix elements $\Gamma^{(\kappa)}_{ij}$), are Hermitian and positive semidefinite [72] and are again used as fit parameters. In order to fix the large-ω behavior of $\underline{\Delta}$, all $\Gamma^{(\kappa)}_{ij}$ with at least one index on the impurity must vanish. On the other hand, in contrast to $\mathbf{E}$, $\mathbf{\Gamma}^{(\kappa)}$ are not restricted to NN terms. This is of great advantage for the fit, as discussed in Sec. III A.

To carry out the self-consistent DMFT loop, we need to evaluate both the noninteracting and the interacting Green's functions of the auxiliary model. First, the noninteracting calculation ($U = 0$), which is fast in comparison to the interacting one, produces the bath hybridization function $\underline{\Delta}_{\rm aux}(\omega)$ of the auxiliary impurity model, which is fitted to (11) in order to obtain the optimal parameters $\mathbf{E}$ and $\mathbf{\Gamma}^{(\kappa)}$. These are used in the interacting model in order to determine the self-energy $\underline{\Sigma}(\omega)$, which is then inserted in (9).

A convenient way to solve the auxiliary problem is to rewrite Eq. (14), expressed by superoperators, into a standard operator problem [74–77]. For this purpose, one enlarges the original Fock space, spanned by the operators ($d_{i,\sigma}/d^\dagger_{i,\sigma}$), by doubling the number of levels via so-called tilde operators $\tilde{d}_{i,\sigma}/\tilde{d}^\dagger_{i,\sigma}$. In addition, one introduces a so-called left vacuum

$$|I\rangle = \sum_S (-1)^{N_S} |S\rangle \otimes |\tilde{S}\rangle, \tag{19}$$

where $|S\rangle$ are many-body states of the original Fock space, $|\tilde{S}\rangle$ the corresponding ones of the tilde space [75], and N_S the number of particles in S. In this formalism, the reduced density operator is mapped onto the state vector

$$|\rho(\tau)\rangle = \rho|I\rangle, \tag{20}$$

and the Lindblad equation is mapped onto a Schrödinger-type equation [75]

$$\frac{d}{d\tau}|\rho(\tau)\rangle = L|\rho(\tau)\rangle, \tag{21}$$

where

$$L = L_0 + L_I \tag{22}$$

is an ordinary operator in the augmented space. Its noninteracting part L_0 reads as

$$iL_0 = \sum_\sigma (\mathbf{d}^\dagger_\sigma \mathbf{h} \mathbf{d}_\sigma - {\rm Tr}(\mathbf{E} + i\mathbf{\Lambda})), \tag{23}$$

where Tr denotes the matrix trace, and

$$\mathbf{d}^\dagger_\sigma = \left(d^\dagger_{0,\sigma},\ldots,d^\dagger_{N_b,\sigma},\tilde{d}_{0,\sigma},\ldots,\tilde{d}_{N_b,\sigma}\right) \tag{24}$$

is a vector of creation/annihilation operators and the matrix $\mathbf{h}$ is given by

$$\mathbf{h} = \begin{pmatrix} \mathbf{E} + \mathbf{i\Omega} & 2\mathbf{\Gamma}^{(2)} \\ -2\mathbf{\Gamma}^{(1)} & \mathbf{E} - i\mathbf{\Omega} \end{pmatrix} \tag{25}$$

with

$$\mathbf{\Lambda} = \mathbf{\Gamma}^{(2)} + \mathbf{\Gamma}^{(1)}, \quad \mathbf{\Omega} = \mathbf{\Gamma}^{(2)} - \mathbf{\Gamma}^{(1)}. \tag{26}$$

Its interacting part has the form

$$iL_I = U n_{0\uparrow} n_{0\downarrow} - U\tilde{n}_{0\uparrow}\tilde{n}_{0\downarrow}, \tag{27}$$

with $\tilde{n}_{0\sigma} := \tilde{d}^\dagger_{0\sigma}\tilde{d}_{0\sigma}$. To evaluate Green's functions, one needs to calculate expectation values of the form

$$G_{BA} = -i\,{\rm tr}_{\mathcal{U}}[B(\tau_2)A(\tau_1)\rho_{\mathcal{U}}(\tau_1)], \tag{28}$$

where $\rho_{\mathcal{U}}(\tau_1)$ is the density operator of the "universe" $\mathcal{U}$ composed of the "system" (the chain in Fig. 2) and the Markovian environment and ${\rm tr}_{\mathcal{U}} = {\rm tr} \otimes {\rm tr}_E$ is the trace over the "universe," which is the tensor product of the trace over the "system" (tr) and the trace over the environment (${\rm tr}_E$). After straightforward calculations, we obtain (more details see Ref. [62]) for the noninteracting retarded Green's function

$$\mathbf{G}^R_{{\rm aux},0} = (\omega - \mathbf{E} + i\mathbf{\Lambda})^{-1} \tag{29}$$

while its Keldysh part reads as

$$\mathbf{G}^K_{{\rm aux},0} = 2i\mathbf{G}^R_{{\rm aux},0}\mathbf{\Omega}\mathbf{G}^A_{{\rm aux},0}. \tag{30}$$

Therefore, we obtain the following expressions for the retarded auxiliary hybridization function

$$\Delta^R_{\rm aux} = \omega - \varepsilon_c - \frac{1}{[\mathbf{G}^R_{{\rm aux},0}]_{00}} \tag{31}$$

and its Keldysh part

$$\Delta^K_{\rm aux} = \frac{[\mathbf{G}^K_{{\rm aux},0}]_{00}}{|[\mathbf{G}^R_{{\rm aux},0}]_{00}|^2}. \tag{32}$$

Here, X_{00} denotes the 00 element (i.e., the one on the impurity) of the matrix $\mathbf{X}$.

To calculate the impurity Green's function for the interacting system, we use Krylov-space based exact diagonalization. A full diagonalization is prohibitive for $N_B \gtrsim 3$ due to the fact that the Hilbert space is exponentially large. Particle conservation translates here into conservation of $N_\sigma - \tilde{N}_\sigma$. To calculate the steady state $|\rho_\infty\rangle$ we use an Arnoldi time evolution [78], while for the calculation of Green's functions we employ the two-sided Lanczos algorithm [62].

To obtain the retarded and the Keldysh Green's functions, we use the following relations (for details see Ref. [62]):

$$\mathbf{G}^R = \mathbf{G}^{>+} + \mathbf{G}^{<+\dagger}, \tag{33}$$

$$\mathbf{G}^K = \mathbf{G}^{>+} + \mathbf{G}^{<+} - \text{H.c.} \tag{34}$$

The expressions for the greater and lesser Green's functions are [79]

$$G^{>+}_{\text{aux},ij\sigma}(\omega) = \sum_n \frac{\langle I|d_{i\sigma}|R_n^{(+1)}\rangle\langle L_n^{(+1)}|d^\dagger_{j\sigma}|\rho_\infty\rangle}{\omega - l_n^{(+1)}} \tag{35}$$

and

$$G^{<+}_{\text{aux},ij\sigma}(\omega) = \sum_n \frac{\langle I|d^\dagger_{i\sigma}|R_n^{(-1)}\rangle\langle L_n^{(-1)}|d_{j\sigma}|\rho_\infty\rangle}{\omega - l_n^{(-1)}}, \tag{36}$$

with the right ($|R_n^{(\pm1)}\rangle$) and left ($\langle L_n^{(\pm1)}|$) eigenstates and eigenvalues $l_n^{(\pm1)}$ of the operator L [Eq. (22)], in the sectors $N_\sigma - \tilde{N}_\sigma = \pm 1$.

Once self-consistency in the DMFT loop (cf. Sec. II C) is achieved, one can calculate desired physical quantities, e.g., the steady-state current. For this purpose, we use the Meir-Wingreen expression [69,80,81] in its symmetrized form, where summation over spin is implicitly assumed:

$$\begin{aligned} J = i \int_{\text{BZ}} \frac{d\mathbf{k}_\parallel}{(2\pi)^2} \int_{-\infty}^{\infty} \frac{d\omega}{2\pi} [&(\gamma_l(\omega,\mathbf{k}_\parallel) \\ &- \gamma_r(\omega,\mathbf{k}_\parallel))G^<(\omega,\mathbf{k}_\parallel) + (\bar{\gamma}_l(\omega,\mathbf{k}_\parallel) \\ &- \bar{\gamma}_r(\omega,\mathbf{k}_\parallel))(G^R(\omega,\mathbf{k}_\parallel) - G^A(\omega,\mathbf{k}_\parallel))], \end{aligned} \tag{37}$$

where $\gamma_\alpha(\omega,\mathbf{k}_\parallel) = -2v_\alpha^2 \text{Im}\, g_\alpha(\omega,\mathbf{k}_\parallel)$ and $\bar{\gamma}_\alpha(\omega,\mathbf{k}_\parallel) = f(\omega - \mu_\alpha)\gamma_\alpha(\omega,\mathbf{k}_\parallel)$.

III. RESULTS

Here, we present results for the steady-state properties of the system displayed in Fig. 1 consisting of a correlated layer, with Hubbard interaction U and onsite energy $\varepsilon_c = -U/2$, coupled to two metallic leads. We restrict to the particle-hole symmetric case. The hopping inside the correlated layer t_c is taken equal to 1 unless stated otherwise, while the hopping inside the leads is $t_l = t_r = 2.5$. The hybridizations between leads and the correlated layer are $v_l = v_r = 0.5$ and $2v_l$ is used as unit of energy. The applied bias voltage Φ enters the values of the onsite energies and the chemical potentials as $\varepsilon_{l/r} = \mu_{l/r} = \pm\Phi/2$. All results presented following are calculated for zero temperature in the leads ($T_l = T_r = 0$) [see Eq. (7)]. Similar models have been studied, e.g., in Refs. [37,38,65,82,83].

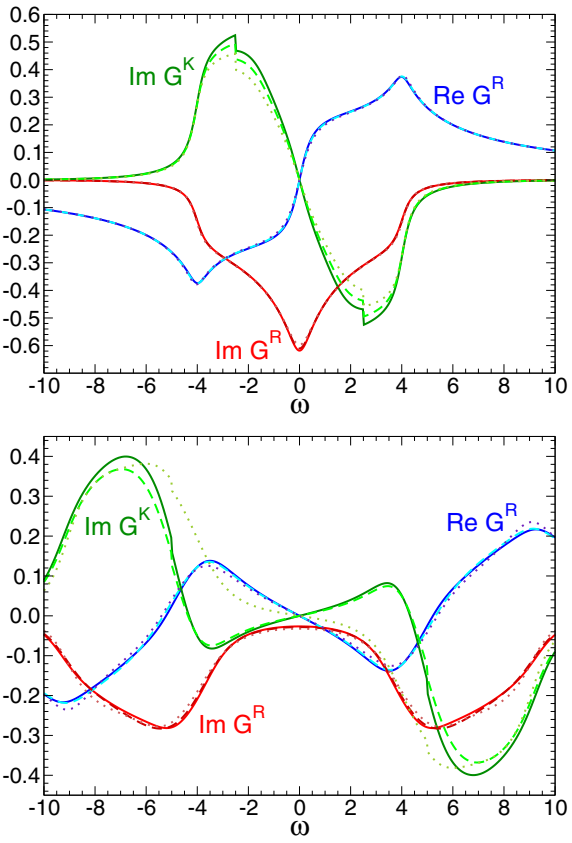

FIG. 3. (Color online) Retarded G^R and Keldysh G^K Green's functions for the correlated layer, for Hubbard interaction $U = 2$ and bias voltage $\Phi = 5$ (upper panel) and for $U = 12$ and $\Phi = 10$ (lower panel). Other parameters are $t_c = 1$, $t_l = t_r = 2.5$, $v_l = v_r = 0.5$ ($2v_l$ is our unit of energy). Solid, dashed, and dotted lines are obtained with $N_b = 6$, 4, and 2 correspondingly.

A. Convergence with respect to the number of auxiliary bath sites N_b

First, we investigate how the number of bath sites N_b of the auxiliary impurity problem influences the results. We compare calculations for the Green's functions (Fig. 3) and for the current (Fig. 4), obtained with $N_b = 2,4,6$. We find that the retarded component is well converged already for $N_b = 4$ even for $U = 12$. For the Keldysh Green's functions, the convergence in terms of N_b is reasonable, but not as fast as for the retarded Green's function. Correspondingly, it is not surprising that also the current voltage characteristics exhibit a fairly good convergence (see Fig. 4). On the whole, the convergence for weak interaction ($U = 2$) is faster than for strong interaction ($U = 12$).

These results indicate that $N_b = 4$ bath sites already produce reasonable results away from the Kondo regime. Therefore, in view of the exponential increase of the numerical effort with N_b, we mainly restrict the following discussion to $N_b = 4$. Only to discuss the low-energy Kondo physics we will present results with $N_b = 6$. The reason for the rapid convergence in N_b is due to the fact that the number of Lindblad parameters increases quadratically with N_b, in contrast to the

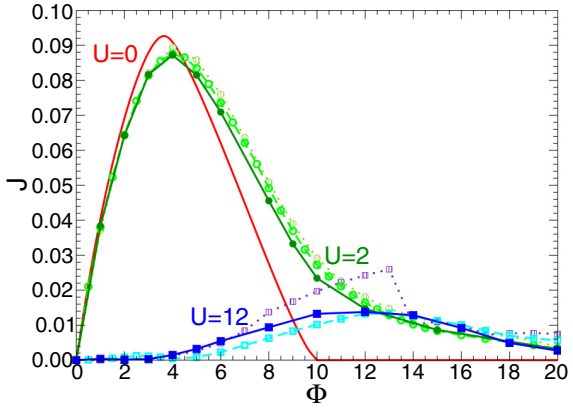

FIG. 4. (Color online) Current J vs bias voltage Φ for different U. The solid red curve represents the $U = 0$ result. The three curves peaked at about $\Phi = 4$ are for $U = 2$ and the remaining three curves show the $U = 12$ results. Solid, dashed, and dotted lines correspond to $N_b = 6$, 4, and 2, respectively. Other parameters are as in Fig. 3.

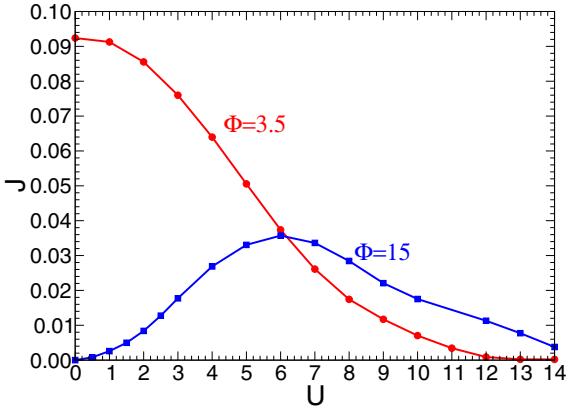

FIG. 5. (Color online) Current J vs interaction U for two values of Φ. Calculations are performed for $N_b = 4$. Other parameters are as in Fig. 3.

energy and hopping parameters $\mathbf{E}$. It is, thus, important, to consider also long-ranged $\mathbf{\Gamma}$ terms (cf. Ref. [62]).

B. Steady-state current

In this section, we discuss the steady-state current in detail. The results for the current as a function of bias voltage are presented in Fig. 4 for different values of the Hubbard interaction U. In the noninteracting case ($U = 0$), particles pass the interface without scattering and therefore the momentum $\mathbf{k}_\parallel$ is conserved. Correspondingly, the problem becomes one dimensional and the current vanishes for bias voltages larger than the one-dimensional bandwidth, i.e., for $W_z = 4t_{l/r} = 10$, which is corroborated by Fig. 4. For nonzero interaction different $\mathbf{k}_\parallel$ are mixed due to scattering and thus all states of the leads are possible final states. Subsequently, the current vanishes for bias voltages larger than the three-dimensional bandwidth, i.e., $W = 3W_z = 30$. In equilibrium, an isolated two-dimensional Hubbard layer is in the metallic phase for weak interaction. As can be seen from Fig. 4, in this case ($U = 2$) the current displays, as expected, a metallic behavior, i.e., a linear increase of the current for small voltages. The overall shape is similar to the $U = 0$ case, however, with a longer tail at large Φ due to the scattering mechanism discussed above. For strong interaction ($U = 12$), an isolated two-dimensional Hubbard layer is a Mott insulator, but in our model there is no insulating phase due to the hybridization to the noninteracting leads. Therefore, strictly speaking the current is always linear in Φ for $\Phi \to 0$. Nevertheless, due to the vicinity of the Mott insulator the current is strongly suppressed [84]. A similar behavior also was observed in Refs. [37,38]. On the other hand, for higher bias voltages ($\Phi \gtrsim 12$) the picture is reversed and the current is more suppressed for $U = 2$ than for $U = 12$.

We investigate this issue in detail and plot the current as a function of Hubbard interaction U for low ($\Phi = 3.5$) and high ($\Phi = 15$) bias voltage in Fig. 5. For the low-voltage case, we find a monotonic Gaussian decrease. The origin of the current reduction with increasing U are backscattering processes that reduce the transmission coefficient. For high-bias voltage, in the region where the current is zero for $U = 0$, the current first increases with increasing interaction, reaches its maximum at approximately $U \simeq 6$, and then decreases again [85]. Qualitatively, this can be explained by the fact that there are two competing effects as a function of U. On the one hand, with increasing U the transport increases due to scattering to different $\mathbf{k}_\parallel$ as discussed above, which enhances the current, but on the other hand, large U means increased backscattering which suppresses transport across the correlated layer. For high-bias voltages and weak interactions, the first effect dominates due to the finite bandwidth of the leads.

C. Nonequilibrium spectral function

To gain further insight into the properties of the steady state we also investigate the nonequilibrium spectral function, which can be calculated from the Green's function via $A(\omega) = -\frac{1}{\pi}\mathrm{Im}\, G^R(\omega)$. The results are shown in Fig. 6 for $U = 2$ and 12. For weak interaction ($U = 2$), the spectral function $A(\omega)$ displays for all bias voltages a peak at $\omega = 0$ and hardly visible Hubbard satellites at the approximate position $\omega = \pm U/2$. The spectral function for $U = 2$ [Fig. 6(a)] depends only very weakly on bias voltage. This is in contrast to the spectral density of the one-dimensional SIAM for which, it is found that, the Kondo peak splits up as a function of voltage and two resonances are observed at the corresponding chemical potentials of the two leads [46,55,62,86–94]. The difference between the two situations is that in the case of the single-impurity model, the resonance and the Hubbard subbands are clearly separated. In contrast, for the correlated layer and for the set of parameters considered here, when the isolated correlated layer is metallic, they overlap due to the broadening induced by the hopping t_c within the correlated layer. And, indeed if we artificially reduce t_c to 0.1 (keeping all other parameters fixed) we observe, for $\Phi = 0$ a resonance, which is clearly separated from the Hubbard subbands (cf. Fig. 7). In this case, the isolated layer would be insulating and the broadening of the resonance is not any more due to t_c, but to an effective energy scale T_K, which can be seen as

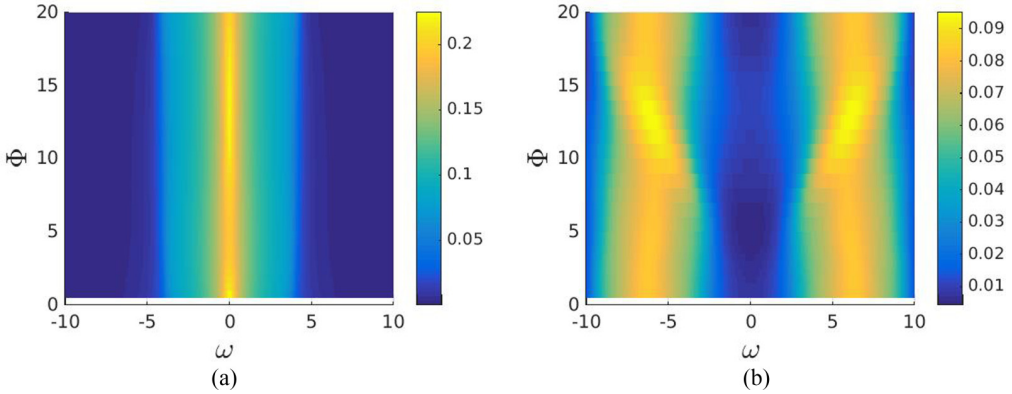

FIG. 6. (Color online) Single-particle spectral function for $N_b = 4$, different values of Φ, $U = 2$ (a), and $U = 12$ (b). Other parameters are as in Fig. 3.

a Kondo temperature. This originates from a combination of coherent scattering from the leads into the insulating layer, as well as from a self-consistent DMFT process as discussed in Ref. [95]. In addition to the broadening mentioned above, there is also a spurious broadening due to the limited accuracy of our calculation. Nevertheless, our resolution is sufficient in order to observe a splitting of the resonance into two peaks at $\mu_{l/r} = \pm V_B/2$ as a function of voltage as in the single-impurity case.

Now, we turn to strong interactions ($U = 12$), for which the results are depicted in Figs. 6(b) and 8. In equilibrium, i.e., for $\Phi = 0$, the hybridization with the leads produces a weak Kondo resonance at the Fermi energy ($\omega = 0$) [96]. A nonzero bias voltage splits the resonance into two peaks at $\mu_{l/r} = \pm\Phi/2$ (see Fig. 8). For $\Phi \gtrsim 3$, the peaks merge into the Hubbard subbands and the spectral function $A(\omega)$ consists of two Hubbard subbands at the approximate position $\omega = \pm U/2$, while $A(\omega = 0)$ is strongly suppressed. For these larger values of Φ, the effect of the bias voltage is small: it modifies only slightly the position and height of the Hubbard subbands. Notice that in order to resolve the Kondo peak and its splitting at low bias, we need to use an auxiliary system with $N_b = 6$. While this allows to resolve the peaks, the limited accuracy makes them broader than they should be and therefore the Friedel sum rule is not satisfied even for equilibrium. The reason for this is that a spurious broadening originating from the limitation of our approach reduces the height of the peak at the Fermi level [97]. To fulfill this, one would have to use more bath sites, and consequently adopt a matrix product state based solution of the auxiliary system, as we did in Ref. [63] for the Anderson impurity model. This, however, in combination with the DMFT self-consistency, would increase considerably the required computation time.

Next, we study the dependence on the Hubbard interaction U in more detail. Results for equilibrium ($\Phi = 0$), low- ($\Phi = 3.5$) and high- ($\Phi = 15$) bias voltages are presented in Fig. 9. As one can see, in the equilibrium case for large U only small excitations are visible at $\omega = 0$. Here, the Friedel sum rule would require the $\omega = 0$ peak to display a U-independent height [98]. However, as discussed above for large U, our approach cannot resolve T_k and the peak becomes strongly suppressed, and for intermediate U the sum rule is not satisfied, as for Fig. 8. Still, Fig. 9(a) displays a crossover from a regime in which the local Fermi liquid peak is already present in the isolated correlated layer (for U below the 2D Mott transition), into a Kondo-Fermi liquid regime in which the peak is produced by coherent spin-flip processes across the

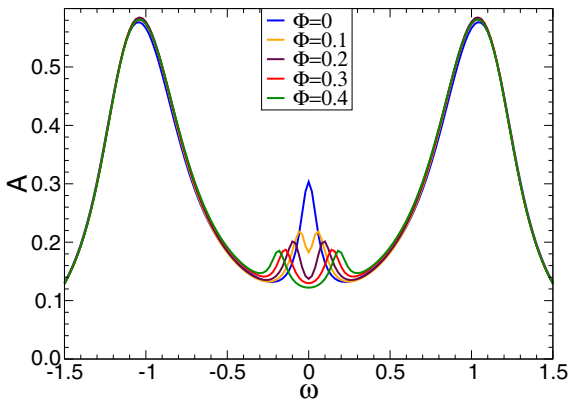

FIG. 7. (Color online) Single-particle spectral function for $N_b = 6$, $U = 2$, $t_c = 0.1$ and for different values of Φ. Other parameters are as in Fig. 3.

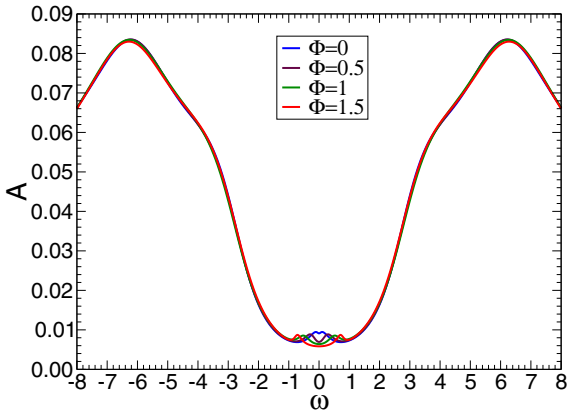

FIG. 8. (Color online) Single-particle spectral function for $N_b = 6$, $U = 12$, $t_c = 1$ and for different values of Φ. Other parameters are as in Fig. 3.

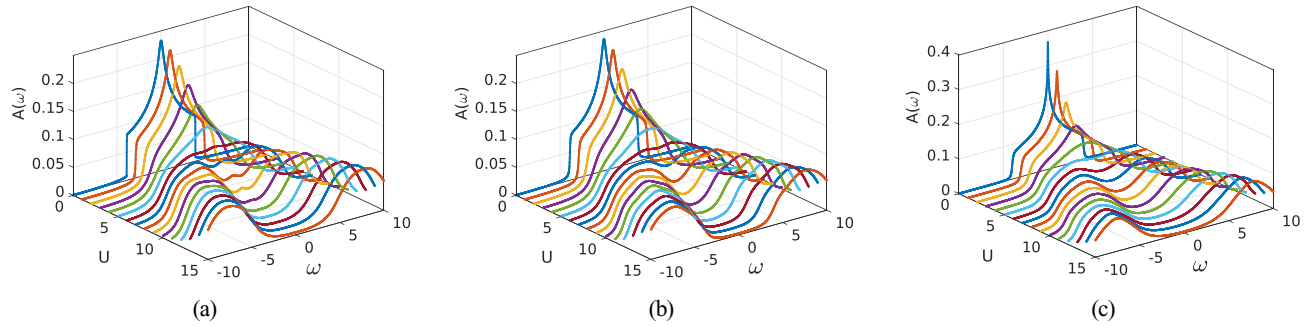

FIG. 9. (Color online) Single-particle spectral function for $N_b = 4$, different values of U, $\Phi = 0$ (a), $\Phi = 3.5$ (b), and $\Phi = 15$ (c). Other parameters are as in Fig. 3.

Mott insulator, originating from the Fermi levels of the leads. Outside of the Kondo regime, the behavior is qualitatively similar in the three cases. In the nonequilibrium cases, upon increasing the interaction the height of the spectral function at $\omega = 0$ decreases and for $U \gtrsim 6$ the spectral function displays a local minimum at $\omega = 0$ instead of a maximum, which becomes vanishingly small with increasing U. Comparison of Figs. 9(b) and 9(c) shows that for higher-bias voltages, this resonance disappears at smaller U. Also, for higher-bias voltages ($\Phi > 10$), the noninteracting spectral function has a sharper peak at $\omega = 0$. This is due to the fact that for high-bias voltage, the leads' density of states does not overlap any more and correspondingly states close to the Fermi level do not dissipate any more into the leads, therefore, the density of states close to the Fermi level is just the two-dimensional density of states, which features a logarithmic divergence. Another effect, clearly visible in Figs. 9(a)–9(c), is the linear shift of the position of the Hubbard subbands with increasing U. The peak position is given by $\omega_\pm \simeq \pm U/2$.

IV. CONCLUSIONS

We have presented an improved application of a DMFT technique for nonequilibrium situations that allows to study directly steady-state properties of strongly correlated devices. Like in equilibrium DMFT, the only approximation is the locality of the self-energy, while the accuracy of the nonequilibrium impurity problem is controlled by the number of bath sites N_b which are attached to Lindblad environments. We find that the accuracy increases exponentially with N_b, both in and out of equilibrium. The approach is benchmarked for a strongly correlated layer coupled to two metallic leads. While the results in Ref. [61] for this model were obtained by full diagonalization of the auxiliary impurity problem and were, thus, restricted to $N_b = 2$, here we invoked the non-Hermitian Krylov-space method, which allows us to use larger values for N_b.

With the Krylov-space solver we were able to go up to $N_b = 6$. For more bath sides (up to $N_b \gtrapprox 14$), the MPS solver [63] could be used, but the Krylov-space solver has the advantage to be quicker and more flexible, which is important for the DMFT iteration. For the single-layer device studied here, we found that $N_b = 4$ already yields very reliable results in most parameter cases. Only the Kondo regime requires larger values for N_b, but with $N_b = 6$ at least semiquantitative results can be achieved.

We have investigated the current-voltage characteristics across a correlated layer. At low-bias voltages, we have observed a linear behavior for weak interactions, while the current was exponentially suppressed for strong interactions [84]. On the other hand, for higher-bias voltages we have observed a reversed picture, whereby the current is larger in the strongly interacting case. In addition, we have investigated the current J as a function of the local Hubbard interaction for low- as well as for high-bias voltages. For lower-bias voltages we found that the J decreases monotonically with U, while for higher-bias voltages, the current first increases, reaches its maximum, and then decreases again. The origin of this behavior can be explained by different scattering processes.

In addition to the current we have also investigated the steady-state spectral function. Our results show that for the set of parameters considered in this paper, the spectral function is only weakly dependent on the bias voltage in contrast to the single-impurity problem. This is due to the fact that the splitting of the Kondo resonance as a function of Φ is strongly broadened due to the hopping within the correlated layer. As to be expected, the Hubbard satellites depend almost linearly on U, like in the equilibrium case.

ACKNOWLEDGMENTS

We thank M. Aichhorn, M. Knap, and M. Nuss for valuable discussions. This work was supported by the Austrian Science Fund (FWF) within projects: P24081, P26508, SFB-ViCoM F04103, as well as by NaWi Graz. The calculations were partly performed on the D-Cluster Graz and on the VSC-3 cluster Vienna.

[1] C. H. Ahn, S. Gariglio, P. Paruch, T. Tybell, L. Antognazza, and J.-M. Triscone, Science **284**, 1152 (1999).

[2] M. Izumi, Y. Ogimoto, Y. Konishi, T. Manako, M. Kawasaki, and Y. Tokura, Mater. Sci. Eng. B **84**, 53 (2001).

[3] A. Ohtomo, D. A. Muller, J. L. Grazul, and H. Y. Hwang, Nature (London) **419**, 378 (2002).

[4] A. Ohtomo and H. Y. Hwang, Nature (London) **427**, 423 (2004).

[5] S. Gariglio, C. H. Ahn, D. Matthey, and J.-M. Triscone, Phys. Rev. Lett. **88**, 067002 (2002).
[6] Q. X. Zhu, W. Wang, X. Q. Zhao, X. M. Li, Y. Wang, H. S. Luo, H. L. W. Chan, and R. K. Zheng, J. Appl. Phys. **111**, 103702 (2012).
[7] S. J. Tans, M. H. Devoret, H. Dai, A. Thess, R. E. Smalley, L. J. Geerligs, and C. Dekker, Nature (London) **386**, 474 (1997).
[8] D. Goldhaber-Gordon, H. Shtrikman, D. Mahalu, D. Abusch-Magder, U. Meirav, and M. A. Kastner, Nature (London) **391**, 156 (1998).
[9] S. M. Cronenwett, T. H. Oosterkamp, and L. P. Kouwenhoven, Science **281**, 540 (1998).
[10] M. Raizen, C. Salomon, and Q. Niu, Phys. Today **50**(7), 30 (1997).
[11] J. Struck, C. Ölschläger, M. Weinberg, P. Hauke, J. Simonet, A. Eckardt, M. Lewenstein, K. Sengstock, and P. Windpassinger, Phys. Rev. Lett. **108**, 225304 (2012).
[12] D. Jaksch, C. Bruder, J. I. Cirac, C. W. Gardiner, and P. Zoller, Phys. Rev. Lett. **81**, 3108 (1998).
[13] M. Greiner, O. Mandel, T. Esslinger, T. W. Hänsch, and I. Bloch, Nature (London) **415**, 39 (2002).
[14] L. Fallani, L. De Sarlo, J. E. Lye, M. Modugno, R. Saers, C. Fort, and M. Inguscio, Phys. Rev. Lett. **93**, 140406 (2004).
[15] S. Iwai, M. Ono, A. Maeda, H. Matsuzaki, H. Kishida, H. Okamoto, and Y. Tokura, Phys. Rev. Lett. **91**, 057401 (2003).
[16] A. Cavalleri, T. Dekorsy, H. H. W. Chong, J. C. Kieffer, and R. W. Schoenlein, Phys. Rev. B **70**, 161102 (2004).
[17] L. Perfetti, P. A. Loukakos, M. Lisowski, U. Bovensiepen, H. Berger, S. Biermann, P. S. Cornaglia, A. Georges, and M. Wolf, Phys. Rev. Lett. **97**, 067402 (2006).
[18] D. Fausti, R. I. Tobey, N. Dean, S. Kaiser, A. Dienst, M. C. Hoffmann, S. Pyon, T. Takayama, H. Takagi, and A. Cavalleri, Science **331**, 189 (2011).
[19] A. Georges, G. Kotliar, W. Krauth, and M. J. Rozenberg, Rev. Mod. Phys. **68**, 13 (1996).
[20] D. Vollhardt, in *Lecture Notes on the Physics of Strongly Correlated Systems*, edited by A. Avella and F. Mancini, AIP Conf. Proc. No. 1297 (AIP, New York, 2010), pp. 339–403.
[21] W. Metzner and D. Vollhardt, Phys. Rev. Lett. **62**, 324 (1989).
[22] P. W. Anderson, Phys. Rev. **124**, 41 (1961).
[23] K. G. Wilson, Rev. Mod. Phys. **47**, 773 (1975).
[24] H. R. Krishna-murthy, J. W. Wilkins, and K. G. Wilson, Phys. Rev. B **21**, 1003 (1980).
[25] R. Bulla, T. A. Costi, and T. Pruschke, Rev. Mod. Phys. **80**, 395 (2008).
[26] J. E. Hirsch and R. M. Fye, Phys. Rev. Lett. **56**, 2521 (1986).
[27] A. N. Rubtsov, V. V. Savkin, and A. I. Lichtenstein, Phys. Rev. B **72**, 035122 (2005).
[28] P. Werner, A. Comanac, L. de' Medici, M. Troyer, and A. J. Millis, Phys. Rev. Lett. **97**, 076405 (2006).
[29] E. Gull, A. J. Millis, A. I. Lichtenstein, A. N. Rubtsov, M. Troyer, and P. Werner, Rev. Mod. Phys. **83**, 349 (2011).
[30] M. Caffarel and W. Krauth, Phys. Rev. Lett. **72**, 1545 (1994).
[31] Q. Si, M. J. Rozenberg, G. Kotliar, and A. E. Ruckenstein, Phys. Rev. Lett. **72**, 2761 (1994).
[32] P. Schmidt and H. Monien, arXiv:cond-mat/0202046.
[33] J. K. Freericks, V. M. Turkowski, and V. Zlatić, Phys. Rev. Lett. **97**, 266408 (2006).
[34] J. K. Freericks, Phys. Rev. B **77**, 075109 (2008).
[35] A. V. Joura, J. K. Freericks, and T. Pruschke, Phys. Rev. Lett. **101**, 196401 (2008).
[36] M. Eckstein, M. Kollar, and P. Werner, Phys. Rev. Lett. **103**, 056403 (2009).
[37] S. Okamoto, Phys. Rev. B **76**, 035105 (2007).
[38] S. Okamoto, Phys. Rev. Lett. **101**, 116807 (2008).
[39] R. Kubo, J. Phys. Soc. Jpn. **12**, 570 (1957).
[40] J. Schwinger, J. Math. Phys. **2**, 407 (1961).
[41] G. Baym and L. P. Kadanoff, Phys. Rev. **124**, 287 (1961).
[42] L. P. Kadanoff and G. Baym, *Quantum Statistical Mechanics: Green's Function Methods in Equilibrium and Nonequilibrium Problems* (Addison-Wesley, Redwood City, CA, 1962).
[43] L. V. Keldysh, Zh. Eksp. Teor. Fiz. **47**, 1515 (1965) [JETP **20**, 1018 (1965)].
[44] M. Eckstein, M. Kollar, and P. Werner, Phys. Rev. B **81**, 115131 (2010).
[45] P. Mehta and N. Andrei, Phys. Rev. Lett. **96**, 216802 (2006).
[46] F. B. Anders, Phys. Rev. Lett. **101**, 066804 (2008).
[47] A. Rosch, J. Paaske, J. Kroha, and P. Wölfle, J. Phys. Soc. Jpn. **74**, 118 (2005).
[48] H. Schoeller, Eur. Phys. J. Special Topics **168**, 179 (2009).
[49] S. R. White and A. E. Feiguin, Phys. Rev. Lett. **93**, 076401 (2004).
[50] A. J. Daley, C. Kollath, U. Schollwöck, and G. Vidal, J. Stat. Mech. (2004) P04005.
[51] F. B. Anders and A. Schiller, Phys. Rev. Lett. **95**, 196801 (2005).
[52] S. Kehrein, Phys. Rev. Lett. **95**, 056602 (2005).
[53] R. Gezzi, T. Pruschke, and V. Meden, Phys. Rev. B **75**, 045324 (2007).
[54] S. G. Jakobs, V. Meden, and H. Schoeller, Phys. Rev. Lett. **99**, 150603 (2007).
[55] J. E. Han and R. J. Heary, Phys. Rev. Lett. **99**, 236808 (2007).
[56] A. Dirks, P. Werner, M. Jarrell, and T. Pruschke, Phys. Rev. E **82**, 026701 (2010).
[57] F. Heidrich-Meisner, A. E. Feiguin, and E. Dagotto, Phys. Rev. B **79**, 235336 (2009).
[58] C. Gramsch, K. Balzer, M. Eckstein, and M. Kollar, Phys. Rev. B **88**, 235106 (2013).
[59] F. A. Wolf, I. P. McCulloch, and U. Schollwöck, Phys. Rev. B **90**, 235131 (2014).
[60] An approach to deal with correlated systems out of equilibrium involving a double analytical continuation from Matsubara space has been developed in Refs. [55,56].
[61] E. Arrigoni, M. Knap, and W. von der Linden, Phys. Rev. Lett. **110**, 086403 (2013).
[62] A. Dorda, M. Nuss, W. von der Linden, and E. Arrigoni, Phys. Rev. B **89**, 165105 (2014).
[63] A. Dorda, M. Ganahl, H. G. Evertz, W. von der Linden, and E. Arrigoni, Phys. Rev. B **92**, 125145 (2015).
[64] M. Eckstein and P. Werner, Phys. Rev. B **88**, 075135 (2013).
[65] G. Mazza, A. Amaricci, M. Capone, and M. Fabrizio, Phys. Rev. B **91**, 195124 (2015).
[66] R. Haydock, *Solid State Physics, Advances in Research and Applications*, edited by H. Ehrenreich, F. Seitz, and D. Turnbull, Vol. 35 (Academic, London, 1980).
[67] M. Potthoff and W. Nolting, Phys. Rev. B **59**, 2549 (1999).
[68] M. Potthoff and W. Nolting, Phys. Rev. B **60**, 7834 (1999).
[69] H. Haug and A.-P. Jauho, *Quantum Kinetics in Transport and Optics of Semiconductors* (Springer, Heidelberg, 1998).
[70] J. Rammer and H. Smith, Rev. Mod. Phys. **58**, 323 (1986).

[71] In practice we compare two consecutive hybridization functions in the DMFT iteration and use as convergence criterion that the root-mean-square deviation becomes smaller than 10^{-5}.
[72] H.-P. Breuer and F. Petruccione, *The Theory of Open Quantum Systems* (Oxford University Press, Oxford, England, 2009).
[73] H. J. Carmichael, *Statistical Methods in Quantum Optics: Master Equations and Fokker-Planck Equations*, Texts and Monographs in Physics, Vol. 1 (Springer, Singapore, 2002).
[74] T. Prosen, New J. Phys. **10**, 043026 (2008).
[75] A. A. Dzhioev and D. S. Kosov, J. Chem. Phys. **134**, 044121 (2011).
[76] M. Schmutz, Z. Phys. B **30**, 97 (1978).
[77] U. Harbola and S. Mukamel, Phys. Rep. **465**, 191 (2008).
[78] M. Knap, E. Arrigoni, W. von der Linden, and J. H. Cole, Phys. Rev. A **83**, 023821 (2011).
[79] The superscript $^+$ denotes the ones restricted to positive times (see Ref. [62]).
[80] Y. Meir and N. S. Wingreen, Phys. Rev. Lett. **68**, 2512 (1992).
[81] A.-P. Jauho, https://nanohub.org/resources/1877
[82] M. Knap, W. von der Linden, and E. Arrigoni, Phys. Rev. B **84**, 115145 (2011).
[83] A. Amaricci, C. Weber, M. Capone, and G. Kotliar, Phys. Rev. B **86**, 085110 (2012).
[84] There should be a tiny contribution to the conductance (of the order of T_K) for Φ much smaller than the insulating gap. However, this is hard to resolve. See also the discussion of the Kondo regime below.
[85] We expect that with increasing bias voltage the maximum of $I = I(U)$ shifts to higher interactions.
[86] N. S. Wingreen and Y. Meir, Phys. Rev. B **49**, 11040 (1994).
[87] E. Lebanon and A. Schiller, Phys. Rev. B **65**, 035308 (2001).
[88] A. Rosch, J. Kroha, and P. Wölfle, Phys. Rev. Lett. **87**, 156802 (2001).
[89] J. König, J. Schmid, H. Schoeller, and G. Schön, Phys. Rev. B **54**, 16820 (1996).
[90] T. Fujii and K. Ueda, Phys. Rev. B **68**, 155310 (2003).
[91] N. Shah and A. Rosch, Phys. Rev. B **73**, 081309 (2006).
[92] P. Fritsch and S. Kehrein, Phys. Rev. B **81**, 035113 (2010).
[93] M. Nuss, C. Heil, M. Ganahl, M. Knap, H. G. Evertz, E. Arrigoni, and W. von der Linden, Phys. Rev. B **86**, 245119 (2012).
[94] G. Cohen, E. Gull, D. R. Reichman, and A. J. Millis, Phys. Rev. Lett. **112**, 146802 (2014).
[95] K. Held, R. Peters, and A. Toschi, Phys. Rev. Lett. **110**, 246402 (2013).
[96] If one looks in more detail, one can in fact notice two peaks for $\Phi = 0$. Within the accuracy of our calculation we cannot state whether these are physical or merely an artifact.
[97] We expect the total weight of the peak not to be substantially affected by this broadening.
[98] The argument is the same as for the Anderson impurity model: Since we are in the Fermi liquid phase, the imaginary part of the self-energy is zero at $\omega = 0$. The real part vanishes in the present particle-hole symmetric case.

3.4. Publication 4: DMFT

3.4.1. Preamble

The article titled *Quasiparticle excitations in steady state transport across a correlated layer* was published in Journal of Physics: Conference Series, **696**, 012003, April 2016 [4].

This work was done by Antonius Dorda (AD) as first author and Irakli Titvinidze (IT) as co-author, under the supervision of Enrico Arrigoni (EA). From a numerical point of view, essentially the same program as developed before was used, i.e. the one from Sec. 3.3, Ref. [3]. EA, AD and IT decided on putting the main focus of this work on investigating the underlying low-energy physics of the considered single layer situation. Therefore, AD searched for an appropriate parameter regime in order to be able to resolve the low-energy physics in more detail. In addition, different nonzero temperatures were introduced in the leads for the purpose of studying the competition of temperature- and bias-induced decoherence on the quasiparticle peak. After first tests conducted by IT, AD carried out the calculations in the article below and wrote a first paper draft, which IT and EA revised. All authors contributed to discussing results and the manuscript itself.

3.4.2. Original article

(see next page)

Journal of Physics: Conference Series **696** (2016) 012003 doi:10.1088/1742-6596/696/1/012003

Quasiparticle excitations in steady state transport across a correlated layer

Antonius Dorda, Irakli Titvinidze, and Enrico Arrigoni

Institute of Theoretical and Computational Physics, Graz University of Technology, 8010 Graz, Austria

E-mail: dorda@tugraz.at, arrigoni@tugraz.at

Abstract. In this work we investigate the spectral and transport properties of a single correlated layer attached to two metallic leads, with particular focus on the low-energy physics. A steady state current is driven across the layer by applying a bias voltage between the leads. Extending previous work we introduce a nonzero temperature in the leads, which enables us to study the influence of quasiparticle excitations on the transport characteristics in detail. Even though the system is clearly three dimensional we obtain current-voltage curves that closely resemble those of single quantum dots. Furthermore, a splitting of the quasiparticle excitation with bias voltage is observed in the spectral function.

1. Introduction

Correlated systems out of equilibrium and in particular electronic transport through quantum dots [1–4] and correlated heterostructures [5–10] have recently attracted increasing interest. Related model systems of paramount importance are the single impurity Anderson model (SIAM) [11] and the Hubbard model [12–14]. At the present time the equilibrium properties of these systems are understood to large extent [15–19]. The so-called dynamical mean field theory (DMFT) [18–21] was a key step in the theoretical description and understanding of Hubbard-like models and furthermore, established a link between correlated lattice systems which exhibit a Mott transition and the Kondo physics of a SIAM. Within this framework, the coherent quasiparticle excitations are described as a self-consistent Kondo effect [19]. The close relation between the SIAM and the Hubbard model poses the question whether analogous behavior is seen in the transport characteristics of the two systems. Exactly this question is the topic of the investigation presented here.

At the heart of DMFT lies the self-consistent solution of a quantum impurity model, the SIAM. An accurate description of the nonequilibrium physics of the SIAM and the related Kondo model is challenging by itself and currently intensively studied with different methods. To mention just a few, central aspects could be established with the noncrossing approximation [22–24], perturbative renormalization group (RG) [25, 26], flow equations [27, 28], real-time RG [29, 30], time-dependent density matrix RG [31–34], numerical RG [35, 36] and Monte Carlo methods [37–39]. A method recently introduced by some of us, which is well-suited for an application within nonequilibrium DMFT, is the so-called auxiliary master equation approach (AMEA) [40, 41]. AMEA has proven to be an accurate method for the study of the nonequilibrium steady state physics of the SIAM [41, 42]. Special emphasis was

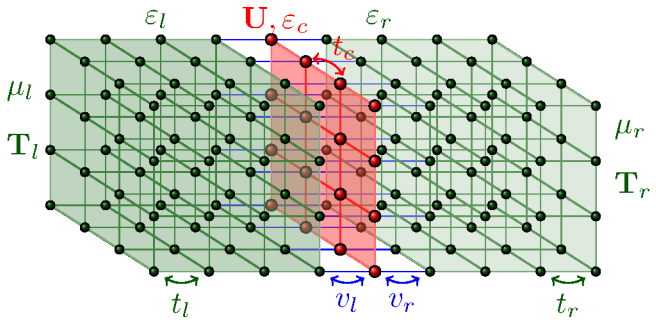

Figure 1. Sketch of the investigated heterostructure, consisting of a single correlated layer of infinite size (red) with local Hubbard interaction U, on-site energy ε_c and in-plane hopping amplitude t_c, sandwiched between two semi-infinite metallic leads (green). The hopping in the leads l and r is isotropic with amplitudes t_l and t_r, respectively, with v_l and v_r denoting the hybridizations between the respective lead and the layer. An applied bias voltage ϕ shifts the on-site energies ε_l and ε_r, as well as the chemical potentials μ_l and μ_r anti-symmetrically, which ensures together with $\varepsilon_c = -U/2$ particle-hole symmetry. All hoppings are for nearest neighbor terms only, and the temperature of the leads is labeled by $T = T_l = T_r$. We take t_c as unit of energy and consider the case with $U = 10\,t_c$, $v_l = v_r = t_c$ and $t_l = t_r = 2\,t_c$. We discuss results for different values of T and ϕ.

laid on investigating the evolution of the Kondo resonance upon driving the impurity model out of equilibrium by applying a bias voltage, and we found a transition from a single peak structure to a linear splitting of the Kondo resonance with bias. Furthermore, the current-voltage characteristics obtained for different temperatures showed clear signatures of the Kondo effect [42].

In the last years, rapid progress was made in the treatment of correlated lattice models out of equilibrium within DMFT, in explicitly time-dependent [43–46] and periodic or steady state situations [47–50]. In the study presented here we consider the special case of transport through a correlated heterostructure, consisting of a single correlated layer attached to two metallic leads at different chemical potentials. A similar setup was already treated in earlier studies with AMEA [40, 51], however, the influence of temperature was not investigated. Here we consider the transport and spectral properties of the system starting from a lowest temperature, which can still be well-resolved with the employed impurity solver and results in a strong quasiparticle excitation, and successively extending to larger values of T up to the quasigapped regime, analogous to a Mott insulator. Besides the bias-dependent spectral function, the experimentally well-accessible current-voltage characteristics is presented.

The work is organized as follows: In Sec. 2 the investigated model is defined, in Sec. 3 we briefly introduce the nonequilibrium DMFT approach together with AMEA, and in Sec. 4 the obtained results are presented and discussed. Concluding remarks are given in Sec. 5.

2. Model

The model system considered in this work is schematically depicted in Fig. 1. The corresponding Hamiltonian is given by

$$H = H_c + \sum_{\alpha=l,r} H_\alpha + H_{\mathrm{coup}}\,, \tag{1}$$

consisting of a part for the central system H_c, a part for each decoupled lead $H_{l/r}$ and a coupling between the leads and the correlated layer $H_{\rm coup}$. In the detail the Hamiltonian reads

$$H_c = -t_c \sum_{\langle ij\rangle,\sigma} c^\dagger_{i\sigma} c_{j\sigma} + U \sum_i n_{i\uparrow} n_{i_\downarrow} + \varepsilon_c \sum_{i,\sigma} n_{i\sigma} \,, \tag{2}$$

$$H_\alpha = -t_\alpha \sum_{\langle ij\rangle\sigma} c^\dagger_{\alpha i\sigma} c_{\alpha j\sigma} + \varepsilon_\alpha \sum_{i\sigma} c^\dagger_{\alpha i\sigma} c_{\alpha i\sigma} \,, \tag{3}$$

$$H_{\rm coup} = \sum_{\langle ij\rangle\alpha\sigma} v_\alpha \left(c^\dagger_{i\sigma} c_{\alpha j\sigma} + h.c. \right) \,, \tag{4}$$

where $\langle i,j\rangle$ indicates neighboring sites, $c^\dagger_{i,\sigma}$ creates an electron at the i-th site of the correlated layer with spin $\sigma =\uparrow,\downarrow$, and $n_{i\sigma} = c^\dagger_{i\sigma} c_{i\sigma}$ denote the corresponding occupation number operators. The analogous fermionic creation/annihilation operators of lead α are labeled by $c^\dagger_{\alpha i\sigma}/c_{\alpha i\sigma}$. For the particular parameters see Fig. 1.

3. Method

In the following we outline the method only briefly and for details we refer to Ref. [40, 41, 51].

Nonequilibrium dynamics are conveniently formulated in terms of Keldysh Green's functions [52–57], whereby for the steady state limit it suffices to consider 2×2 objects on the Keldysh contour

$$\underline{G} = \begin{pmatrix} G^R & G^K \\ 0 & G^A \end{pmatrix} \,, \tag{5}$$

which we denote by an underscore. Here, the retarded G^R and the Keldysh component G^K are independent functions in a generic nonequilibrium situation, and the advanced part is given by $G^A = (G^R)^\dagger$. The spectral function is defined as usual: $A = i/2\pi\,(G^R - G^A)$.

Since the model outlined in Sec. 2 is translationally invariant in the in-plane direction, it is convenient to introduce the corresponding momentum variable $\mathbf{k}_{||}$. Furthermore, time translational invariance applies in the steady state limit and the governing equations can be formulated in the frequency domain ω. With this the Green's function of the correlated layer is given in terms of Dyson's equation by

$$\underline{G}^{-1}(\omega,\mathbf{k}_{||}) = \underline{g}_0^{-1}(\omega,\mathbf{k}_{||}) - \sum_{\alpha=l,r} v_\alpha^2 \, \underline{g}_\alpha(\omega,\mathbf{k}_{||}) - \underline{\Sigma}(\omega,\mathbf{k}_{||}) \,. \tag{6}$$

Here, the decoupled non-interacting Green's function of the layer is denoted by $\underline{g}_0(\omega,\mathbf{k}_{||})$, and those of the leads by $\underline{g}_\alpha(\omega,\mathbf{k}_{||})$. The non-interacting Green's functions are known exactly but the determination of the self-energy of the correlated layer $\underline{\Sigma}(\omega,\mathbf{k}_{||})$ is challenging and one has to resort to approximations. In particular we neglect spatial correlations and restrict ourselves to a local self-energy $\underline{\Sigma}(\omega,\mathbf{k}_{||}) = \underline{\Sigma}(\omega)$, as usually done in the context of DMFT [18–21, 43, 47]. Within DMFT, the local quantity $\underline{\Sigma}(\omega)$ is determined by mapping the lattice problem onto an equivalent quantum impurity model, with the same local parameters U and ε_c. However, the bath degrees of freedom of the impurity model depend on $\underline{\Sigma}(\omega)$, such that a self-consistent solution is needed, which is commonly obtained in an iterative manner. The bath for the impurity model is fully specified by the hybridization function

$$\underline{\Delta}_{\rm ph}(\omega) = \underline{g}_0^{-1}(\omega) - \underline{G}_{\rm loc}^{-1}(\omega) - \underline{\Sigma}(\omega) \,, \tag{7}$$

where $\underline{g}_0^{-1}(\omega)$ is the non-interacting Green's function of the disconnected impurity and the local Green's function is obtained by

$$\underline{G}_{\mathrm{loc}}(\omega) = \int_{\mathrm{BZ}} \frac{d\mathbf{k}_{||}}{(2\pi)^2} \underline{G}(\omega, \mathbf{k}_{||})\,. \tag{8}$$

In order to solve the nonequilibrium impurity problem we resort to AMEA, cf. [40, 41], which maps the original impurity problem onto an auxiliary one, with a finite number of bath sites N_B and additional Markovian environments. The resulting open quantum system is described by a Lindblad equation and is small enough to be solved accurately by numerical techniques. In contrast to other approaches, the parameters of the Lindblad equation are not obtained perturbatively but through an optimization procedure. In particular, we consider the hybridization function of the auxiliary system $\underline{\Delta}_{\mathrm{aux}}(\omega)$ and vary the auxiliary bath parameters in order to minimize the difference to the physical hybridization function $\underline{\Delta}_{\mathrm{ph}}(\omega)$, Eq. (7). In the limit of large N_B the approach becomes exact but even for small values of N_B we obtain $\underline{\Delta}_{\mathrm{aux}}(\omega) \approx \underline{\Delta}_{\mathrm{ph}}(\omega)$ to very good approximation. Typically, an exponential convergence with increasing N_B is achieved. After the mapping procedure, which can be done in a $U = 0$ calculation, the interacting impurity problem is solved. For this we introduced two different strategies in previous work: On the one hand, an implementation of AMEA which makes use of Krylov space methods, cf. Ref. [41], and on the other hand, a matrix product states based solution, cf. Ref. [42]. The latter allows for a highly accurate solution of the impurity problem but requires a rather large amount of CPU time. The former is not as accurate at low temperatures but faster in many cases and is used in the present work. The Krylov space solver enables us to consider up to $N_B = 6$ bath sites, which suffices to treat cases with strong Kondo or quasiparticle excitations reliably, cf. Ref. [41, 51]. Once the many-body problem of the auxiliary system is solved one obtains an approximation for the self-energy

$$\underline{\Sigma}(\omega) = \underline{G}_{\mathrm{aux},0}^{-1}(\omega) - \underline{G}_{\mathrm{aux}}^{-1}(\omega)\,, \tag{9}$$

from the knowledge of the non-interacting and the interacting auxiliary Green's functions. By inserting $\underline{\Sigma}(\omega)$ from Eq. (9) into Eqs. (6),(7),(8) we close the DMFT cycle and iterate until a self-consistent point is reached.

4. Results

In the following we present results for the transport and spectral properties of a correlated layer in a nonequilibrium steady state situation. The particular model is defined in Sec. 2 and depicted in Fig. 1. We place special emphasis on the low-energy properties and consider cases with rather low bias voltages ϕ. To investigate the role of resonant quasiparticle excitations, different temperatures $T = T_l = T_r$ are introduced in the leads. In contrast to previous work [51], a nonzero temperature is considered in the leads and additionally, the hopping parameters are chosen such that each correlated site has an equal hopping amplitude to neighboring sites ($v_l = v_r = t_c$). By this we expect to be in a regime in which a competition between the physics of an isolated 2D layer and the one of single quantum dots occurs.

In Fig. 2 the current-voltage characteristics $j(\phi)$ together with the differential conductance $\partial j/\partial\phi$ are displayed for various T. At low bias voltages $\phi \lesssim 2\,t_c$ the temperature has large influence on $j(\phi)$ and $\partial j/\partial\phi$, whereas for larger voltages $\phi \gtrsim 2.5\,t_c$ we find quantitatively similar current values for all of the temperatures. This is in close analogy to what was observed in Ref. [42] for the nonequilibrium properties of a quantum dot. In $\partial j/\partial\phi$ we obtain for $\phi \lesssim 1\,t_c$ a strong dependence on T. Again, the behavior is similar to what is known from Kondo systems [3, 4, 29, 30]. However, the accuracy of the present calculations does not permit

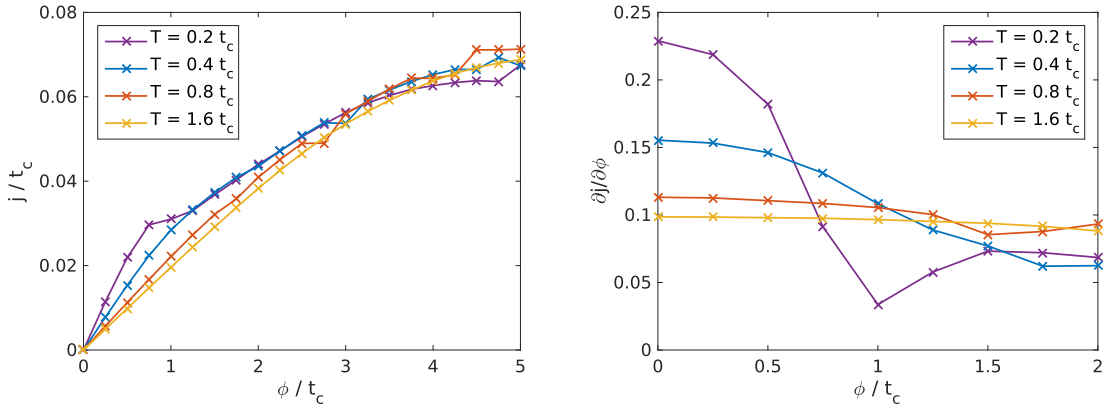

Figure 2. Current $j(\phi)$ and differential conductance $\partial j/\partial\phi$ as a function of bias voltage ϕ and for different temperatures T. For the particular model parameters see Fig. 1. Calculations for $T = 1.6\,t_c$ were performed with $N_B = 4$ and all others with $N_B = 6$.

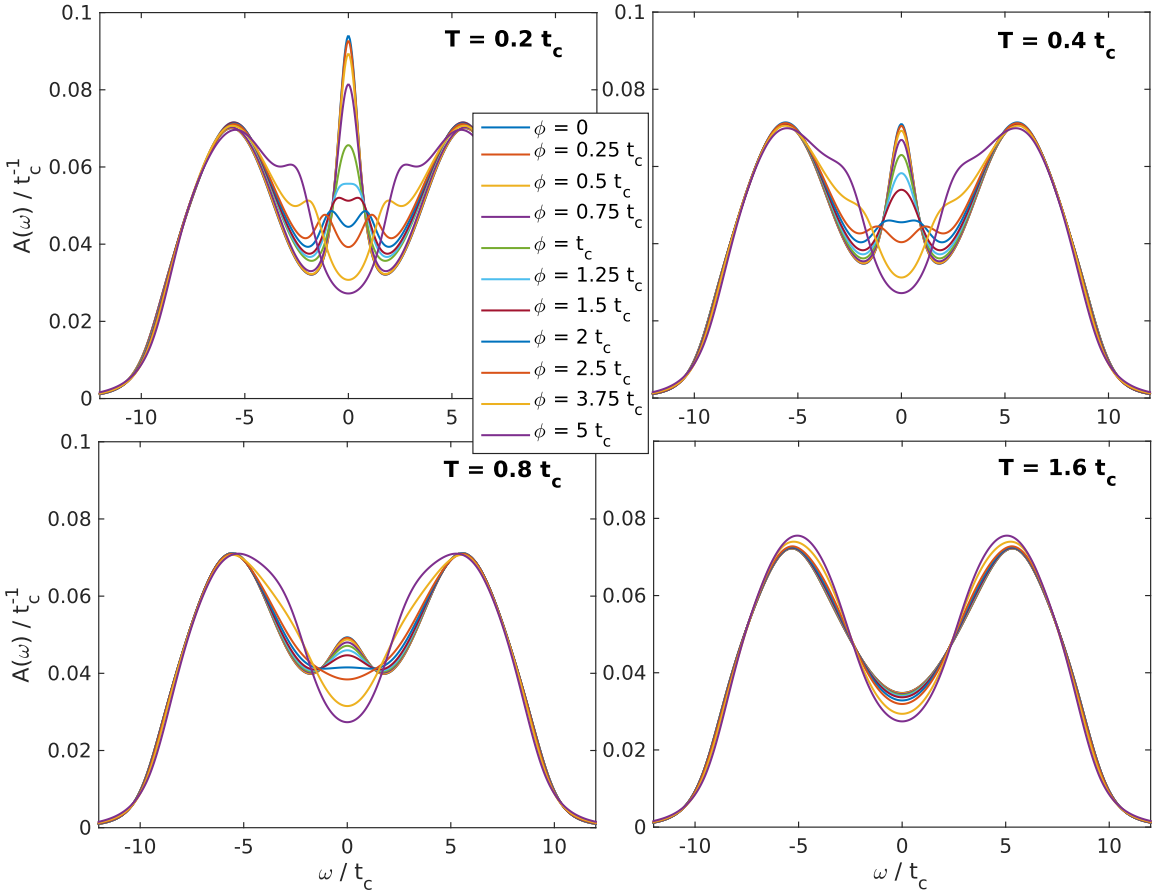

Figure 3. Spectral function $A(\omega)$ as a function of bias voltage ϕ and for different temperatures T. The parameters are the same as in Fig. 2

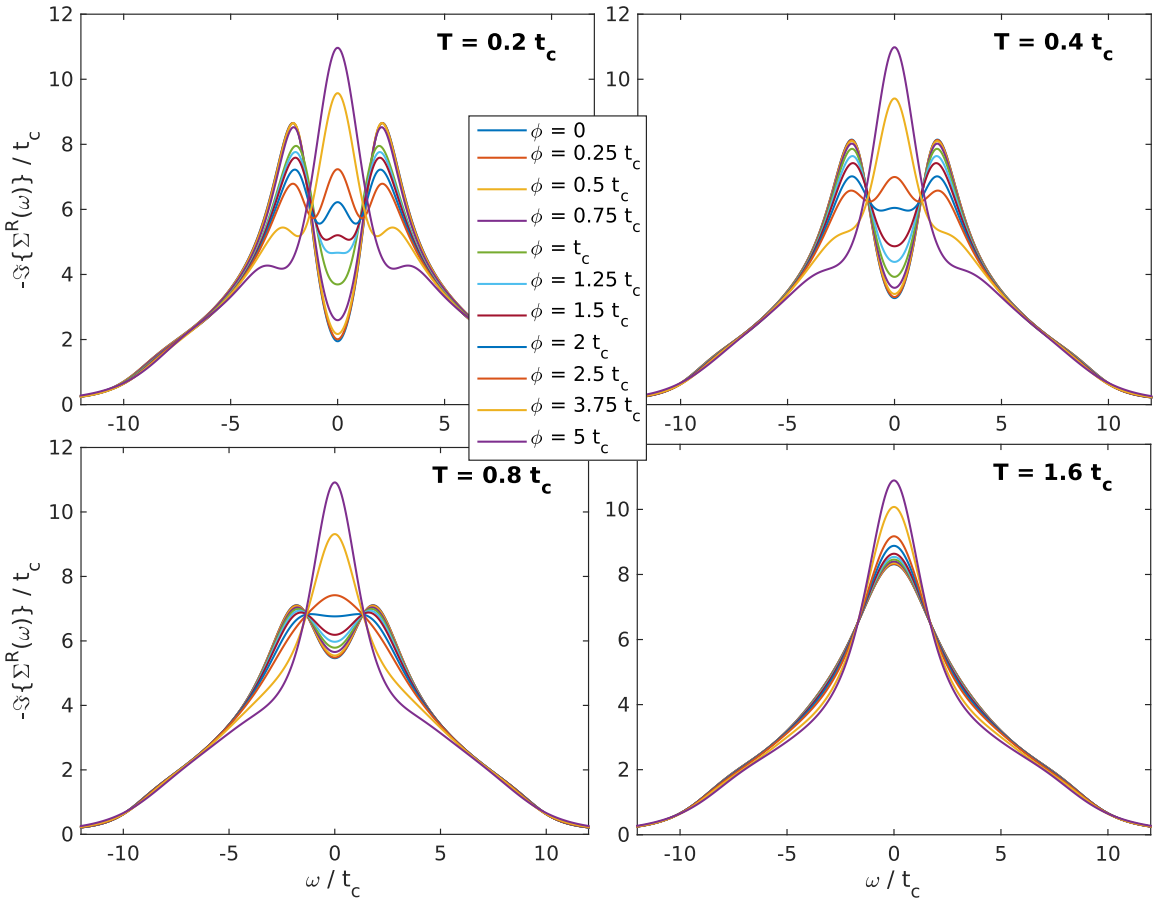

Figure 4. Retarded self-energy $\Sigma^R(\omega)$ as a function of bias voltage ϕ and for different temperatures T. The parameters are the same as in Fig. 2

us to investigate the scaling with ϕ in detail, in particular if a logarithmic dependence as in quantum dots is present. Still, one observes that the experimentally well-accessible quantity $\partial j/\partial\phi$ exhibits a strong temperature dependence and clear signatures of a Kondo-like behavior are visible for low T. From a technical point of view one should note that slight kinks or jumps in $j(\phi)$ are present, at different values of ϕ for the various T. These artefacts originate in the mapping procedure and appear at values $\phi = \phi_c$ at which more than one parameter set for the auxiliary system minimizes the difference to the physical hybridization function. Usually, one of these minima is better for $\phi < \phi_c$ while the other one for $\phi > \phi_c$. Therefore, such a crossing of minima leads to an abrupt change in parameters of the auxiliary system and may result in a slight shift of spectral weight, cf. Ref. [41]. In general, this effect is smallest in situations in which the difference between $\underline{\Delta}_{\mathrm{aux}}(\omega)$ and $\underline{\Delta}_{\mathrm{ph}}(\omega)$ is small in any case and thus, is reduced upon increasing the number of bath sites N_B.

A more detailed picture of the state of the system is obtained by investigating the spectral function, see Fig. 3. In the equilibrium case, $\phi = 0$, we find a strong quasiparticle excitation at $\omega = 0$ for $T = 0.2\,t_c$, which is attenuated with increasing temperature ($T = 0.4\,t_c$ and $T = 0.8\,t_c$) and is completely suppressed for $T = 1.6\,t_c$.[58] Especially interesting are the low temperature situations $T = 0.2\,t_c$ and $T = 0.4\,t_c$ in which a strong zero frequency excitation is visible in equilibrium, and for which we observe with increasing ϕ at first a reduction of the peak height before a splitting sets in. Similar to a quantum dot system [41, 42], we find two

resonant excitations at the Fermi-energies of the two leads and thus a linear splitting with ϕ. For the case of $T = 0.2\,t_c$ the excitations are still clearly visible at rather large voltages up to $\phi \approx 5\,t_c$. The results for $T = 0.8\,t_c$ and $T = 1.6\,t_c$ reveal dissimilar spectral functions at low bias voltages, but surprisingly, the obtained current values in Fig. 2 are comparable. The reason for this is that the high temperatures average out details in $A(\omega)$ to large extent.

The presence of resonant excitations is also clearly visible in the retarded part of the self-energy, displayed in Fig. 4. For $\phi = 0$ we find for temperatures up to $T = 0.8\,t_c$ a local minimum in $-\Im\{\Sigma^R(\omega)\}$ at $\omega = 0$, indicating a quasiparticle excitation. But only in the cases $T = 0.2\,t_c$ and $T = 0.4\,t_c$ the temperature induced decoherence is weak enough to obtain a splitting of the single minimum when increasing the bias voltage. In contrast, the self-energy for $T = 1.6\,t_c$ is rather featureless and only weakly dependent on the bias voltage.

5. Conclusions

In this work we investigated the steady state properties of a correlated layer sandwiched between two metallic leads at different chemical potentials, induced by an externally applied bias voltage. For this we made use of a nonequilibrium DMFT approach together with AMEA as impurity solver. In addition to previous work [51], we studied the influence of temperature on the transport characteristics and on the bias-dependent spectral function, with focus on the low-bias regime. The parameters of the system were chosen such that a certain direction was not preferred in advance. In particular, all of the hopping amplitudes of a correlated site to its neighbors were of equal size. From investigating the spectral function and the differential conductance as a function of bias voltage and for various temperatures, we found that the considered system bore close analogy to the case of a single quantum dot. A result like this could be expected when considering the limit in which the hopping parallel to the 2D layer is much smaller than the longitudinal one, regarding the layer and the leads. But, since the hoppings to correlated sites were isotropic the result is not intuitive nor trivial.

Acknowledgements

We acknowledge valuable discussions with Martin Nuss, Markus Aichhorn, Michael Knap, and Wolfgang von der Linden. This work was supported by the Austrian Science Fund (FWF): P24081, P26508, as well as SFB-ViCoM project F04103, and NaWi Graz. The calculations were partly performed on the D-cluster Graz and on the VSC-3 cluster Vienna.

References

[1] Goldhaber-Gordon D, Shtrikman H, Mahalu D, Abusch-Magder D, Meirav U and Kastner M A 1998 *Nature (London)* **391** 156
[2] Cronenwett S M, Oosterkamp T H and Kouwenhoven L P 1998 *Science* **281** 540–544
[3] Kretinin A V, Shtrikman H and Mahalu D 2012 *Phys. Rev. B* **85**(20) 201301
[4] Zhang Y, Kahle S, Herden T, Stroh C, Mayor M, Schlickum U, Ternes M, Wahl P and Kern K 2013 *Nat Commun* **4**
[5] Ahn C H, Gariglio S, Paruch P, Tybell T, Antognazza L and Triscone J M 1999 *Science* **284** 1152–1155
[6] Izumi M, Ogimoto Y, Konishi Y, Manako T, Kawasaki M and Tokura Y 2001 *Materials Science and Engineering: B* **84** 53 – 57
[7] Ohtomo A, Muller D A, Grazul J L and Hwang H Y 2002 *Nature* **419** 378–380
[8] Ohtomo A and Hwang H Y 2004 *Nature* **427** 423–426
[9] Gariglio S, Ahn C H, Matthey D and Triscone J M 2002 *Phys. Rev. Lett.* **88**(6) 067002
[10] Zhu Q X, Wang W, Zhao X Q, Li X M, Wang Y, Luo H S, Chan H L W and Zheng R K 2012 *Journal of Applied Physics* **111** 103702
[11] Anderson P W 1961 *Phys. Rev.* **124**(1) 41–53
[12] Hubbard J 1963 *Proc. R. Soc. London* **276** 238
[13] Gutzwiller M C 1963 *Phys. Rev. Lett.* **10** 159
[14] Kanamori J 1963 *Prog. Theor. Phys.* **30** 275
[15] Hewson A C 1993 *The Kondo Problem to Heavy Fermions* (Cambridge University Press)

[16] Bulla R, Costi T A and Pruschke T 2008 *Rev. Mod. Phys.* **80** 395–450
[17] LeBlanc J P F, Antipov A E, Becca F, Bulik I W, Chan G K L, Chung C M, Deng Y, Ferrero M, Henderson T M, Jimnez-Hoyos C A, Kozik E, Liu X W, Millis A J, Prokof'ev N V, Qin M, Scuseria G E, Shi H, Svistunov B V, Tocchio L F, Tupitsyn I S, White S R, Zhang S, Zheng B X, Zhu Z and Gull E 2015 ArXiv:1505.02290
[18] Vollhardt D 2012 *Annalen der Physik* **524** 1–19
[19] Georges A 2004 *AIP Conference Proceedings* **715**
[20] Georges A, Kotliar G, Krauth W and Rozenberg M J 1996 *Rev. Mod. Phys.* **68**(1) 13–125
[21] Metzner W and Vollhardt D 1989 *Phys. Rev. Lett.* **62** 324
[22] Wingreen N S and Meir Y 1994 *Phys. Rev. B* **49**(16) 11040–11052
[23] Lebanon E and Schiller A 2001 *Phys. Rev. B* **65**(3) 035308
[24] Rosch A, Kroha J and Wölfle P 2001 *Phys. Rev. Lett.* **87**(15) 156802
[25] Rosch A, Paaske J, Kroha J and Wölfle P 2003 *Phys. Rev. Lett.* **90** 076804
[26] Shah N and Rosch A 2006 *Phys. Rev. B* **73**(8) 081309
[27] Kehrein S 2005 *Phys. Rev. Lett.* **95** 056602
[28] Fritsch P and Kehrein S 2010 *Phys. Rev. B* **81**(3) 035113
[29] Pletyukhov M and Schoeller H 2012 *Phys. Rev. Lett.* **108**(26) 260601
[30] Reininghaus F, Pletyukhov M and Schoeller H 2014 *Phys. Rev. B* **90** 085121
[31] Heidrich-Meisner F, Feiguin A E and Dagotto E 2009 *Phys. Rev. B* **79** 235336
[32] Holzner A, McCulloch I P, Schollwöck U, von Delft J and Heidrich-Meisner F 2009 *Phys. Rev. B* **80**(20) 205114
[33] Nuss M, Ganahl M, Evertz H G, Arrigoni E and von der Linden W 2013 *Phys. Rev. B* **88** 045132
[34] Nuss M, Ganahl M, Arrigoni E, von der Linden W and Evertz H G 2015 *Phys. Rev. B* **91** 085127
[35] Anders F B 2008 *Phys. Rev. Lett.* **101** 066804
[36] Schmitt S and Anders F B 2011 *Phys. Rev. Lett.* **107**(5) 056801
[37] Werner P, Oka T, Eckstein M and Millis A J 2010 *Phys. Rev. B* **81** 035108
[38] Han J E and Heary R J 2007 *Phys. Rev. Lett.* **99** 236808
[39] Cohen G, Gull E, Reichman D R and Millis A J 2014 *Phys. Rev. Lett.* **112**(14) 146802
[40] Arrigoni E, Knap M and von der Linden W 2013 *Phys. Rev. Lett.* **110** 086403
[41] Dorda A, Nuss M, von der Linden W and Arrigoni E 2014 *Phys. Rev. B* **89** 165105
[42] Dorda A, Ganahl M, Evertz H G, von der Linden W and Arrigoni E 2015 *Phys. Rev. B* **92**(12) 125145
[43] Freericks J K, Turkowski V M and Zlatić V 2006 *Phys. Rev. Lett.* **97** 266408
[44] Eckstein M, Kollar M and Werner P 2009 *Phys. Rev. Lett.* **103** 056403
[45] Aoki H, Tsuji N, Eckstein M, Kollar M, Oka T and Werner P 2014 *Rev. Mod. Phys.* **86** 779–837
[46] Balzer K, Wolf F A, McCulloch I P, Werner P and Eckstein M 2015 *Phys. Rev. X* **5**(3) 031039
[47] Schmidt P and Monien H ArXiv:cond-mat/0202046
[48] Joura A V, Freericks J K and Pruschke T 2008 *Phys. Rev. Lett.* **101** 196401
[49] Okamoto S 2008 *Phys. Rev. Lett.* **101** 116807
[50] Aron C, Kotliar G and Weber C 2012 *Phys. Rev. Lett.* **108** 086401
[51] Titvinidze I, Dorda A, von der Linden W and Arrigoni E 2015 ArXiv:1508.02953
[52] Kadanoff L P and Baym G 1962 *Quantum Statistical Mechanics: Green's Function Methods in Equilibrium and Nonequilibrium Problems* (Redwood City, CA: Addison-Wesley)
[53] Schwinger J 1961 *J. Math. Phys.* **2** 407
[54] Keldysh L V 1965 *Sov. Phys. JETP* **20** 1018
[55] Haug H and Jauho A P 1998 *Quantum Kinetics in Transport and Optics of Semiconductors* (Heidelberg: Springer)
[56] Rammer J and Smith H 1986 *Rev. Mod. Phys.* **58**(2) 323–359
[57] van Leeuwen R, Dahlen N E, Stefanucci G, Almbladh C O and von Barth U 2006 *Introduction to the Keldysh Formalism* (*Lect. Notes. Phys.* vol 706) (Berlin: Springer-Verlag) chap 3, pp 33–59
[58] One should note that the $T = 0$ Fermi liquid limit is given by $A(\omega = 0) \approx 0.1667\, t_c^{-1}$. The accurate consideration of temperatures below $T = 0.2\, t_c$ would require more bath sites N_B and thus more advanced manybody solution strategies, cf. Ref. [42].

3.5. Further publications and work in progress

Besides these publications on AMEA, AD contributed in the course of this thesis as co-author to the publication Ref. [5] and the preprint Ref. [6]. In Ref. [5] a systematic improvement of nonequilibrium cluster perturbation theory (nCPT) was introduced and studied. A principal problem in nCPT, in contrast to its equilibrium counterpart, is, that an ambiguity exists in choosing the appropriate reference state for the decoupled cluster. In equilibrium, it is natural to choose the same temperature and chemical potential as in the final, coupled system. However, in nonequilibrium such macroscopic quantities are not well-defined. A possible solution to this problem was introduced by constructing an appropriate reference state through a quantum master equation. Its importance for transport phenomena in molecular junctions such as current blocking was demonstrated.

The main goal of Ref. [6] was to present a systematic approach on how to extend the ideas of NRG to the nonequilibrium regime. For this a bath discretization with additional Lindblad drivings was introduced, which could then be mapped on a linear chain with nearest neighbor couplings only. One of the crucial steps hereby was to achieve that the Lindblad drivings remain local in the unitary transformation from a star to a chain geometry. This could be done by replacing partially filled bath sites by a linear combination of twice as many filled and empty sites, whereby each of the two sets separately had identical on-site Lindblad drivings. As a result, the Lindblad terms were not affected when mapping the filled and empty sites separately onto two Wilson chains, and one thus retained a local setup. In a first study this approach was thoroughly tested in the noninteracting limit. For this, an alternative and compact derivation of the noninteracting Green's functions for a Lindblad lattice problem was presented in addition. It avoided the necessity to introduce an augmented fermion Fock space, cf. Refs. [70], [1] and [2]. After this preliminary study, the group of Jan von Delft at LMU Munich is currently investigating the challenging nonequilibrium Kondo regime with the approach, by employing MPS methods to solve the interacting Lindblad problem.

In the context of AMEA, further extensions of the method and further applications to different physical situations are on the way. At first, a manuscript is in preparation which is devoted to more details on the mapping procedure itself, together with an analysis of different geometries for the auxiliary system. Secondly, on the level of the SIAM, we currently investigate and prepare manuscripts for the thermoelectric properties in a true nonequilibrium state, and also for nonequilibrium Kondo physics in magnetic fields. On the level of DMFT, a paper is in preparation which addresses transport through heterostructures of correlated layers. Also, optical driving in the framework of Floquet and DMFT is an interesting topic which is currently investigated in the group.

4. Summary and outlook

Development of the auxiliary master equation approach (AMEA): The main topic of this dissertation was the development and improvement of AMEA, and its application to strongly correlated quantum manybody systems out of equilibrium. The approach itself was originally put forward by Arrigoni *et al.* in Ref. [106], where the basic idea and first results for transport through a correlated layer within dynamical mean field theory (DMFT) were presented. The key step in AMEA is to map a general nonequilibrium impurity problem, as encountered for instance in the self-consistent DMFT cycle, onto an auxiliary open quantum system. For the open quantum system a finite number N_B of bath sites embedded in Markovian environments is chosen, whose dynamics is governed by a Lindblad equation. By this, the original physical impurity model $\mathrm{IM}_{\mathrm{ph}}$, which is interacting and of infinite size, is mapped onto this auxiliary system $\mathrm{IM}_{\mathrm{aux}}$, which is of finite size only and can thus be solved exactly or at least with high numerical precision. The two major steps in the approach are firstly the mapping procedure, in which the parameters of $\mathrm{IM}_{\mathrm{aux}}$ are adjusted to the particular $\mathrm{IM}_{\mathrm{ph}}$, and secondly, the manybody solution, in which the interacting $\mathrm{IM}_{\mathrm{aux}}$ is solved and by this an approximate solution of $\mathrm{IM}_{\mathrm{ph}}$ is obtained. The overall accuracy is controlled by the parameter N_B and can be systematically improved by increasing it. In fact, in practice we found already for small values of $N_B \approx \mathcal{O}(10)$ a very good mapping and even an exponential convergence when incrementing N_B, which enabled us to obtain very accurate spectral functions and observables. In order to make optimal use of the chosen number of bath sites for $\mathrm{IM}_{\mathrm{aux}}$, efficient optimization algorithms are needed for the mapping procedure. Moreover, sophisticated manybody solution strategies must be employed to solve the interacting Lindblad problem precisely. As is commonly true, the solution of the interacting nonequilibrium manybody problem is a difficult task and sets also within AMEA the main limitation to the accessible values of N_B.

The mapping procedure is build upon the demand that the hybridization function of $\mathrm{IM}_{\mathrm{aux}}$, $\underline{\Delta}_{\mathrm{aux}}(\omega)$, reproduces the one of $\mathrm{IM}_{\mathrm{ph}}$, $\underline{\Delta}_{\mathrm{ph}}(\omega)$, as accurately as possible for a chosen number of bath sites N_B. This is analogous to what is known as exact diagonalization DMFT in equilibrium [52], only that the criterion is here generalized to the nonequilibrium regime by formulating the equations in the framework of Keldysh Green's functions. Therefore, the retarded as well as the Keldysh part of the hybridization function must be considered simultaneously. Since the hybridization function contains per definition only the bath degrees of freedom of an impurity model and is independent of the interaction terms on the impurity site, it can be obtained through a noninteracting calculation. This greatly speeds up computations in practice and allows us to quickly compute $\underline{\Delta}_{\mathrm{aux}}(\omega)$ for different parameters of $\mathrm{IM}_{\mathrm{aux}}$ and by this, to optimally fit $\underline{\Delta}_{\mathrm{aux}}(\omega)$ to $\underline{\Delta}_{\mathrm{ph}}(\omega)$. The number of parameters in $\mathrm{IM}_{\mathrm{aux}}$ increases hereby up to quadratically with N_B, which results in a multi-dimensional optimization problem for the mapping procedure. Different techniques for this were tested in the course of the thesis. Gradient-based minimization routines turned out to be well-applicable for rather small system sizes ($N_B \lesssim 6$), and for larger values of N_B Monte Carlo schemes were tested and implemented. Their advantage

is the ability to overcome local minima. In particular, a parallel tempering routine with feedback optimization has proven most efficient for our purposes and enabled us to accurately perform the mapping procedure with as many as $30 - 60$ optimization parameters in $\mathrm{IM}_{\mathrm{aux}}$. This was one important step in the development of the approach and made it possible to obtain a high overall accuracy.

For the solution of the interacting Lindblad problem two different strategies were pursued. In the first published work in this thesis, Ref. [1], Sec. 3.1, an exact diagonalization (ED) approach was chosen, and in the second work in Ref. [2], Sec. 3.2, a drastic improvement of the method was achieved by making use of matrix product states (MPS). In the work on the ED-solver we employed Krylov space methods for non-Hermitian sparse matrices in order to compute the desired interacting Green's functions. Already in Ref. [106] an ED-approach was used, however, with a full diagonalization which allowed only for two bath sites at most. Due to the Krylov space techniques we could extend the range up to $N_B = 6$. One has to bear in mind the exponential dependence of the Hilbert space size $N_{\mathcal{H}}$ on N_B, so that $N_B = 2$ corresponds to $N_{\mathcal{H}} \approx 400$ whereas $N_B = 6$ to $N_{\mathcal{H}} \approx 10^7$. Due to this and due to the exponential increase in accuracy in the mapping procedure with N_B, the application of Krylov space techniques can be seen as a first important improvement of the approach. Another important advancement of AMEA was achieved with MPS techniques. In Ref. [2], Sec. 3.2, we explored possible modifications in the geometry of $\mathrm{IM}_{\mathrm{aux}}$ in order to reduce the bipartite entanglement entropy, which increased the applicability of MPS methods. As a result, it was possible for us to treat as large systems as $N_B = 16$ bath sites, and by this we could greatly improve the achievable accuracy within AMEA.

Results: From the physical point of view the achievements in this thesis were twofold. On the one hand, in the course of the development of solution strategies for AMEA the single impurity Anderson model (SIAM) driven by a bias voltage was investigated, and on the other hand, transport through a correlated layer was studied within DMFT. All of these calculations were performed for steady state equilibrium and especially nonequilibrium situations. Details are provided in the papers included in this thesis, Sec. 3. Regarding the first application, in the work on the ED-solver Ref. [1], Sec. 3.1, the spectral properties of the nonequilibrium SIAM and corresponding observables such as the current density were examined for a large range of external parameters. In particular, we could accurately capture interaction effects on the current-voltage characteristics and obtained a close agreement with quasi-exact reference values. Furthermore, we achieved to resolve a distinct Kondo resonance in the spectral function in the equilibrium regime and studied its linear splitting with applied bias voltage. This behavior was confirmed with the MPS-solver and the calculations performed in Ref. [2], Sec. 3.2. In addition, owing to the greatly increased accuracy of the latter solver we were able to accurately capture Kondo physics and we could resolve the behavior on small energy scales in detail. In particular, a comparison against a numerical renormalization group (NRG) calculation in the equilibrium limit revealed a very close agreement, for a situation with large values of the interaction and at temperatures well below the Kondo scale. Furthermore, the suppression and subsequent splitting of the Kondo peak at voltages just above the Kondo temperature could be precisely resolved. To our knowledge this was one of the most accurate calculations of the spectral properties of the nonequilibrium SIAM in the steady state up to this time and demonstrated the great capabilities and potential of AMEA.

In the investigations of transport through a correlated layer within DMFT, reported in

Ref. [3], Sec. 3.3, and Ref. [4], Sec. 3.4, we examined the spectral and transport properties and found distinct signatures for the transition from a nearly insulating Mott state to a strongly correlated metal when varying the interaction strength U. In the current-voltage characteristics the transition became particularly apparent at low bias voltages, but also in the high-bias regime drastic effects of the electron-electron interactions were found. In the equilibrium limit, the spectral properties revealed a quasi-gapped density of states at large U and the build-up of a Kondo or quasiparticle peak at the Fermi level when lowering U. Similar to the single impurity case, also here we found a splitting of the Kondo peak with increasing bias voltage and furthermore, the temperature dependence of the current-voltage characteristics bore close analogy to those of a SIAM. In all of these calculations we employed the above mentioned ED-solver. It is well-suited for the purposes of the self-consistent DMFT iteration since a single solution of the impurity problem is rather quick and the solver still provides a good accuracy.

Outlook: Possible extensions of the method in future are numerous. On the level of DMFT improved results could be obtained by employing the developed MPS-solver. This would require a higher computational effort but could provide a greatly improved accuracy, especially in situations with prominent Kondo physics for instance. Further extensions in the context of DMFT such as transport through multilayer heterostructures, the calculation of thermoelectric properties and also optical driving is current work in progress. These are interesting questions on their own and additionally first steps towards a treatment of multilayer heterostructures under light incidence. Such studies would yield important information for the applicability of strongly correlated heterostructures as solar cells [107]. In order to realize ab-initio calculations of real materials the combination with density functional theory would be a key step. This is possible in principle, however, for real materials one often needs a multi-orbital description. Therefore, further improvements on the level of the impurity solver are needed.

Other solution strategies for the auxiliary impurity problem still have to be studied and could yield important advances, in particular for multi-level impurity models and also for the inclusion of phonons. The latter represents a realistic dissipation mechanism and is important for any room temperature situation. Possible candidates for alternative manybody solution techniques are for instance stochastic wave functions, configuration interaction or quantum Monte Carlo schemes. The first is also known as quantum jumps and constitutes a well-known and effective approach for open quantum systems [66–69,84], which could be implemented for the purposes of AMEA either within ED or MPS. Such alternative solution strategies are an interesting topic to be explored and could greatly improve the applicability of AMEA to different physical situations.

With the present ED- and especially the MPS-solver many unresolved properties of the nonequilibrium SIAM still have to be studied. Of advantage is hereby the freedom in AMEA to choose different parameters in the physical impurity problem and the accurate resolution over the whole frequency domain. This enables us to directly extend the range and to look into other parameter regimes away from particle-hole symmetry as well. In particular, the interesting situation of the SIAM in magnetic fields is currently examined, which is furthermore very relevant for experiments. In general, since the developed solvers allow us to address the nonequilibrium Anderson and not only the Kondo model, a realistic effective description of true experimental systems up to larger energy scales can probably be achieved. Such comparisons are presently undertaken and may give valuable input for

experiments. Besides the nonequilibrium SIAM in a magnetic field, also its thermoelectric properties are currently investigated. This is an interesting fundamental issue and furthermore, is again relevant for experiments due to the controlled realization in semiconductor quantum dots for instance. In addition to these steady state properties, AMEA is generalized on the impurity level in a straight-forward manner to the time-dependent case, in order to treat quench dynamics or periodically driven systems for instance. The temporal modulation of the bias voltage or impurity parameters is directly realizable, and would enable one to investigate transient dynamics away from equilibrium and the resolution of the involved time scales. With device applications in view this constitutes important information since any molecular transistor or single electron device should ultimately operate at high frequencies.

In general, the development of AMEA is still at an early stage and the first studies presented in this thesis have demonstrated that the approach has great potential for the solution of general nonequilibrium impurity problems. It is probably not exaggerated to optimistically look forward to extensions of the method and to hope that it may contribute to improve the understanding of nonequilibrium impurity problems and to the application of the very successful DMFT idea to nonequilibrium systems.

A. Appendix

A.1. Comments on the chosen Lindblad equation

Here, we briefly want to show that the form of the Lindblad operator stated in Sec. 2.1.2 is the most general one for our purposes. The summation in Eq. (2.8) runs over all system sites so that the number of Lindblad operators scales polynomially in N_B. Usually, the most general Lindblad equation for a system with Hilbert space size $N_{\mathcal{H}}$ contains all possible trace-less system operators and thus on the whole $N_{\mathcal{H}}^2 - 1$. This comes about by combining a complete set of local operators on one site, e.g. $\{c_i^\dagger, c_i, n_i, \mathbb{1}\}$ in the spinless case, with every other site and by forming trace-less expressions [53, 54]. From this one would arrive at a number of Lindblad operators that scales exponentially in N_B and therefore, Eq. (2.8) might seem too restrictive at the first glance. However, since the bath of a generic $\mathrm{IM}_{\mathrm{ph}}$ is noninteracting we need to demand for consistency reasons the same for $\mathrm{IM}_{\mathrm{aux}}$, so that the Markovian environments are only allowed to be quadratic in the fermionic operators. Furthermore, spin-flip terms in $\mathrm{IM}_{\mathrm{ph}}$ and thus also in $\mathrm{IM}_{\mathrm{aux}}$ are not considered, and in order to treat a normal conducting bath anomalous terms are excluded. By this we arrive exactly at the expression as stated in Eq. (2.8).[1]

For the purpose of better understanding the physical picture behind Eqs. (2.6) and (2.8) we briefly consider an arbitrary dissipator written in the usual diagonal form [53, 54]

$$\mathcal{L}_D^{\mathrm{diag.}}\rho = \sum_{k\sigma} 2L_{k\sigma}\rho L_{k\sigma}^\dagger - \{\rho, L_{k\sigma}^\dagger L_{k\sigma}\}\,, \tag{A.1}$$

whereby $L_{k\sigma}$ denotes some set of Lindblad operators. Eq. (2.8) can be brought into this form by diagonalizing the combined coefficient matrix $\mathbf{\Gamma^{(1)}} \oplus \mathbf{\Gamma^{(2)}}$. For simplicity we consider only the second term $\Gamma_{ij}^{(2)} = \sum_k U_{ik}\gamma_k^{(2)}U_{kj}^\dagger$ for which we find the corresponding Lindblad operators

$$L_{k\sigma}^{(2)} = \sum_i \sqrt{\gamma_k^{(2)}}U_{ik}c_{i\sigma}^\dagger\,, \tag{A.2}$$

which are apparently a linear combination of fermionic creation operators. The anti-commutator in Eq. (A.1) affects the propagation of particles inside the system similar to Eq. (2.6) and $L_{k\sigma}\rho L_{k\sigma}^\dagger$ is commonly referred to as jump operator [53, 54] due to its simultaneous action on both sides of the density operator, see also Ref. [66–69, 84]. For our particular case, $L_{k\sigma}^{(1/2)}\rho L_{k\sigma}^{(1/2)\dagger}$ mediates between sectors of different particle number, whereby terms with $\mathbf{\Gamma^{(2)}}$ correspond to particle insertion into the system and terms with $\mathbf{\Gamma^{(1)}}$ to particle extraction. This may further be interpreted as couplings of the system to Markovian environments which are either completely filled or completely empty. Its linear combination eventually determines the particular filling of the system.

[1] Note that terms such as $2n_i\rho\mathbb{1}_j - \{\rho, \mathbb{1}_j n_i\} = [n_i, \rho]$ are absorbed in the unitary part Eq. (2.6).

A.2. Unitary transformations in the auxiliary impurity problem

As noted in Sec. 2.1.2 and Sec. 2.2.1 in the main text, $\mathrm{IM}_{\mathrm{aux}}$ is fully specified by the bath parameters $\boldsymbol{E}$, $\boldsymbol{\Gamma^{(1)}}$ and $\boldsymbol{\Gamma^{(2)}}$, but, on the level of the impurity site an equivalent $\mathrm{IM}_{\mathrm{aux}}$ is obtained when performing a unitary transformation among bath sites only. Consider an arbitrary transformation $\boldsymbol{U}\boldsymbol{U}^\dagger = \boldsymbol{U}^\dagger\boldsymbol{U} = \mathbb{1}$ with $U_{if} = \delta_{if}$ and $U_{fk} = \delta_{fk}$ to new fermionic operators

$$c^\dagger_{k\sigma} = \sum_i c^\dagger_{i\sigma} U_{ik}\,, \tag{A.3}$$

which results in an analogous $\mathrm{IM}_{\mathrm{aux}}$ with modified bath parameters $\boldsymbol{E'} = \boldsymbol{U}^\dagger\boldsymbol{E}\boldsymbol{U}$, $\boldsymbol{\Gamma^{(1)'}} = \boldsymbol{U}^\dagger\boldsymbol{\Gamma^{(1)}}\boldsymbol{U}$ and $\boldsymbol{\Gamma^{(2)'}} = \boldsymbol{U}^\dagger\boldsymbol{\Gamma^{(2)}}\boldsymbol{U}$. Inserting this into Eq. (2.18) yields

$$\begin{aligned}\boldsymbol{G}_0^{R\prime}(\omega) &= \boldsymbol{U}^\dagger\boldsymbol{G}_0^R(\omega)\boldsymbol{U}\,,\\ \boldsymbol{G}_0^{K\prime}(\omega) &= \boldsymbol{U}^\dagger\boldsymbol{G}_0^K(\omega)\boldsymbol{U}\,,\end{aligned} \tag{A.4}$$

which leaves the ff-component of the impurity site unchanged. Since all three matrices $\boldsymbol{E}$, $\boldsymbol{\Gamma^{(1)}}$ and $\boldsymbol{\Gamma^{(2)}}$ are transformed simultaneously it is in general not possible to bring all three into sparse form. Without loss of generality we choose $\boldsymbol{E}$ to be sparse, so that $\boldsymbol{\Gamma^{(1)}}$ and $\boldsymbol{\Gamma^{(2)}}$ are in the most general case dense matrices with $\mathcal{O}(N_B^2)$ parameters. Hereby the particular geometry does not matter and equivalent forms for $\mathrm{IM}_{\mathrm{aux}}$ are obtained when choosing $\boldsymbol{E}$ to be diagonal for bath sites, i.e. a so-called star geometry, or to contain nearest neighbor couplings only, i.e. a single or double chain of bath sites, as long as the Γ-matrices are transformed accordingly. Such a general geometry with $\mathcal{O}(N_B^2)$ is used for the ED-solver described in Sec. 2.2.2.1, since it gives the best possible map $\underline{\Delta}_{\mathrm{aux}}(\omega) \approx \underline{\Delta}_{\mathrm{ph}}(\omega)$ for a chosen system size $N_B + 1$. However, for the MPS-solver described in Sec. 2.2.2.2 it is of great advantage to deal with a $\mathrm{IM}_{\mathrm{aux}}$ with nearest neighbor terms only, i.e. with tridiagonal matrices $\boldsymbol{E}$, $\boldsymbol{\Gamma^{(1)}}$ and $\boldsymbol{\Gamma^{(2)}}$. Since in this case all matrices are sparse, auxiliary systems with a single or a double chain are not equivalent anymore. Also a star geometry with on-site Γ-terms is possible within MPS, in principle. However, tests revealed that the best mapping is obtained in the double chain geometry with nearest neighbor couplings in all three matrices. And interestingly, when further restricting $\mathrm{IM}_{\mathrm{aux}}$ to a setup where $\boldsymbol{\Gamma^{(1)}}$ has nonzero terms only in one of the chains and $\boldsymbol{\Gamma^{(2)}}$ in the other, nearly identical results are obtained. Since this can be interpreted as a filled/empty geometry, see also Sec. 2.2.2.2, it indicates that only $\mathcal{O}(N_B)$ bath parameters are needed to represent a filled/empty bath. To show this, let us briefly consider the toy-model that $\underline{\Delta}_{\mathrm{ph}}(\omega)$ is completely filled, so that $\Delta^K_{\mathrm{ph}}(\omega) = -2i\Im\,\Delta^R_{\mathrm{ph}}(\omega)$ by virtue of Eq. (1.12), which we try to represent with a $\mathrm{IM}_{\mathrm{aux}}$ with $\boldsymbol{\Gamma^{(1)}} = 0$. For any thereby obtained $\mathrm{IM}_{\mathrm{aux}}$ we can always perform a non-unitary transformation $\boldsymbol{V}\boldsymbol{V}^{-1} = \boldsymbol{V}^{-1}\boldsymbol{V} = \mathbb{1}$ among bath sites only which diagonalizes $\boldsymbol{E} - i\boldsymbol{\Gamma^{(2)}}$ for bath indices. In analogous manner as for Eq. (A.4), one finds that $\boldsymbol{G}_0^R$ on the impurity site is not changed by this and thus depends solely on $\mathcal{O}(N_B)$ parameters. Since $\Delta^K_{\mathrm{aux}}(\omega) = -2i\Im\,\Delta^R_{\mathrm{aux}}(\omega)$ no extra degrees of freedom are available for the Keldysh component in this case. On the whole, one thus has effectively $\mathcal{O}(N_B)$ bath parameters to represent a completely filled or empty $\underline{\Delta}_{\mathrm{ph}}(\omega)$.

Bibliography

Own publications within this thesis

[1] A. Dorda, M. Nuss, W. von der Linden, and E. Arrigoni, *Phys. Rev. B* **89**, 165105 (2014).

[2] A. Dorda, M. Ganahl, H. G. Evertz, W. von der Linden, and E. Arrigoni, *Phys. Rev. B* **92**, 125145 (2015).

[3] I. Titvinidze, A. Dorda, W. von der Linden, and E. Arrigoni, *Phys. Rev. B* **92**, 245125 (2015).

[4] A. Dorda, I. Titvinidze, and E. Arrigoni, *Journal of Physics: Conference Series* **696**, 012003 (2016).

[5] M. Nuss, G. Dorn, A. Dorda, W. von der Linden, and E. Arrigoni, *Phys. Rev. B* **92**, 125128 (2015).

[6] F. Schwarz, M. Goldstein, A. Dorda, E. Arrigoni, A. Weichselbaum, and J. von Delft, *ArXiv e-prints, 1604.02050* (2016).

Others

[7] W. Nolting, *Grundkurs Theoretische Physik 7: Viel-Teilchen-Theorie (Springer-Lehrbuch) (German Edition)*, Springer Spektrum, 2009.

[8] J. P. F. LeBlanc, A. E. Antipov, F. Becca, I. W. Bulik, G. K.-L. Chan, C.-M. Chung, Y. Deng, M. Ferrero, T. M. Henderson, C. A. Jiménez-Hoyos, E. Kozik, X.-W. Liu, A. J. Millis, N. V. Prokof'ev, M. Qin, G. E. Scuseria, H. Shi, B. V. Svistunov, L. F. Tocchio, I. S. Tupitsyn, S. R. White, S. Zhang, B.-X. Zheng, Z. Zhu, and E. Gull, *Phys. Rev. X* **5**, 041041 (2015).

[9] W. Metzner and D. Vollhardt, *Phys. Rev. Lett.* **62**, 324 (1989).

[10] A. Georges and G. Kotliar, *Phys. Rev. B* **45**, 6479 (1992).

[11] A. Georges, G. Kotliar, W. Krauth, and M. J. Rozenberg, *Rev. Mod. Phys.* **68**, 13 (1996).

[12] D. Vollhardt, *Annalen der Physik* **524**, 1 (2012).

[13] T. Maier, M. Jarrell, T. Pruschke, and M. H. Hettler, *Rev. Mod. Phys.* **77**, 1027 (2005).

[14] A. Toschi, A. A. Katanin, and K. Held, *Phys. Rev. B* **75**, 045118 (2007).

[15] A. N. Rubtsov, M. I. Katsnelson, and A. I. Lichtenstein, *Phys. Rev. B* **77**, 033101 (2008).

[16] R. Bulla, T. A. Costi, and T. Pruschke, *Rev. Mod. Phys.* **80**, 395 (2008).

[17] E. Gull, A. J. Millis, A. I. Lichtenstein, A. N. Rubtsov, M. Troyer, and P. Werner, *Rev. Mod. Phys.* **83**, 349 (2011).

[18] D. J. Garcia, K. Hallberg, and M. J. Rozenberg, *Phys. Rev. Lett.* **93**, 246403 (2004).

[19] K. G. Wilson, *Rev. Mod. Phys.* **47**, 773 (1975).

[20] P. Schmidt and H. Monien, *ArXiv e-prints, 0202046* (2002).

[21] H. Aoki, N. Tsuji, M. Eckstein, M. Kollar, T. Oka, and P. Werner, *Rev. Mod. Phys.* **86**, 779 (2014).

[22] C. Giannetti, M. Capone, D. Fausti, M. Fabrizio, F. Parmigiani, and D. Mihailovic, *ArXiv e-prints, 1601.07204* (2016).

[23] M. Schiro and M. Fabrizio, *Phys. Rev. Lett.* **105**, 076401 (2010).

[24] M. Eckstein, M. Kollar, and P. Werner, *Phys. Rev. Lett.* **103**, 056403 (2009).

[25] G. Cohen, E. Gull, D. R. Reichman, and A. J. Millis, *Phys. Rev. Lett.* **112**, 146802 (2014).

[26] G. D. Mahan, *Many-Particle Physics*, Plenum Press, New York, 1990.

[27] P. Coleman, *Introduction to Many-Body Physics*, Cambridge University Press, 2016.

[28] A. C. Hewson, *The Kondo Problem to Heavy Fermions*, Cambridge University Press, 1997.

[29] A. M. Clogston, B. T. Matthias, M. Peter, H. J. Williams, E. Corenzwit, and R. C. Sherwood, *Phys. Rev.* **125**, 541 (1962).

[30] M. P. Sarachik, E. Corenzwit, and L. D. Longinotti, *Phys. Rev.* **135**, A1041 (1964).

[31] W. de Haas, J. de Boer, and G. van dën Berg, *Physica* **1**, 1115 (1934).

[32] J. Kondo, *Progress of Theoretical Physics* **32**, 37 (1964).

[33] F. Reininghaus, M. Pletyukhov, and H. Schoeller, *Phys. Rev. B* **90**, 085121 (2014).

[34] P. W. Anderson, *Phys. Rev.* **124**, 41 (1961).

[35] J. R. Schrieffer and P. A. Wolff, *Phys. Rev.* **149**, 491 (1966).

[36] D. C. Langreth, *Phys. Rev.* **150**, 516 (1966).

[37] D. Goldhaber-Gordon, H. Shtrikman, D. Mahalu, D. Abusch-Magder, U. Meirav, and M. A. Kastner, *Nature (London)* **391**, 156 (1998).

[38] S. De Franceschi and W. G. van der Wiel, Kondo Effect in Quantum Dots, in *Handbook of Nanophysics: Nanoparticles and Quantum Dots*, edited by K. D. Sattler, pp. 646–664, CRC, Boca Raton, FL, 2010.

[39] A. Rosch, J. Kroha, and P. Wölfle, *Phys. Rev. Lett.* **87**, 156802 (2001).

[40] P. Fritsch and S. Kehrein, *Phys. Rev. B* **81**, 035113 (2010).

[41] H. Haug and A.-P. Jauho, *Quantum Kinetics in Transport and Optics of Semiconductors*, Springer, Heidelberg, 1998.

[42] J. Schwinger, *J. Math. Phys.* **2**, 407 (1961).

[43] L. P. Kadanoff and G. Baym, *Quantum Statistical Mechanics: Green's Function Methods in Equilibrium and Nonequilibrium Problems*, Addison-Wesley, Redwood City, CA, 1962.

[44] L. V. Keldysh, *Sov. Phys. JETP* **20**, 1018 (1965).

[45] J. Rammer and H. Smith, *Rev. Mod. Phys.* **58**, 323 (1986).

[46] G. Stefanucci and R. van Leeuwen, *Nonequilibrium Many-Body Theory of Quantum Systems*, Cambridge University Press, 2013, Cambridge Books Online.

[47] P. Danielewicz, *Annals of Physics* **152**, 239 (1984).

[48] M. Wagner, *Phys. Rev. B* **44**, 6104 (1991).

[49] A.-P. Jauho, Introduction to the Keldysh nonequilibrium Green's function technique, `https://nanohub.org/resources/1877`, 2006, [Online; accessed May-2016].

[50] Y. Meir and N. S. Wingreen, *Phys. Rev. Lett.* **68**, 2512 (1992).

[51] E. Pavarini, E. Koch, F. Anders, and M. E. . Jarrell, *Correlated electrons: from models to materials*, volume 2 of *Schriften des Forschungszentrums Jülich. Reihe Modeling and simulation*, Forschungszentrum Jülich GmbH, Jülich, 2012.

[52] A. Liebsch and H. Ishida, *Journal of Physics: Condensed Matter* **24**, 053201 (2012).

[53] H.-P. Breuer and F. Petruccione, *The Theory of Open Quantum Systems*, Oxford University Press, 2002.

[54] H. J. Carmichael, *Statistical Methods in Quantum Optics 1: Master Equations and Fokker-Planck Equations*, Springer, 2010.

[55] G. Schaller, Non-Equilibrium Master Equations, `http://wwwitp.physik.tu-berlin.de/~schaller/download/NEQME1.pdf`, 2014, [Online; accessed May-2016].

[56] A. Donarini, G. Begemann, and M. Grifoni, *Nano Letters* **9**, 2897 (2009).

[57] H. G. Evertz, Computer Simulations, `https://itp.tugraz.at/~evertz/Computersimulationecs2009.pdf`, 2009, [Online; accessed May-2016].

[58] B. A. Berg, *Introduction to Markov Chain Monte Carlo Simulations and their Statistical Analysis*, chapter 1, pp. 1–52, World Scientific Publishing Company, 2005.

[59] B. A. Berg, *Fields Inst.Commun.* **26**, 1 (2000), ArXiv e-prints: 9909236.

[60] K. Hukushima and K. Nemoto, *Journal of the Physical Society of Japan* **65**, 1604 (1996).

[61] D. J. Earl and M. W. Deem, *Phys. Chem. Chem. Phys.* **7**, 3910 (2005).

[62] D. A. Kofke, *The Journal of Chemical Physics* **117**, 6911 (2002).

[63] N. Rathore, M. Chopra, and J. J. de Pablo, *The Journal of Chemical Physics* **122** (2005).

[64] A. Kone and D. A. Kofke, *The Journal of Chemical Physics* **122** (2005).

[65] H. G. Katzgraber, S. Trebst, D. A. Huse, and M. Troyer, *Journal of Statistical Mechanics: Theory and Experiment* **2006**, P03018 (2006).

[66] J. Dalibard, Y. Castin, and K. Mølmer, *Phys. Rev. Lett.* **68**, 580 (1992).

[67] K. Mølmer, Y. Castin, and J. Dalibard, *J. Opt. Soc. Am. B* **10**, 524 (1993).

[68] H.-P. Breuer, B. Kappler, and F. Petruccione, *Phys. Rev. A* **56**, 2334 (1997).

[69] B. Kappler, *Beschreibung offener Quantensysteme durch stochastische Prozesse im Hilbertraum*, PhD thesis, Albert-Ludwigs-Universität Freiburg, 1998.

[70] A. A. Dzhioev and D. S. Kosov, *J. Chem. Phys.* **134**, 044121 (2011).

[71] Y. Saad, *Numerical Methods for Large Eigenvalue Problems, Revised Edition*, Society for Industrial and Applied Mathematics, 2011.

[72] P. Arbenz, Lecture Notes on Solving Large Scale Eigenvalue Problems, `http://people.inf.ethz.ch/arbenz/ewp/lnotes.html`, 2012, [Online; accessed May-2016].

[73] Z. Bai, J. Demmel, J. Dongarra, A. Ruhe, and H. van der Vorst, *Templates for the Solution of Algebraic Eigenvalue Problems: A Practical Guide (Software, Environments and Tools)*, Society for Industrial and Applied Mathematics, 1987.

[74] M. H. Gutknecht, The Unsymmetric Lanczos Algorithms And Their Relations To Pade Approximation, Continued Fractions, And The QD Algorithm, `http://www.math.ethz.ch/~mhg/`, 1990, [Online; accessed May-2016].

[75] B. N. Parlett, D. R. Taylor, and Z. A. Liu, *Mathematics of Computation* **44**, pp. 105 (1985).

[76] R. Freund, M. Gutknecht, and N. Nachtigal, *SIAM Journal on Scientific Computing* **14**, 137 (1993).

[77] H.-G. Weikert, H.-D. Meyer, L. S. Cederbaum, and F. Tarantelli, *The Journal of Chemical Physics* **104**, 7122 (1996).

[78] H.-D. Meyer and S. Pal, *The Journal of Chemical Physics* **91**, 6195 (1989).

[79] G. H. Golub and G. Meurant, *Numerical Analysis 1993* **303**, 105 (1994).

[80] G. L. Lagomasino, L. Reichel, and L. Wunderlich, *Linear Algebra and its Applications* **429**, 2540 (2008), Special Issue in honor of Richard S. Varga.

[81] T. J. Park and J. C. Light, *The Journal of Chemical Physics* **85**, 5870 (1986).

[82] N. Mohankumar and S. M. Auerbach, *Computer Physics Communications* **175**, 473 (2006).

[83] J. Eisert, M. Cramer, and M. B. Plenio, *Rev. Mod. Phys.* **82**, 277 (2010).

[84] U. Schollwöck, *Annals of Physics* **326**, 96 (2011).

[85] F. Verstraete, V. Murg, and J. Cirac, *Advances in Physics* **57**, 143 (2008).

[86] S. R. White and A. E. Feiguin, *Phys. Rev. Lett.* **93**, 076401 (2004).

[87] T. Barthel, U. Schollwöck, and S. R. White, *Phys. Rev. B* **79**, 245101 (2009).

[88] J. Haegeman, J. I. Cirac, T. J. Osborne, I. Pižorn, H. Verschelde, and F. Verstraete, *Phys. Rev. Lett.* **107**, 070601 (2011).

[89] C. Karrasch, J. H. Bardarson, and J. E. Moore, *Phys. Rev. Lett.* **108**, 227206 (2012).

[90] F. A. Wolf, I. P. McCulloch, and U. Schollwöck, *Phys. Rev. B* **90**, 235131 (2014).

[91] P. Corboz, R. Orús, B. Bauer, and G. Vidal, *Phys. Rev. B* **81**, 165104 (2010).

[92] M. Zwolak and G. Vidal, *Phys. Rev. Lett.* **93**, 207205 (2004).

[93] T. Prosen and M. Žnidarič, *J. Stat. Mech.* **2009**, P02035 (2009).

[94] T. Prosen and M. Žnidarič, *Phys. Rev. B* **86**, 125118 (2012).

[95] L. Bonnes, D. Charrier, and A. M. Läuchli, *Phys. Rev. A* **90**, 033612 (2014).

[96] L. Bonnes and A. M. Läuchli, *ArXiv e-prints, 1411.4831* (2014).

[97] J. Cui, J. I. Cirac, and M. C. Bañuls, *Phys. Rev. Lett.* **114**, 220601 (2015).

[98] E. Mascarenhas, H. Flayac, and V. Savona, *Phys. Rev. A* **92**, 022116 (2015).

[99] H. Weimer, *Phys. Rev. Lett.* **114**, 040402 (2015).

[100] G. Vidal, *Phys. Rev. Lett.* **91**, 147902 (2003).

[101] G. Vidal, *Phys. Rev. Lett.* **93**, 040502 (2004).

[102] X. Wang and H.-G. Matuttis, *Journal of the Physical Society of Japan* **81**, 104002 (2012).

[103] G. Strang, *SIAM Journal on Numerical Analysis* **5**, 506 (1968).

[104] R. I. McLachlan and P. Atela, *Nonlinearity 5* , 541 (1992).

[105] D. Kennes and C. Karrasch, *Computer Physics Communications* **200**, 37 (2016).

[106] E. Arrigoni, M. Knap, and W. von der Linden, *Phys. Rev. Lett.* **110**, 086403 (2013).

[107] E. Assmann, P. Blaha, R. Laskowski, K. Held, S. Okamoto, and G. Sangiovanni, *Phys. Rev. Lett.* **110**, 078701 (2013).